On the Radiative Processes Associated with the Tropical Mesoscale Convective Systems

By
Takmeng Wongand Graeme L. Stephens

Department of Atmospheric Science
Colorado State University
Fort Collins, Colorado

Research supported by NSF grant ATM-8617856, ATM-8812353 and ATM-9100795, and by the NASA grant NAG5-1592S-03.
PI: G. Stephens

Colorado State University

Department of Atmospheric Science

Paper No. 547

ON THE RADIATIVE PROCESSES ASSOCIATED WITH THE TROPICAL MESOSCALE CONVECTIVE SYSTEMS

Takmeng Wong and Graeme L. Stephens

Research supported by National Science Foundation grants #ATM-8617856, #ATM-8812353, & #ATM-9100795, and by the National Aeronautics and Space Administration (NASA) grant #NAG5-1592S-03.

Principal Investigator: Graeme L. Stephens

Department of Atmospheric Science
Colorado State University
Fort Collins, CO 80523

February, 1994
Atmospheric Science Paper No. 547

ABSTRACT

ON THE RADIATIVE PROCESSES ASSOCIATED WITH THE TROPICAL MESOSCALE CONVECTIVE SYSTEMS

The goal of this research is to improve our understanding of the spatial and temporal characteristics of the radiative budget of the tropical mesoscale convective systems (MCSs) and to explore any possible effects of radiation on the atmosphere and the evolution of the tropical MCSs. A combination of two dimensional cloud model simulations, two-stream radiative transfer model calculations, observational analyses, and comparisons with other published results are used to achieve this goal.

The observational analyses of the two tropical cloud clusters show significant similarities in the internal structures of these two systems even though the large scale background environments of these cloud clusters are very different from each other. The results of the cloud model simulations for these two tropical cloud clusters using the Regional Atmospheric Modeling System (RAMS) developed at Colorado State University, in general, agree well with observations. Some disagreements exist however due to uncertainties in the initial conditions and to the two dimensionality of the cloud simulations. These cloud simulations are then used to provide microphysical and thermodynamical information for the radiative transfer model. The resultant radiative calculation indicates that the tropical cloud clusters can significantly affect both the radiative budget and the radiative heatings profile of the tropical atmosphere. These radiation calculations also indicate significant spatial variability in the radiative heating associated with these tropical cloud systems. While the major effects of the tropical cloud clusters in the infrared spectrum are to decrease the net outgoing radiative energy to space and to increase the net infrared flux to

the surface, the consequences of solar processes in these systems are to redistribute the vertical solar heating from the surface to the upper troposphere through reduction in surface solar insolation and increment of solar absorption in the atmosphere. This reduction in surface insolation can play an important role in the surface energy budget in the tropics. While the combined effects of both solar and infrared processes of these cloud systems can create an area of positive energy surplus in the cloudy atmosphere during the daytime hours, the persistence of the infrared radiative processes throughout the night produce an area of relative energy surplus in the cloudy atmosphere with respect to the surrounding clear skies. The differences in the radiative heating profiles between the clear skies and the cloudy atmosphere can be as large as 2 to 8 K/day. Furthermore, the temporal effects of these tropical MCSs are the increases in the domain-average radiative convergence/column radiative heating with time. Relative to the clear skies, these tropical MCSs represent an effective radiative heat source for the tropical atmosphere.

A cloud microphysics-radiation-thermodynamics-dynamics feedback is hypothesized to link the cloud-induced atmospheric radiative heat source to the evolution of the tropical clusters. The physical principle behind this proposed coupling is based on the interactions between the surface which supplies the energy to the systems and a forced secondary circulation produced by differential radiative heating between the clear sky and the cloudy atmosphere (i.e., Gray and Jacobson, 1977). Due to the nature of this coupling, it is hypothesized further that the strength of this feedback is a function of both the profile of the vertical shear and the lower level stability conditions of the background environment. For example, this coupling is shown to be most effective in modifying the energy budget and the circulation of the tropical MCSs and their surrounding tropical atmosphere when the background atmosphere is characteristized by a weak vertical shear profile and unstable lower levels. Furthermore, this feedback is also shown to become important in the latter stages of the MCS evolution, significantly prolonging the convective activity of theses systems. As the background environmental shear or lower levels stability increases, the effects of this feedback are shown to decrease. In addition to these sensitivities, these results also indicate the effects of atmospheric infrared radiative cooling in modifying

the behavior of this cloud radiative feedback. For example, numerical simulations with background environment characteristized by a weak vertical shear and stable lower level indicate that the persistence effects of atmospheric infrared cooling at night can weaken or destroy the stability of the lower level and allow the coupling between the cloud radiation-induced secondary circulation and the tropical MCSs to occur. Since a significant portion of the tropical atmosphere can be classified by these two examples of background environments, this cloud radiative feedback can have significant consequences in (1) the energy and the water budget of the tropical atmosphere, (2) the diurnal variations of tropical cloud clusters/deep convections, and (3) the equilibrium regional climate of the tropical atmosphere.

Takmeng Wong
Department of Atmospheric Science
Colorado State University
Fort Collins, Colorado 80523
Spring, 1994

ACKNOWLEDGEMENTS

We are indebted to many others for their support during the researching, preparing, and writing of this work. We would like to specially thank the following individuals, William Cotton, Steven Rutledge, Mel Nicholls, Paul Stackhouse, Frank Evans, Bill Thorson, Robert Cifelli, Raymond Zehr, and Brian Mapes. We also gratefully acknowledge Sue Lini for secretarial supports and Judy Dunn for drafting the figures.

This research was supported by the National Science Foundation (NSF) grant ATM-8617856, ATM-8812353, and ATM-9100795, and the National Aeronautics and Space Administration (NASA) grant NAG5-1592S-03. Computer calculations were partially carried out using the super computer facilities at National Center for Atmospheric Research (NCAR). NCAR is partially supported by NSF. EMEX aircraft data were provided by the National Hurricane Center of the National Oceanic and Atmospheric Administration (NOAA). The EMEX aircraft Doppler radar data were made available by Brian Mapes. The AMEX sounding and AMEX synoptic data set were furnished by the Australian Bureau of Meteorological Research Center (BMRC). The STEP radiation data were obtained from the NASA AMES Research Center. The satellite data set were kindly made available by Raymond Zehr. The DUNDEE Radar and wind profiler data set were provided by Professor Steven Rutledge and his students.

CONTENTS

LIST OF FIGURES

LIST OF TABLES

Chapter 1

INTRODUCTION

It is generally recognized that most of the weather occurring in the tropics is associated with the passage of the tropical mesoscale convective systems (MCSs) or the so-called tropical cloud clusters (Hamilton and Archbold, 1945; Ramage, 1971; Houze, 1976; Simpson, Adler, and North, 1988). These systems, once formed, last several hours and are thought to provide significant impacts on the dynamics, thermodynamics, radiation, and the water budgets of the large-scale atmosphere (Hartmann *et al.*, 1984; Cotton and Anthes, 1989).

1.1 Structures of Tropical Mesoscale Convective Systems

Composite studies from field experiments such as Barbados Oceanographic and Meteorological Experiment (BOMEX), the Global Atmospheric Research Program's Atlantic Tropical Experiment (GATE), and Winter Monsoon Experiment (WMONEX) have provided conceptual ideas of the structure of these tropical cloud systems (Nitta and Esbensen, 1974; Zipser, 1977; Houze, 1977; Gamache and Houze, 1982, 1983, 1985; Houze and Rappaport, 1984; Churchill and Houze, 1984, and others). Specifically, these studies have identified the existence of two basic types of MCSs in the tropics; the intense squall-type and the weaker nonsquall MCSs. These two types of MCSs can either exist separately or coexist together in the tropics. The life cycle of these tropical cloud clusters can be characteristized by a formative or intensification stage in which convective cells dominate, a mature stage in which convective and stratiform precipitation coexist, and a dissipating stage in which the stratiform precipitation prevails and slowly decays.

The tropical squall-type MCS is composed of a line of vigorous convective cells (shown in Fig. 1.1) with a horizontal dimension of 100's km along its major axis and is formed in

a background environment which has a strong vertical shear profile along its direction of propagation. The initialization of these MCSs is usually associated with local instability (i.e., surface heating), cloud to cloud interaction (such as collision of cloud surface outflow boundaries), and sea/land breezes. These types of MCSs most often exist over land surfaces, but are also observed over the open ocean. A cross-sectional view of a mature squall-type tropical cloud cluster (shown in Fig. 1.2) is characterized by a leading convective region (order of 10's km) and a trailing mesoscale stratiform area (order of 100's km). The convective region contains active cumulonimbus cells with strong, small-scale, nonhydrostatic vertical motion (LeMone, 1983). These convective cells tend to merge into the mesoscale region as they mature. The mesoscale region, on the other hand, fills with middle to upper tropospheric stratiform cloud in which gentle broad-scale hydrostatic vertical motion exists (Houze, 1982). Upward motion above the melting level is considered to be an important source for precipitation in the stratiform region (Rutledge, 1986). This type of system can last for an extensive period of time with new cells forming at the leading edge of the line and older mature cells merging into the mesoscale region in the rear of the system.

The nonsquall-type tropical MCSs, on the other hand, dominate over the tropical oceanic area and do not have distinct mesoscale precipitation features. The mesoscale region in this type of system can be found either to the rear of or surrounding the convective cells (shown in Fig. 1.3) and are composed of left-over debris from the previous convection. Mesoscale ascent is also an important source of hydrometeors in these systems. Their formation is usually associated with the passage of large-scale disturbances in the tropical atmosphere (i.e., monsoon trough, easterly wave, and ITCZ). The convective cells seem to be incorporated into the surrounding stratiform region as they mature. The large stratiform region in these systems can produce significant amount of precipitation (Cotton and Anthes, 1989). The updraft speeds and the background vertical shear profile in these cloud clusters are generally weaker than those found in the squall-type MCSs. Nonsquall tropical MCSs can last for days depending on the lifetime of the large-scale disturbances.

Although there are differences within these two types of MCSs, many similarities also exist. For example, the individual cell elements within them do go through similar life

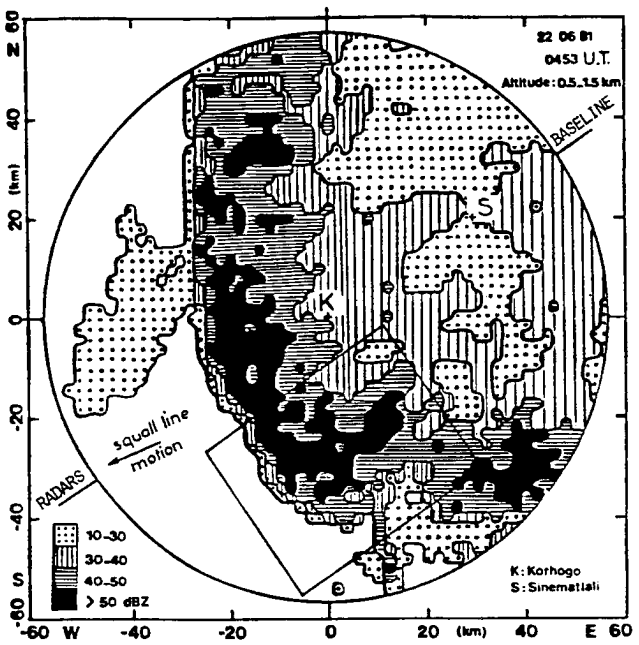

Figure 1.1: Low level horizontal radar scan of a squall-type tropical MCS showing leading convections and trailing stratiform region (after Chauzy *et al.*, 1985).

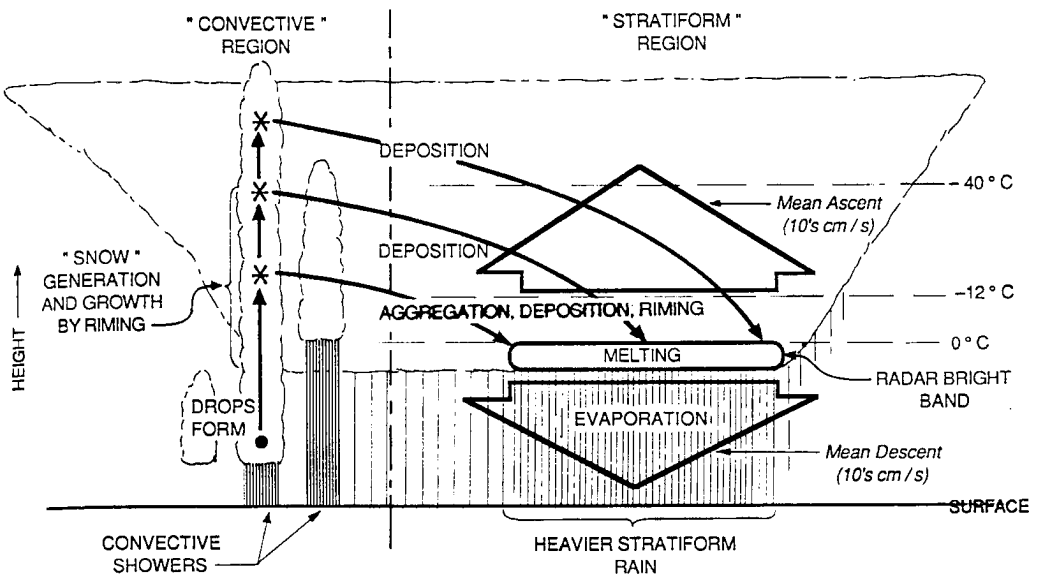

Figure 1.2: A composited vertical structures of squall-type tropical MCS (after Houze, 1989).

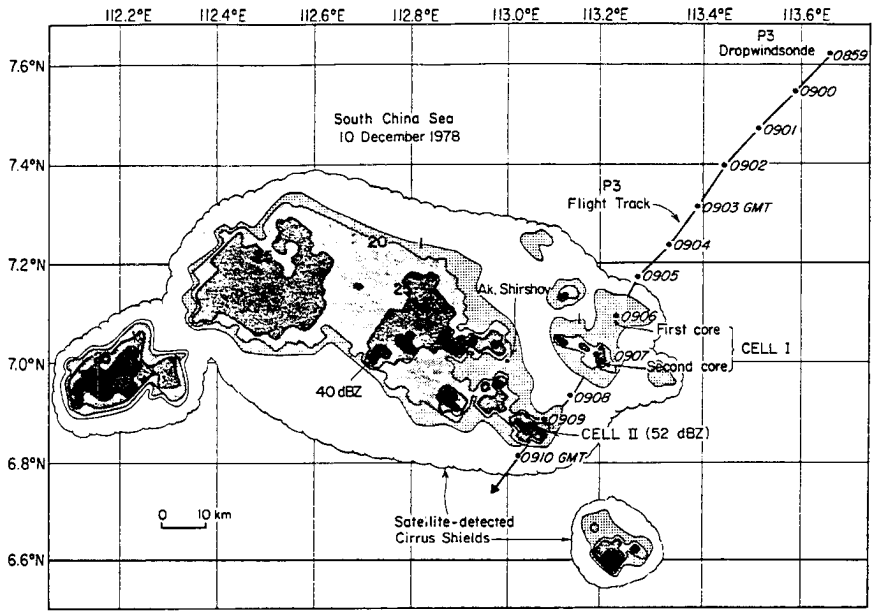

Figure 1.3: Low level horizontal radar view of a nonsquall-type tropical MCS showing an extensive region of stratiform area with embedded convections (after Churchill and Houze, 1984).

cycles, and they produce significant precipitation. The precipitation structures during the mature stage of the nonsquall MCSs often resemble those of the mature squall-type MCSs with new convective cells forming and merging and being incorporated into the stratiform region. Furthermore, the presence of these systems (squall or nosquall) can significantly modify the diabatic energy budget (i.e., latent and radiative energy) of the larger scale atmosphere.

1.2 Diabatic Heating Processes Associated with Tropical MCS

The diabatic heating (latent plus radiative heating) associated with tropical MCSs is an important source of energy for large-scale tropical circulation (Riehl and Malkus, 1958). A number of studies (Yamasake, 1969; Lindzen, 1974; Chang, 1976; Stevens *et al.*, 1977, and others) of tropical storm movement and propagation based on wave-CISK theory indicate that the phase speed and the intensity of tropical systems are very sensitive to the initial profile of diabatic heating. For example, Houze (1982,1989), using a composite vertical motion field and a very crude radiative heating profile of a tropical MCS, estimated

that the net diabatic heating (latent plus radiative heating) associated with a tropical MCS has a peak above 600 mb (see Fig. 1.4). This upper level heating maximum is a product of the effects of (a) latent heating which is distributed throughout the entire troposphere and (b) radiative heating which is confined only to the upper portion of the troposphere. Hartmann *et al.* (1984) using this profile of diabatic heating and a general circulation model claim that the tropical general circulation pattern is significantly altered based on the position of the heating maximum. Therefore a correct representation of the diabatic heating (i.e., latent and radiative heating) processes is very important to our understanding on the dynamics and energetics of the large-scale tropical environment as well as the earth climate system.

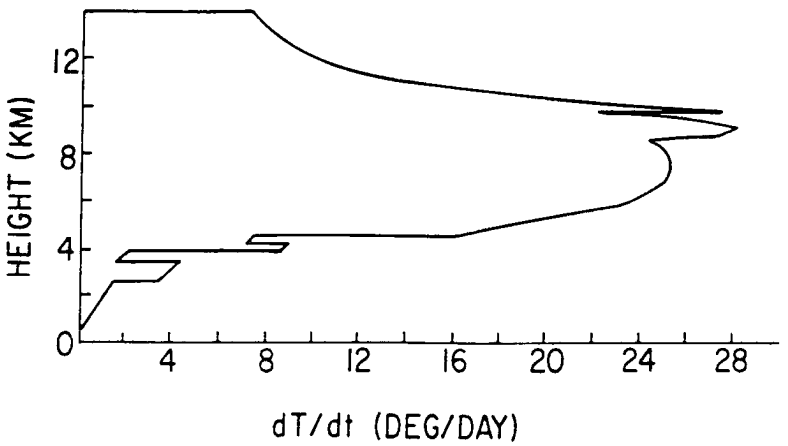

Figure 1.4: An estimated vertical structures of diabatic heating profile associated with an idealized tropical MCS (after Houze, 1989).

1.2.1 Latent Heating

Latent heat processes, such as condensation, evaporation, and melting associated with vertical air motion in the tropical cloud clusters, have been studied extensively in the literature. According to these studies, latent heating is a primary source for the initialization of many tropical MCSs (Riehl and Malkus, 1961; Ooyama, 1964; Charney and Eliassen, 1964) and affects the large-scale motion fields through vertical transports of energy, moisture, and momentum (Zipser, 1977; Houze and Betts, 1981) once the MCS is

formed. Many recent studies (i.e., Houze, 1989) have also pointed out that the vertical latent heating profile in a mature MCS is composed of heating by both convective and mesoscale processes. In the convective region, the vertical latent heating profile (shown in Fig. 1.5a) is dominated by the release of latent heat due to condensation. The latent heating profile in the mesoscale region (given in Fig. 1.5b), on the other hand, is dominated by condensational and depositional heating in the middle to the upper troposphere and evaporational cooling in the lower troposphere. The combined latent heating profile (convective plus mesoscale) shows an enhanced heating profile in the upper troposphere and a suppressed heating profile in the lower troposphere. This is consistent with results given by the early study of the large-scale Q1 (i.e., apparent heat source) and Q2 (i.e., moisture sink) budgets (Yani *et al.*, 1973) from large-scale sounding data, which indicated that the effects of MCSs are to heat the upper troposphere; and to export moisture or latent energy from the lower to the upper troposphere.

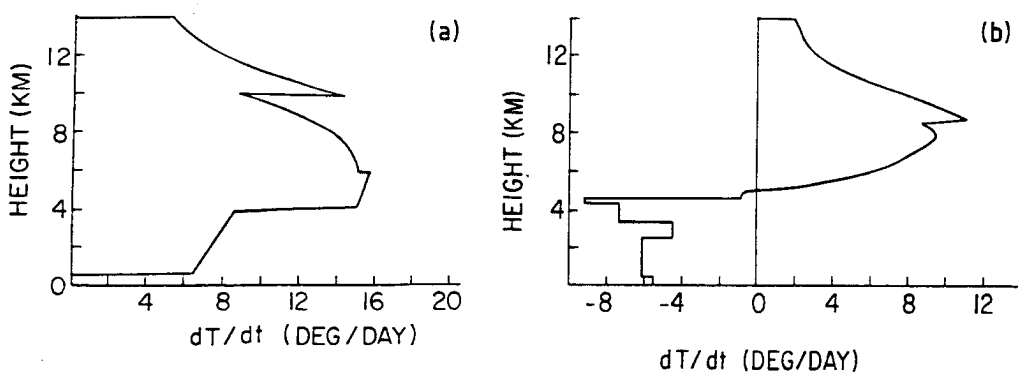

Figure 1.5: An estimated vertical structures of latent heating profile in (a) the convective and (b) the stratiform region of an idealized tropical MCS (after Houze, 1989).

1.2.2 Radiative Heating

In contrast to latent heating, the radiative heating processes associated with these tropical MCSs have not been addressed extensively in the literature. A number of recent

studies are now beginning to point to the active role of radiative processes both to the tropical MCSs and to the large-scale tropical circulation. For example, radiative budgets derived from both the Line Islands Experiment (Albrecht and Cox, 1975) and the GATE experiment (Cox and Griffith, 1978) indicate significant modulation of radiation by these tropical cloud clusters. Albrecht and Cox (1975) and Gray and Jacobson (1977) propose that a large-scale secondary circulation may be induced by these differences in clear air and cloudy air radiative heating. In addition, this cloud-radiatively-induced secondary circulation is also thought to provide a source of feedback that may recharge the dynamics of these tropical cloud clusters during the early morning hours of the day (Gray and Jacobson, 1977). In the mesoscale region of these cloud systems, the contribution of radiation to the total diabatic heating profile is believed to be significant due to radiative flux divergence in the presence of the extensive upper tropospheric cloud shields (Webster and Stephens, 1980). Ackerman *et al.* (1988) have further demonstrated that radiative heating on the order of 20 to 30 K/day is realized in tropical anvil clouds. Radiative heating rates may be a source for buoyant turbulence in the anvils (Lilly, 1988), and perhaps produce significant mesoscale circulations. The modeling study of Chen and Cotton (1988) also shows how radiative heating and cooling modulate circulation patterns in the mesoscale region of a mid-latitude MCS by destabilizing the stratiform cloud region. Churchill and Houze (1991), however, conclude that radiation does not substantially change the hydrometeor fields in their two-dimensional kinematic model, and thus had no effect on the water budget of the tropical precipitating stratiform region. Since radiation does not directly affect the water budget of the stratiform region, they propose any radiative effect on hydrometeors must involve interaction with dynamics. Dudhia (1989) proposes that radiative heating is an important forcing of the vertical motion in the upper troposphere. In addition, radiative clear-air cooling can further aid the convection by continuously destabilizing the troposphere. Stuhlmann and Smith (1988a,b) further suggest that cloud-generated radiative heating can affect the general circulation of the atmosphere by altering the generation of the available potential energy.

Although these studies provide insight into the roles of radiative processes in cloud clusters, they did not fully address many topics that are important to the overall radiative

energy budgets of the tropical atmosphere. For example, it is well known that tropical MCSs significantly influence both the surface radiation energy budget and the radiative heating of the tropical atmosphere. The changes in the vertical structure of this heating are important to the general circulation of the tropical atmosphere (i.e., those proposed by Hartmann *et al.*, 1984). The nature of the radiative heating and the radiative budget profile (i.e., identifying spatial and temporal characteristics) associated with these tropical systems, however, have not been studied adequately. The composite study of Cox and Griffith (1978) has provided some insights into this problem. Their results, however, are somewhat limited and represent only a spatial and temporal averaged radiative profile due (1) to the lack of detailed descriptions of cloud microphysical characteristics of the cloud clusters, (2) to the large spatial domain of the experiment, and (3) to the poor temporal resolution of the data set. Without detailed radiation information, it is difficult to quantify the actual effects of these cloud systems on the global climate or to parameterize them in a general circulation model. Furthermore, previous studies on how these radiative effects can feedback to the dynamics and energetics of these cloud systems have been quite limited and emphasized only the mesoscale-anvil structures of these cloud systems. Thus, there is a need to study this cloud-induced radiative feedback on the evolution of tropical MCS in a more general and quantitative fashion. Specifically, the new study should be based on a theory that emphasizes physical relationships between the cloud-induced vertical heating profile, the circulation of the tropical atmosphere, the evolution of the whole cloud cluster, and the background environment associated with these cloud systems. This cloud-induced radiative feedback is an important issue in the tropical atmosphere since it can alter the transport of total moisture and energy by these systems. The work of Gray and Jacobson (1977) is an example of this type of study. Their proposed feedback, however, is based on observational evidence and has not been studied with a detailed cloud-resolving model.

1.3 Scientific Objectives and Methodology

The main goal of this work aims to improve the scientific understanding on the nature (i.e., spatial/temporal characteristics and variability) of the radiative heating/budget

associated with the tropical MCSs and their effects on both the environment and the evolution of the tropical MCSs. In order to obtain the radiation budget/heating distribution within a tropical MCS, one can approach this problem either from an observational perspective or from numerical modeling perspective.

In the first approach the radiation heating fields can be obtained either by measuring the cloud radiation field directly or by calculating the radiation field given relevant information about the observed cloud systems. This approach poses a significant challenge for the present research. It is clearly not possible to provide a complete three dimensional distribution of observed radiation fluxes nor is it possible to provide all other necessary information (i.e., cloud hydrometeor fields, temperature fields) about the observed cloud systems that can be used to reconstruct the radiation fields. The alternative approach to this problem is to simulate the bulk time evolution of the cloud thermodynamical and bulk hydrometeor's fields from a numerical dynamical cloud/mesoscale model and calculate the radiation budget/heating fields using the information from these simulations. The disadvantage of the latter method is that it depends on the quality of the numerical simulations in capturing the structure and the physics of these cloud systems. Thus additional steps (i.e., comparison with available observation or other published results) must be taken to ensure the quality of these numerical results. The latter approach is chosen for this research due to the lack of specified observations needed to complete our tasks.

For the current study a combination of cloud model simulations, radiation model simulations, and analyses of observations for two case studies of tropical squall lines; one case from the joint Equatorial Mesoscale Experiment (EMEX), the Stratospheric Tropospheric Exchange Program (STEP), and the Australian Monsoon Experiment (AMEX) and another case from the Down Under Doppler and Electricity Experiment (DUNDEE); are used to achieve this goal. Specifically, the following tasks are carried out.

1. Analyze observational data for the two case studies provided by the EMEX-STEP-AMEX and the DUNDEE experiment. This involves studying data collected from aircraft, satellite, conventional rawinsonde, and Doppler radars and identifying major observational features associated with the cloud systems. The purpose of this

is to establish the observational bases for which the numerical simulations are compared with and (if possible) to identify physical processes that are important to the formation and evolution of the cloud system.

2. Perform numerical simulation of two case studies, analyze the results, and verify them against observation to the fullest extent possible. The goal here is to establish the credibility of the numerical simulated cloud system and to set up the basis for further analysis in the study.

3. Study the spatial and temporal characteristic and variability of the radiation profiles produced by these cloud simulations and examine their effects on the atmosphere.

4. Derive vertical structures of radiative heating profile associated with these cloud cluster simulations and their relationship to the clear sky radiative heating profile.

5. Propose a theory of cloud microphysics-radiation-thermodynamics-dynamics couplings associated with the tropical cloud clusters, which emphasized on physical relationships between the cloud-induced vertical heating profile, the circulation of the tropical atmosphere, the evolution of the whole cloud cluster, and the background environment associated with these tropical cloud systems.

6. Evaluate this theory using numerical modeling.

1.4 Plan of This Research

Chapter 2 and 3 give an overview of the numerical cloud/mesoscale model and the radiative transfer model that were used in simulating the cloud structures and cloud radiation fields in this work. Chapter 4 describes the observational experiments and the data analyses associated with the case studies considered. The cloud model results for the case studies are given in Chapter 5. Their corresponding radiation heating/budget fields are shown in Chapter 6 along with analyses of their effects on the tropical environment. In Chapter 7 a theory of cloud microphysics-radiation-thermodynamics-dynamics couplings associated with the tropical MCSs, which is based on those of Gray and Jacobson (1977),

is proposed and a set of numerical experiments is used to address this hypothesized feedback (i.e., the responses of the tropical atmosphere to cloud-induced radiative heating, the effects of these radiative heating on the evolution of the tropical MCS, and their relationships to the background environments). Final summary of this research is presented in Chapter 8.

Chapter 2

DYNAMICAL CLOUD/MESOSCALE MODEL

The main goals of this research are to document the spatial characteristic and the temporal evolution of radiation budget/heating associated with tropical mesoscale convective systems (MCSs) and to evaluate the possible effects of radiative heatings on the tropical environment and on the evolution of these tropical cloud systems. In order to obtain the radiation budget/heating distribution within a tropical MCS, a combination of numerical cloud modeling and radiative transfer modeling is used. The dynamical cloud/mesoscale model and its mathematical framework will be the subject of discussion in this chapter. The general features of the diagnostic radiation model used to calculate the radiation budget/heating fields are given in the next chapter.

2.1 General Description

The dynamical cloud/mesoscale model used in this research is the Regional Atmospheric Modeling System (RAMS) developed at Colorado State University. This numerical model is a flexible general purpose dynamical model for simulating atmospheric phenomena with scales ranging from tens of meters (i.e., non-hydrostatic and compressible large eddies simulation) to thousands of kilometers (such as hydrostatic regional weather forecasting). It has been used extensively for studies of cumulus, stratus, cirrus, tornadoes, thunderstorms, mesoscale convective systems, frontal cloud, orographic clouds, tropical systems, and other atmospheric systems (i.e., Cotton and Tripoli, 1978; Tripoli, 1986; Chen and Cotton, 1987; Nicholls, 1987; Cram *et al.*, 1992; Pielke *et al.*, 1992; and others).

There are ten predictive variables in the model including three dynamical (i.e., all three components of the velocity (u, v, and w)) and seven thermodynamical variables (the exner function (π), ice-liquid water potential temperature (θ_{il}), total water mixing

ratio (r_T), rain mixing ratio (r_r), pristine ice crystal mixing ratio (r_i), graupel mixing ratio (r_g), and aggregate mixing ratio (r_a)). Other thermodynamical quantities, such as atmospheric pressure (p), potential temperature (θ), cloud water mixing ratio (r_c), water vapor mixing ratio (r_v), and air density (ρ), are diagnostically determined from the predictive variables. The physical parameterizations in the model include those describing subgrid-scale turbulences, the surface fluxes of heat, moisture, and momentum, radiative heating tendencies, and microphysics.

In the following sections a brief mathematical framework of this numerical model based on those described by Cotton and Tripoli (1978), Tripoli and Cotton (1980,1982), Cotton *et al.* (1982, 1986), Tripoli (1986), and Cotton and Anthes (1989) will be given. Readers are referred to these references for more details of the model.

2.2 Basic Setup for Model Variables and Model Coordinate System

The non-hydrostatic and fully compressible version of the RAMS model is utilized in the current study. As described by Cotton and Tripoli (1978), Tripoli and Cotton (1980, 1982), and Cotton *et al.* (1982, 1986), this model is based on quasi-Boussinesq approximation of Dutton and Fichtl (1967). Since the model permits both elasticity and variation of the base state with height, it is valid for deep convective clouds over a large area as long as the departure of any variables from their base state in the domain is small. Using this approximation, a variable A in the model may be broken down as

$$\begin{aligned} A(x,y,z,t) &= \overline{A}(x,y,z,t) + A''(x,y,z,t) \\ &= A_o(z) + \overline{A'}(x,y,z,t) + A''(x,y,z,t) \end{aligned} , \tag{2.1}$$

where the overbar term represents the averaging operator over a time and space scale resolvable by the numerical model and the double prime term represents the perturbation from that average (i.e., the subgrid-scale fluctuations from the resolvable scale perturbation). The overbar term can be decomposed further into two separate terms; an arbitrary horizontally homogeneous reference state (i.e., the null term) and the resolvable deviations from that reference state (such as the single prime term). As in the full Boussinesq form, the terms involving the ratios of perturbation quantities to their base state is neglected in the equations of motion except for the case where the ratio is multiplied by gravity.

The model is formulated on an energy-conserving, Arakawa-C, staggered grid (Arakawa and Lamb, 1977). The vertical coordinate system is based on the terrain following sigma-z system of Gal-Chen and Sommerville (1975), in which the normal Cartesian coordinates (x,y,z) are transformed into the new coordinate system (x^*,y^*,z^*) by

$$x^* = x \quad , \quad y^* = y \quad , \quad z^* = H\frac{(z - z_s)}{(H - z_s)}, \tag{2.2}$$

where H is the height of the model and z_s is the height of the topography. Using these new coordinates, the spatial derivatives of a variable A can be transformed (Clark, 1977) into the following derivative

$$\frac{\partial A}{\partial x_i} = \left(\frac{1}{a}\right)\left[\frac{\partial a b^{ij} A}{\partial x_j^*}\right], \tag{2.3}$$

where variable a and tensor b^{ij} are given by

$$a\left(x^*, y^*\right) = 1 - \frac{z_s\left(x^*, y^*\right)}{H} = \frac{\partial z}{\partial z^*} \quad , \quad b^{ij} = \begin{bmatrix} 1 & 0 & \frac{1}{a}\frac{\partial z_s}{\partial x}\left[\frac{z^*}{H} - 1\right] \\ 0 & 1 & \frac{1}{a}\frac{\partial z_s}{\partial y}\left[\frac{z^*}{H} - 1\right] \\ 0 & 0 & \frac{1}{a} \end{bmatrix}, \tag{2.4}$$

respectively. For example, the three components of velocity from the original Cartesian coordinates (u, v, w) can be transformed under the new system to

$$u^* = u \quad , \quad v^* = v \quad , \quad w^* = \frac{(uab^{13} + vab^{23} + w)}{a}. \tag{2.5}$$

2.3 Diagnostic Equations for Thermodynamics

As mention in the previous section, atmospheric pressure, potential temperature, cloud droplets mixing ratio, water vapor mixing ratio, and air density are calculated from the predictive variables (i.e., π, θ_{il}, r_T, r_r, r_i, r_a, and r_g) in the model. The diagnostic equations for determining these thermodynamical variables are the follows.

The ambient atmospheric pressure (p) is diagnostically determined from the exner function (π). The exner function is defined as

$$\pi = C_{pa}\left(\frac{p}{p_{oo}}\right)^{\frac{R_a}{C_{pa}}}, \tag{2.6}$$

where p_{oo} is 100 kpa, C_{pa} is the specific heat of dry air at constant pressure, and R_a is the gas constant of dry air.

The potential temperature (θ) is determined using the ice-liquid potential temperature (θ_{il}). The empirical formula which relates these two variables is given by Tripoli and Cotton (1981) as

$$\theta = \theta_{il}\left[1.0 + \frac{L_{vl}r_l + L_{il}r_{ice}}{C_p MAX\,(T, 253)}\right], \tag{2.7}$$

where T, r_l, r_{ice}, L_{vl} and L_{il} are the temperature, liquid water mixing ratio, ice water mixing ratio, latent heats of condensation and sublimation, respectively. $MAX\,(T, 253)$ is a function which takes the maximum value between the value of T and the value of 253. This empirical formula is shown to produce relatively accurate solutions for θ over the range of pressure encountered inside a typical deep convective cloud. The value of temperature (T) is determined from θ and π through the Poisson equation,

$$T = \theta\frac{\pi}{C_{pa}}. \tag{2.8}$$

The liquid water mixing ratio (r_l) and ice water mixing ratio (r_{ice}) in Eq. (2.7) are given as

$$r_l = r_c + r_r \quad , \quad r_{ice} = r_i + r_a + r_g, \tag{2.9}$$

respectively.

The cloud water (r_c) and water vapor (r_v) mixing ratio are calculated from total water (r_T), rain (r_r), ice (r_i), aggregates (r_a), and graupel (r_g) mixing ratio assuming zero supersaturation (i.e., the excess moistures above 100% relative humidity are instantaneously converted into either cloud water or ice particles depending on the ambient temperature). For ambient conditions warmer than the homogeneous ice nucleation temperature value (such as 233K), the excess moisture is converted into cloud water mixing ratio and the water vapor mixing ratio is then readjusted using

$$r_c = \mathcal{H}\left(r_T - r_{vs} - r_r - r_{ice}\right) \quad , \quad r_v = r_T - r_l - r_{ice}, \tag{2.10}$$

where r_T is the total water mixing ratio given by

$$r_T = r_v + r_l + r_{ice} = r_v + r_c + r_r + r_i + r_g + r_a, \tag{2.11}$$

and r_{vs} is the saturation water vapor mixing ratio, and $\mathcal{H}$ is the Heavside step function. If the temperature drops below the homogeneous ice nucleation temperature, the excess moistures are converted into ice crystal mixing ratio by

$$r_c^* = r_c \quad , \quad r_i = r_i + r_c^* + \mathcal{H}\left(r_T - r_{vs} - r_{ice}\right) \quad , \quad r_c = 0, \tag{2.12}$$

where r_c^* donated temporary values.

The air density is not a predictive variable in the model. It is determined from potential temperature (θ), atmospheric pressure (p) and water vapor mixing ratio (r_v) using the quasi-Boussinesq form of the equation of state,

$$\frac{\rho'}{\rho_o} = \left(\frac{C_{va}}{C_{pa}}\right)\frac{p'}{p_o} - \frac{\theta'}{\theta_o} + 1.61 r_v, \tag{2.13}$$

where C_{va} is the specific heat of dry air at constant volume.

Since the values for these diagnostic variables (p,θ,T,r_v, r_{vs},r_c,r_i) are interdependent on the value of each other, a change in the value of one variable will offset the value for other variables. Therefore, the iterative scheme of Tripoli and Cotton (1982) is used to solve for these quantities in a manner which is consistent with the the model predictive variables.

2.4 Predictive Equations

Since there are ten predictive variables in the model, one will need at least ten equations to close this system of ten unknowns. This set of equations, including three dynamical (u,v,w), two thermodynamical (π,θ_{il}), and five mass continuity equations for water and ice phase particles (r_T,r_r,r_i,r_g,r_a), are now discussed.

The equations describing the evolution of the three dimensional wind fields are based on the quasi-Boussinesq approximation of Dutton and Fichtl (1967) for deep convection. These equations, which are linearized in the thermodynamic variables, expressed in tensor notation (Tripoli, 1986) are

$$\frac{\partial}{\partial t}(\rho_o u_i) + \frac{\rho_o \theta_o}{a}\frac{\partial}{\partial x_i^*}\left(ab^{ij}\pi'\right) = ADV(\rho_o u_i) + \rho_o\, TURB(u_i)$$
$$+g\left(\frac{\theta'}{\theta_o} + 1.61 r_v - r_T\right)\delta_{i3} + \epsilon_{ijk} f_3 \left(\overline{u_{ik}} - u_{ok}\right), \tag{2.14}$$

where ρ_o, u_i, θ_o, θ', π' are the base state dry air density, the three components of wind (u, v, w), the base state potential temperature, the perturbation potential temperature, and the perturbation exner function, respectively. Both a and b^{ij} result from coordinate transformation between the normal Cartesian system (x,y,z) to the terrain following system (x^*,y^*,z^*). The ADV and $TURB$ are advection and turbulence operator, which will be described later in this chapter. The gravitational acceleration is g, δ_{13} is the kronecker delta function, and f_3 is the vertical component of the coriolis term. Equation (2.14) states that the local rate of change of momentum flux is a function of the advection, buoyancy, coriolis forces, pressure, and subgrid-scale turbulences. Since the base state of the model is set up on a dry atmosphere, the introduction of water variables into the model will produce perturbations into the dynamics of the system. These perturbations are included into the buoyancy term in the equation of motion. Equation (2.14) is also written in the form of the so-called time-splitting numerical schemes (Klemp and Wilhelmson, 1978) in which the acoustically excited high frequency exner function or pressure term is on one side of the equation and the low frequency advective time-scale terms are on the other. This set up allows for efficient use of computer power because the LHS of Eq. (2.14) can be integrated separately from the RHS. For example, the acoustic terms on the LHS can be resolved using a small time step while the RHS is done on a longer time step to calculate the lower frequency features.

The equation describing conservation of mass for dry air is written in form of the exner function (π) tendency by combining the continuity equation and the linearized form of the equation of state. The advantages of using π as a predictive variable is that the pressure perturbation term is eliminated from the buoyancy term in the equation of motion (Cotton and Anthes, 1989). This equation is based on Klemp and Wilhelmson (1978)

$$\frac{\partial \pi'}{\partial t} + \frac{1}{a}\frac{R_a}{C_{va}}\frac{\pi_o}{\rho_o \theta_o}\frac{\partial}{\partial x_j^*}\left(ab^{ij}\rho_o\theta_o u_j\right) = 0, \tag{2.15}$$

which states the local tendency of the exner function is due to mass divergence or mass convergence.

The thermodynamic energy equation for predicting the tendency of ice-water potential temperature (θ_{il}) is given by

$$\frac{\partial \rho_o \theta_{il}}{\partial t} = ADV\left(\rho_o \theta_{il}\right) + \rho_o TURB\left(\theta_{il}\right) + \rho_o S\left(\theta_{il}\right), \tag{2.16}$$

where the S operator represents the source or sink to θ_{il} due to precipitation movement relative to the air molecules and radiative heating. This source operator will be discussed later in this chapter. Since θ_{il} is a conservative variable under both adiabatic liquid and ice transformations and it reduces to θ in the absence of cloud or precipitation, it is an ideal predictive variable for cloud/mesoscale model in which its value varies continuously from clear sky to cloudy air and from ice cloud to water cloud. Equation (2.16) states that the local changes in the θ_{il} are resulted from the advection of θ_{il}, the subgrid-scale turbulent transport of θ_{il}, and the source and the sink of θ_{il} within the atmosphere.

The mass continuity equation for water species (r_k) in the model are

$$\frac{\partial \rho_o r_k}{\partial t} = ADV\left(\rho_o r_k\right) + \rho_o TURB\left(\rho_o r_k\right) + PR\left(\rho_o r_k\right) + \rho_o S\left(r_k\right), \tag{2.17}$$

where the subscript k represents any of the predictive water variables (r_T,r_r,r_i,r_g,r_a) in the model, S is the source and the sink of r_k, and PR is the precipitation advection tendency,

$$PR\left(r_k\right) = \begin{bmatrix} \frac{-1}{a\rho_o} \frac{\partial(\rho_o V_k r_k)}{\partial x_3^*} & k \neq T \\ \\ \sum\limits_{k \neq T} PR\left(r_k\right) & k = T \end{bmatrix}, \tag{2.18}$$

where V_k is the terminal velocity for the water species r_k. The source and sink to Eq. (2.17), which include the rate of transfer of water mass from one water species to other water species, will be discuss in the later sections.

The advective operator, which appeared in the predictive equations, for a variable A is given as

$$ADV\left(\rho_o A\right) = -\left(\frac{1}{a}\right)\left[\frac{\partial}{\partial x_k^*}\left(ab^{ij}\rho_o u_j A\right) - A\frac{\partial}{\partial x_k^*}\left(ab^{ij}\rho_o u_j\right)\right]. \tag{2.19}$$

This equation has been written in a form which utilizes the difference between the mass flux divergence and the momentum divergence to improve conservation of mass in the numerical model.

Equations (2.14) to (2.17) are a set of ten equations for the model predictive variables. These equations are not completely closed since the turbulent and the source operators have not been specified. In the following section, the mathematical representation of these operators are shown.

2.5 Turbulence Parameterization

RAMS, similar to other numerical models, can only simulate those atmospheric features which have scales larger than the model resolutions. The subgrid-scale processes that are unresolved by the model grid volume must be represented in some ways to allow for energy dissipation in the dynamical model. If these processes are not taken into account properly, the built-up of energy in the model can ruin the final numerical solutions. These subgrid-scale turbulences, including those representing momentum, mass, and energy transport by turbulent fluctuations, are incorporated into the model using a simple first-order closure scheme (Tripoli, 1986, Cotton and Anthes, 1989) in which eddy exchange coefficients for heat and momentum are calculated as a function of Brunt-Vaisalla frequency, fluid deformation, and Richardson number. As in many other first order schemes, this parameterization assumes that the turbulence always acts to diffuse any variables down their mean gradient.

The basic form of this turbulent operator for a variable A is given by

$$TURB\left(A\right) = -\left(\frac{1}{a}\right)\frac{\partial\left[ab^{jk}\left(\overline{A''u_j''}\right)\right]}{\partial x_k^*}, \tag{2.20}$$

where the turbulent eddy transport term is parameterized in terms of gradient of mean variables, and it takes a slightly different form between velocity variables (u_i) and any other scalar properties (A). These turbulent flux terms are parameterized as

$$-\overline{u_i''u_j''} = K_{m_j}D_{ij} \quad , \quad -\overline{A''u_j''} = K_{h_j}\left(\frac{1}{a}\right)\left[\frac{\partial\left(ab^{il}A\right)}{\partial x_l^*}\right], \tag{2.21}$$

where D_{ij} is the mean rate of deformation tensor and is given by

$$D_{ij} = \left(\frac{1}{a}\right)\left[\frac{\partial\left(ab^{jl}\overline{u_i}\right)}{\partial x_l^*} + \frac{\partial\left(ab^{il}\overline{u_j}\right)}{\partial x_l^*}\right], \tag{2.22}$$

where K_{m_j} and K_{h_j} are eddy exchange coefficients for momentum and other scalar variables. Following Klemp and Wilhelmson (1978), these eddy exchange coefficients can be related by

$$K_{h_j} = 3K_{m_j}. \tag{2.23}$$

The eddy momentum exchange coefficient in the model is based on Lilly (1967) and Hill (1974). It is calculated as a function of brunt-Vaisalla frequency, fluid deformation and Richardson number, and it has the form of

$$K_{m_j} = \left(\frac{0.25^2 l^2}{\sqrt{2}}\right)\left[D + \mathcal{H}\left(-N^2\right)^{0.5}\right], \tag{2.24}$$

where $\mathcal{H}$ is the Heavside function and it takes the value in the argument if that value is greater than zero and zero if that value is less than zero, and

$$l_1^2 = l_2^2 = \left(\triangle x^2 + \triangle y^2\right) \quad , \quad l_3 = MIN\left[L^2 MIN\left[\left(1 - 3Ri\right)^{0.5}, 1.0\right], \triangle x\right], \tag{2.25}$$

where L is zero if $Ri < 0.25$, $\triangle z^2$ if $0.25 \leq Ri \geq 0.0$, and $-\left(z - z_l\right)^2$ if $Ri < 0.0$ and MIN is a function which takes the minimum value of the variables in the argument of the function. The Brunt-Vaisalla frequency and Richardson number are defined by

$$N^2 = \frac{g}{\theta}\frac{\partial\theta}{\partial z} \quad , \quad Ri = \frac{N^2}{D^2}, \tag{2.26}$$

respectively.

2.6 Surface Layer Parameterization

The effects of vertical heat ($\overline{w'\theta'}$), vapor ($\overline{w'r_v'}$), and momentum fluxes ($\overline{w'u'}$,$\overline{w'v'}$, $\overline{w'w'}$) within the surface boundary layer are important to the simulation of cloud systems. These effects are parameterized separately from the turbulent flux described in the last section. The turbulent transports within this surface boundary layer are parameterized according to Lious (1979) and Manton and Cotton (1977) in the model as a simple algebraic

function of the vertical gradient of θ, r_v, u, and v between the surface and the top of the surface layer (i.e., the first θ point in the numerical model) for both stable and unstable conditions. These fluxes have the following forms

$$\begin{aligned}
\overline{w'u'} &= U_*^2 = a^2 U^2 F\left(\tfrac{z}{z_o}, Ri_B\right) \\
\overline{w'v'} &= U_*^2 = a^2 U^2 F\left(\tfrac{z}{z_o}, Ri_B\right) \\
\overline{w'w'} &= W_*^2 = \left(0.27 q_o^2 - 1.18\eta\psi\right) U_*^2 \quad , \\
\overline{w'\theta'} &= U_*\theta_* = a^2 R^{-1} U \triangle\theta F\left(\tfrac{z}{z_o}, Ri_B\right) \\
\overline{w'r_v'} &= U_* R_{v_*} = a^2 R^{-1} U \triangle r_v F\left(\tfrac{z}{z_o}, Ri_B\right)
\end{aligned} \tag{2.27}$$

where the subscript $*$ represents turbulent quantities, z is the height of the surface layer, z_o is the roughness length, U is the mean wind speed in the boundary layer, $\triangle\theta$ and $\triangle r_v$ are the change of potential temperature and vapor mixing ratio between surface and the top of the boundary layer, respectively. The variables q_o, η, and ψ are simple algebraic functions of z and the Monin-Obukhov length (Manton and Cotton, 1977), a and F are another simple algebraic function of $\frac{z}{z_o}$ and Richardson number Ri_B (Lious, 1979), and R is 0.74.

2.7 Radiation Parameterization

A simple broadband type radiative transfer model (Chen and Cotton, 1983) is used to parameterize radiative heating tendencies in the model. This radiation model, however, lacks the complexity needed for the detailed radiation budget studies described later. It is used only to provide estimates of radiative heating effects for use in the dynamical model. For the more detailed diagnostic radiation calculations, we will use the multiband two-stream radiation model of Stackhouse and Stephens (1991). For the sake of completeness, we will give a short discussion of this simple radiation model and show comparison of the radiative budget fields derived from both schemes in the next chapter.

The longwave radiation scheme in the model is based on the broadband emissivity approach which parameterizes the effects of clear sky absorption by water vapor and carbon dioxide. The absorption, scattering, and transmission effects of cloud in the longwave

spectrum are modeled as cloud effective emittance based on Stephens (1978) and it is given by

$$\epsilon_{up,dn} = 1 - exp\left(-a_{o_{up,dn}} W\right), \tag{2.28}$$

where $a_{o_{up}}$ is 0.130 and $a_{o_{dn}}$ is 0.158. These coefficients are derived from pure water clouds. The liquid/ice-water path, W, is defined by

$$W = LWC\triangle z \quad , \quad W = IWC\triangle z, \tag{2.29}$$

where LWC and IWC are the liquid and ice water content in gm^{-3} and are given by

$$IWC = LWC = \frac{4}{3}\pi\rho \int_0^\infty r^3 n(r)\, dr, \tag{2.30}$$

where r is the radius of the hydrometeor, $n(r)$ is the hydrometeor size distribution, and ρ is the density of the hydrometeor. Figure 2.1 shows the cloud emissitivity calculated by this parameterization against those from the theoretical models calculation which suggests the parameterization performed quiet well in capturing the physics of the problem associated with water clouds.

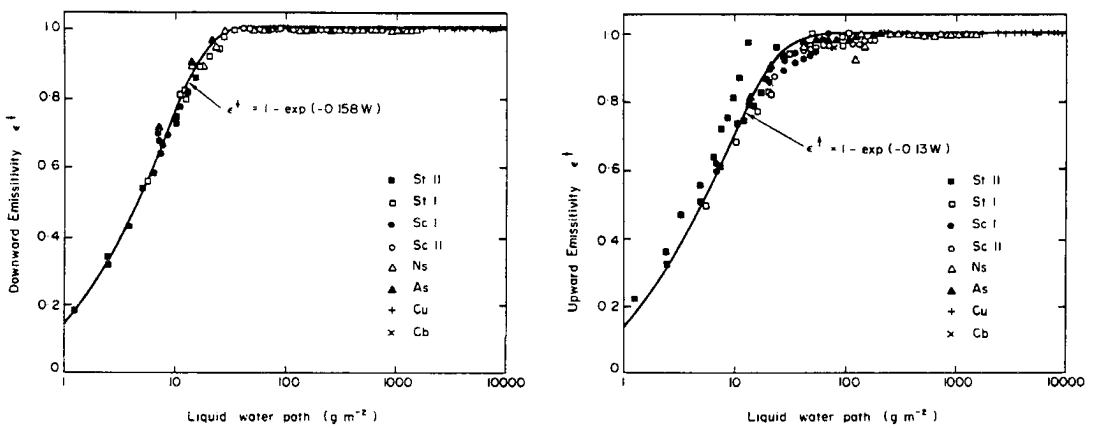

Figure 2.1: Comparison of longwave parameterization (shown as solid lines) of water cloud with theoretical calculations (given as points; after Stephens, 1978).

The shortwave radiative model consists of one nonabsorbing and one absorbing spectral band which include effects of Rayleigh scattering by air molecules and clear sky gaseous absorption by water vapor and ozone. Shortwave absorption (A), scattering (Re),

and transmission (Tr) in the cloudy atmosphere are again based on empirical scheme of Stephens (1978), which related these cloud radiative quantities with liquid/ice-water path (W) and solar zenith angle (μ_o). For the nonabsorbing band (i.e., $\tilde{\omega}_o = 1$), these cloud optical parameters are modeled as

$$\begin{aligned} Re(\mu_o) &= [\beta(\mu_o)\tau_N\mu_o^{-1}][1+\beta(\mu_o)\tau_N\mu_o^{-1}]^{-1} \\ Tr(\mu_o) &= 1 - Re(\mu_o) \\ A(\mu_o) &= 0 \end{aligned} \quad , \tag{2.31}$$

and in the case of absorbing band (i.e., $\tilde{\omega}_o < 1$), these cloud parameters become

$$\begin{aligned} Re(\mu_o) &= (u^2-1)\,exp(\tau_{eff}) - exp(-\tau_{eff})\,R^{-1} \\ Tr(\mu_o) &= 4uR^{-1} \\ A(\mu_o) &= 1 - Re(\mu_o) - Tr(\mu_o) \end{aligned} \quad , \tag{2.32}$$

where u, τ_{eff}, and R are

$$\begin{aligned} u^2 &= [1-\tilde{\omega}_o + 2\beta(\mu_o)\tilde{\omega}_o][(1-\tilde{\omega}_o)]^{-1} \\ \tau_{eff} &= [(1-\tilde{\omega}_o)[1-\tilde{\omega}_o + 2\beta(\mu_o)\tilde{\omega}]]^{0.5}\tau_N\mu_o^{-1} \\ R &= (u+1)^2\,exp(\tau_{eff}) - (u-1)^2\,exp(-\tau_{eff}) \end{aligned} \quad , \tag{2.33}$$

and τ_N for the nonabsorbing band and absorbing band are

$$\begin{aligned} log_{10}(\tau_N) &= 0.2633 + 1.7095 log_e[log_{10}(W)] \\ log_{10}(\tau_N) &= 0.3492 + 1.6518 log_e[log_{10}(W)] \end{aligned} \quad , \tag{2.34}$$

respectively. The values of β and $\tilde{\omega}_o$ are determined using polynomial equations which parameterized these two variables based on τ_N and μ_o. The coefficients in these equations are again derived from pure water clouds. Figure 2.2 shows a comparison of this parameterization against theoretical model calculation for a pure water cloud, which again suggests that this parameterization is quite accurate in representing these cloud radiative parameters in the solar region.

The disadvantage of this model is that the in-cloud longwave and shortwave absorption are parameterized based on observations from water clouds. Since there are significant differences in the optical properties between ice cloud and water cloud, the use of

a Marshall-Palmer distribution with a constant slope (i.e., fixed effective radius). These constant slopes can be specified in the model. The cloud droplets are assumed to condense/evaporate instantaneously in the model in order to maintain zero supersaturation (i.e., Eq. (2.10)). While the cloud water and ice crystals in the model are assumed to have negligible terminal velocity and drift with the wind, the rain drops, aggregates, and graupel have specific terminal velocities which move relative to the wind system. Once formed, these water species can interact with the environment and with each other.

The model does not have predictive equations for all of these variables since some of the water species can be diagnosed from other species. The water species that are predictive in the model are r_T, r_r, r_i, r_a, and r_g. The water vapor and cloud water are diagnosed from the other water species. The predictive equations for the five water species are

$$\begin{aligned}
\frac{\partial \overline{r_T}}{\partial t} &= ADV\left(\overline{r_T}\right) + TURB\left(\overline{r_T}\right) + PR_r + PR_g + PR_i + PR_a \\
\frac{\partial \overline{r_r}}{\partial t} &= ADV\left(\overline{r_r}\right) + TURB\left(\overline{r_r}\right) + PR_r - VD_{rv} - CL_{ri} + CL_{cr} \\
&\quad + CN_{cr} + ML_{ir} - CL_{rg} - FR_{rg} + ML_{gr} + SH_{gr} - CL_{ra} \\
&\quad + ML_{ar} + SH_{ar} \\
\frac{\partial \overline{r_i}}{\partial t} &= ADV\left(\overline{r_i}\right) + TURB\left(\overline{r_i}\right) + PR_i + NUA_{vi} + NUB_{vi} + NUC_{vi} \\
&\quad + NUD_{vi} + SP_{vi} + VD_{vi} + CL_{ci} + CL_{ri} - ML_{ir} - CL_{ig} - CN_{ig} \;, \qquad (2.35) \\
&\quad - CL_{ia} - CN_{ia} \\
\frac{\partial \overline{r_g}}{\partial t} &= ADV\left(\overline{r_g}\right) + TURB\left(\overline{r_g}\right) + PR_g - VD_{gv} + CL_{cg} + CL_{rg} \\
&\quad + FR_{gr} - ML_{gr} - SH_{gr} + CL_{ig} + CN_{ig} + CL_{ag} + CN_{ag} \\
\frac{\partial \overline{r_a}}{\partial t} &= ADV\left(\overline{r_a}\right) + TURB\left(\overline{r_a}\right) + PR_a + VD_{va} + CL_{ca} + CL_{ra} \\
&\quad - ML_{ar} - SH_{ar} + CL_{ia} + CN_{ia} - CL_{ag} - CN_{ag}
\end{aligned}$$

where $\overline{r_T}$, $\overline{r_r}$, $\overline{r_i}$, $\overline{r_g}$, and $\overline{r_a}$ are the mean mixing ratios of total water, rain water, ice crystals, graupel, and aggregates, respectively. The sources and sinks in the equation are parameterized after Tripoli and Cotton (1980) and Cotton *et al.* (1982, 1986) and are represented by capital letters. These microphysical parameterizations include the process of conversion (CN), depositional nucleation (NUA), Brownian nucleation (NUB),

In this study, the vertical boundaries in the model are assumed to be rigid walls. A weak dissipative sponge layer is applied to the highest 8 km of the domain to reduce wave reflection from the upper rigid walls. This weak dissipative layer is formulated in the form of Rayleigh friction zone similar to Clark (1977). At the lower boundary, a free-slip surface is assumed. Furthermore, fluxes of latent and sensible heat are also prescribed to allow for momentum, heat, and moisture transport into the cloud system. The lateral boundaries in the model include a mesoscale compensating region (MCR, Tripoli and Cotton, 1982) to provide a large-scale balance adjustment of circulation generated within the interior of the model domain. The purpose of these special regions is to absorb extra mass generated in the limited model and to prevent the mass built up in the simulation. Furthermore, the Klemp-Lilly (1978) gravity wave radiative conditions are also applied as the lateral boundaries of the fine-mesh to allow propagation of gravity waves through the fine mesh/MCR walls.

Chapter 3

DIAGNOSTIC RADIATIVE TRANSFER MODEL

As previously stated one of the main objectives of this research is to investigate the spatial characteristics and temporal variations of the radiation budget and radiative heating field associated with tropical MCSs. To accomplish this task, the multiband two-stream radiation model developed by Stackhouse and Stephens (1991) is used to diagnose these quantities based on the thermodynamical and microphysical information produced from the dynamical mesoscale/cloud model. The mesoscale/cloud model was outlined in the last chapter. In this chapter, a description of this diagnostic radiation model is given.

3.1 General Radiative Transfer Theory

The equation describing the transfer of monochromatic radiation through an absorbing, emitting, and scattering medium (i.e., the earth atmosphere) can be found in many introductory atmospheric radiation texts. In its most general form, this equation is written as

$$\underline{\zeta} \cdot \nabla I_\nu = -\rho K_{ext,\nu}(p,T) \cdot [I_\nu - S], \tag{3.1}$$

where ρ is the density of the medium, $K_{ext,\nu}(p,T)$ is the spectral volume extinction coefficient of the medium, which is a function of temperature and pressure, I_ν is the monochromatic intensity field of the radiation, $\underline{\zeta}$ is the spherical coordinate's unit vector and S represents the source of radiation within the medium.

Equation (3.1) states that the divergence or leakage of radiation from a beam of direction ζ as it passes along some path of the atmosphere is caused by the attenuation of radiation within the medium plus the addition of radiation from internal (or external) sources. In the study of atmospheric radiation it is customary to separate this source

optical depth, τ, measures the true depth of the medium in optical space. It starts with a zero value at the top of the atmosphere and increasing downward to some value τ_1 at the surface. Under a cloudy condition, this quantity is a product of both gaseous and cloud particles (i.e.,$\tau = \tau_{gas} + \tau_{cloud}$) in the atmosphere. The single scattering albedo, $\tilde{\omega}_o$, describes the amount of scattering to the total extinction of the single particles (or of a small volume of particles), $P(\mu, \mu')$ is the phase function which describes the probability of scattering associated with each of the scatter angle, S_{sw} is the shortwave source term, and S_{lw} is the longwave source term within the atmosphere. The optical depths due to gaseous and cloud particles are determined as

$$\tau_{gas} = ku \quad , \quad \tau_{cloud} = \sigma_{ext} \triangle z, \tag{3.3}$$

where σ_{ext} is the spectral particle extinction, k is the spectral gaseous extinction, $\triangle z$ is the layer thickness, and u is the optical path. These parameters will be discussed further in later sections. The optical path u is given by

$$u = \left(\frac{\bar{p}}{p_{ref}}\right)^n \left(\frac{T_{ref}}{\bar{T}}\right)^m \frac{\bar{w} \triangle p}{g}, \tag{3.4}$$

where $\bar{p}$, $\bar{T}$, p_{ref}, T_{ref}, $\bar{w}$, $\triangle p$, and g arethe mean pressure, mean temperature, reference pressure, reference temperature, mean mixing ratio of the gas, pressure thickness of the layer, and gravitational acceleration, respectively. The scaling parameters m and n depend on how k was computed from the model.

The first term on the right hand of Eq. (3.2) is the sink for radiation due to attenuation within the atmosphere while the remaining terms on the right hand side represent the sources of radiation. These include the pseudo-source term due to scattering of diffuse radiation from the surrounding atmosphere, the shortwave source term arise from the scattering of the direct solar beam, and longwave source term due to emission processes within the atmosphere. The exact form of these source terms will be discussed in the later sections.

Equation (3.2) represents the general monochromatic radiative transfer equation in intensity form. In the study of radiative energy budget, Eq. (3.2), however, is not very

useful since it describes only the flow of radiation at some specific wavelength and along some specific direction. For these studies Eq. (3.2) has to be transformed into the broadband net flux form by intergating over zenith angles and wavelengths. It is customary to further divide this quantity into its upward and downward components. The broadband net flux can be expressed as

$$F_{net}(\tau) = \int_0^\infty \int_{-1}^{1} I_\nu(\tau,\mu)\,\mu d\mu d\nu = \int_0^\infty \int_0^1 I_\nu(\tau,\mu)\,\mu d\mu d\nu - \int_0^\infty \int_0^{-1} I_\nu(\tau,\mu)\,\mu d\mu d\nu$$
$$= F_{dn}(\tau) - F_{up}(\tau), \tag{3.5}$$

where F_{dn} and F_{up} represent the downward and upward broadband flux of the radiation at some level τ in the medium. For a given vertical profile of atmospheric broadband net fluxes, the radiation budget and the radiative heating/cooling rate can be computed easily.

3.1.2 Radiation Budget

The conservation law describing the radiative budget of any layer with an optical depth of $\tau = \tau_1 - \tau_0$ in the atmosphere is given by

$$F_{net}(\tau_1,\tau_0) = F_{net}(\tau_1) - F_{net}(\tau_0), \tag{3.6}$$

where $F_{net}(\tau_0)$ and $F_{net}(\tau_1)$ are the net flux values at the boundary of the layer. A positive value of $F_{net}(\tau_1,\tau_0)$ indicates that the layer is gaining energy while a negative value, on the other hand, represents energy loss within the layer. In the study of solar radiative budget, it is customary to study the radiative budget by defining the solar transmission, reflection, and absorption of a layer from the upward and downward fluxes at the boundaries by

$$\mathcal{TRAN}(\tau_1,\tau_0) = \frac{F_{dn}(\tau_1)}{F_{dn}(\tau_0)}$$
$$\mathcal{REFL}(\tau_1,\tau_0) = \frac{F_{up}(\tau_0)}{F_{dn}(\tau_0)} \tag{3.7}$$
$$\mathcal{ABSO}(\tau_1,\tau_0) = 1 - \mathcal{TRAN}(\tau_1,\tau_0) - \mathcal{REFL}(\tau_1,\tau_0).$$

These variables are very useful in understanding the partitioning of solar energy in the atmosphere.

3.1.3 Radiative Heating

The radiative heating/cooling rate of the atmosphere can be computed for a given vertical profile of atmospheric net fluxes. The conservation law describing the radiative temperature tendency is

$$\frac{d}{dt}T(\tau) = \frac{g}{C_p}\left[\frac{d}{dp}F_n(\tau)\right] = \frac{-1}{\rho_a C_p}\left[\frac{d}{dz}F_n(\tau)\right], \tag{3.8}$$

where p is air pressure, z is height, ρ_a is the air density, C_p is specific heat of air at constant pressure, g is gravitational acceleration, τ is optical depth, t is time, T is temperature, and $dFn(\tau)$ is the local change in net radiative flux at that point.

The physical interpretation of Eq. (3.8) can be stated simply as the potential for a local rate of change of the temperature at some point in the atmosphere with optical depth of τ due to the imbalance in the flow of radiation into and out of that point (or by the local gradient of net flux at that point). If the net amount of radiation is diverging from a given level, then a small volume at that level loses energy and cools. Conversely, if the net flux is converging into a small volume, that volume experiences radiative warming.

3.2 Major Atmospheric Constituents that Influence Radiation Profile

Table 3.1 summarized the most common atmospheric constituents (neglecting water and ice) found on earth. Only the trace gases H_2O, CO_2, and O_3 have a dominant effect on the absorption of radiation. Figure 3.2 provided an example of the measured longwave emission spectrum of the earth's atmosphere obtained from the Nimbus 4 satellite. The absorption bands which mainly contribute to longwave radiation of the atmosphere are defined in the figure to be those of the $6.3\mu m$ vibration band, the rotation band and the continuum region all associated with water vapor, the $15\mu m$ band of carbon dioxide and the $9.6\mu m$ band of ozone. In the shortwave spectral region, the absorption is mainly due to oxygen, ozone in the ultraviolet and visible region, and water vapor with somewhat weaker contribution by carbon dioxide in the near infrared region of the spectrum as illustrated in Fig. 3.3. In view of this, only the radiative effects from these gases will be modeled in the present study.

Table 3.1: Composition of the earth's atmosphere (after Ahrens, 1982).

Constituent	Percent by Volume
Nitrogen (N_2)	78.0800
Oxygen (O_2)	20.9500
Argon (A)	0.93000
Carbon dioxide (CO_2)	0.03000
Water vapor (H_2O) *	0. -4.
Neon (Ne)	0.00180
Ozone (O_3) *	0.00050
Helium (He)	0.00050
Hydrogen (H_2)	0.00020
Carbon monoxide (CO)*	0.00001
Sulfur dioxide (SO_2)*	0.00001
Nitrogen dioxide (NO_2)*	0.00001
Particles (dust, soot, etc.)*	0.00001

*Highly variable constituents

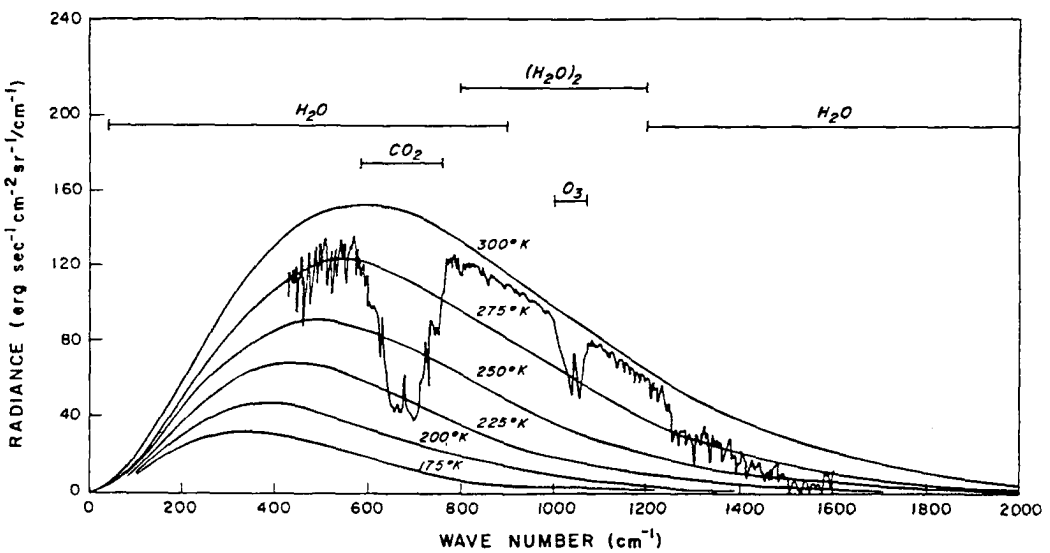

Figure 3.2: The terrestrial infrared spectra and various absorption bands. Also shown is an actual atmospheric emission spectrum taken by the Nimbus IV IRIS instrument near Guam at 15.1 N and 215.3 W on April 27, 1970 (after Liou, 1980).

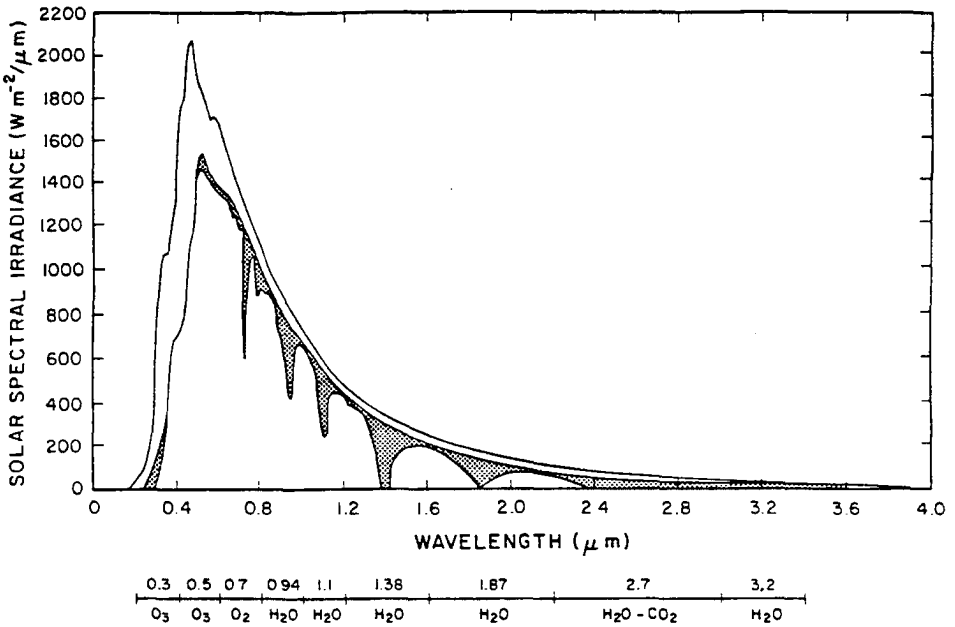

Figure 3.3: Spectral irradiance distribution curves related to the sun: (1) the observed solar irradiance at the top of the atmosphere (after Thekaekara, 1976) and (2) solar irradiance observed at sea level. The shaded areas represent absorption due to various gases in a clear atmosphere (after Liou ,1980).

In addition to absorption by trace gases in the solar region, Rayleigh scatter by gas molecules (i.e., by N_2 and O_2) is also important to the radiative energy budget of our atmosphere, and together they account for 6 percent of the total reflected solar radiation at the top of the atmosphere (shown in Fig. 3.4). This process is included in the model. In the infrared region, the water vapor continuum absorption in the window region (8 to 12 μm) can be important for the longwave radiative budget of the tropical atmosphere due to abundance of water vapor in the lower atmosphere. This process is also accounted for in the model.

3.3 Monochromatic Two-Stream Radiative Transfer Model

In order to solve Eq. (3.5) for broadband fluxes, two procedures must be performed. First, it is necessary to transform the differential Eq. (3.2) into its downward and upward (i.e., two stream) monochromatic flux components and find the solutions for these fluxes. Second, we need to perform spectral integration of the monochromatic flux solutions across

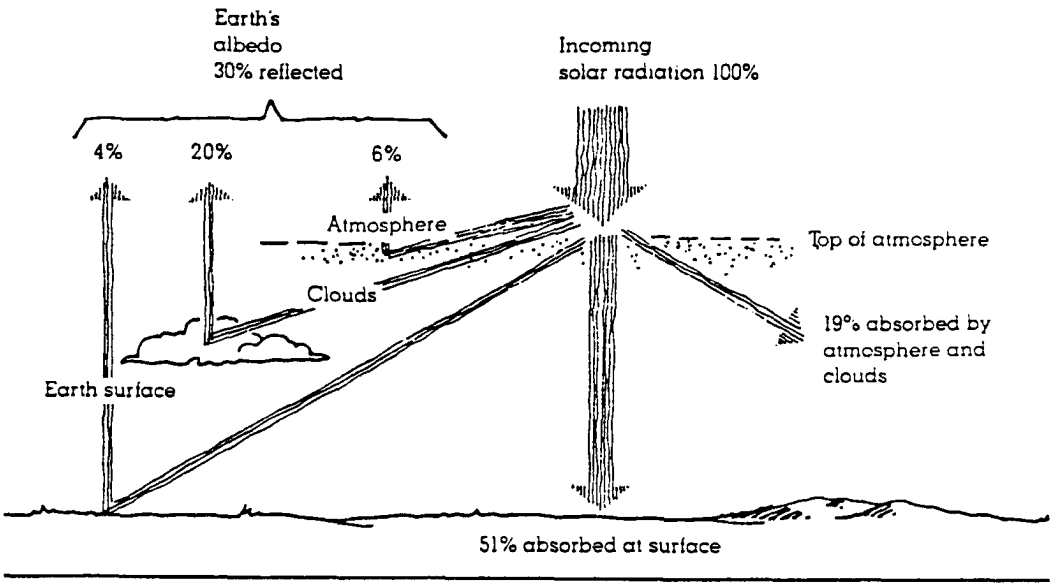

Figure 3.4: On the average, of all the solar energy that reaches the earth's atmosphere, about 30 percent is reflected back to space, 19 percent is absorbed by the atmosphere and clouds, and 51 percent is absorbed at the surface (after Ahrens, 1981).

the radiation spectrum to obtain the broadband radiation field. These are now discussed briefly. Readers who are interested in these procedures are referred to Stackhouse and Stephens (1989) for more details. In order to simply further the discussion, the spectral dependency in this section is implicitly assumed.

3.3.1 Monochromatic Two-Stream Equations

The flux form of the monochromatic radiative transfer equation can be obtained by integrating Eq. (3.2) over the upward and downward hemisphere, (i.e., $\int_{-1,0}^{0,1}(3.2)\,d\mu$). The resultant equations have the following forms

$$-\tfrac{d}{d\tau}F_{up}(\tau) = -(a+b)\,F_{up}(\tau) + bF_{dn}(\tau) + Usw_{up}(\tau) + Ulw_{up}(\tau)\ , \qquad (3.9a)$$

$$\tfrac{d}{d\tau}F_{dn}(\tau) = -(a+b)\,F_{dn}(\tau) + bF_{up}(\tau) + Usw_{dn}(\tau) + Ulw_{dn}(\tau)\ , \qquad (3.9b)$$

where F_{up}, F_{dn}, a, and b, are the upward flux, downward flux, diffusive absorption fraction, and backscatter fraction, respectively. The diffuse absorption fraction and the backscatter fraction can be determined by

$$a = (1-\tilde{\omega}_o)\,D \quad , \quad b = b\,(\tilde{\omega}_o, gg)\,, \qquad (3.10)$$

where D and gg are the diffusivity factor and asymmetry factor, respectively. While the diffusivity factor is a measure of the increases in the optical path due to scattering and absorption-emission processes in the atmosphere, the asymmetry factor describes the direction of scattering within the layer.

Figure 3.5 shows a conceptual view of Eq. (3.9), which states that the change in the upward/downward flux as a function of optical depth is due to (1) attenuation by both absorption of energy and scattering of energy away from the upward/downward flux component, (2) the scattering or reflection of the downward/upward flux component back to the upward/downward direction, (3) the emission of longwave energy within the medium, and (4) the scattering of the direct solar beam in the medium.

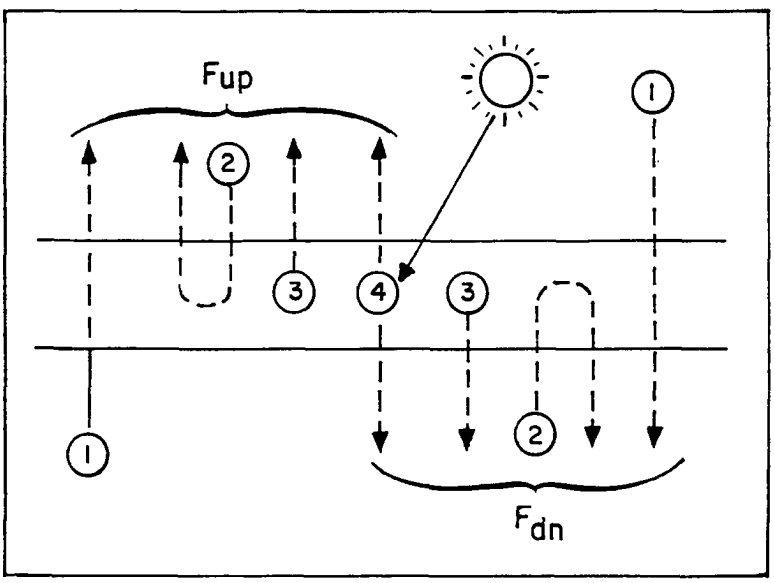

Figure 3.5: Conceptual view of the flow of radiation in the model.

3.3.2 Monochromatic Two-Stream Solutions

Equation (3.9) is a set of two differential equations with two unknowns (i.e., F_{up} and F_{dn}). The solutions to these equations in matrix form with the boundary conditions of

$$F_{dn}(\tau = 0) = F_{dn}(0) \quad , \quad F_{up}(\tau = \tau_1) = F_{up}(\tau_1)$$

are

$$\begin{bmatrix} F_{up}(\tau) \\ F_{dn}(\tau) \end{bmatrix} = \mathcal{M} \begin{bmatrix} F_{up}(\tau_1) \\ F_{dn}(0) \end{bmatrix} + \begin{bmatrix} S_{sw,up}(\tau) \\ S_{sw,dn}(\tau) \end{bmatrix} + \begin{bmatrix} S_{lw,up}(\tau) \\ S_{lw,dn}(\tau) \end{bmatrix}, \qquad (3.11)$$

where

$$\mathcal{M} = \begin{bmatrix} \mathcal{T}(\tau_1,\tau,0) & \mathcal{R}(0,\tau,\tau_1) \\ \mathcal{R}(\tau_1,\tau,0) & \mathcal{T}(0,\tau,\tau_1) \end{bmatrix}, \tag{3.12}$$

and

$$\begin{bmatrix} S_{sw/lw,up}(\tau) \\ S_{sw/lw,dn}(\tau) \end{bmatrix} = \begin{bmatrix} F_{s,sw/lw,up}(\tau) \\ F_{s,sw/lw,dn}(\tau) \end{bmatrix} + \begin{bmatrix} F_{s,sw/lw,up}(\tau_1) \\ F_{s,sw/lw,dn}(0) \end{bmatrix}. \tag{3.13}$$

The transmittance–reflectance matrix, $\mathcal{M}$, is composed of the transmittance function $\mathcal{T}$ and reflectance function $\mathcal{R}$. This matrix can be calculated given $\tilde{\omega}_o$, gg, and $P(\mu,\mu')$ within the layer.

The longwave source terms, $F_{s,lw,up}$ and $F_{s,lw,dn}$, appeared in Eq. (3.13) are formulated as a function of temperature and optical depth of the medium in this model. They have the following form

$$\begin{aligned} F_{s,lw,up}(\tau) &= \tfrac{2\pi(1-\tilde{\omega}_o)x}{v}[B(T_0)[1-\mathcal{R}(0,\tau,\tau_1)] - B(T_1)\mathcal{T}(\tau_1,\tau,0)] - \\ &\quad \tfrac{2\pi(1-\tilde{\omega}_o)x}{v}[B(T_1)-B(T_0)]\left[\tfrac{1-\mathcal{T}(\tau_1,\tau,0)+\mathcal{R}(0,\tau,\tau_1)}{x\tau_1}\right] \end{aligned}, \tag{3.14a}$$

$$\begin{aligned} F_{s,lw,dn}(\tau) &= \tfrac{2\pi(1-\tilde{\omega}_o)x}{v}[B(T_1)[1-\mathcal{R}(\tau_1,\tau,0)] - B(T_0)\mathcal{T}(0,\tau,\tau_1)] + \\ &\quad \tfrac{2\pi(1-\tilde{\omega}_o)x}{v}[B(T_1)-B(T_0)]\left[\tfrac{1-\mathcal{T}(0,\tau,\tau_1)+\mathcal{R}(\tau_1,\tau,0)}{x\tau_1}\right] \end{aligned}, \tag{3.14b}$$

where x and v are function of a and b

The solar source terms, $F_{s,sw,up}$ and $F_{s,sw,dn}$, in Eq. (3.13) are calculated based on the given value of solar flux (F_o), the cosine of the solar zenith angle (μ_o), and the backward scatter fraction (β_o). They have the following forms when $k_2 + \frac{1}{\mu_o} \neq 0$,

$$F_{s,sw,up}(\tau) = \tilde{\omega}_o F_o \frac{\left(t+\frac{1}{\mu_o}\right)\beta_o - b(1-\beta_o)}{\left(k_1+\frac{1}{\mu_o}\right)\left(k_2+\frac{1}{\mu_o}\right)} exp\left(\frac{-\tau}{\mu_o}\right), \tag{3.15a}$$

$$F_{s,sw,dn}(\tau) = \tilde{\omega}_o F_o \frac{\left(t-\frac{1}{\mu_o}\right)(1-\beta_o) - b\beta_o}{\left(k_1+\frac{1}{\mu_o}\right)\left(k_2+\frac{1}{\mu_o}\right)} exp\left(\frac{-\tau}{\mu_o}\right), \tag{3.15b}$$

and

$$F_{s,sw,up}(\tau) = \tfrac{1}{2}\tilde{\omega}_o\mu_o\tau F_o\left[b(1-\beta_o) - \left(t+\tfrac{1}{\mu_o}\right)\beta_o\right] exp\left(\tfrac{-\tau}{\mu_o}\right), \tag{3.16a}$$

$$F_{s,sw,dn}(\tau) = \tfrac{1}{2}\tilde{\omega}_o\mu_o\tau F_o\left[b\beta_o - \left(t-\tfrac{1}{\mu_o}\right)(1-\beta_o)\right] exp\left(\tfrac{-\tau}{\mu_o}\right), \tag{3.16b}$$

when $k_2 + \frac{1}{\mu_o} = 0$, where k_1, k_2, and t are function of a and b, and β_o is the related to the phase function $P(\mu,\mu_o)$.

For a given set of the optical parameters (i.e.,τ, $\tilde{\omega}_o$, gg, $P(\mu', \mu)$) within a layer, Eq. (3.11) can be used to solve the monochromatic diffuse fluxes associated with that layer. These optical parameters (i.e.,τ, $\tilde{\omega}_o$, gg, and $P(\mu', \mu)$), which describe the absorption and scattering properties of the gases and particles within the medium, will be discuss later.

For solar radiative transfer, a direct component of the solar radiation of the form

$$F_{direct,dn}(\tau) = \mu_o F_o exp\left(\frac{-\tau}{\mu_o}\right) \tag{3.17}$$

must be added to the diffuse downward solution to obtain the total downward flux.

3.3.3 Optical Parameters

The optical parameters τ, $\tilde{\omega}_o$, gg, and $P(\mu, \mu')$ appearing in Eqs. (3.9) to (3.17) are important elements of the monochromatic two-stream model since they describe the absorption and scattering properties of the medium. These parameters are function of both gaseous and cloud particles in the atmosphere. The total optical depth (τ) in the layer can be calculated as the sum of the optical depth from separated radiative processes by

$$\tau_{lw} = \tau_{lw,cloud} + \tau_{lw,gas} + \tau_{e-type} \quad , \quad \tau_{sw} = \tau_{sw,cloud} + \tau_{sw,gas} + \tau_{rayleigh}, \tag{3.18}$$

where τ_{cloud}, τ_{gas}, τ_{e-type}, $\tau_{rayleigh}$ represent optical depth of the cloud hydrometeors, atmospheric gases, e-type absorption, and rayleigh scattering, respectively. The subscript lw and sw represent the corresponding longwave and the shortwave optical components. The single scattering albedo ($\tilde{\omega}_o$), asymmetry factor (gg), and the phase function ($P(\mu, \mu_o)$) in the layer are calculated using formulas of Slingo and Schrecker (1982), which include effects of molecular and particulate processes. These formulae have the following form,

$$\tilde{\omega}_{o,lw} = \frac{\tilde{\omega}_{o,lw,cloud}\tau_{lw,cloud}}{\tau_{lw}} \quad , \quad \tilde{\omega}_{o,sw} = \frac{\tau_{rayleigh} + \tilde{\omega}_{o,sw,cloud}\tau_{sw,cloud}}{\tau_{sw}}, \tag{3.19}$$

$$gg_{lw} = gg_{lw,cloud}\left(\frac{\tilde{\omega}_{o,lw,cloud}\tau_{lw,cloud}}{\tilde{\omega}_{o,lw}\tau_{lw}}\right) \quad , \quad gg_{sw} = gg_{sw,cloud}\left(\frac{\tilde{\omega}_{o,sw,cloud}\tau_{sw,cloud}}{\tilde{\omega}_{o,sw}\tau_{sw}}\right), \tag{3.20}$$

$$P(\mu, \mu_o) = \frac{\tau_{rayleigh}P_{rayleigh} + \tilde{\omega}_{o,sw,cloud}\tau_{sw,cloud}P_{cloud}}{\tau_{rayleigh} + \tilde{\omega}_{o,sw,cloud}\tau_{sw,cloud}}, \tag{3.21}$$

where $\tilde{\omega}_{o,cloud}$, gg_{cloud}, and P_{cloud} are the single scattering albedo, asymmetry factor, and the phase function of the cloud particle, respectively. $P_{rayleigh}$ is the phase function of Rayleigh scattering and the subscripts sw and lw represent the shortwave and the longwave components, respectively. The exact form of these optical parameters is a function of the radiation model and will be discuss in the later sections.

3.4 Multiband Radiation Model

The monochromatic radiative transfer model described in the last section must be integrated over wavelengths to obtain the desired broadband fluxes for energy budget analysis. This integration requires detailed information on the spectral variation of τ, $\tilde{\omega}_o$, gg, and $P(\mu, \mu')$ within the medium. For the spectral integration to perform properly these parameters must also vary smoothly with wavelength. While the spectral variations of these parameters associated with cloud particles, Rayleigh scatter, and e-type absorption vary smoothly with wavelength, the extinction and optical depth features for molecular absorption, however, vary in a complex way with wavelength. Therefore, some methods of treating these gaseous absorptions have to be derived in order to allow for integration of these optical parameters across the broadband spectrum. These methods have to be formulated in such a way as to allow for consistent treatment of optical properties by both molecules and particles which occur during the interaction of cloud and radiation in the atmosphere.

The most accurate method to accomplish the broadband integration is the line-by-line type technique in which monochromatic radiative calculations are performed over hundred of thousands of small discrete radiation lines/frequencies and their results are summed to obtain the broadband fluxes (Ramaswamy and Freidenreich, 1991). The advantage of this technique is that the optical parameters are resolved almost completely and we do not have to parameterize their effects. The disadvantage of this method is that it is computationally expensive and is not recommanded for analysis over a large area of the atmosphere. The broadband type radiation model, on the other hand, tries to represent the entire radiation spectrum using one shortwave band and one longwave band. Since

this type of model does not resolve the structure of individual absorption lines, it is the least accurate method for radiation budget analysis. The advantage of this type of model is the speed of its calculation. It is for this reason that this method is used in most general circulation/climate models today.

For our current study, we adopt a middle-of-the-road approach by using the multiband radiation model of Stackhouse and Stephens (1991). The concept of the multiband model as represented in Fig. 3.6 is to divide the solar/infrared spectrum into a number of small bands with a specific bandwidth over which τ, $\tilde{\omega}_o$, gg, and $P(\mu, \mu')$ can be assumed to vary smoothly. The method used to represent these optical parameters within each small band will be discuss later in this section. The radiative flux calculations are then performed over each of these bands. The results from these calculations are summed together to obtain the broadband solar/infrared fluxes. This method can be expressed mathematically as

$$F_{up,broadband} = \sum_{l=1}^{n} F_{up,band_l} \quad , \quad F_{dn,broadband} = \sum_{l=1}^{n} F_{dn,band_l}, \tag{3.22}$$

where n is the total number of band used to represent the spectrum and the subscript l represents any band within the spectrum. The choices of the number of bands and on the length of the bandwidth in the multiband model are usually depended on the molecular absorption features of the atmospheric gases and on the desired accuracy of the model.

3.4.1 Molecular Absorption

Since molecular absorption by atmospheric gaseous are important to the transfer of radiation in the atmosphere, proper modeling of these processes are essential to the simulation of the radiative profiles of the atmosphere. According to Stackhouse and Stephens (1989), there are two methods that allow for consistent treatment of optical properties by both molecules and particles which occur during the interaction of cloud and radiation in the atmosphere. They are the K-distribution method and the sum of exponential fit technique. Even though these two methods have the same mathematical representation, they are based on two very different principles. The parameters in the K-distribution method are real features from laboratory measurements while those in the sum of exponential fit technique are merely empirical values from the fitting of extinction data. Both of these

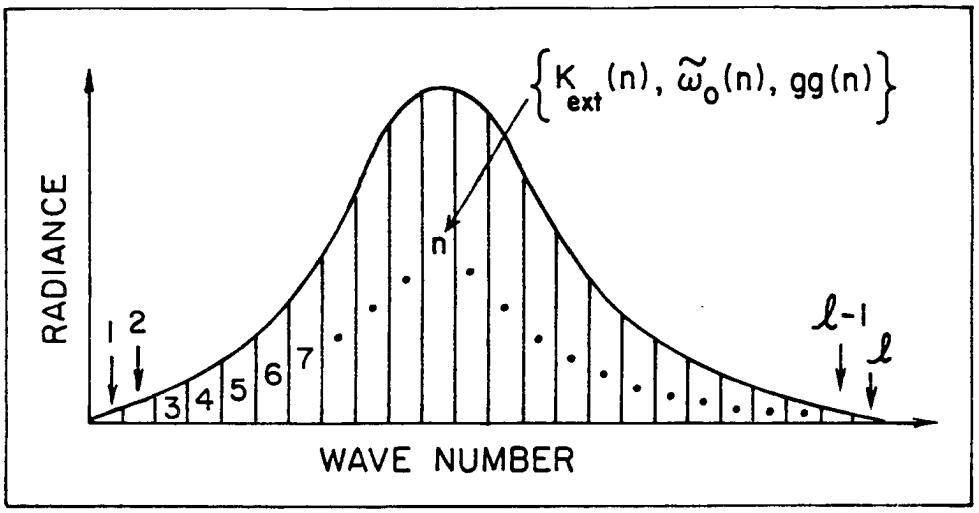

Figure 3.6: A conceptual view of the multiband radiation model.

methods are used in this study. In the following, a brief discussion of the K-distribution method and the way that it is used to represent the gaseous optical depth in the band model will be given.

The purpose of K-distribution method is to represent the mean transmittance over a specific spectral band "l" with a known spectral bandwidth as

$$\mathcal{T}_{band_l}(u) = \int_0^\infty f(k) exp(-ku)\, dk, \tag{3.23}$$

where $f(k)$ is the probability distribution function and $f(k)\, dk$ represents the fractional wavenumber interval in which the extinction values are used for. This mean transmittance can be written in discrete form as

$$\mathcal{T}_{band_l}(u) = \sum_{i=1}^{n} w_i exp(-k_i u), \tag{3.24}$$

where n is the total number of extinction values (k_i) used to represent the transmission of this band and w_i is the weight associated with each of the extinction values. In other words, the mean transmission of this particular band can be represented by a number of discrete optical depth values (i.e., $\tau_{gas_i} = k_i u$), and Eq. (3.24) can be rewritten as

$$\mathcal{T}_{band_l}(\tau_i) = \sum_{i=1}^{n} w_i exp(\tau_i). \tag{3.25}$$

Since the fluxes derived from the two-stream model are function of optical depth, it is straight forward to show that they must also be a function of τ_{gas_i}. Thus the use of this technique to represent gas absorption will lead to the following flux solution for a particular band in the multiband radiation model.

$$F_{up,band_l}(\tau_l) = \sum_{i=1}^{n} w_i F_{up,i}(\tau_i) \quad , \quad F_{dn,band_l}(\tau_l) = \sum_{i=1}^{n} w_i F_{dn,i}(\tau_i) . \tag{3.26}$$

For the spectral region where there is more than one gas active (i.e., the overlap region), the transmission in this overlap region is assume to be

$$\mathcal{T}_{12,band_l}(u) \approx \mathcal{T}_{1,band_l}(u)\,\mathcal{T}_{2,band_l}(u) = \sum_{i=1}^{n_1}\sum_{j=1}^{n_2} w_{1,i} w_{2,j} exp\left(-u\left(k_{1,i} + k_{2,j}\right)\right), \tag{3.27}$$

and the upward and downward fluxes are

$$F_{up,12,band_l}(\tau_{12,l}) = \sum_{i=1}^{n1}\sum_{j=1}^{n2} w_{1,i} w_{2,j} F_{up,ij}(\tau_{ij}), \tag{3.28}$$

$$F_{dn,12,band_l}(\tau_{12,l}) = \sum_{i=1}^{n1}\sum_{j=1}^{n2} w_{1,i} w_{2,j} F_{dn,ij}(\tau_{ij}) .$$

Combining these equations with those of Eq. (3.22) the broadband fluxes of the atmosphere can now be calculated. These fluxes can then be used to calculate radiative budget and radiative heating profile using Eqs. (3.6) to (3.8).

In this study, a total of 24 bands (identified in Tables 3.2 and 3.3) are used in the radiative transfer model to model the absorption spectra of the atmospheric gases in both the solar (0.28 μm – 3.8 μm) and infrared (3.8 μm – 200.0 μm) region. Specifically, solar absorption by O_3 for wavelengths less than 0.68 μm is treated by dividing the spectrum into 3 bands using cross-section data based on the exponential sum fit technique (Stamnes and Tsay, 1991). For wavelengths greater than 0.687 μm, the K-distribution method is applied for 11 bands and 10 bands for infrared wavelengths greater than 3.8 μm. The optical paths (u) associated with each gas are computed using simple pressure–temperature scaling parameterization with scaling constants as given for each gas by Chou and Arking (1980), Chou and Arking (1981), Chou and Peng (1983), Chou (1984), and Chou (1990). These scalings are summarized in Tables 3.4 and 3.5.

Table 3.2: Infrared spectral bandwidths of absorbing gases.

Band No.	Infrared Spectral Bandwidth (cm^{-1})	Absorber
1	20 – 340	H_2O
2	340 – 540	H_2O
3	540 – 620	$H_2O + CO_2$
4	620 – 720	$H_2O + CO_2$
5	720 – 800	$H_2O + CO_2$
6	800 – 980	H_2O
7	980 – 1100	$H_2O + O_3$
8	1100 – 1380	H_2O
9	1380 – 1900	H_2O
10	1900 – 2620	H_2O

Table 3.3: Solar spectral bandwidths of absorbing gases.

Band No.	Solar Spectral Bandwidth (cm^{-1})	Absorber
1	2600 – 3300	H_2O
2	3300 – 4000	$H_2O + CO_2$
3	4000 – 4600	H_2O
4	4600 – 5300	$H_2O + CO_2$
5	5300 – 6000	H_2O
6	6000 – 7000	$H_2O + CO_2$
7	7000 – 12850	H_2O
8	12850 – 13150	$H_2O + O_2$
9	13150 – 14300	H_2O
10	14300 – 14450	$H_2O + O_2$
11	14450 – 14550	O_2
12	14550 – 25000	O_3
13	25000 – 31746	O_3
14	31746 – 35710	O_3

Table 3.4: Infrared scaling parameters.

Gas	Bandwidth (cm^{-1})	P_{ref} (mb)	n	T_{ref} (K)	m	$R(T_{ref}-40K, T_{ref})$	$R(P_{ref}-40K, P_{ref})$
H_2OCenters	20– 340,1380–1900	275	1.00	225	0.0	0.90	1.16
H_2OWings	340–1380,1900–3000	550	1.00	256	0.0	0.58	1.78
CO_2Centers	620–720	30	0.85	240	0.0	0.74	0.44
CO_2Wings	540–620,720–800	300	0.50	240	0.0	0.51	2.03
O_3	980–1100	100	1.00	240	1.0	—	—

Table 3.5: Solar scaling parameters.

Gas	$P_{\mathbf{ref}}$ (mb)	n	$T_{\mathbf{ref}}$ (K)	m
H_2O	300	0.80	240	0.0
CO_2	300	0.80	240	0.0
O_2	500	0.80	240	0.0
O_3	—	—	—	—

3.4.2 Molecular Scattering and e-Type Absorption

As pointed out in the previous section, Rayleigh scattering and e-type absorption are important components of the radiation budget of the atmosphere. Unlike molecular absorption, these effects are smooth functions of wavelength so they can be more readily incorporated into the multiband model. The effects of Rayleigh scattering are parameterized in this study using the empirical fit of Paltridge and Platt (1976) which calculates the Rayleigh optical depth as

$$\tau_{rayleigh} = 0.0088\lambda^{(-4.15+0.2\lambda)} exp\left(-0.1188H - 0.00116H^2\right), \tag{3.29}$$

where λ is wavelength (μm) and H is the distance between the level of interest and the surface in kilometers. The effects of water vapor continuum absorption are a function of partial pressure of water vapor in the layer. These effects are parameterized using the formulas of Roberts *et. al.*, (1976) which gives

$$k_{e-type} = \frac{\Phi\left(\bar{T}\right)}{\Phi\left(T_o\right)} \Psi\left(\nu, T_o\right) e_c, \tag{3.30}$$

where

$$\Phi\left(T\right) = exp\left(\frac{1800}{T}\right), \tag{3.31}$$

$$\Psi\left(\nu, T_o\right) = 4.2 + 5588 exp\left(-0.00787\bar{\nu}\right),$$

and

$$e_c = e_{h_2o} + 0.002\left(p - e_{h_2o}\right), \tag{3.32}$$

where $T_o = 298K$, $\bar{T}$, $\bar{\nu}$, e_{h_2o}, and p are the mean temperature and the mean wavenumber of the spectral band, water vapor partial pressure, and total atmospheric pressure, respectively.

3.4.3 Particles Absorption and Scattering

Cloud particles in the atmosphere significantly modify the radiative budget and radiative heating distributions of the atmosphere. In order to model the absorption and scattering processes associated with water and ice phase particles in the atmosphere, one will need to resolve the complex radiative interactions that occur inside the particles. The solutions to these complex interactions for spherical particles are known as Lorenz-Mie (L-M) solutions.

In this study, the optical properties (i.e., extinction, optical depth, single scattering albedo, asymmetry factor) of the cloud particles, including cloud water, rain water, pristine ice crystals, graupel, and aggregates, are determined using L-M solutions based on the values of refractive index for ice and water and assuming equivalent diameter sphere from particles size spectrum. The size distributions used in the L-M calculations are prescribed from the bulk hydrometeors species mixing ratios that are an output of the dynamical mesoscale/cloud model assuming a specific form for the size distribution. The forms of the size distributions assumed for each species are summaried in Table 3.6. The total concentration of each species is diagnosed from both the prescribed size distributions and the mixing ratio predicted by the dynamical mesoscale/cloud model. Since the actual ice crystal size distribution is perhaps less well known, we chose to represent this variable using the ice crystal size spectrum data obtained from the aircraft measurements during the FIRE IFO experiment (Stackhouse and Stephens, 1989 and Heymsfield *et al.*, 1990). The resultant spectral optical parameters for each species used in the radiative transfer model are given in Appendix A.

Table 3.6: Size distribution for different water species.

Water Species	Size distribution	$R_{\mathbf{eff}}(cm)$
Cloud	Modified gamma	0.0016
Rain	Marshall-Palmer	0.0810
Ice Crystal	FIRE Ice	0.0043
Aggregate	Marshall-Palmer	0.4950
Graupel	Marshall-Palmer	0.1500

Once these optical parameters are determined, the two-stream multiband radiation model can be used to solve the fluxes to obtain the radiative budget and radiative heating profile of the atmosphere.

3.5 Some Uncertainties of the Radiation Model

The radiation model described in this chapter represents a conceptual view of the flow of radiation in the earth-atmosphere system. Many assumptions have been used to achieve the current model. These assumptions will, of course, affect the final solution of the radiative budget fields. In addition to these deficiencies, the uncertainties in the actual optical properties of the atmosphere can also add to the uncertainty in the final radiative budget calculations. We will briefly discuss these problems below.

The biggest problems associated with the formulation of the two-stream model are usually associated with (1) the horizontal homogeneous assumption of the radiation field and (2) the inaccurate representation of the multiple scattering processes in the two-stream solutions. The assumption of horizontally homogeneity can have large effects on certain aspects of the radiative budget of the cloudy atmosphere due to both the finite boundaries of the actual cloud scenes (Davis and Cox, 1978) and the internal inhomogeneity of the cloud systems (Barker 1992). For example, internal inhomogeneity can reduces cloud albedo below homogeneous values by as much as 10% for overcast sky. Furthermore, the inherent problem associated with the representation of the multiple scattering processes in the two-stream model can also add to as much as 10% errors in the final radiation calculations under certain conditions (King and Harshvardhan, 1986; and Harshvardhan and King, 1993). However, it is not clear that that inhomogeneities affect our estimate of the vertical profile of radiative heating (Duda, personal communication).

Perhaps the most significant uncertainties are in defining the actual optical properties of the clouds (i.e., single scattering albedo, asymmetry factor, and extinction). These uncertainties are related to the uncertainties in the size distributions, shapes, and orientations of the particles. For example, the existence of ice crystals with stable orientations in cirrus cloud can significantly lower the value of asymmetry factor (Takano and Liou,

1989), which can lead to both the enhancement in shortwave reflection and the reduction of shortwave absorption of these cloud systems. However, this enhancement in shortwave reflection can be reduced significantly by the internal inhomogeneity of the cloud systems.

3.5.1 Sensitivity of the Radiation Model to Microphysics

In order to address the uncertainties of the cloud optical properties on the radiative budget calculations, sensitivity experiments with different mean radius and different asymmetry factor (given in Table 3.7) are performed using information from the third hour of the EMEX simulation, which will be discussed in a later chapter.

Table 3.7: Setup for the sensitivity experiments.

Experiment	Water Species	Size distribution	$R_{\mathbf{eff}}(cm)$	Asymmetry
1a	Cloud	Modified gamma	0.0016	Diagnosed
1b	Cloud	Modified gamma	0.0033	Diagnosed
1c	Cloud	Modified gamma	0.0008	Diagnosed
2a	Ice Crystal	FIRE Ice	0.0043	Diagnosed
2b	Ice Crystal	FIRE Ice	0.0083	Diagnosed
2c	Ice Crystal	FIRE Ice	0.0031	Diagnosed
3a	Ice Crystal	FIRE Ice	0.0043	0.85
3b	Ice Crystal	FIRE Ice	0.0043	0.70

Figures 3.7 and 3.8 show the sensitivity of the shortwave radiative budget to changes in the effective radius of both the ice crystal and the cloud water, respectively. As the effective radius increases/decreases by a factor of two, both cases show an increase/decrease in shortwave transmission and a decrease/increase in the shortwave albedo of the cloud system. These changes in the shortwave transmission and albedo are on the order of 10 percent. The changes in the effective radius associated with the cloud water do not significant affect the absorption of the cloud cluster. The changes in the effective radius of ice crystals, however, tend to increase slightly (i.e., less than 4 percent) the absorption of the MCS. Figure 3.9 shows the sensitivity of the shortwave radiative budget to changes in the asymmetry factor of the ice crystals. The results are similar to Fig. 3.8. As the asymmetry factor decreases, the transmission and the absorption of the MCS increases while the albedo of the cloud cluster decreases. While the changes in the transmission and

the albedo value of the cloud cluster are on the order of 10 to 15 percent, the changes in the absorption are much smaller (i.e., less than 4 percent).

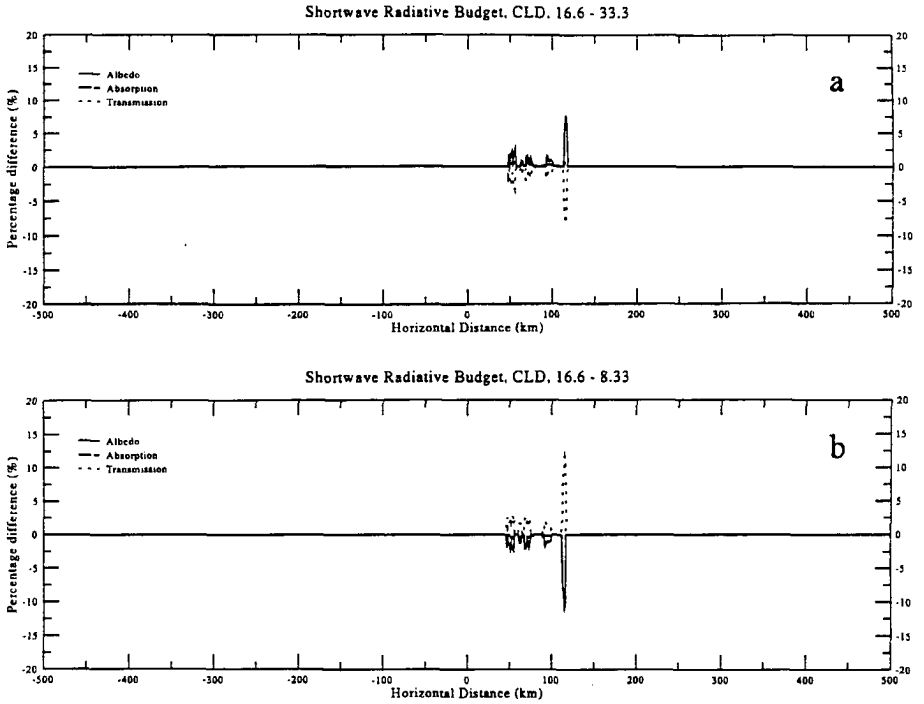

Figure 3.7: Relative differences in shortwave radiative budget associated with the change in effective radius of the cloud water for (a) Reff(16) - Reff(33) and (b) Reff(16) - Reff(8).

These calculations indicate that the uncertainties associated with the cloud optical properties as specified in this study produce an uncertainty of about 10 percent in both the transmission and the albedo of the MCS. Furthermore, the results also indicate that these uncertainties do not affect the shortwave absorption properties of the cloud cluster (i.e., less than 4 percent).

3.6 Comparison of Radiation Models

In this section we will compare the radiative budget profile produced by the current multiband two-stream radiation model against those given by the simplier broadband radiation model of Chen and Cotton (1983). The purpose of these comparisons is to establish some guidelines on the magnitude of differences (i.e., radiative budget) between the detailed radiation model described in this chapter and the simpler broadband radiation model which are used in the simulation of the tropical cloud clusters. Since the detailed

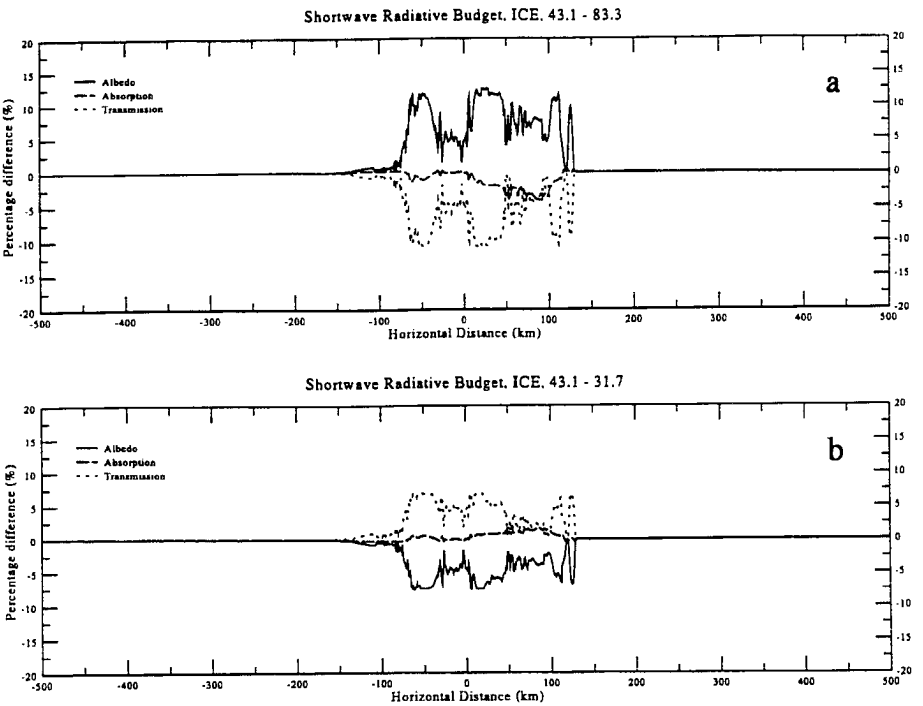

Figure 3.8: Relative differences in shortwave radiative budget associated with the change in effective radius of the ice crystals for (a) Reff(43) - Reff(83) and (b) Reff(43) - Reff(31).

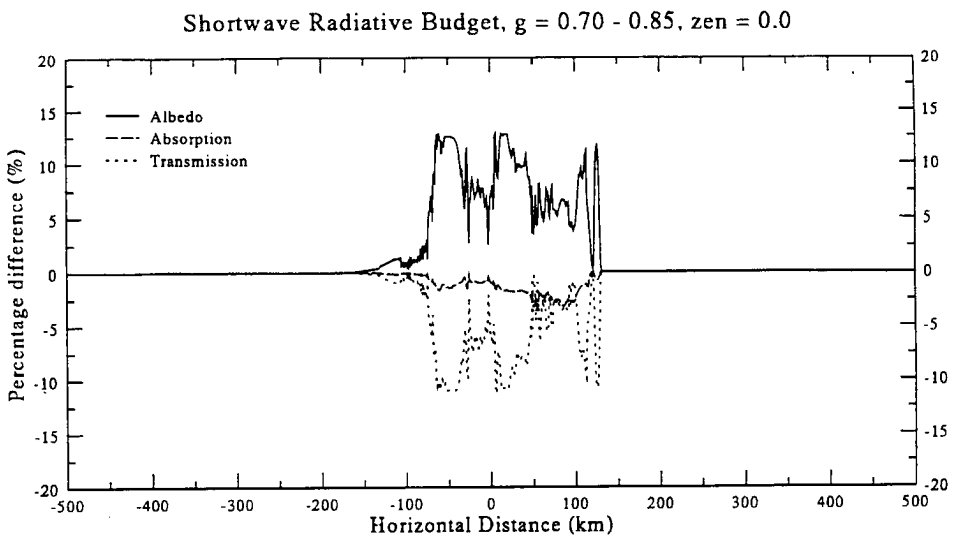

Figure 3.9: Relative differences in shortwave radiative budget associated with the change in asymmetry factor (Asy(0.70) - Asy(0.85)) of the ice crystals.

model is designed to represent the optical properties of the atmosphere in a more accurate fashion, it is, therefore, believed that it can produce a better radiative budget profile than those of the simple model.

Figure 3.10 shows the relative differences (i.e., relative to the two stream multiband radiation model) for various components of the radiative budget produced by the simple broadband radiation models using information from the third hour of the EMEX simulation, which will be discussed in a later chapter. The convention in this figure is that a positive value indicates a larger value (i.e., overestimation) of radiative budget by the simple broadband model and that a negative value indicates a smaller value (such as underestimation) by the simple model with respect to the detailed model.

At the top of the atmosphere, the results (given in Fig. 3.10a) indicate that the simple broadband radiation model is overestimating/underestimating the amount of longwave/shortwave energy into the earth-atmosphere system in both the clear sky and the cloudy region. While the simple broadband model is underestimating the amount of longwave energy (shown in Fig. 3.10b) into the surface in the clear sky region, it overestimates the longwave energy into the surface at the cloudy region by as much as 100%. In addition the simple model also underestimates the amount of shortwave energy into the surface in both the clear sky and the cloudy region.

The relative differences for the atmospheric radiation budget is given in Fig. 3.10c. The atmospheric radiation budget is calculated from the differences between the net flux at the top and the net flux at the surface. In the atmosphere, this figure indicates that the simple model overestimates the longwave energy loss in both the clear sky and the cloudy region, which suggests a systematic bias of the simple model toward a cooler atmosphere (i.e., too much cooling). This cooling is much larger in both the convective and the ice stratiform-anvil region than the clear skies, indicating that this overcooling in the cloud region is due to the systematic differences in the longwave parameterization of ice clouds in the model. The shortwave energy, on the other hand, shows an underestimation in both the clear sky and the thin cloud region, indicating too little heating in these areas. In the thicker parts of the cloud, the broadband model overestimates the shortwave energy

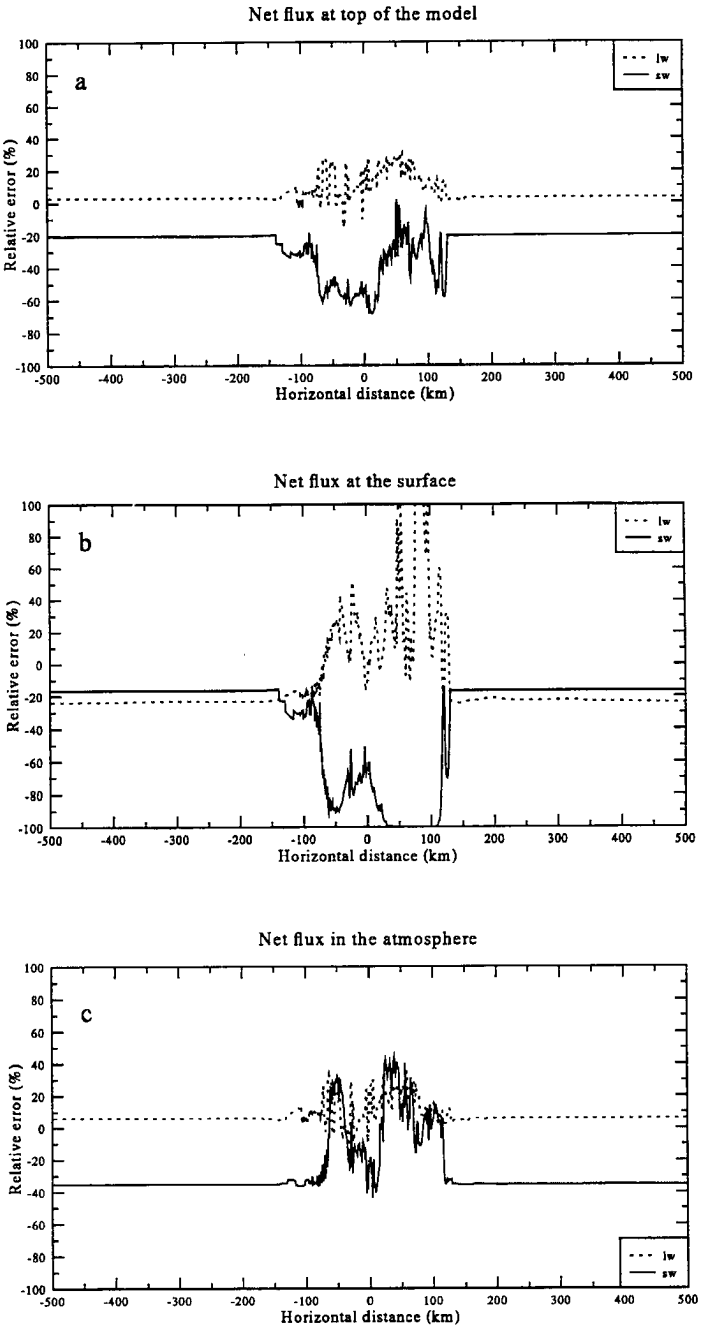

Figure 3.10: Relative differences associated with the broadband radiation model at (a) the top of the atmosphere, (b) the surface, and (c) in the atmosphere.

which again indicates too much heating in those regions. These differences can be as large as 40%.

Even though the simple broadband radiation model does contain significant systematic differences in the radiative budget calculations with respect to the more accurate detailed radiation model, the needs for a fast and speedy radiation model (i.e., a few minutes instead of few hours of computing time) that can be incorporated into the cloud model outweigh many of these shortfalls. Therefore, the simple broadband model is only used to obtain an estimate of radiative heating for the cloud simulations in the later chapters. The actual radiative budgets and radiation heating profiles in this work are estimated using the more accurate two stream multiband radiation model discussed early in this chapter.

Chapter 4

OBSERVATIONAL DATA AND ANALYSES

This chapter provides the description of observational data and the specific analyses concerning two case studies of tropical squall-type MCS employed in this research. The purposes of this chapter are (1) to furnish initial conditions for the numerical cloud simulations, (2) to establish the observational bases for which the numerical simulations are compared with, (3) to identity physical processes that are important to the formation and evolution of the two cloud systems, and (4) to give a comparison on the structures and properties of these cloud clusters.

4.1 Description of the Field Experiments

The data used in the two case studies derived from two different experiments conducted off the northern coast of Australia during the southern summer which are designed to investigate the nature of both the maritime and the continental tropical mesoscale convective systems. The first data set comes from three different but overlapping field experiments conducted during January and February of 1987. The three programs are the Equatorial Mesoscale Experiment (EMEX), the Stratospheric and Tropospheric Exchange Project (STEP), and the Australian Monsoon Experiment (AMEX). These programs provide a unique and valuable data set on the structure of maritime tropical MCSs, the larger-scale environment in which they form, and the interactions between the two. Figure 4.1 offers a simplified and integrated view of the EMEX-STEP-AMEX field programs. EMEX provides measurements inside and below the cloud systems, STEP provides data at levels above the convection, and AMEX provides the synoptic conditions in which these cloud systems were embedded. The second data set derives from experiments conducted during two different periods from November, 1988 to February, 1989 and from November,

1989 to February, 1990 over the vicinity of Darwin, Australia. This experiment, the Down Under Doppler and Electricity Experiment (DUNDEE), provides another unique set of data to examine the life cycle of the tropical MCSs as they occur during monsoon and monsoon break periods over the northern Australian region. A brief description for each of these experiments is given in below.

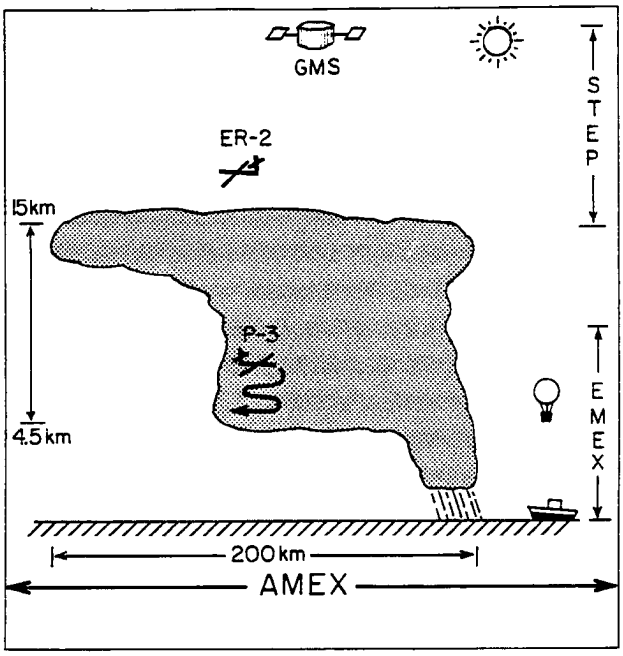

Figure 4.1: A schematic of the syergism between EMEX, STEP, and AMEX.

4.1.1 EMEX

The aim of EMEX was to examine the net diabatic heating associated with equatorial cloud cluster systems by carefully documenting the vertical and the horizontal kinematic motion structures of these systems (Webster and Houze, 1991). The experiment sought to test the hypothesis that evolved out of both GATE and WMONEX, namely that the vertical diabatic heating profile in tropical MCSs has a maximum in the middle to upper troposphere (Houze, 1989). This proposal stems from the observational studies that condensational heating in the lower troposphere in the convective regions of the MCS is offset by the evaporation cooling and melting of precipitation in the stratiform mesoscale region. Reinforcement of the heating from condensation and freezing of moisture in both

the convective region and the mesoscale area, in addition to radiative heating in the widespread stratiform cloud, are thought to produce a strong heating tendency in the middle to upper troposphere.

This hypothesis could not be tested with the conventional synoptic sounding data network for the Northern Australia region since the circulation and heating fields of the mesoscale cloud system could not be explicitly resolved by such network. Additional data platforms, and more extensive observational arrays, were thus provided during EMEX. The primary data sources for the analysis of EMEX cloud clusters were obtained from aircraft, satellites and from a ship platform.

Satellite observations provide time continuity and detailed information on the evolution of these tropical MCSs. These satellite data also provide information about the larger-scale environment in which these tropical MCSs were embedded. Data from three satellites, the visible/infrared image data from the Japanese GMS-3 geostationary satellite and visible/infrared AVHRR data from the NOAA-9, and NOAA-10 polar orbitary satellites, were archived for EMEX (Stephens and Greenwald, 1988).

The research vessel 'Xiangyanghong No. 5' from the People's Republic of China was located at latitude 10.5° South and longitude 138° East during the entire EMEX period and provided vital atmospheric sounding information over the open ocean using conventional rawinsonde. On board the 'Xiangyanghong No. 5' was the NOAA-TOGA C-band 5 cm coherent radar which was used to construct both the Doppler wind profile and radar reflectivity fields around the vessel. Unfortunately, the ship radar data were limited since many of the tropical MCSs investigated during EMEX were located outside the range of the radar.

Three aircraft were used during the experiment; the NOAA WP-3D, the NCAR Electra, and the Australian CSIRO F-27 (e.g. Gamache et al., 1987). These aircraft facilities were the primary data platforms during EMEX since they could directly penetrate the maritime mesoscale cloud cluster systems. Flight plans were carefully constructed so that profiles of the vertical and horizontal kinematic motion in both the convective and stratiform regions could be determined, as well as the radiative flux profiles in the mesoscale

stratiform area. These aircraft were low altitude platforms primarily used for probing the atmosphere below 8 km. Each aircraft was equipped with a suite of instruments to measure the dynamic, thermodynamic, and radiative properties of the atmosphere. In addition, PMS cloud microphysical measurements were also made on both the P-3 and the Electra. These PMS cloud microphysical data, however, have not been extensively analyzed. The P-3 was also equipped with a lower fuselage C-band 5 cm noncoherent and a tail X-band 3 cm coherent radar for both horizontal reflectivity scans (PPI) and vertical reflectivity scans (RHI), respectively. These radars provide a way of tracing and reconstructing cloud hydrometeors fields at/near the aircraft's location as well as the Doppler-derived motion field within 30 km of the aircraft.

A total of 10 research aircraft missions and 1 intercomparison calibration mission were conducted during EMEX between 1/14/87 and 2/4/87. A summary of these aircraft missions and the large-scale environmental condition during the entire EMEX experiment can be found in Webster and Houze (1991).

4.1.2 STEP

The NASA STEP was an experiment designed to measure the physical and chemical properties in the tropopause region of the tropical atmosphere and to understand the mechanisms that contribute to the chemical transports between the upper troposphere and lower stratosphere (Russell *et al.*, 1991, 1993). A key physical process under investigation concerns the role that cirrus anvil clouds play, if any, in the drying of the lower stratosphere (i.e., Danielson, 1982). To investigate these processes the NASA ER-2 aircraft, which was equipped with instruments that provided dynamical, thermodynamical, radiative and cloud microphysical measurements of the upper troposphere and lower stratosphere, was used. Only the radiative data are used in this study to provide estimates of the upper level radiative boundary conditions at infrared wavelengths. Among the radiative instruments on the ER-2 are two broadband solar pyranometers (0.3–3.0 micron) and one rotating net flux infrared (4.0–40 micron) pyrgeometer. The pyranometers were located at the top and bottom of the fuselage to measure the downward and upward solar fluxes respectively. These shortwave instruments, however, were mounted at an angle relative to the aircraft's

plane of reference which makes the calibration correction somewhat difficult. The net infrared instrument protruded from the rear of one wing. These radiometers allow the calculation of heating rates in various layers of the atmosphere within or above the cloud top of the cirrus anvils. The ER-2 flew step flight paths at several different altitudes ranging from cloud top to the lower stratosphere between approximately 16–20 km.

4.1.3 AMEX

AMEX was a field experiment designed to study the Australian Monsoon system during the northern winter and to improve understanding of the interactions between the large-scale circulation and the maritime convection that occurs during the monsoon period (Holland *et al.*, 1986). These tropical MCSs are generally characterized by convective cloud bands and rainy weather. They are also formed in a region of lower tropospheric westerlies. This program was sponsored by the Australian Bureau of Meteorology Research Center (BMRC) for the period between 1/10/87 and 2/14/87.

In addition to the normal sounding stations, a special sounding and surface synoptic network (reported every four hours) was established so that the weather systems in the Australian Monsoon could be documented and the interaction between the cloud clusters and the large-scale flow diagnosed. Besides these observations, temperature and wind data retrieved from satellite data were also collected and included in an objective analysis scheme provided by the BMRC to produce a set of synoptic data fields with 1.25 degree resolution for the entire AMEX period. Other data collected during AMEX included information from conventional ground based noncoherent radars located at Darwin, Gove, and Weipa.

4.1.4 DUNDEE

The main goal of DUNDEE was to investigate the dynamical and electrical features of tropical mesoscale convective systems and isolated deep convective storms around Darwin, Australia (Rutledge et al., 1992). The observational network (shown in Fig. 4.2) used for this experiment centered around two Doppler radars. The network also included a number of surface mesonet weather stations, upper-air soundings from Darwin and the

MIT Doppler radar station, and cloud electricity instruments. In addition a 50 Mhz vertical-pointing wind profile was also installed at the TOGA Doppler radar station during the second DUNDEE season. Furthermore, synoptic data were also collected along with satellite data during these periods. This experiment was conducted during the southern hemisphere summer of 1988/1989 and 1989/1990.

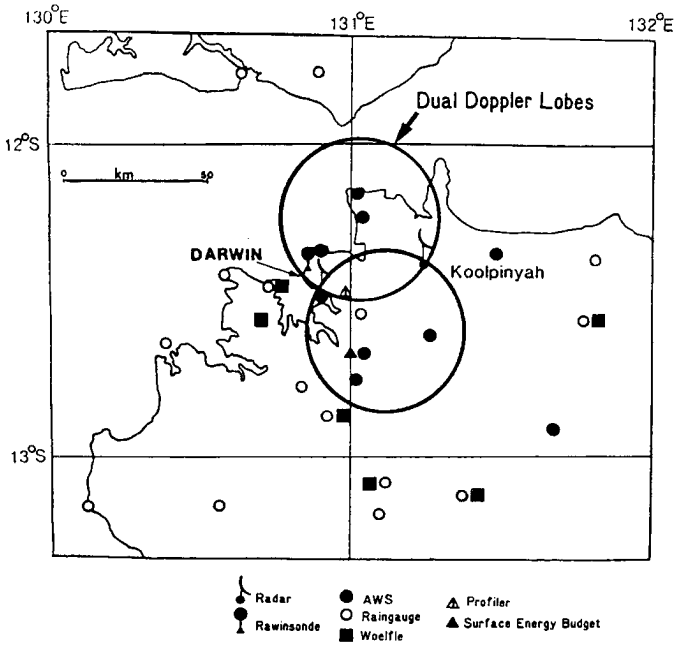

Figure 4.2: Observational network of DUNDEE.

The Two Doppler radars used in DUNDEE were the MIT C band and the NOAA TOGA C band radar. These radars were set up on a 29 km east-west oriented baseline, allowing for dual-Doppler scanning of the storms. The scanning procedure of these two radars consists of time-synchronized 360 degree volume scans for dual-Doppler coverage, coordinated 150 and 90 degree sector dual-Doppler scans for better temporal and spatial resolution of convective storms, volume scans to allow for diagnosis of mesoscale vertical motions using Extended Velocity Azimuth Display technique (EVAD), and rapid-update small-sector scans and vertical cross-sections to study evolution of convective cells for cloud electricity studies. These radars provide important information on the precipitation and kinematic motion structures throughout the life cycle of the MCSs.

Surface observation and upper air soundings were collected during DUNDEE. Regular wind soundings (6 hourly) and thermodynamic soundings (12 hourly) were released throughout the program at Darwin to record the atmospheric conditions around the region. In addition, an event-related sounding program was set up at the MIT radar site using a OMEGA sonde system developed by the National Center for Atmospheric Research (NCAR) to monitor the changes of the atmospheric thermodynamic and momentum field related to the passage of tropical MCSs. The surface observation network included 10 Automatic Weather Station (AWS) mesonet within 100 km of Darwin and an outer network of Woefle chart recorders to provide spatial and temporal information of the planetary boundary layer associated with local and storm-induced mesoscale circulation. In addition, rainfall was also recorded within 75 km of Darwin using a network of tipping bucket gauges.

Digitized satellite data from the Japanese GMS–3 and GMS-4 geostationary satellite were not collected at the time of experiment. They were obtained after the experiments from NOAA National Satellite Service at Washington D.C. These GMS data, containing both visible and infrared images, provide additional temporal and spatial information of these tropical MCSs. Furthermore, microwave data from the Defense department DMSP satellite were also collected to provide radiometric information below the cloud top region.

Limited synoptic data were collected in the form of weather maps during the experiment from the Australian Breau of Meteorology at Darwin. Additional large-scale conditions were provided using European Center for Medium Range Weather Forecasting (ECMWF) 2.5 degree resolution gridded data sets obtained from NCAR after the experiments. The area between 0° to 30° south and 110° to 155° east were extracted from the ECMWF data set for analysis. These data provide information concerning the state of the large-scale atmosphere in the northern Australian region during the experiment.

4.2 EMEX Case Study

The first case study focuses on an oceanic monsoonal MCS with embedded squall type convection that developed during EMEX mission 9 (hereafter referred to as EMEX-9 cloud

cluster) between 2/2/87 and 2/3/87. On 2/2/87, a cloud cluster system was observed to move into the observational area of EMEX off the Northern Australian coast. All four aircraft (P-3, Electra, F-27, and ER-2) were dispatched into the area to document the cloud cluster system. This aircraft mission provided an excellent opportunity for studying the radiative budgets of the tropical mesoscale convective system. In this section, we will describe and analyze both the large-scale observations (i.e., AMEX synoptic data and EMEX satellite measurements) and the in-cloud measurements (i.e., EMEX and STEP aircraft data) associated with this cloud cluster system. The information obtained below will be used to set up and to verify the EMEX cloud simulation in the next chapter.

4.2.1 Large-Scale Environment of EMEX-9 Case

The synoptic conditions prevailing over the AMEX area at 2300 UTC (0916 LST), 2/2/87 are presented in Fig. 4.3a and 4.3b in the form of the 500-mb streamline and geopotential height field. The significant features of these fields are the strong cyclonic vortex associated with tropical cyclone Damina located off the west coast of Australia, the strong anticyclonic New Guinea vortex (Webster and Houze, 1991) stationed off the west coast of New Guinea island, and a strong mid-level westerly monsoon trough that extends from the northern Australian continent and across into New Guinea. This intense mid-level monsoon trough extended to the surface, and presumably provided the necessary large-scale lifting mechanism for the formation of the MCS identified as the EMEX-9 cloud cluster. The land breeze also provided additional mesoscale forcing for the MCS (Alexander, personal communication). The large-scale synoptic vortex pair, the New Guinea anticyclone and the Australia low or tropical cyclone, was also a common feature during other EMEX missions. The strength and location of these vortices may be strongly correlated to the beginning of the strengthing monsoon westerlies and the inception of the mesoscale convective activities during EMEX (Webster and Houze, 1991).

The wind profile north of the Gulf of Carpentaria at this time was dominated by lower level westerlies backing (counterclockwise rotation) with height into stronger easterlies aloft. This is apparent when the surface and 100-mb streamlines, shown in Fig. 4.3c and 4.3d, are compared. Wind speeds exceeding 40 knots existed in the upper troposphere. In

the vicinity of the pre-monsoon trough (i.e, region to the west of the monsoon trough), low level surface northwesterly flow helped feed the cloud cluster with warm, moist equatorial air. The equivalent potential temperature field in Fig. 4.3e has a minimum at 850-mb surface located over the monsoon trough. We speculate that this feature results directly from the presence of the cloud cluster which acts to warm and dry out the lower troposphere.

4.2.2 Satellite Image Analysis of the Cloud Life Cycle

The time series of enhanced infrared GMS satellite images shown in Fig. 4.4 provides a sense of the life-history of the EMEX-9 MCS. The image of Fig. 4.4a suggests that the EMEX-9 cloud cluster originated off the northern coast of Australia along the mid-level monsoon trough before 1530 UTC (0146 LST) on 2/2/87. This early morning development in mesoscale cloud systems is a typical nocturnal characteristic of this oceanic region, which lies between the land masses of the maritime continent (Williams and Houze, 1987). This cloud cluster system propagated along the monsoon trough and lasted for approximately 12 hours. The estimated speed and direction of propagation of the system, based on cloud motion analysis from these satellite images, is about 12 m/s towards the northeast. The MCS was fully developed by 1730 UTC (0346 LST) as suggested by the broad area of cold cloud top temperatures in Fig. 4.4b and had moved out into the open ocean. Cloud cluster scale interactions are evident in the 2030 UTC (0646 LST) image (i.e., Fig. 4.4c) as the EMEX-9 cloud cluster merged with another cluster that had formed in the Gulf of Carpentaria. This merger seemed to enhance the circulation in the MCS, as indicated by the extensive area of cold cloud top temperature, and presumably extended the life cycle of the convection. This particular cluster-cluster interaction is not a topic of investigation in this study and the model simulation discussed in the next chapter of this dissertation is only of the non-merger phase of the MCS. At 2330 UTC (0946 LST), i.e., Fig. 4.4d, the EMEX-9 cloud cluster was centered at latitude 9° S and longitude 139° E with a minimum recorded cloud top temperature less than $-70°$ C. According to the Darwin temperature sounding data taken at 2300 UTC, this cold cloud top temperature indicates that the vertical extent of this cloud system had penetrated well above the 150-mb (15

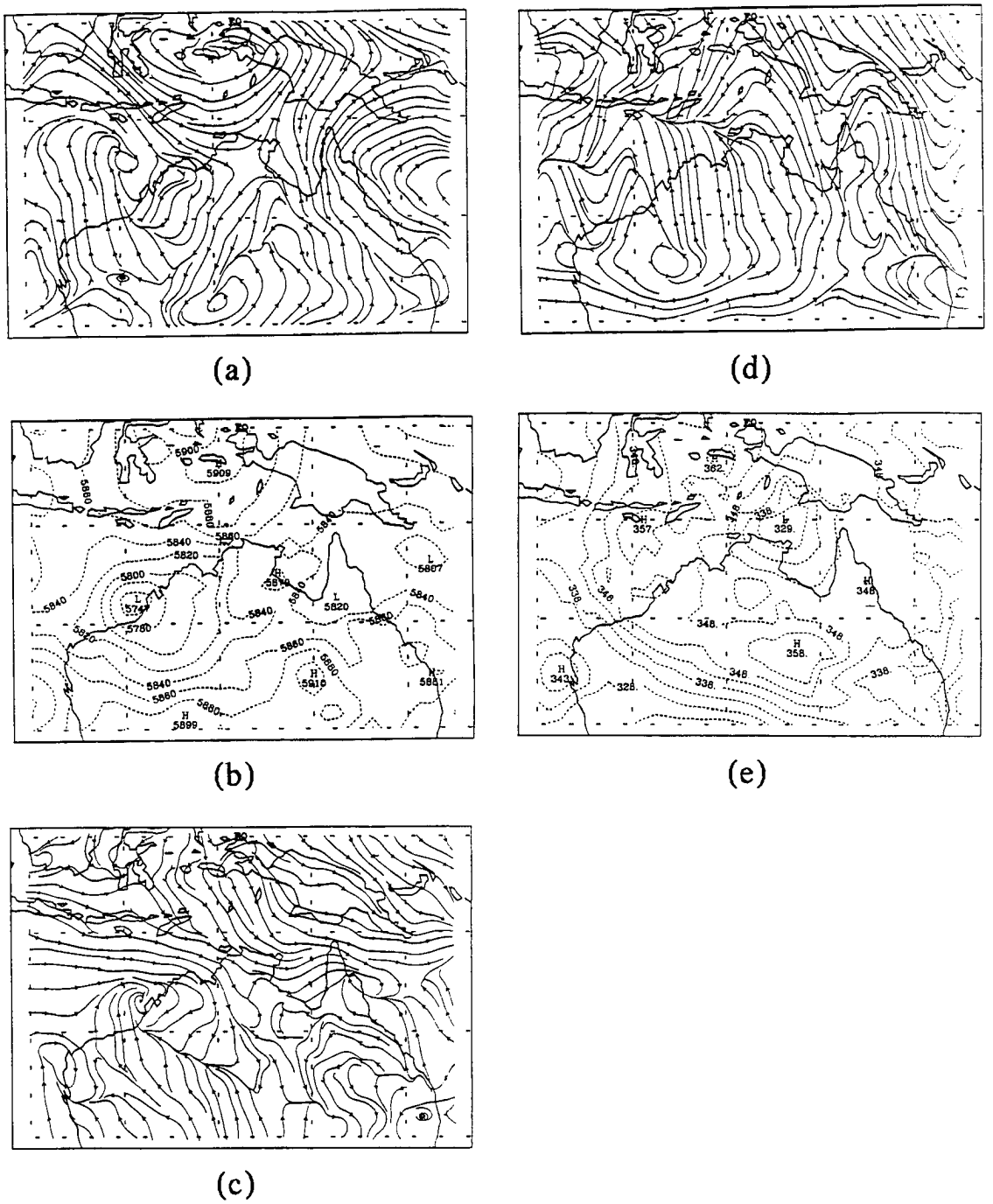

Figure 4.3: Large-scale synoptic condition at 2300 UTC on 2/2/87 over the AMEX regions for (a) 500-mb streamline pattern, (b) 500-mb geopotential height field, (c) surface streamline pattern, (d) 100-mb streamline pattern, and (e) 850-mb equivalent potential temperature field.

km) height surface. Furthermore, the satellite data reveal an extended area of cirrus cloud in the cloud cluster with cloud top temperatures less than $-60°$ C. The EMEX-9 cloud cluster had slowly decayed by 0230 UTC (1246 LST) on 2/3/87 (given in Fig. 4.4e) as it approached New Guinea.

4.2.3 EMEX-9 Aircraft Data

Aircraft measurements collected during EMEX-9 provide important information on the vertical motion, kinematic structure and radiation profile within maritime tropical monsoonal cloud systems. In the following sections, we will discuss the findings concerning the mature stage (i.e., the Doppler radar data from the convective/transition and the stratiform period of the aircraft mission) and the decaying stage (i.e., the *in-situ* data from the radiation sounding period) of this MCS.

4.2.3.1 Data from Convective/Transition and Stratiform Period

The determination of the vertical motion and kinematic structure in both the convective and the stratiform region of tropical MCSs were two of the most important objectives of the EMEX experiment. These objectives were accomplished through the use of an airborne Doppler radar system on the NOAA WP-3D aircraft. During the convective/transition and stratiform periods of the aircraft mission, the P-3 flight plan called for a series of Doppler flight legs, track back and forth at 60 degree angle with each other directly across the area of interests in the mature stage of the MCS. The advantage of this special pattern is that it allows reconstruction of the steady-state composited pseudo-dual Doppler wind fields as well as producing a steady-state composite of the vertical velocity profile. For EMEX-9 this flight pattern was performed at an altitude of about 5 km. The discussion below is a brief summary of the results published by Webster and Houze (1991) on the Doppler data collected from P-3 aircraft during the convective/transition period (2040 to 2201 UTC) and the stratiform period (2302 to 2350 UTC) on 2/2/87.

During the mature stage of the EMEX-9 cloud cluster the non-coherent lower-fuselage radar data showed regions of strong to moderate convection surrounded by a broad area of stratiform precipitation. The P-3 vertical-incidence Doppler radar reflectivity data

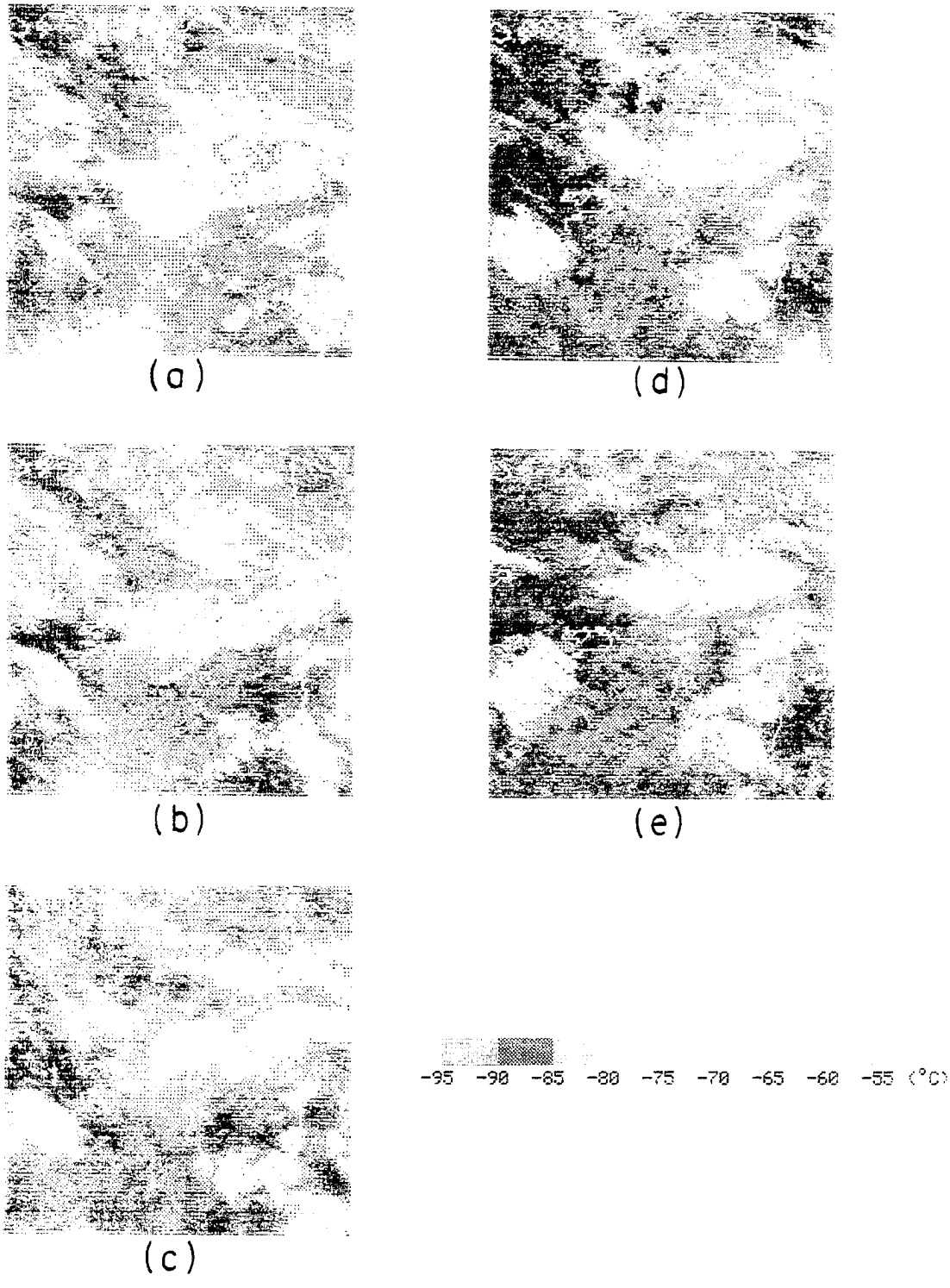

Figure 4.4: GMS infrared satellite images at (a) 1530 UTC, 2/2/87, (b) 1730 UTC, 2/2/87, (c) 2030 UTC, 2/2/87, (d) 2330 UTC, 2/2/87, and (e) 0230 UTC, 2/3/87 over the EMEX region. Cloud tops colder than $-55°$ C are enhanced in the images.

recorded from the tail radar during this period indicated two types of embedded convection associated with this cloud cluster system; an upright vertical structure (illustrated in Fig. 4.5a) and a pronounced rearward slope (shown in Fig. 4.6a). The angle of the rearward sloping convection is about 17 degree. Both types of convection extended up to 14.5 km and above and had a horizontal scale of about 40 km. The vertical motion fields retrieved from the vertical-incidence Doppler velocity data showed that the upright convection was composed of relatively weak upper-level upward and downward motion fields (shown in Fig. 4.5b). The vertical motion fields for the pronounced rearward-sloping convection (shown in Fig. 4.6b), on the other hand, possessed much stronger updraft. The maximum updraft for this squall line-like convection was located at about 10 km. Strong downdrafts was also present in the lower troposphere ahead of the strong updraft aloft. These vertical motion structures are a feature characteristic of a sloping system. The contrasting radar data collected during the stratiform precipitation period are shown in Fig. 4.7. In comparison to the convective region, the radar reflectivity data in the stratiform region indicate a relatively more uniform precipitation field with a bright band echo region near the freezing level (between 4 to 4.5 km), which are typical features to both the tropical and the mid-latitude mesoscale cloud systems (i.e., Houze, 1977 and Srivastava *et al.*, 1986).

4.2.3.2 Data from the Radiation Sounding Period

Estimation of the total (solar plus infrared) radiation budget in the widespread stratiform region of the cloud system was another primary objective of EMEX. EMEX proposed to accomplish this, in part, using radiometeric measurements from the P-3 aircraft operating in a special radiation survey pattern. This flight pattern consisted of 5 minute straight and level legs of approximately 40 km in length flown in a stair-step fashion, with each leg directly below the previous one. Since the entire radiation sounding flight pattern took approximately one hour to complete, the aircraft measurements at each level were actually taken at slightly different locations to account for cloud cluster movement during this period. *In-situ* data collected by the aircraft during this radiation sounding period are used in this study to reconstruct the mean vertical profiles of radiation, dynamic, and

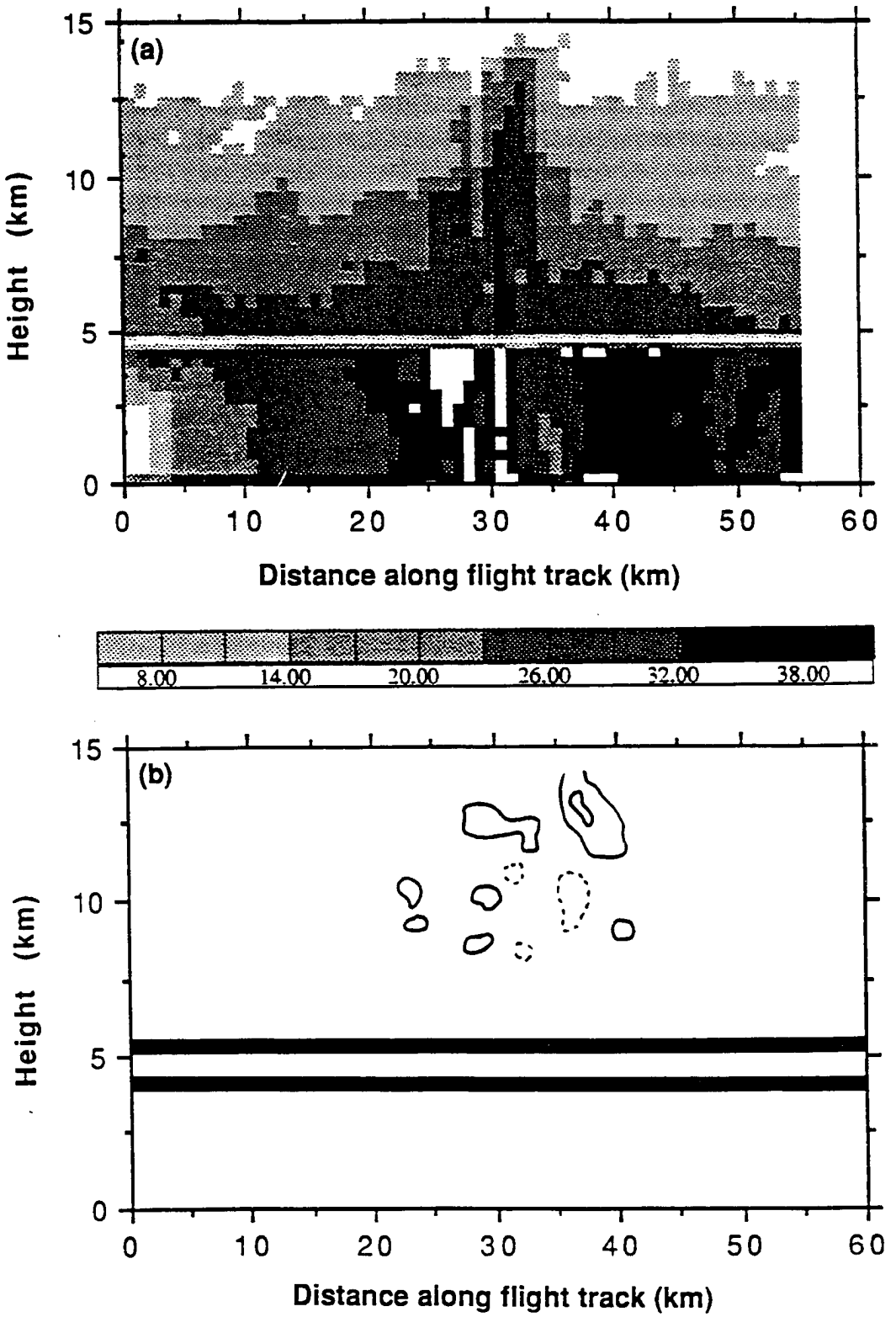

Figure 4.5: Time-height section of vertically pointing data from the NOAA WP-3D tail radar for the convective region of EMEX-9 cloud cluster showing upright vertical structure. (a) Radar reflectivity (dBZ) and (b) Doppler vertical velocity of precipitation particles (m/s: solid contours +1, +3; dashed contour -4). From Webster and Houze, 1991.

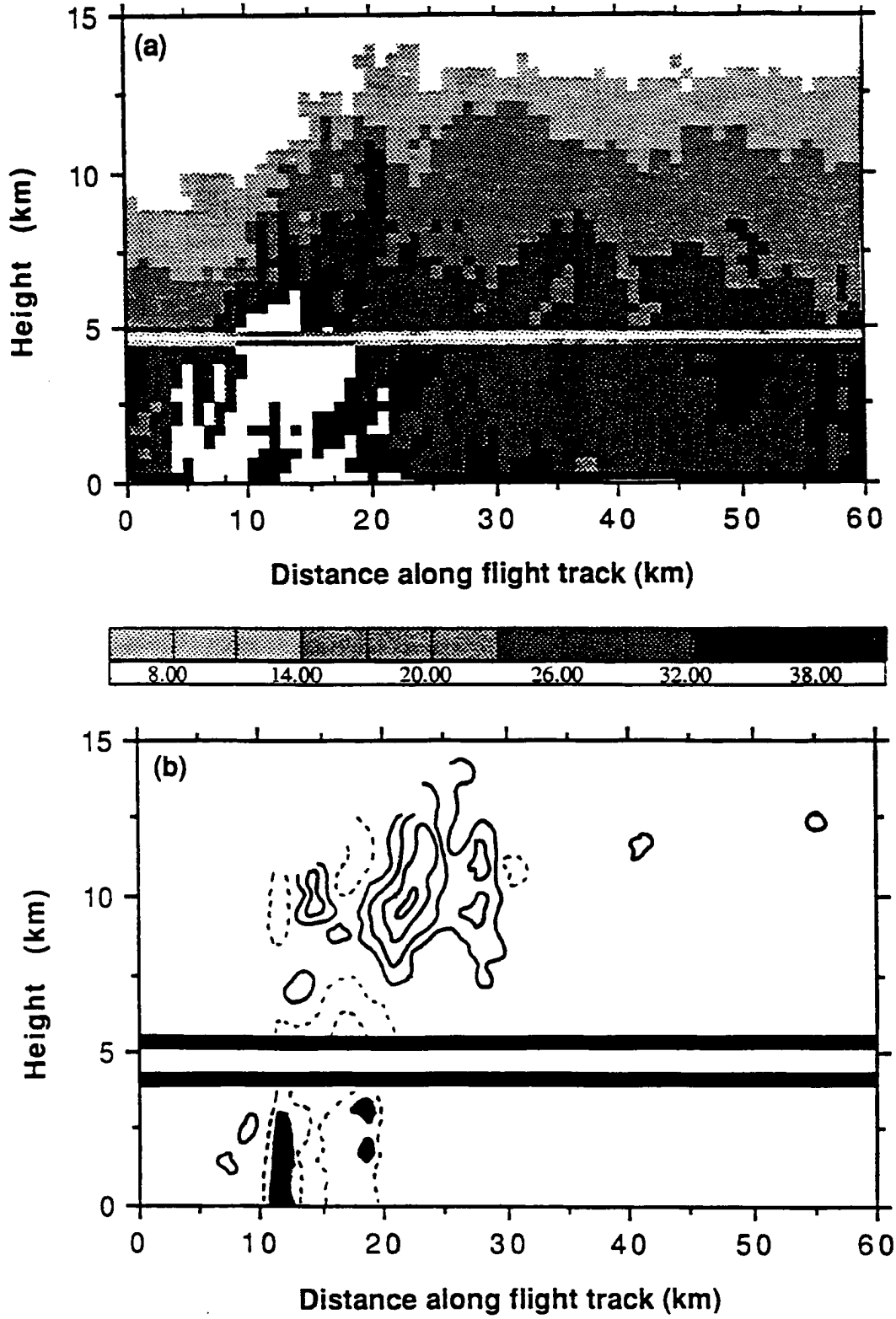

Figure 4.6: Time-height section of vertically pointing data from the NOAA WP-3D tail radar for the convection region of EMEX-9 cloud cluster showing pronounced rearward slope. (a) Radar reflectivity (dBZ) and (b) Doppler vertical velocity of precipitation particles (m/s: solid contours +1, +3, +5, and +7; dashed contour -4 (above melting level only), -10: filled areas (-12 m/s). From Webster and Houze, 1991.

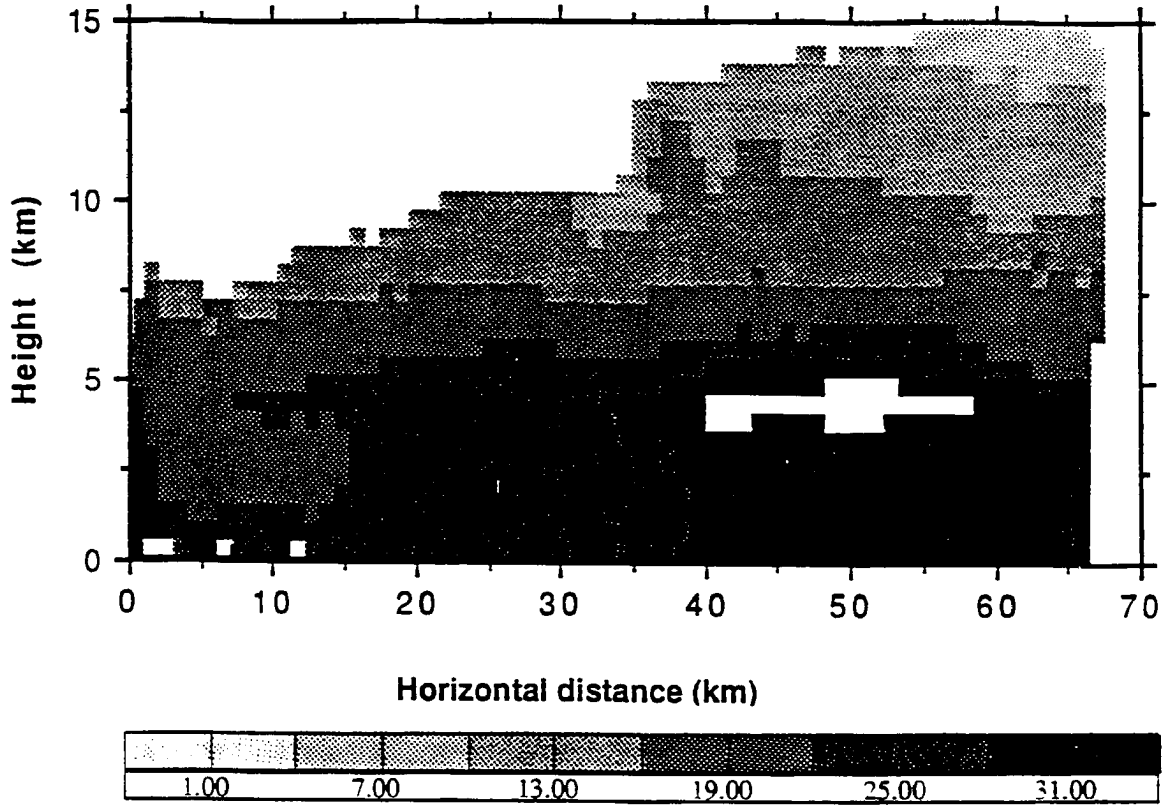

Figure 4.7: Vertical cross-section of radar reflectivity (dBZ) from the NOAA WP-3D for the stratiform region of EMEX-9 cloud cluster showing relatively uniform horizontal structures. From Webster and Houze, 1991.

thermodynamic fields of the atmosphere in and below the stratiform cloud region by assuming that the structures of the stratiform cloud remained relatively unchanged over the entire one hour sounding period. This assumption is not always valid since solar insolation varied during the period of the sounding although its validity may arguably be reasonable in the dynamically weak stratiform region. The P-3 flight pattern during EMEX-9 began at the highest altitude of 6.8 km at 0026 UTC (1042 LST) and ended at about 1.3 km at 0117 UTC (1133 LST) on 2/3/87. The data collected during this time represent atmospheric conditions of the stratiform region during the decaying stage in the life cycle of the EMEX-9 cloud system. Only the radiative fluxes in and below the stratiform cloud were measured by the P-3. Radiative fluxes above cloud top measured by the NASA ER-2 aircraft were used to complete the cloud radiation budgets in the stratiform region.

Figure 4.8 provides a composite of the vertical profile of the observed dynamical and thermodynamical fields averaged over each flight leg during the P-3 radiation survey period in the stratiform region of the EMEX-9 cloud cluster. The temperature and dew point profiles show a typical 'onion' type sounding found to the rear of the convective system. This 'onion' type sounding is a consequence of the subsidence warming below the cloud base which tends both to warm and to dry the air and therefore amplifies the separation between the temperature and dew point curves in the sounding (Zipser, 1977). The cloud base altitude at 4.8 km is determined when the air at a particular level is completely saturated with respect to the ambient air temperature in the P-3 sounding. The cloud top altitude is estimated from matching the Darwin temperature sounding data with the GMS cloud top infrared brightness temperature and is determined to be between 15 to 16 km. A mid- to low-level rear-to-front flow is also observed in the mean sounding with a maximum value of 19 m/s at about 750-mb surface. This flow is consistent with early findings by Johnson and Hamilton (1988) and by Doppler radar data for mid-latitude MCS. The mean vertical profile of vertical velocity field (solid line in Fig. 4.8b), calculated from both the P-3 aircraft's vertical acceleration and navigation data, shows downward vertical motion at and below the melting level (4.8 km) and upward vertical motion 2 km above this level. This is also consistent with the results derived from GATE and winter MONEX

(i.e., Houze, 1982 and Johnson, 1982). The effects of the downward motion below the melting level are also evident in the mean temperature sounding in Fig. 4.8a. The lapse rate below the cloud base in Fig. 4.8a lies somewhere between a dry and moist adiabat which is indicative that mixing of moist cloud air with drier environmental air below the cloud base has occurred. The mean vertical profile of liquid water content obtained with the Johnson-Williams hot wire probe is also shown in Fig. 4.8b (dash line). This profile indicates that liquid water generally increases with height to the freezing level and slowly decreases above this level as water freezes to form ice particles. The maximum liquid water content recorded in this stratiform region is on the order of 0.4 g/m^3.

Figure 4.9 presents a composite of the radiation measurements averaged over each flight leg. Because of the variation of the solar fluxes with time due to changes in the solar elevation angle, the solar fluxes are normalized relative to the mean time of the P-3 radiation profile at 0050 UTC (1106 LST) on 2/3/87. We performed this normalization using an appropriately chosen factor that relates the ratio of the cosine of the solar zenith angle at the time of observation to the cosine of the solar zenith angle at 0050 UTC (1106 LST). While the measurements above the cloud top were taken by the NASA ER-2 high altitude aircraft above altitudes of 16 km, the measurements inside and beneath the tropical MCS at altitudes below 7 km were obtained from the NOAA WP-3D aircraft between 0026 and 0117 UTC. Cloud top and cloud base level were determined from methods mentioned above. There are no data in the region between 7 to 16 km and a simple linear interpolation is used merely to connect the data. A linear extrapolation is also applied to extend radiation profiles to the surface. The shortwave radiation measurements from the ER-2 are not used in this composite due to calibration problem with the shortwave radiometer as mentioned in the earlier section. Instead, the two-stream radiation model discussed in Chapter 3 is used to give the best estimate of the downward flux of shortwave radiation above cloud top.

The shortwave values in the figure shows a significant attenuation of shortwave flux through the EMEX-9 cloud cluster. The estimated transmission is 14% at cloud base for the example shown. The upward and downward solar flux profiles are almost parallel to

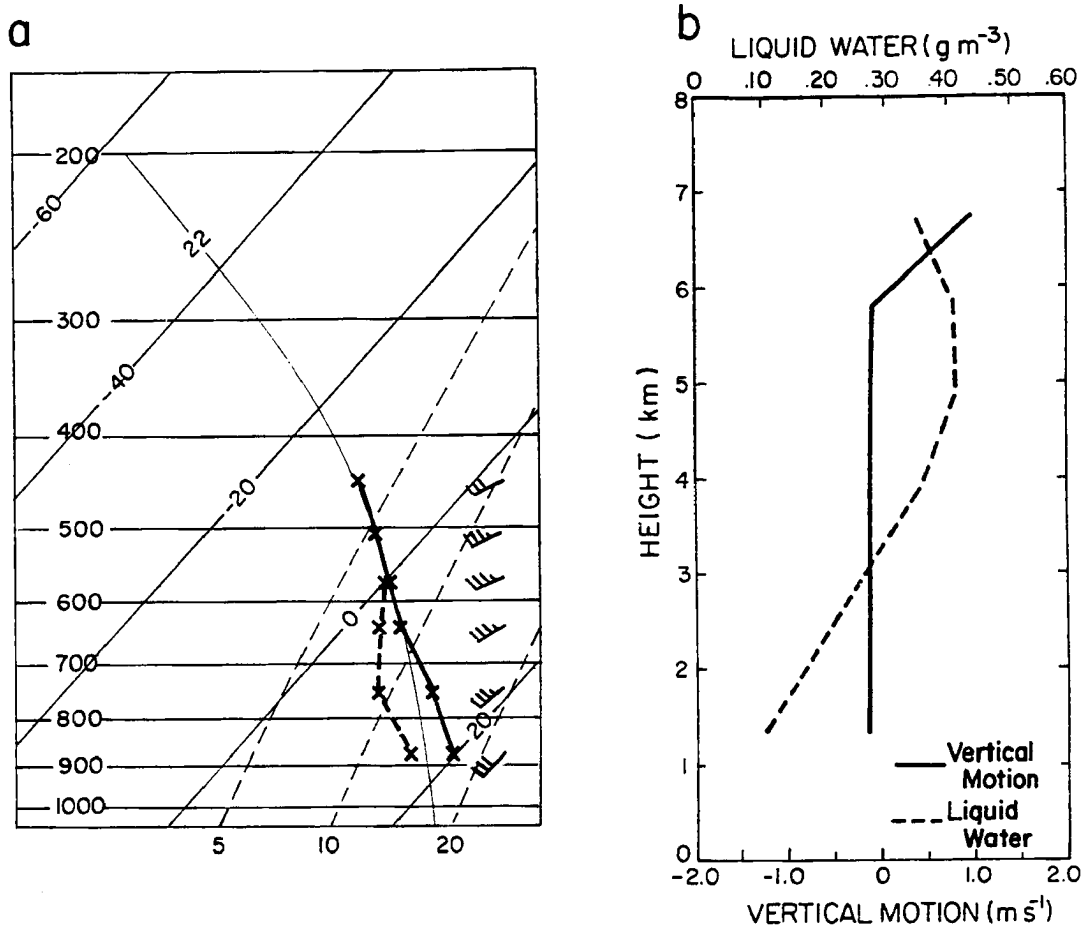

Figure 4.8: The reconstructed vertical profiles of (a) temperature (solid), dew point (dashed), and horizontal wind field (wind bar) and (b) vertical motion (solid) and liquid water content (dashed) in the stratiform region of EMEX-9 cloud cluster from the NOAA WP-3D aircraft.

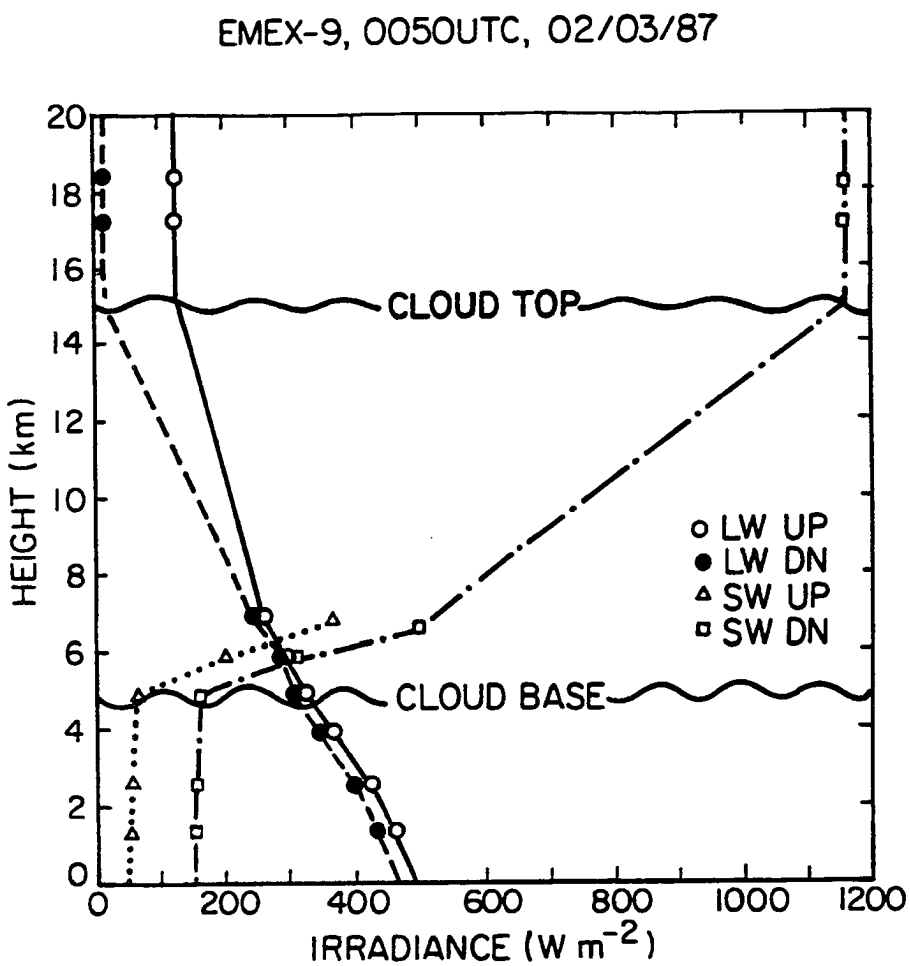

Figure 4.9: The reconstructed vertical profiles of the observed radiation fields (infrared and shortwave) in the stratiform region of EMEX-9 cloud cluster from the NOAA WP-3D and the NASA ER-2 aircraft. The solar measurements are normalized to 00500 UTC on 2/3/87. The actual radiation observations are given by various symbols (i.e., open circle for upward infrared flux, closed circle for downward infrared flux, open triangle for upward shortwave flux, and open square for downward shortwave flux) on the graph. Simple linear interpolation and extrapolation schemes have been used to connect the data points on the graph together (i.e., solid line for upward infrared flux, dashed line for downward infrared flux, dotted line for upward shortwave flux, and dot-dashed line for downward shortwave flux).

each other in the atmosphere inside and below the cloud base suggesting very little solar heating in these regions. The upward and downward infrared radiation fluxes measured in this tropical MCS also show features similar to those of the solar fluxes. We infer little infrared heating above and below the cloud since the upward and downward infrared profiles are approximately parallel to each other. The measured infrared fluxes are also close to the black body fluxes in the region from 4.8 to 6.8 km but the upward and downward fluxes diverge at levels both above and below the inner blackbody layer of the cloud. Unfortunately, the level at which the profiles diverge from the black body profile could not be estimated from the data and therefore we cannot estimate from observations the depth to which the longwave cooling penetrates into cloud top or the height to which longwave heating extends above the cloud base. The data do however suggest the expected general trend of cloud top infrared cooling and cloud base longwave heating. The upward infrared flux at the cloud top is associated with brightness temperature of about $-60°$ C which is roughly consistent with the GMS infrared satellite brightness temperature from 2300 and 0230 UTC. There is also significant variability in the radiation data (not shown). The solar fluxes vary more than infrared fluxes since they are more sensitive to the broken cloudiness.

4.3 DUNDEE Case Study

The second case study focuses on a continental squall-type tropical MCS that occurred during the synoptically undisturbed monsoon-break period on 12/05/89 over the northern region of Australia. During this day, a tropical MCS (hereafter referred to as DUNDEE cloud cluster) was observed to form south of the DUNDEE's dual Doppler radar array at about 0700 UTC (1630 LST) and begin to move directly north into the dual Doppler array. Radar collection for this case started at approximately 0710 UTC (1640 LST). Although the cloud radiation fields were not measured during DUNDEE, this case study does offer valuable information on the life cycle features of the continental tropical MCSs that will be used to model the radiative budgets of this cloud system. The large-scale environment (i.e., synoptic and satellite data) and the structures of this MCS (i.e., Dopplar radar and

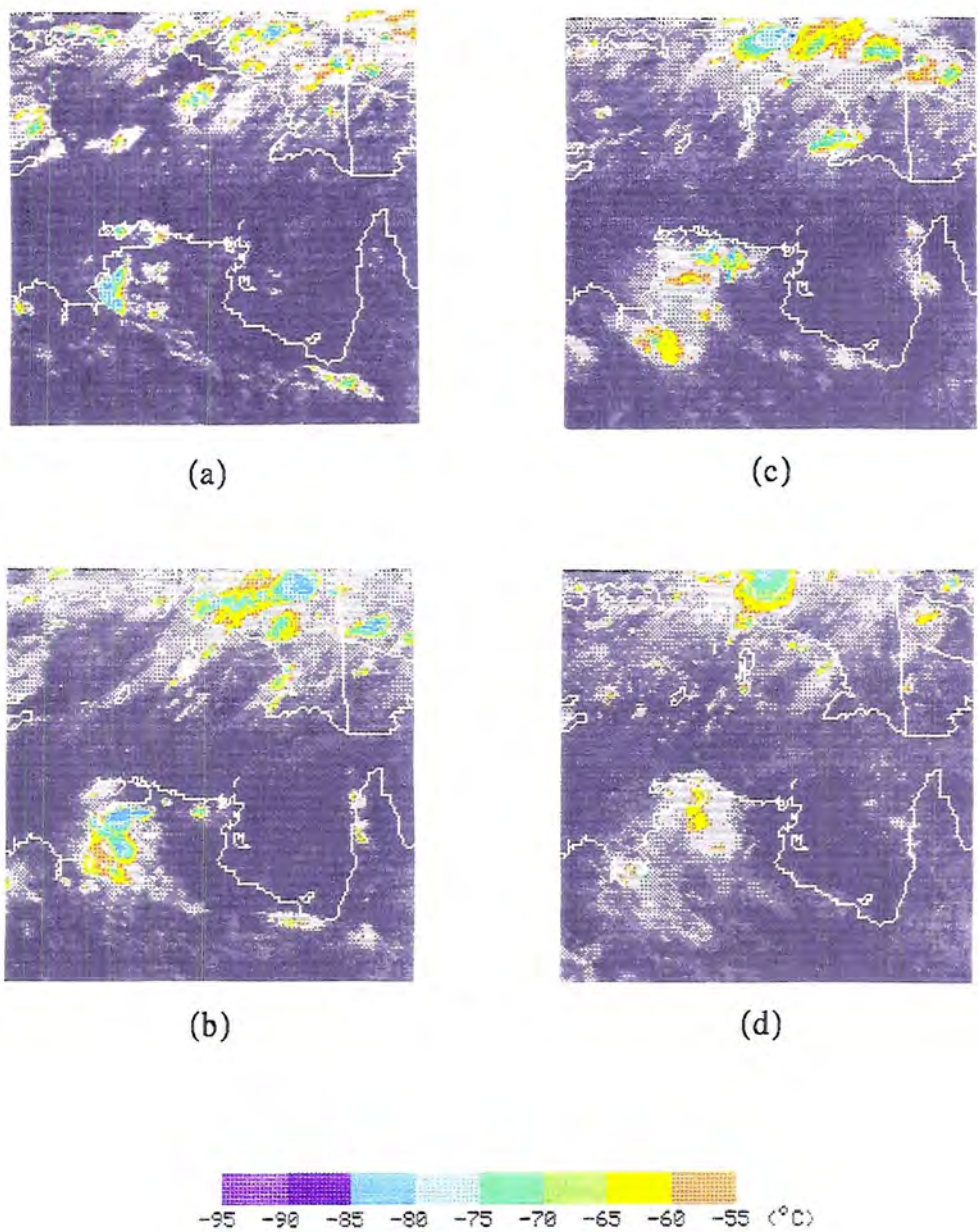

Figure 4.11: GMS infrared satellite images at (a) 530 UTC, 12/5/89, (b) 830 UTC, 12/5/89, (c) 1130 UTC, 12/5/89, and (d) 1530 UTC, 12/5/89 over the same EMEX region. Cloud tops colder than $-55°$ C are enhanced in the images.

motion profiles retrieved from the BMRC vertical pointing wind profiler will also be used to determine the vertical motion field in this tropical MCS (Cifelli and Rutledge, 1993).

Figures 4.12 and 4.13 give a time series of low level (< 2.0 degree elevation angle) reflectivity scans (PPI) from the MIT radar showing the evolution of the DUNDEE cloud cluster. At 0710 UTC (1640 LST, Fig. 4.12a) a broken line of clusters was evident 40 km south of the radar. This broken line began to merge into a solid line of cloud clusters as it moved north over the radars (Fig. 4.12b to d). At 0910 UTC (1850 LST, Fig. 4.12e), this cloud cluster was located 20 km to the north of the MIT Radar with a trailing stratiform area that extended to about 40 km south of the radar. An area of new stratiform cloud was also seen to move into the radar site from the south (lower left corner of the diagram) at this time. This new radar echo feature corresponded very well with those of satellite image at 0830 UTC (i.e., Fig. 4.10b) suggesting the merging of this cluster with a new cluster to the southeast of the radar site (hereafter, referred as the secondary cluster). As the original cluster moved further north into the open ocean (such as Fig. 4.12f), it slowly decayed. In the period between 1010 UTC and 1200 UTC (shown in Fig. 4.13), the secondary cluster began to move into the radar site and brought with it an extensive region of stratiform area.

The vertical reflectivity scans (RHI) for this case (shown in Figs. 4.14 and 4.15) indicate a region of strong vertically-erected convection at 0740 UTC (i.e., Fig. 4.14a), extending to 18 km. The horizontal dimension of this system was about 25 km at this time. The convection moved quickly to the right (i.e., north) at a speed of about 12 m/s. At 0840 UTC (such as Fig. 4.14b) this tropical MCS developed a small stratiform area situated over the MIT radar site. This tropical MCS continued to move north (to the right in the figure) and it seemed to reach its mature at 0910 UTC (shown in Fig. 4.14c) according to the analysis of the reflectivity fields in both Figs. 4.14 and 4.15. The system began to slow down after this time to a speed of 5 m/s. The horizontal extent of the system at this time was about 100 km and it had reached the height of 15 km. A rearward-sloping radar echo structure having a slope of 41 degree with respect to the surface was also evident in the convective region. This slope was much larger than the tilt of the rearward-sloping

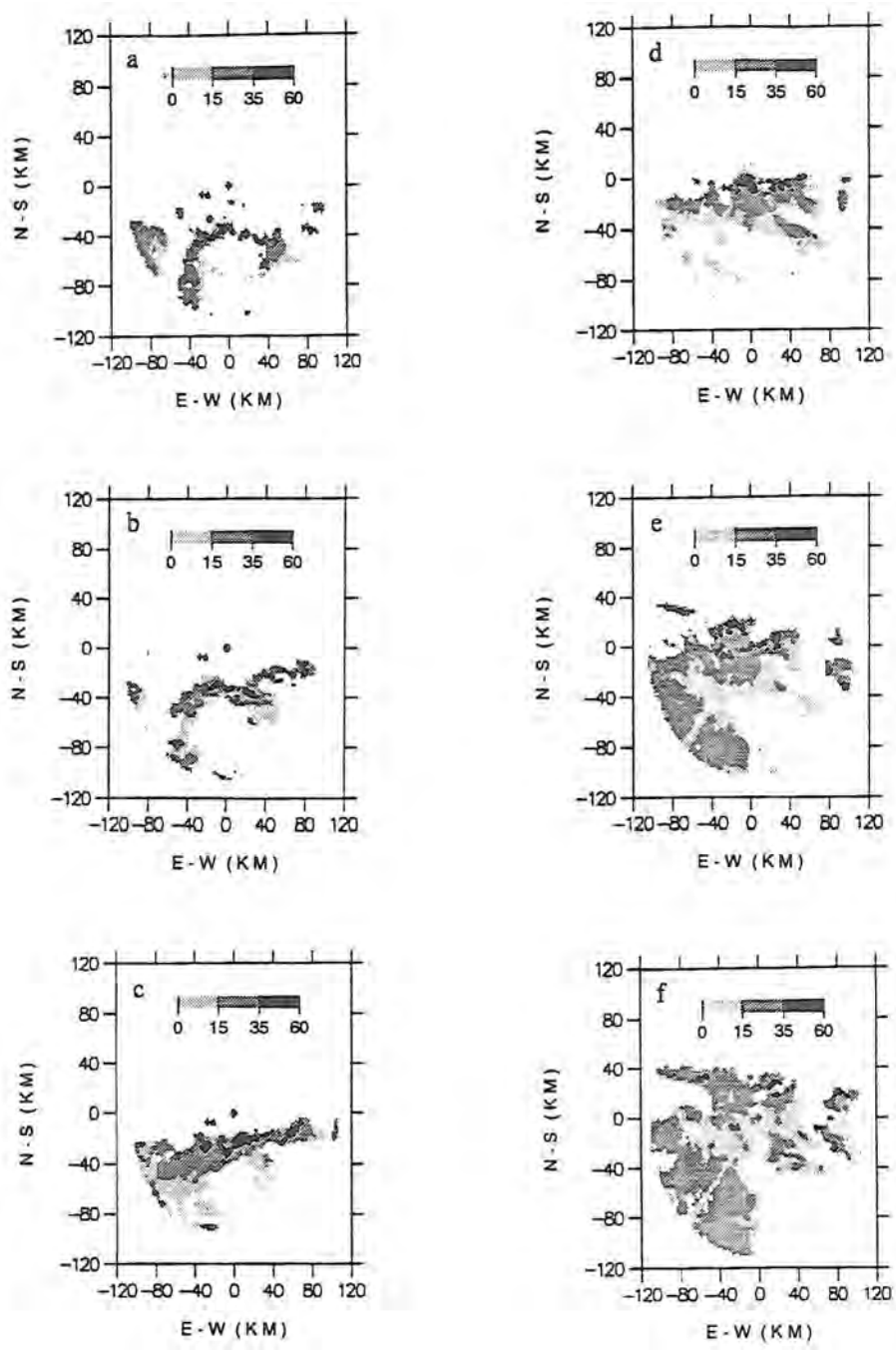

Figure 4.12: Time series of the low level (< 2.0 degree elevation angle) reflectivity scans from the MIT Doppler radar on 12/5/89 showing the horizontal evolution of a tropical cluster ((a) 0710 UTC, (b) 0740 UTC, (c) 0810 UTC, (d) 0840 UTC, (e) 0910 UTC, and (f) 0940 UTC).

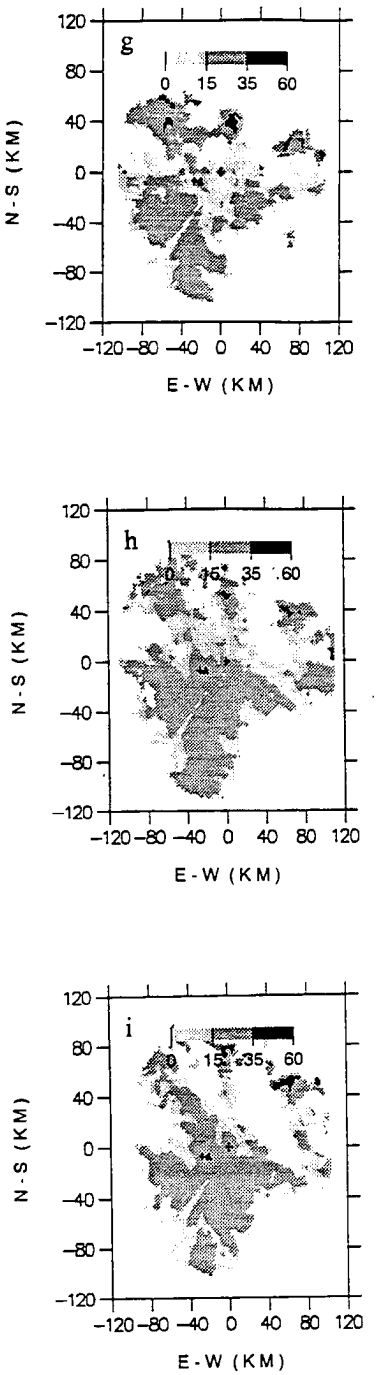

Figure 4.13: Same as Fig. 4.12 except for (a) 1010 UTC, (b) 1041 UTC, and (c) 1111 UTC.

convection found in the EMEX-9 case and is indicative of the weaker background vertical shear profile associated with this system. At 0940 UTC (i.e., Fig. 4.14d), the original cluster seemed to lose most of it strength as indicated by the absence of the strong radar echo above the freezing level and slowly decayed into a stratiform systems. At 1010 UTC (such as Fig. 4.15a) the remaining stratiform systems merged with the secondary cluster. A level of enhanced precipitation was evident between 1040 UTC (shown in Fig. 4.15b) and 1110 UTC (given in Fig. 4.15c) as the secondary cluster moved into the radar site bringing with it an extensive region of stratiform cloudiness.

The time-composited vertical motion fields (shown in Fig. 4.16) retrieved from the vertically-pointing wind profiler at the TOGA radar site showed a low level maximum upward motion at about 0845 UTC (1815 LST) which changed into an upper level maximum upward motion by about 0915 UTC (1845 LST). These upward motion features are consistent with the rearward-sloping radar echo shown in Fig. 4.14. The slope of this rearward-sloping structure is estimated to be on the order of 40 degree with respect to the surface if a 5 m/s propagation speed is assumed for the cloud cluster. This is again consistent with the slope inferred from the RHI radar scans (i.e., Fig. 4.14c). The maximum vertical velocity retrieved from the wind profile is about 9 m/s centered at around 9 km. The vertical velocities in the stratiform region, which developed after 1000 UTC, was generally much weaker with magnitudes on the order of 10's cm/s. These weak vertical motions in the stratiform region are consistent with previous published results of vertical velocity structures in both the tropical and the mid-latitude cloud clusters.

4.4 Comparison of the Two Cases

There are many differences between the two tropical MCSs discussed above. Particularly, the most striking differences are the large-scale conditions in which these systems formed. While the EMEX-9 case formed in a synoptically-disturbed monsoonal environment, the DUNDEE case, on the other hand, was developed in a relatively calm and undisturbed atmosphere. The large-scale forcing may partially explain why the EMEX-9 case had a relatively longer life span and larger horizontal dimension than that of the

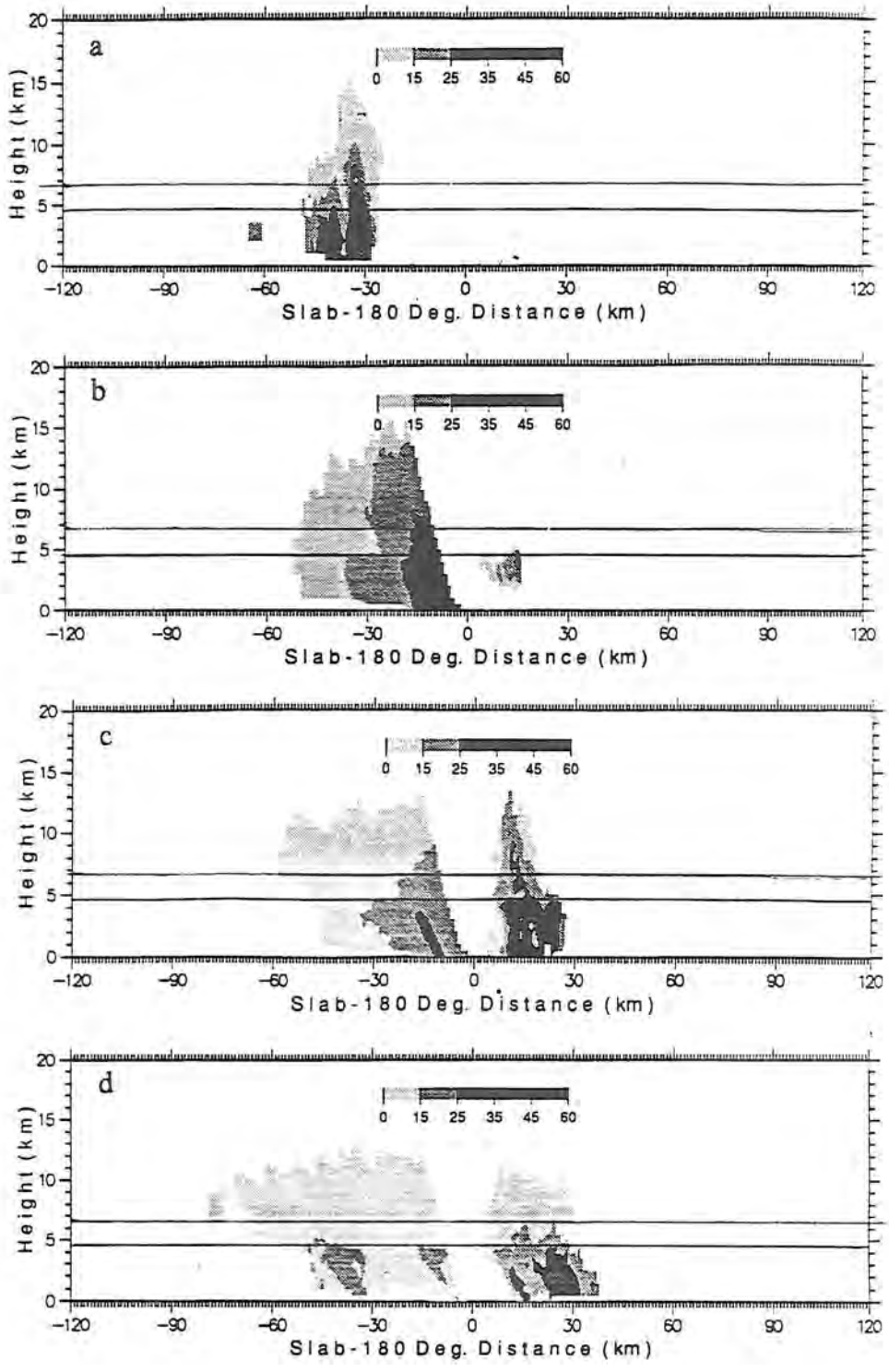

Figure 4.14: Time series of the vertical reflectivity scans from the MIT Doppler radar on 12/5/89 showing the vertical evolution of a tropical cluster ((a) 0740 UTC, (b) 0840 UTC, (c) 0910 UTC, and (d) 0940 UTC).

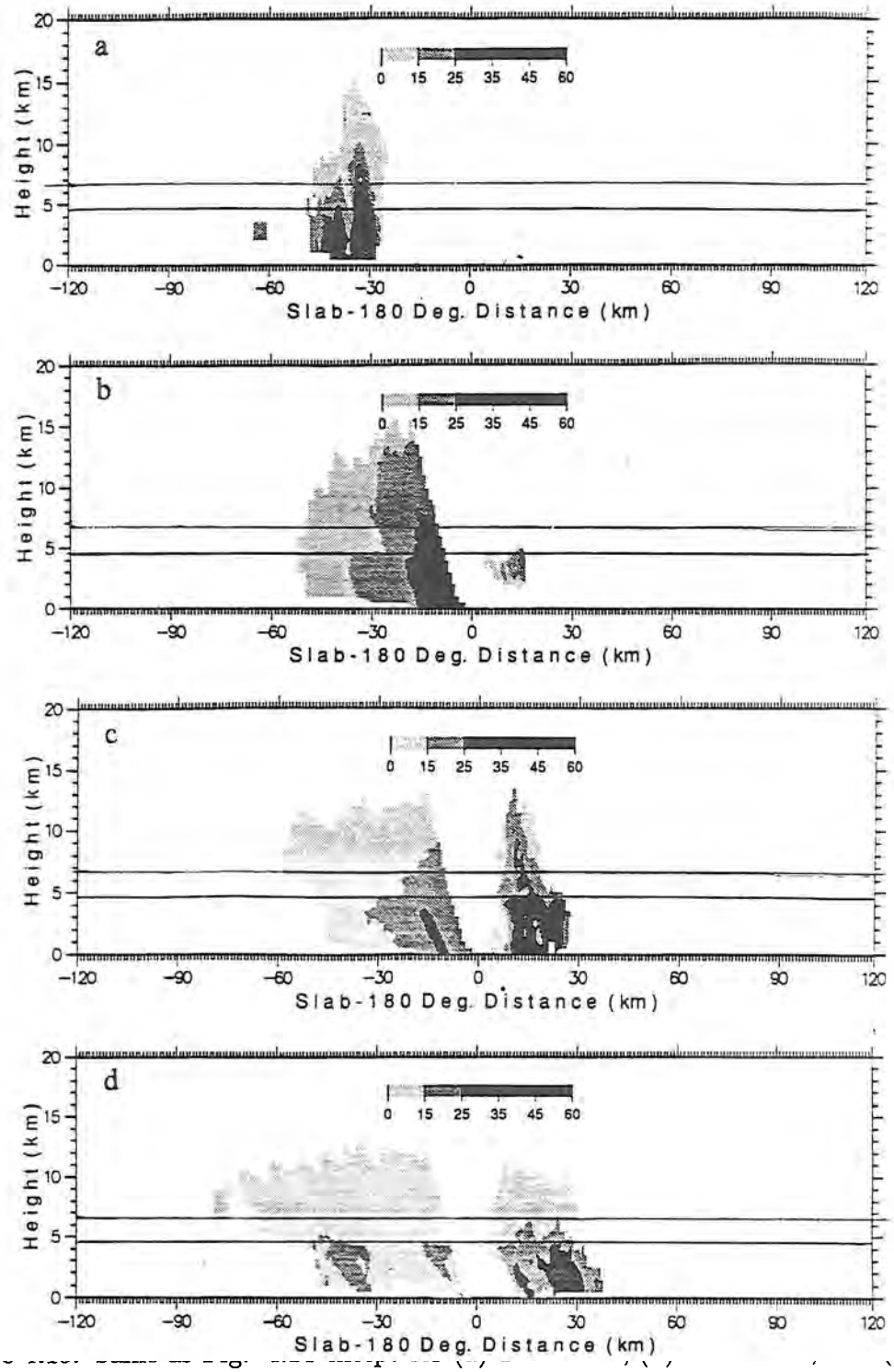

Figure [illegible] 1111 UTC.

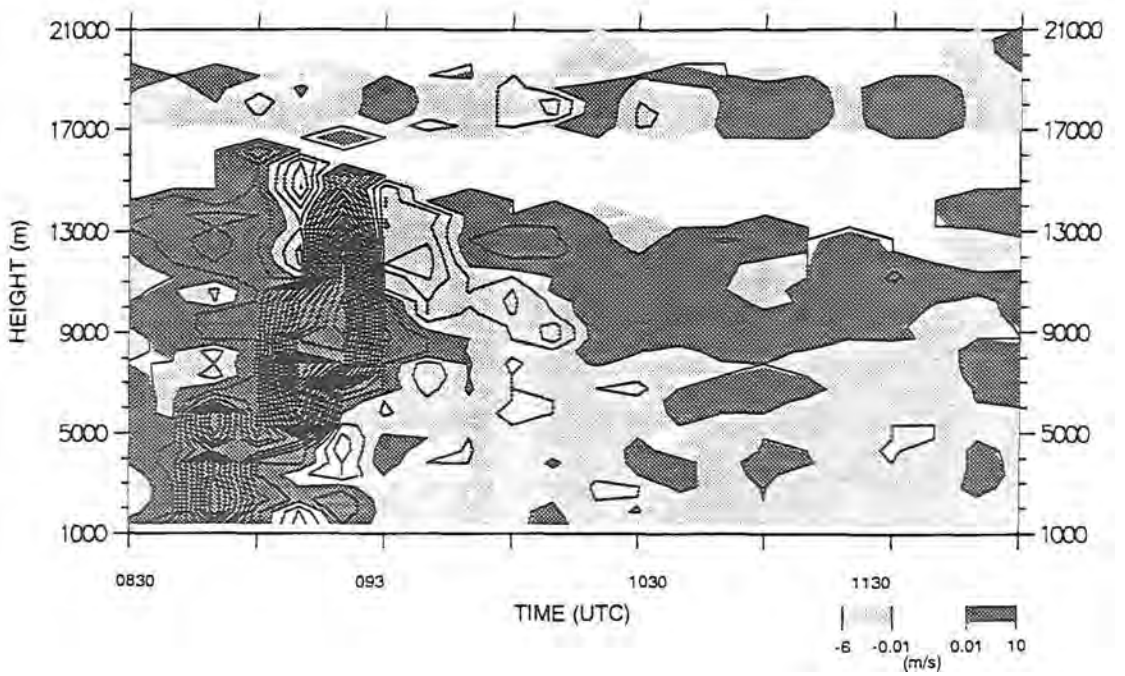

Figure 4.16: Time series of vertical motion fields retrieved from the TOGA vertical-pointing wind profiler between 0830 and 1200 UTC.

DUNDEE case. The EMEX-9 case formed over the tropical ocean while the DUNDEE case was a continental system. Thus, the surface heating effects played a more important role in initialization of the DUNDEE convection. The surface frictional effects may also explain the slower propagation speeds of the DUNDEE system. However, this weak propagation speed is more likely due to the weak background wind condition of the DUNDEE environment. The EMEX-9 case formed early in the morning and lasted to local noon. The DUNDEE case, on the other hand, started in the afternoon and lasted until midnight. These local time differences can have a large influence on the radiative budget of these MCSs as shown in the later chapter.

Although there are significant differences in the larger-scale features of these two cases, the internal structures of these tropical MCSs exhibit qualitatively similar structures. Both systems had a rearward-sloping squall structure during the mature stage and reached an altitude of about 15 km. They both had a distinct convective region and a trailing stratiform area, which are similar to MCSs found elsewhere in the tropics and in the mid-latitudes. These two cases also showed significant cluster to cluster interactions (i.e., cloud merger) and they both seemed to have the effects of drying out the lower atmosphere.

Furthermore, their presence can have a large effect on the radiative budget/heating of the tropical atmosphere due to the large differences in the optical properties between the clear sky and the cloudy atmosphere.

Chapter 5

SIMULATIONS OF TROPICAL CLOUD CLUSTERS

This chapter discusses the numerical simulations of both the EMEX-9 and the DUNDEE cloud clusters. The microphysical and thermodynamical information derived from these cloud simulations will be used to calculate radiative budgets and radiative heating profiles in the next chapter. Due to the intense computational requirements of the radiation model, the scope of this study is restricted to a two dimensional (2-D) framework. Even though the conclusions of the present work are drawn from these 2-D results, they can generally be extended to three dimensions (3-D) as well. Previous works on tropical MCSs (i.e., Tao *et al.*, 1987, Nicholls and Weissbluth, 1988, and Xu and Krueger, 1990) have demonstrated the validity of 2-D cloud simulation for studying the physical processes associated with these intense 3-D squall-type tropical cloud systems. The model set up and initialization method for the cloud simulation are discussed in the section 5.1. Sections 5.2 and 5.3 present the model results for the EMEX and the DUNDEE case, respectively. These 2-D results are also compared with observation and other published results of cloud clusters in these sections (when possible) to establish validity of these simulations. Finally, a brief summary on these cloud simulations is given at the end of this chapter.

5.1 Model Grid Set Up and Initialization Method

The 2-D cloud model used for both the EMEX and the DUNDEE simulation is set up on a grid system of 1000 by 32 points which represents a domain of 1000 km in the horizontal and 21 km in the vertical. The horizontal resolution chosen to resolve convection in the tropical MCS is 1 km and the vertical grid (shown in Table 5.1) is stretched slowly from 400 m near the surface to 1 km at top of the model to minimize gravity wave refraction

due to rapid changes in vertical spacing (Nicholls, 1987). The large horizontal and vertical domain of this cloud model is required to completely contain these deep tropical cloud clusters over the time integration period. The boundary conditions for the model have already been described in Chapter 2.

Table 5.1: Vertical grid configuration for the cloud model

Level	Height (m)	Level	Height (m)
1	0.0	17	8800.0
2	400.0	18	9520.0
3	820.0	19	10260.0
4	1260.0	20	11020.0
5	1720.0	21	11800.0
6	2200.0	22	12600.0
7	2700.0	23	13420.0
8	3220.0	24	14260.0
9	3760.0	25	15120.0
10	4320.0	26	16000.0
11	4900.0	27	16900.0
12	5500.0	28	17820.0
13	6120.0	29	18760.0
14	6760.0	30	19720.0
15	7420.0	31	20700.0
16	8100.0	32	21700.0

Following Nicholls (1987), the squall-type convection in both EMEX and DUNDEE simulations is initialized by perturbing a horizontally homogeneous environment, which is representative of the atmospheric conditions before the formation of the cloud clusters. Detailed discussions of these horizontally homogeneous initial atmospheric conditions are presented later in this chapter for each of the case studies. The perturbation, which is used to represent the temperature and moisture jump across the leading edge of the squall-type tropical system, has the form of a warm moist bubble with a small cool pool upwind of the bubble. The size of the warm bubble is approximately 10 km in width and 3 km in height. It has a temperature excess of 1 K and a moisture excess of 4 g/kg. This warm moist bubble is applied only at the time of initialization. The cool pool is represented by applying a cooling rate of 0.006 K/sec to an area 15 km in width and 3 km in height, for the first 20 minutes of the model simulation time. As Nicholls (1987) notes, this type of initialization will quickly produce a long lasting tropical MCS.

Microphysical information are also needed to initialize the cloud model. These include the specification of certain cloud microphysical parameters (such as the mean radius of hydrometeors, and the cloud condensation nuclei concentration). The cloud model in this study includes parameterizations for cloud water, rainwater, ice crystals, graupel and aggregates. Since these types of microphysical information are not presently available from observation for both EMEX and DUNDEE, we are forced to initialize these parameters for both simulations using information obtained from tropical cloud clusters as part of the GATE program. In this regard, we follow Nicholls (1987) and use an oceanic cloud condensation nuclei concentration of 100 cm^{-3}, and characteristic mean radii of 0.027 cm and 0.05 cm for rainwater and graupel, respectively. These parameter values are also consistent with the results of Carlson and Prospero (1977), Leary and Houze (1979), and Houze et al. (1979).

5.2 EMEX Case

As described in the last chapter, the EMEX-9 cloud cluster was an oceanic monsoonal type tropical mesoscale convective system with embedded squall-type deep convection. The cloud cluster system formed off the northern Australian coast and propagated along the 500 mb monsoon trough with a speed of about 12 m/s. The model initial conditions and results for this case are discussed below.

5.2.1 Model Initial Atmospheric Conditions

The atmospheric conditions used to initialize the EMEX cloud cluster are based on both the observational data discussed in Chapter 4 and the sounding data from Darwin, Australia (1700 UTC) on 2/2/87. The temperature profile (shown in Fig. 5.1a) closely follows a moist adiabat and the dew point temperature indicates the presence of a warm moist surface air layer with a drier region above. Surface temperature and mixing ratios values exceeds 27° C and 23 g/kg, respectively. The tropopause is located at about 100-mb height with a minimum temperature of −83° C. This sounding is similar to the GATE sounding used previously by Nicholls (1987) in his simulation of a GATE's tropical squall

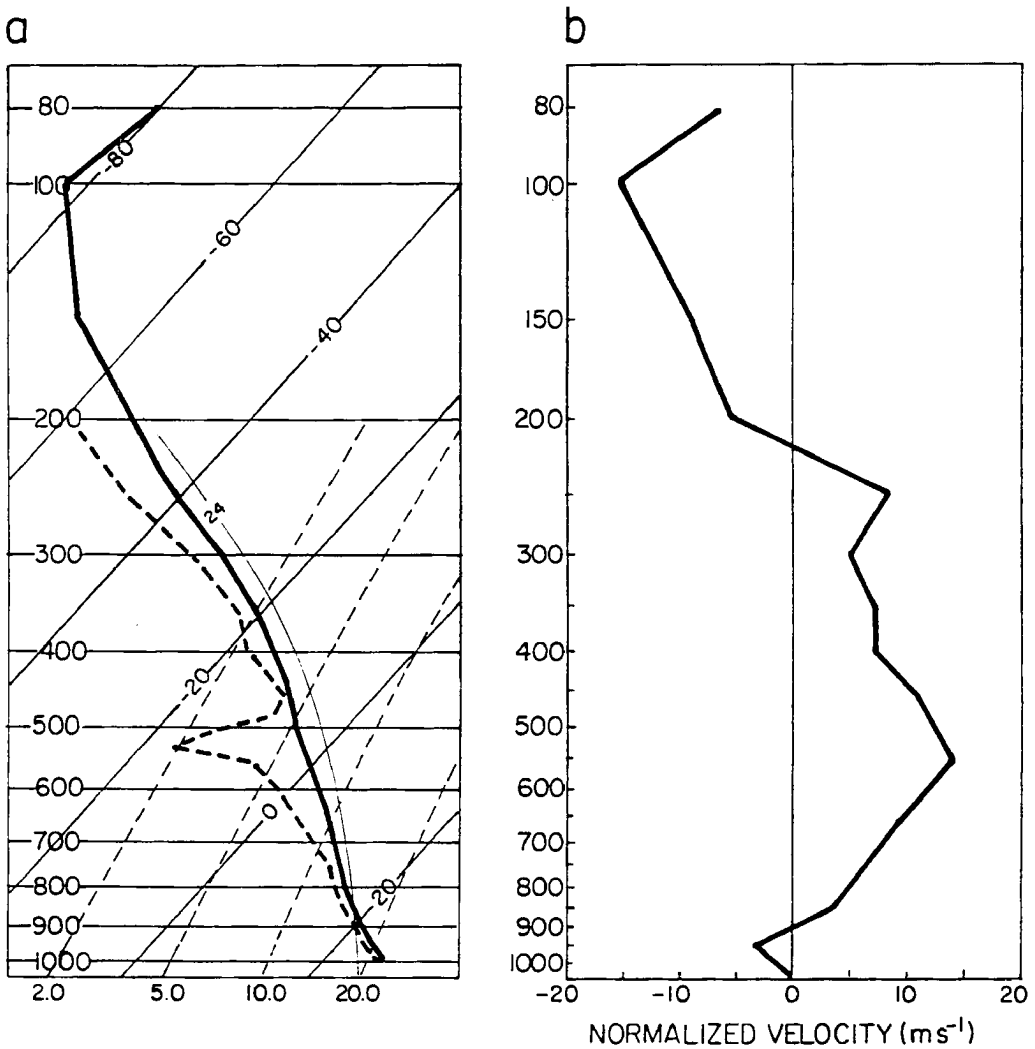

Figure 5.1: The Darwin's sounding profile of (a) temperature (solid) and dew point (dashed) and (b) horizontal wind normalized to the direction normal to the motion of the EMEX-9 cloud cluster at 1700 UTC on 2/2/87.

lines. The convective available potential energy (CAPE), calculated based on this Darwin sounding, is about 1500 J/kg.

The wind profile, defined relative to the propagation direction of the tropical MCS, which in turn, is based on cloud motion estimation from satellite data, is given in Fig. 5.1b. This profile indicates a shallow system relative easterly flow near the surface, a deep layer of strong westerlies above 900-mb level, and strong easterly flow above about 200-mb heigth. The deep layer of westerlies has a bimodal structure with the major peak at 550-mb height and a secondary peak at 250-mb surface and may be responsible for the fast eastward propagation of the EMEX cloud cluster. Vertical wind shear in the lower 2 km of the sounding is large with a difference of 8 m/s across this layer. Strong vertical shear also exits between 200- and 250-mb surface. The maximum westerly wind speed is about 14 m/s at 550-mb level and the maximum easterly wind speed is observed to be 18 m/s at 100-mb surface.

The cloud model for the EMEX-9 cloud cluster is initialized at approximately 0516 LST on 2/3/87 at latitude 9° S and is integrated forward in time for seven hours ending at 1116 LST using a 10 second time step. This particular time integration period is chosen in our study so that we can match the time period of the aircrafts observations. The model sunrise occurred at 0550 LST.

5.2.2 General Features of the Model Simulations

The simulated EMEX-9 MCS quickly develops after its initialization as indicated by the time series of the domain total hydrometeors field and the peak upward vertical motion field (shown in Fig. 5.2). The peak upward vertical motion in this figure is related to the convective activity of the system and occurs in the convective region of the MCS. This variable provides a convenient way of objectively defining the different stages of the simulated MCS, which is also outlined in Fig. 5.2. In this study, we define

- the formation/intensification stage (i.e., the period when the MCS is intensifying with time) from the beginning of the model simulation to the end of the first group of pulses in the time series of the peak upward vertical motion field. This stage

is marked by the continuous increase of domain total hydrometeor field and strong convective activity.

- the mature stage (i.e., the period when the MCS has becomed a fully-organized cloud system) from the end of the formation stage to the end of the pulses in the time series of peak vertical motion field. This stage is marked by coexistence of both strong convective activity and the presence of a large stratiform cloud region. This stage is also marked by the highest value of the domain total hydrometeor field during the life of the system.

- the decaying stage (i.e., the period when the MCS is slowly decaying) from the end of the mature stage to the disappearance of the MCS or the end of the simulation. This stage is marked by absence of convective activity, the preponderance of the weak stratiform cloud, and decrease in the domain total hydrometeor content.

Using this definition, the peak vertical motion at the intensification stage of this simulation was about 12.5 m/s. The cloud cluster attained its mature stage between 1.25 and 3.5 hour into the simulation with a maximum vertical velocity ranging between 10 m/s at the beginning of the period to 2.5 m/s at the end of this stage. The cloud cluster slowly decayed after this period until the end of the simulation.

Figure 5.3 shows a series of the X-Z cross-sections of cloud cluster total hydrometeors fields for each hour of the first six hours of simulation. During the intensification stage (shown in Fig. 5.3a) the cluster is composed of an upright cell having a horizontal dimension of 40 km at the surface and vertical extent of 16 km. This convective cell seems to split into two separate features at the upper levels.

The cloud cluster expands very quickly and covers almost 260 km of area by the beginning of the mature stage (given in Fig. 5.3b). At the third hour into the simulation (shown in Fig. 5.3c), the MCS consists of a convective-stratiform region which is approximately 370 km in extent with a trailing anvil cloud extending from the front to the rear of the system. Areas of higher concentrations of cloud hydrometeors also exist at the rear of the stratiform region associated with the splitting of the convection noted

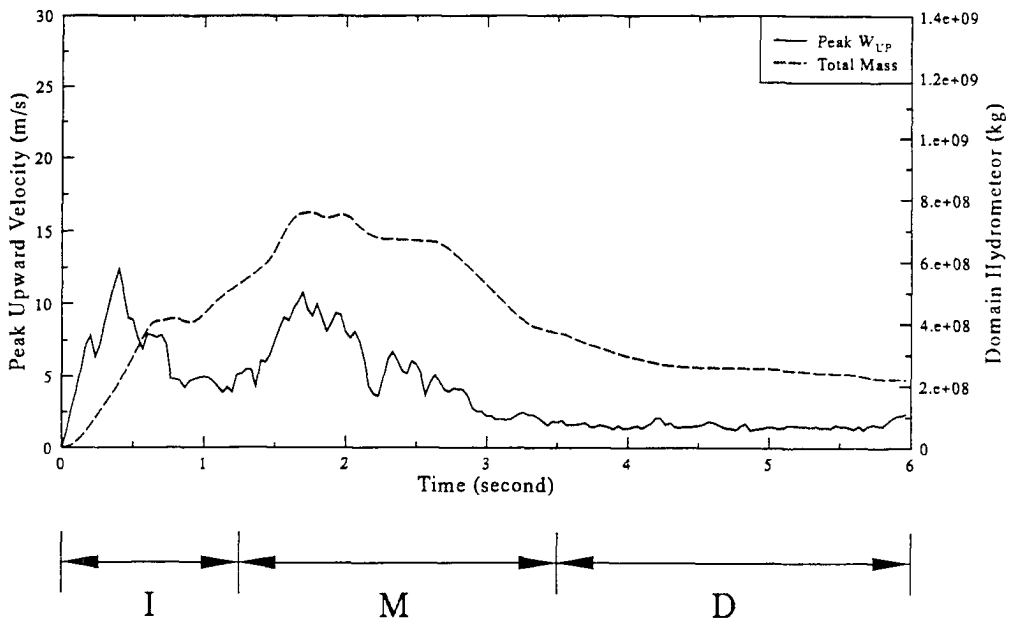

Figure 5.2: The time series of the simulated EMEX-9 domain intergated total hydrometeors field (dashed) and domain peak vertical motion field (solid). The intensification, mature, and decaying stages are also shown in the figure as I, M, and D, respectively.

earlier in the simulation. The convective area in the leading portion of the MCS has a rearward sloping structure and seems to merge into the stratiform area. The rearward slope in the simulation has an angle of about 16.5 degree with respect to the surface and is similar to the observed structure of EMEX-9 cloud structure (specifically, the 17 degree rearward sloping angle noted in Fig. 4.6a and b of Chapter 4). The merging of the convective line into a stratiform precipitation area is also observed during EMEX-9 in which the convective portion of the system was embedded in the broader area of stratiform precipitation. The horizontal scale of the convective region extends approximately 40 km and the stratiform-anvil region has a horizontal scale of 300 km. The vertical extent of the simulated system is 15 to 17 km. Both the horizontal and vertical scales match the observed scales of the EMEX-9 cloud system noted earlier from infrared satellite imagery and also noted previously from composite P-3 airborne Doppler radar data (Houze *et al.*, 1988; Webster and Houze, 1991).

The cloud cluster enters into its decaying stage between 3.5 and 7 hour into the simulation as the domain total amount of hydrometeors decrease and the cloud cluster

shrinks in size and as another new shallow convective cell begins to initialize in front of the cloud cluster. The MCS at the 6 hour simulation time (given in Fig. 5.3f) is characterized as a weak decaying stratiform cloud system with an extensive anvil region that fills almost half of the entire 1000 km model domain. These extensive upper tropospheric cloud shields are also a noted feature of tropical systems (Webster and Stephens, 1980).

The lifetime of the simulated system is approximately six to seven hours compared to 12 hours observed from the satellite observation. This disagreement may be due partly to the fact that we did not attempt to include the previously mentioned cloud cluster merger in the simulation. The satellite observations discussed in Chapter 4 indicated how this merger seemed to strengthen the EMEX-9 cloud cluster and presumably to maintain the system. In addition, the lack of large-scale forcing (i.e., imposing large-scale vertical motion) in the model may also constitute to this inconsistency. Our simulated system moved eastward (from left to right) at an approximate speed of 9 m/s compared to 12 m/s derived from satellite data. The slower speed of the simulated system may be due to weaker wind speeds in the sounding used to initialize the model.

5.2.3 Dynamical Fields

The X-Z cross-sections of the horizontal and vertical motion fields are shown in Fig. 5.4 and 5.5 matching the same time periods of the hydrometeor fields described above. A 30 km horizontal averaging operator has been applied to the vertical motion fields to obtain Fig 5.5 due to the fine horizontal resolution of the cloud model. During the intensification stage, the horizontal motion (given in Fig. 5.4a) is significantly altered by the cloud cluster as indicated by the bending of the contour lines at the location x = 0 km. A low level gust front is evident in the simulation at this time near the location at x = 25 km as the surface easterlies inflow collided with the surface westerlies outflow of the cloud cluster. The vertical motion field (shown in Fig. 5.5a) at this time generally shows upward motion within and near the front of the cloud cluster. Strong downward motion is evident at a distance both ahead of and behind the cloud system. An area of downward motion is also shown within the cloud system splitting the upper region of updrafts.

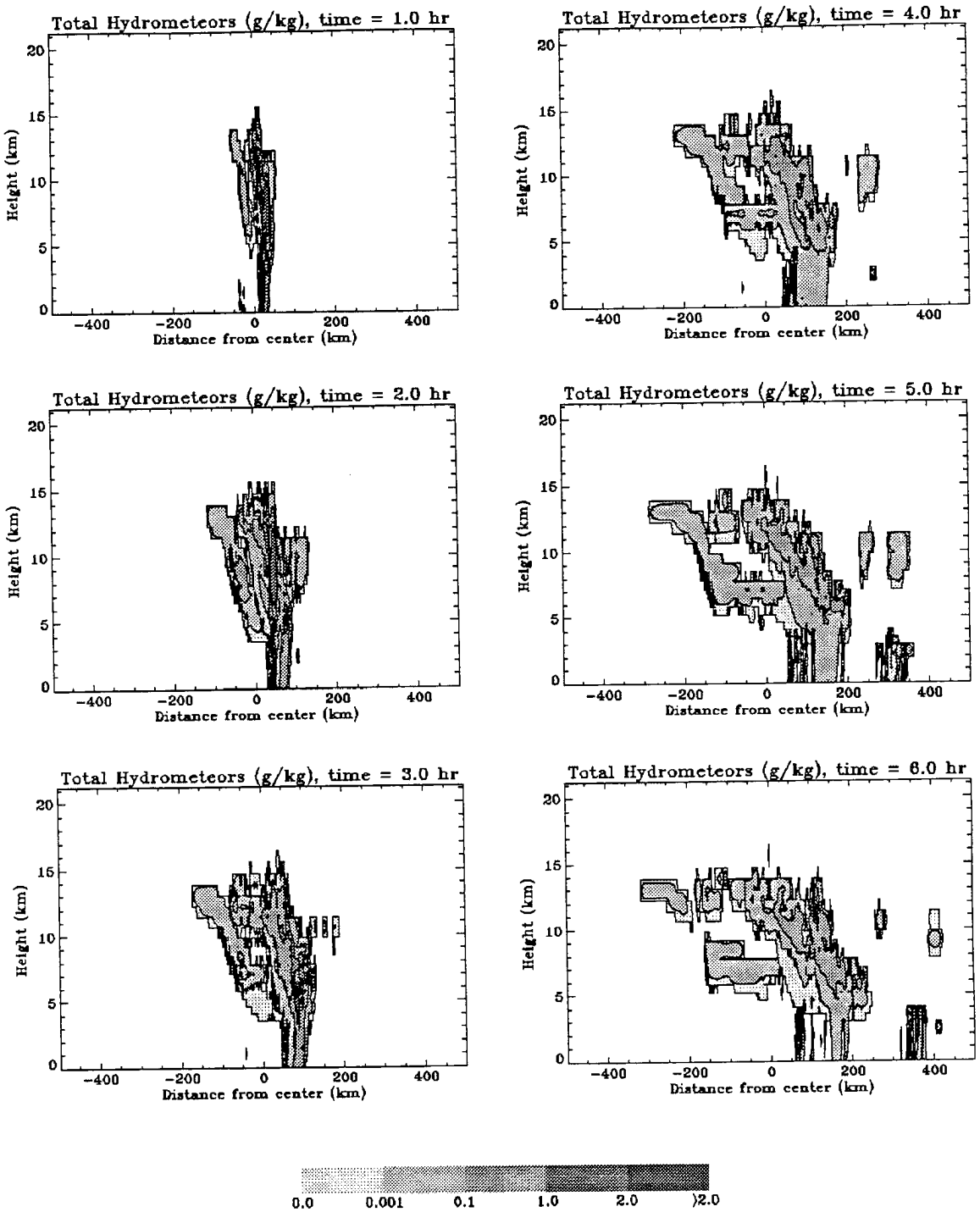

Figure 5.3: Simulated two dimensional field (X-Z cross-section) of total hydrometeor mixing ratio (g/kg) as predicted by the RAMS cloud model at (a) 1 hour, (b) 2 hours, (c) 3 hours, (d) 4 hours, (e) 5 hours, and (f) 6 hours into the simulation of the EMEX-9 cloud cluster.

As the area of the cloud expands in size between the second (given in Figs. 5.4b and 5.5b) and third hour (shown in Figs. 5.4c and 5.5c) into the simulation, the perturbation horizontal and vertical motion fields also spread out. The X-Z cross-sections of horizontal and vertical velocity predicted at the third hour indicate the classical circulation that consists of a low level inflow into the leading convection, a low level outflow behind this convection, an upper level outflow in front, and a upper level outflow behind of the system. These upper level outflows to the front and rear of the system help to carry cloud particles away from the convective cells and produce the stratiform anvil clouds in front of and behind the main MCS. The low level easterly wind ahead of the system continuously feeds the convective region of the cloud cluster with warm moist surface air. This result is consistent with our synoptic analysis in the last chapter which suggested that the low level northwesterly flow in the vicinity of the pre-monsoon trough area helped feed the cloud cluster with warm, moist surface equatorial air. The simulated circulation is also consistent with cloud model simulations described previously by Moncrieff and Miller (1976), Thorpe *et al.* (1982), and LaFore and Moncrieff (1989) as well as those observed by Chong *et al.* (1987). The convective region consists of small cells of upward and downward motion with horizontal scales of about 1-5 km. The convective updrafts have a rearward sloping structure with maximum upward velocity at upper troposphere (centered about 10 km). Strong low level convective downdrafts are found in the region just ahead of the intense upper level updrafts due to the rearward sloping nature of the convection. These simulated convective-scale vertical motions are consistent with the observed vertical motion structure of the EMEX-9 cloud cluster as noted in the Chapter 4 (i.e., Fig. 4.6b). In the region far away from the cloud system, broad-scale downward compensating air motion is observed. While the leading convective region is comprised of strong upward motion, a complicated pattern of downward and upward motions exists in the stratiform region. A mid-level rear descending inflow is also a feature of this stratiform region. This descending flow is similar to some of the observed features during the decaying stage of the EMEX-9 cluster mentioned in the last chapter. Downward/upward motions are also found scattered inside/below the cloud deck at the anvil region. The strong horizontal

wind shear near the cloud top at 200-mb surface is produced by the wind profile used to initialize the model (i.e., Fig 5.1b) and is maintained throughout the entire simulation. As the cloud cluster enters into its decaying stage (Figs. 5.4d and 5.5d) the horizontal wind slowly recovers to its pre-storm condition and the vertical motion field continues to weaken.

5.2.4 Thermodynamical Fields

Six-hourly X-Z cross-sections of the potential temperature perturbation and pressure perturbation fields are given in Figs. 5.6 and 5.7 corresponding to the same time periods discussed above. At the intensification stage, Figs. 5.6a and 5.7a show a general in-cloud warming and a cooling at the surface under the cloud cluster. An area of atmospheric cooling is also evident in the center of the cloud and is surrounded by warming, which is related to the strong downward motions noted in this area earlier. These temperature patterns translate into low pressure at the surface and higher pressure aloft at and around the cloud cluster location. At a distance away from the cluster, weak subsidence warming creates a broad area of high pressure. The low pressure at low levels and high pressure aloft are somewhat symmetric around the center of the system. However, the pressure patterns to the rear of the system have a larger slope than those found in the front of the system due to the strong wind shear of this environment. Packets of gravity waves excited by the convection are also shown to propagate away from the source region.

During the mature stage (i.e., second and third hour into the simulation), the potential temperature perturbation (given in Fig. 5.6b and c) has complicated features due to heating and cooling at the cluster location. Some distance away from the cloud system, a warming trend is evident as the heating generated by the cloud system slowly propagates away from the center to the edges of the model domain. In the cloud region, a middle level cooling region is found between the upper and lower level heating. A surface cool pool is still evident at this stage. The pressure perturbation pattern (shown in Fig. 5.7b and c) echoes much of the same features as the temperature fields with low pressure away from the cloud region due to the propagating heat source. At the cloud region, low pressure aloft and high pressure below are evident. The surface pressure perturbation features in

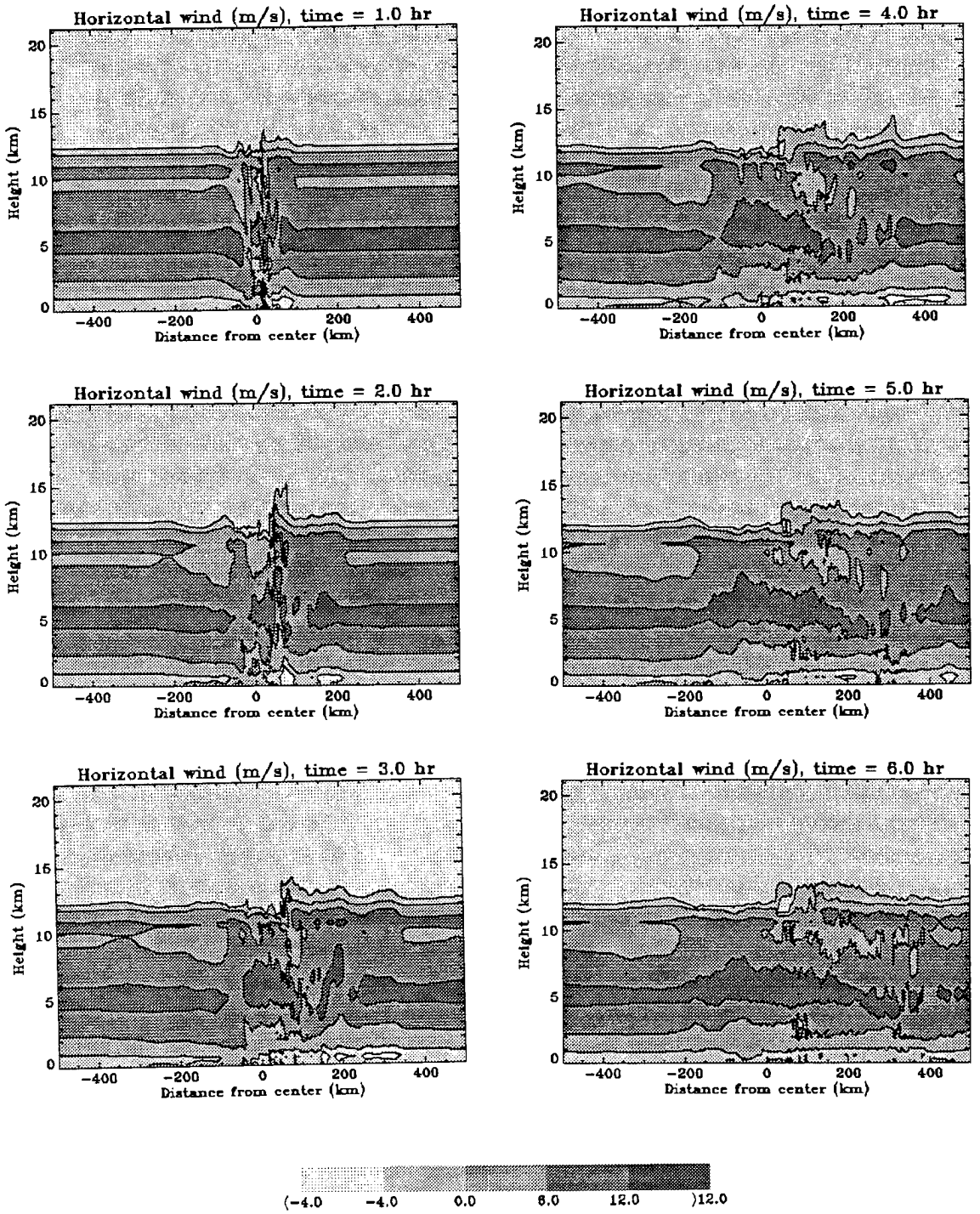

Figure 5.4: Simulated two dimensional (X-Z cross-section) fields of horizontal wind (m/s) as given by the RAMS cloud model at (a) 1 hour, (b) 2 hours, (c) 3 hours, (d) 4 hours, (e) 5 hours, and (f) 6 hours into the simulation of the EMEX-9 cloud cluster.

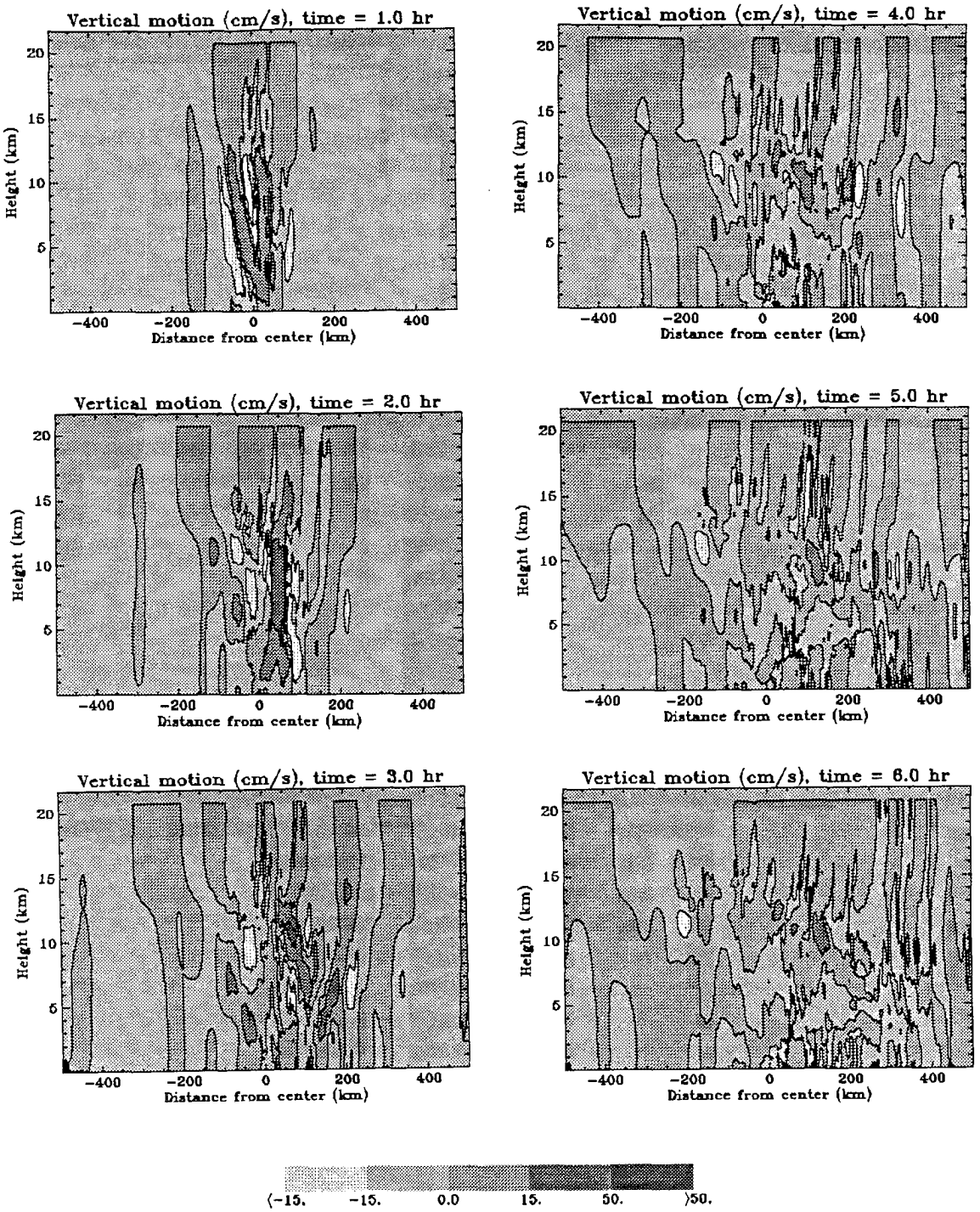

Figure 5.5: Simulated two dimensional (X-Z cross-section) fields of vertical motion (cm/s) as given by the RAMS cloud model at (a) 1 hour, (b) 2 hours, (c) 3 hours, (d) 4 hours, (e) 5 hours, and (f) 6 hours into the simulation of the EMEX-9 cloud cluster.

Fig. 5.7b show a meso-high in the vicinity of the convection and meso-lows in the region to the rear and in the front of the system. These surface features are common to mid-latitude and tropical mesoscale convective cloud systems (i.e., Johnson and Hamilton, 1988 and others) and seem to be well simulated by the cloud model. Packets of gravity waves are continuously excited by the convection. Wave trapping is evident at the rear of the cloud system as indicated by the absence of gravity waves above 10 km surface as comparing to many waves in front of the system.

The decaying stage (i.e., Fig. 5.6e to f and Fig. 5.7e to f) of the system is marked by a general warming and decreased pressure aloft and cooling and higher pressure at lower levels. The warming aloft seems to caused by the strong radiative heating at this time. The cooling at the lower levels is probably due to evaporative cooling processes. Gravity waves cease to exist during the decaying stage which is correlated well with the disappearance of the convective region in the cloud cluster.

5.2.5 Water Fields

Tropical MCSs are known to exert a significant influence on the water budget of the atmosphere (Cotton and Anthes, 1989), but the quantitative details of this influence are not completely understand. A more detailed breakdown of the water perturbation fields obtained from the simulation is presented in Figs. 5.8 to 5.10.

During the intensification stage significant amounts of water in the form of vapor, liquid, and solid phase (shown in Fig. 5.8a to Fig. 5.10a) are transported vertically from the lower levels aloft. A lower level drying in the water vapor perturbation is also evident behind the cloud system in Fig. 5.8a. The individual breakdown of the solid and liquid water (given in appendix B) at this time shows ice crystal and aggregates to be the most dominant water species above the freezing level (at about 5 km) and ice crystals to be the most abundant water species above 10 km. Graupel is only concentrated in the area of strongly active convection between 1 and 8 km in altitude. Rainwater and cloud water are the dominant water species in the lower levels.

In its mature stage, the water budget pattern of the MCS remains very much unchanged. However, the area cover of the water perturbation fields have been increased

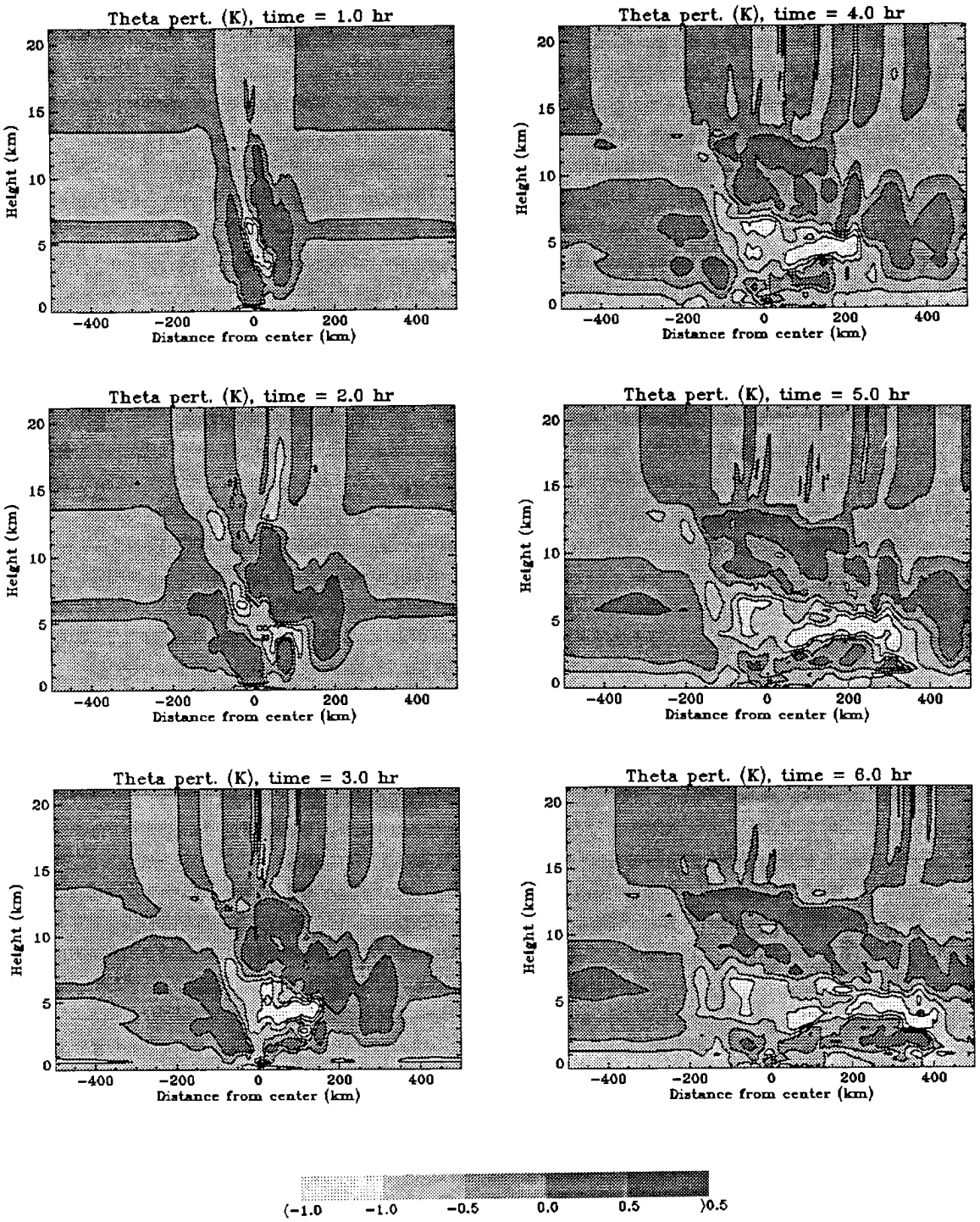

Figure 5.6: Simulated two dimensional (X-Z cross-section) fields of potential temperature perturbation (k) as predicted by the RAMS cloud model at (a) 1 hour, (b) 2 hours, (c) 3 hours, (d) 4 hours, (e) 5 hours, and (f) 6 hours into the simulation of the EMEX-9 cloud cluster.

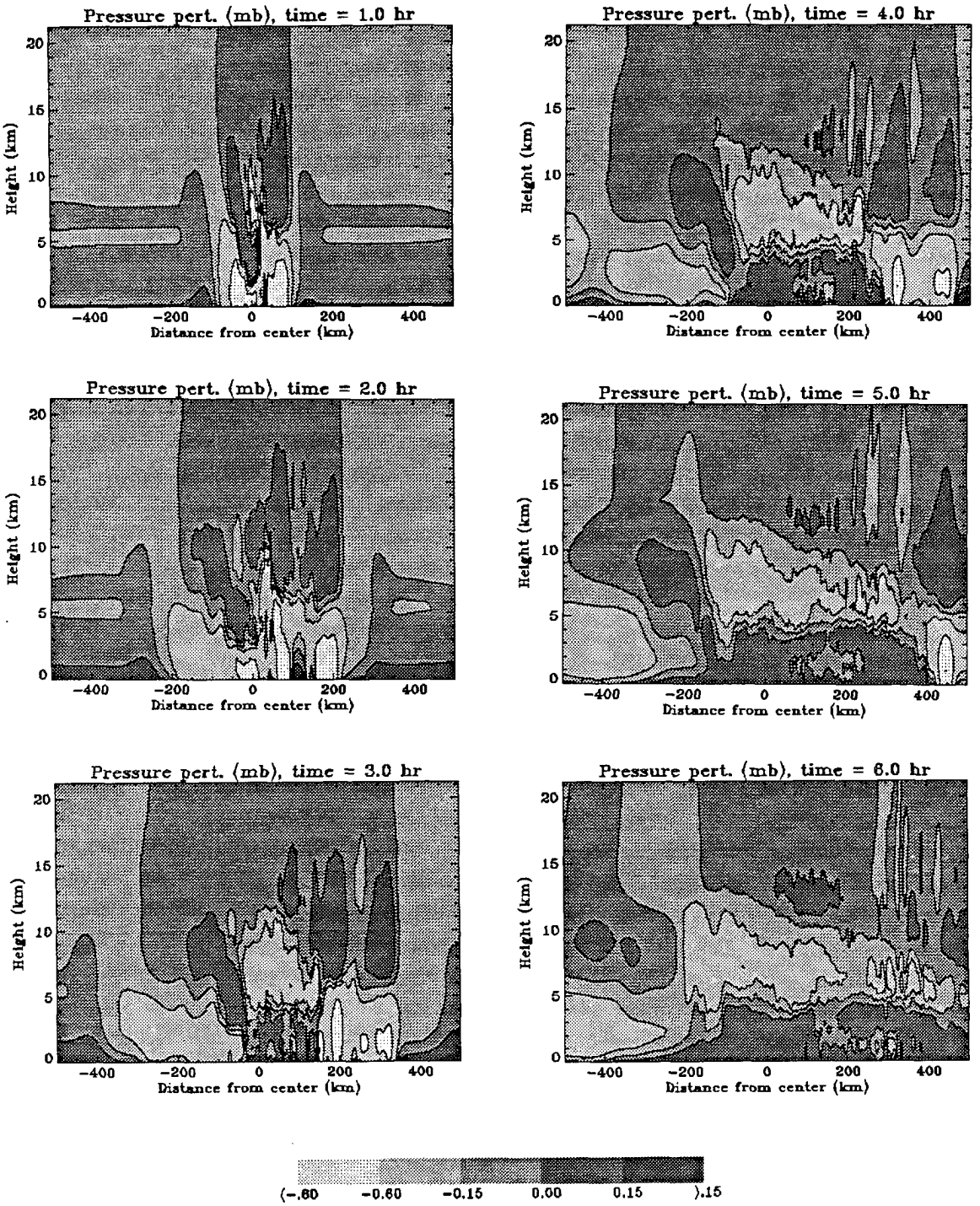

Figure 5.7: Simulated two dimensional (X-Z cross-section) fields of pressure perturbation (mb) as predicted by the RAMS cloud model at (a) 1 hour, (b) 2 hours, (c) 3 hours, (d) 4 hours, (e) 5 hours, and (f) 6 hours into the simulation of the EMEX-9 cloud cluster.

significantly as shown in Fig. 5.8b and c to Fig. 5.10b and c. Most of the total liquid water (cloud plus rain water) and the graupel still exist in the convective region. The graupel mixing ratio field is concentrated between 1 km and 8 km in the convective region. The rain water mixing ratio field spreads across the convective region and some part of the stratiform area below 7 km. Regions of large rain water mixing ratio are also predicted at the surface in the convective region. Ice crystals and aggregates in the simulated cloud system are now found in both the convective and stratiform region above the freezing level (above 5 km). Ice crystals are mostly found between cloud top and 8 km and aggregates are located at lower levels in the stratiform region. High mixing ratios of both ice crystals and aggregates are also found in the convective region. At a height above 10 km, the mixing ratio of these two species begins to tilt backward with height and merges into the stratiform region. The thin anvils located to the rear of the system are mostly ice crystals.

During the decaying stage (shown in Fig. 5.8d, e, and f to Fig. 5.10d, e, and f), the water fields continue to indicate the influences of the cloud system. The water vapor perturbation field shows a general moistening aloft and drying below due to the vertical transport of water (i.e., in the form of vapor, liquid, or solid) from the lower atmosphere to aloft by the cloud cluster. This is consistent with observations which suggest that the effects of MCSs are to dry out the lower levels water vapor field (i.e., the low value of the 850-mb surface of equivalent potential temperature field in Fig. 4.3e and the 'onion sounding' in Fig. 4.8a).

5.3 DUNDEE Case

The DUNDEE cloud cluster on 12/5/89 differs from the EMEX-9 cluster in the origination region, time of the day when the system developed, and the background environmental conditions. While the EMEX case formed over the open ocean during the early morning on 2/2/87, the DUNDEE cluster was triggered over the land surface in the late afternoon on 12/5/89. The EMEX case formed under disturbed conditions with strong vertical wind shear and lower CAPE whereas the DUNDEE case developed under undisturbed conditions with weak vertical shear and higher surface temperature due to

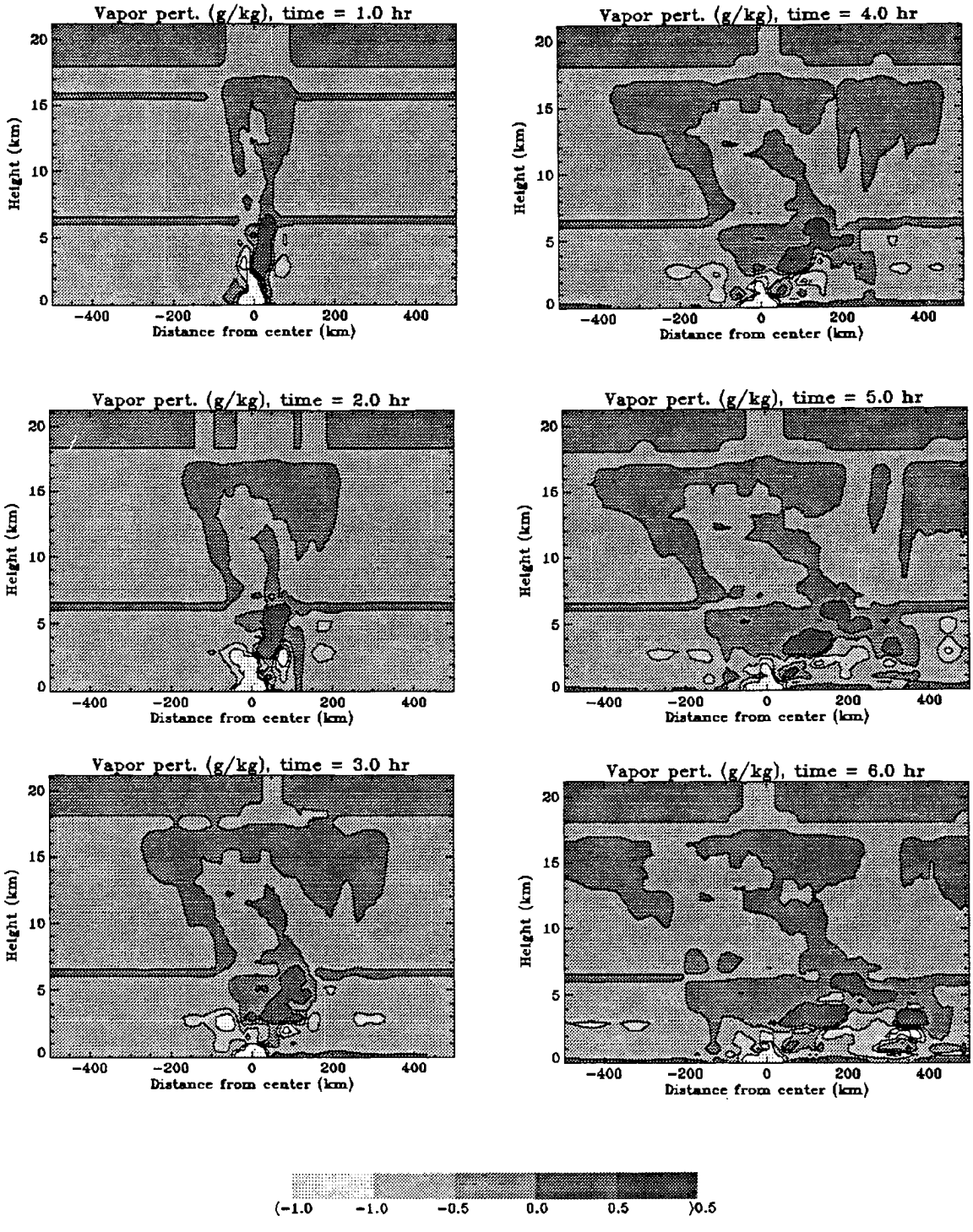

Figure 5.8: Simulated two dimensional (X-Z cross-section) mixing ratio fields (g/kg) of water vapor perturbation as predicted by the RAMS cloud model at (a) 1 hour, (b) 2 hours, (c) 3 hours, (d) 4 hours, (e) 5 hours, and (f) 6 hours into the simulation of the EMEX-9 cloud cluster.

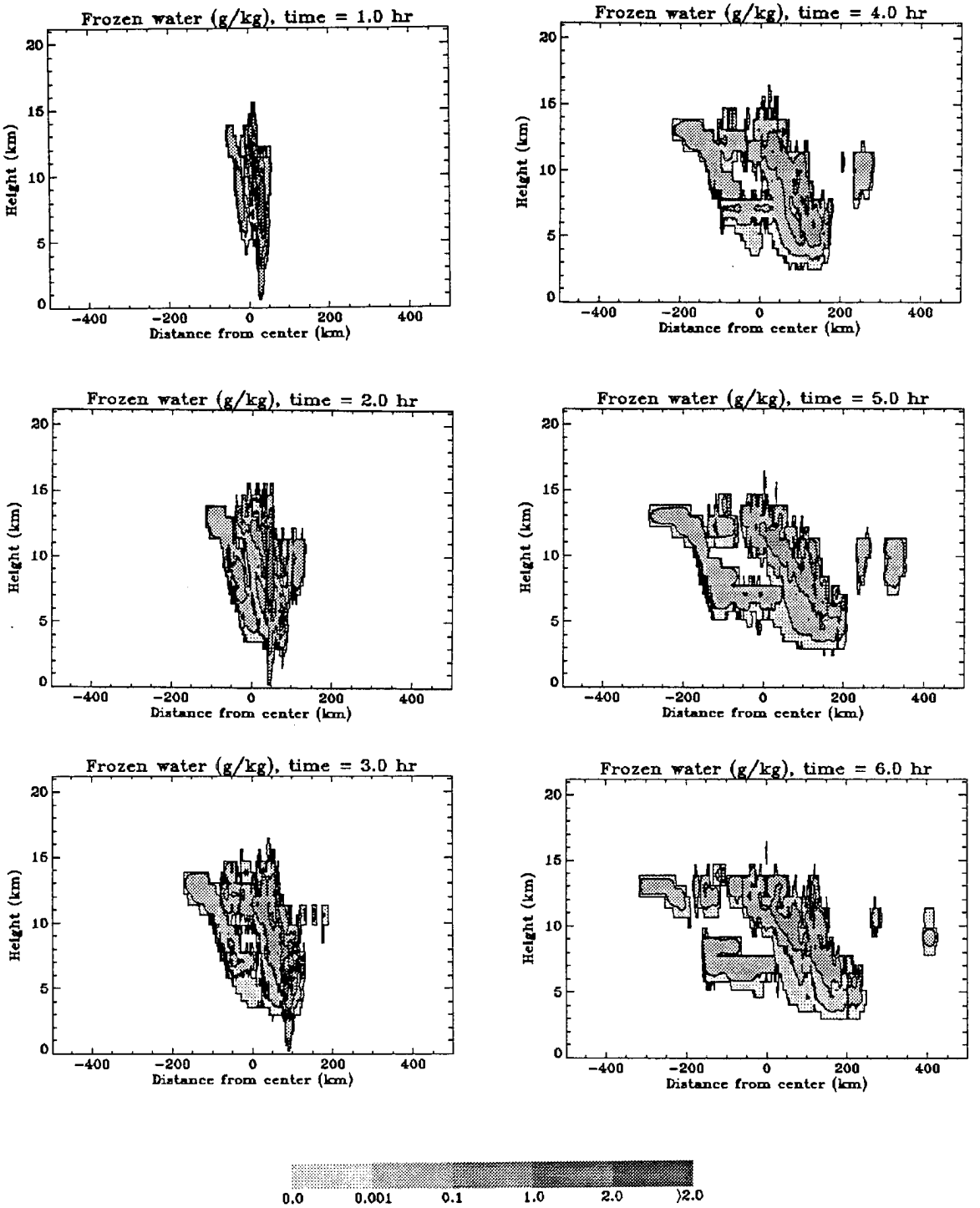

Figure 5.9: Simulated two dimensional (X-Z cross-section) mixing ratio fields (g/kg) of total ice water species as predicted by the RAMS cloud model at (a) 1 hour, (b) 2 hours, (c) 3 hours, (d) 4 hours, (e) 5 hours, and (f) 6 hours into the simulation of the EMEX-9 cloud cluster.

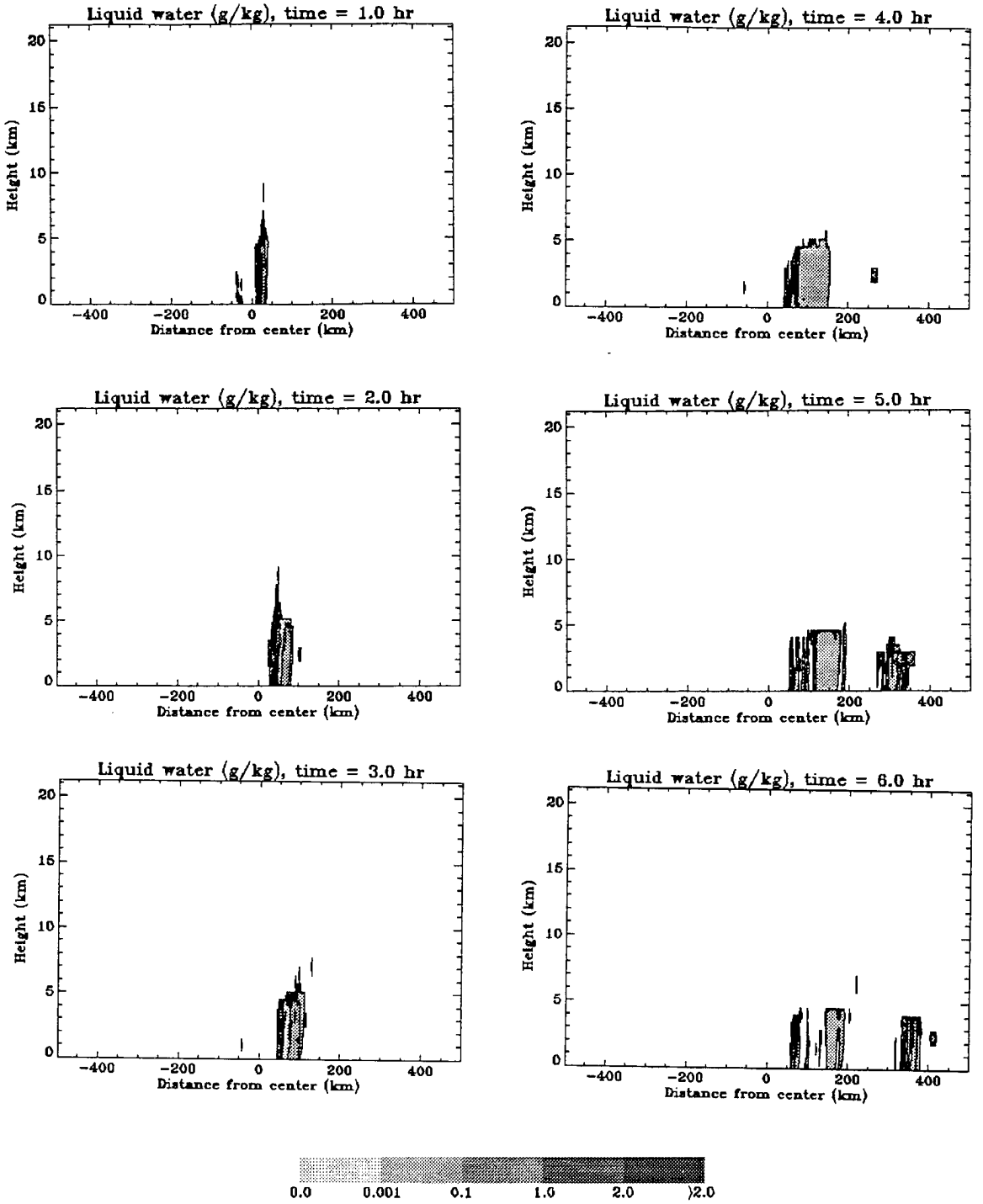

Figure 5.10: Simulated two dimensional (X-Z cross-section) mixing ratio fields (g/kg) of total liquid water species as predicted by the RAMS cloud model at (a) 1 hour, (b) 2 hours, (c) 3 hours, (d) 4 hours, (e) 5 hours, and (f) 6 hours into the simulation of the EMEX-9 cloud cluster.

solar heating. These differences, as we will show in this section, significantly alter the vertical structures and the intensity of the convection, the propagation speed of the cloud clusters, and the radiative heating of these two systems.

5.3.1 Initial Conditions

Using the same initialization technique as in EMEX case, the DUNDEE simulation was initialized by perturbing a horizontally homogeneous environment with a warm moist bubble and a cooling function. The initial atmospheric conditions are based on both the observational data described in Chapter 4 and the sounding data from Darwin, Australia (0000 UTC) on 12/5/89 (shown in Fig. 5.11a). This sounding profile is very similar to the EMEX sounding in which the temperature profile closely follows a moist adiabat and the dew point temperature indicates the presence of a warm moist surface layer with a drier region above. The surface temperature and mixing ratios values are slightly less than the EMEX case at this time, with value of 26.6° C and 21.3 g/kg, respectively. However, the surface temperature can increase significantly during the daytime hours due to solar heating of the land surface. The tropopause is located at 90-mb surface with a minimum temperature of −84° C. The convective available potential energy (CAPE) for this case is 1850 J/kg and is about 23 percent more than the EMEX's CAPE value. Theoretically, this extra CAPE energy should result in a dynamically stronger and deeper cloud cluster.

The wind profile, defined relative to the propagation direction of the tropical MCS, which in turn, is based on cloud motion estimation from both the satellite data and the Dopplar radar data, is given in Fig. 5.11b. This profile indicates weak vertical shear with a shallow system-relative northerly flow near the surface, a layer of system-relative southerly above 900-mb level, and system relative northerly flow above about 200-mb surface. The layer of southerly flow peaks at 750-mb height. Vertical wind shear in the lower 2 km of the sounding is moderate with a difference of 3 m/s across this layer. The maximum southerly wind speed is about 4.5 m/s at 750-mb surface and the maximum northerly wind speed is observed to be 8.3 m/s at 150-mb level. The weak vertical shear and the weaker wind condition of this sounding should result in a slower moving MCS in this case.

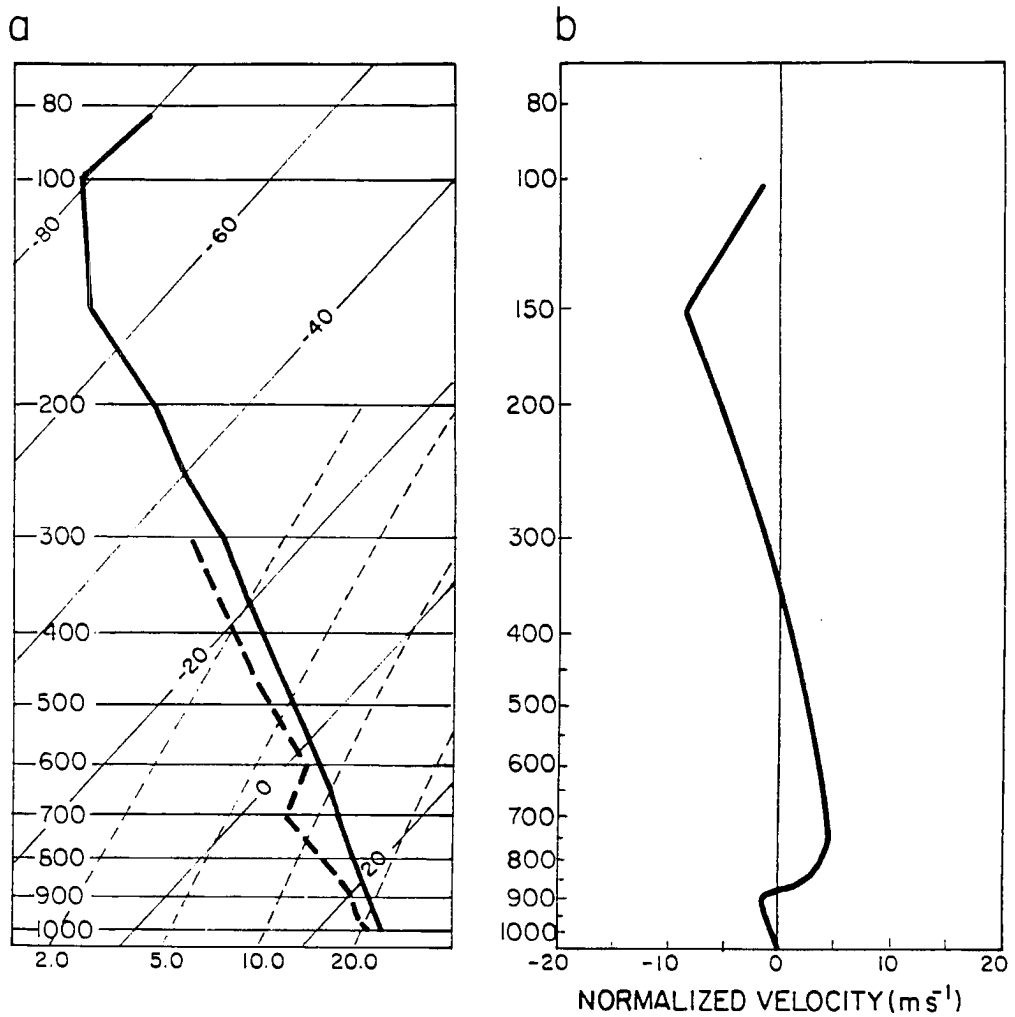

Figure 5.11: The Darwin's sounding profile of (a) temperature (solid) and dew point (dashed) and (b) horizontal wind normalized to the direction normal to the motion of the DUNDEE cloud cluster at 0000 UTC on 12/5/89.

We initialize the cloud model at approximately 1530 LST (i.e., 3:30 pm in the afternoon) on 12/5/87 at latitude 12.4° S using a surface temperature of 30° C to represent the effect of surface heating by solar radiation between 0930 LST (such as the last available sounding time) and 1530 LST (i.e., the starting time of the simulation). The cloud model is again integrated forward in time for 7 hours ending at 2330 LST using a 10 second time step. This particular time integration period is chosen in our study so that we can match the time period of the Dopplar radar observations. The cloud model results for this case are described in detail below.

5.3.2 General Features of the Model Simulations

The simulated DUNDEE's MCS develops quickly (as in the EMEX case) after its initialization as indicated by the time series of the domain total hydrometeors field and the peak vertical motion field (shown in Fig. 5.12). Using the previous definition, we can again objectively identify the three stages (also shown in Fig. 5.12) of this cloud cluster. During the intensification stage (i.e., the first hour), the peak vertical motion of this cloud cluster has reached a value of 27.5 m/s due to the higher CAPE and lower vertical wind shear condition in contrast to the EMEX case which achieved only 12.5 m/s peak vertical motions in this stage. The cloud cluster reaches its mature stage between 1.25 and 4.5 hour into the simulation with a maximum vertical velocity ranging between 20 m/s at the beginning of the period to 2.5 m/s at the ending of this stage. The cluster slowly decayed after this period to the end of the simulation.

Figure 5.13 shows a series of the X-Z cross-section of total hydrometeors fields for the first six hours of the DUNDEE simulation. During the intensification stage (given in Fig. 5.13a) the cluster was composed of a very intense upright cell having a horizontal dimension of only 50 km and a vertical extend of 19 km which is similar to the observed dimensions of the DUNDEE system at that time (i.e., Fig. 4.14).

The cloud cluster expands very quickly and covers almost 200 km of distance by the beginning of the mature stage (shown in Fig. 5.13b). This expansion in cloud mass is also seem in the observations. At the third hour into the simulation (given in Fig. 5.13c), the MCS consists of a strong leading convective region which is approximately 15 km in

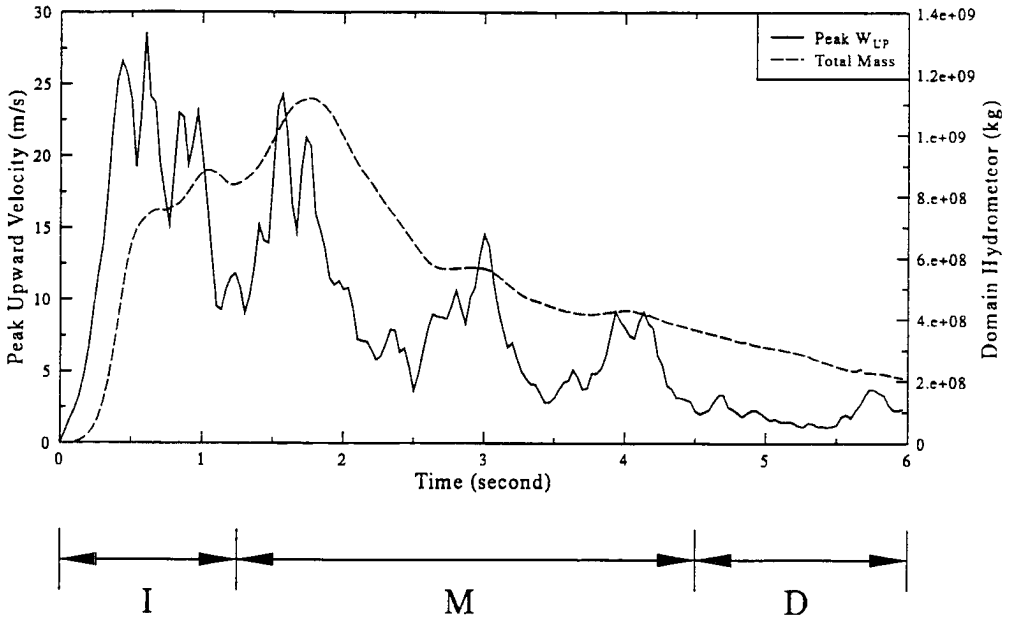

Figure 5.12: Same as Fig 5.2 but for the DUNDEE simulation.

vertical extent, a transition zone behind the convection, a stratiform region about 110 km in width to the rear of the transition zone, a rear non-precipitating anvil region of the size of 80 km and a front non-precipitating anvil of about 70 km in horizontal extent. The convective area in the leading portion of the MCS has an upright structure. This narrow convective region is also found in the Doppler radar observations (i.e., Fig. 4.14). The transition zone is a narrow region which separates the newly formed cell in the convective region from the decaying cells in the stratiform region. The stratiform region consists of remnant decaying cells from the previous convection as the MCS propagates forward with newly formed cells. This stratiform feature is also observed in the DUNDEE cloud cluster. The upper level anvil extends both from the front of the cloud and to the rear of the system and arise from both the advection of ice particles from the convective area of the MCS and the *in-situ* production of ice crystals inside the anvil. The horizontal scale of the entire MCS at this time, including upper level anvil, is about 270 km. The vertical extent of the simulated system is 15 to 17 km. The vertical scale agrees well with the observed scale of the DUNDEE cloud system noted earlier from radar observations and infrared satellite imagery. While the horizontal scale is broadly consistent with the satellite data, it seems

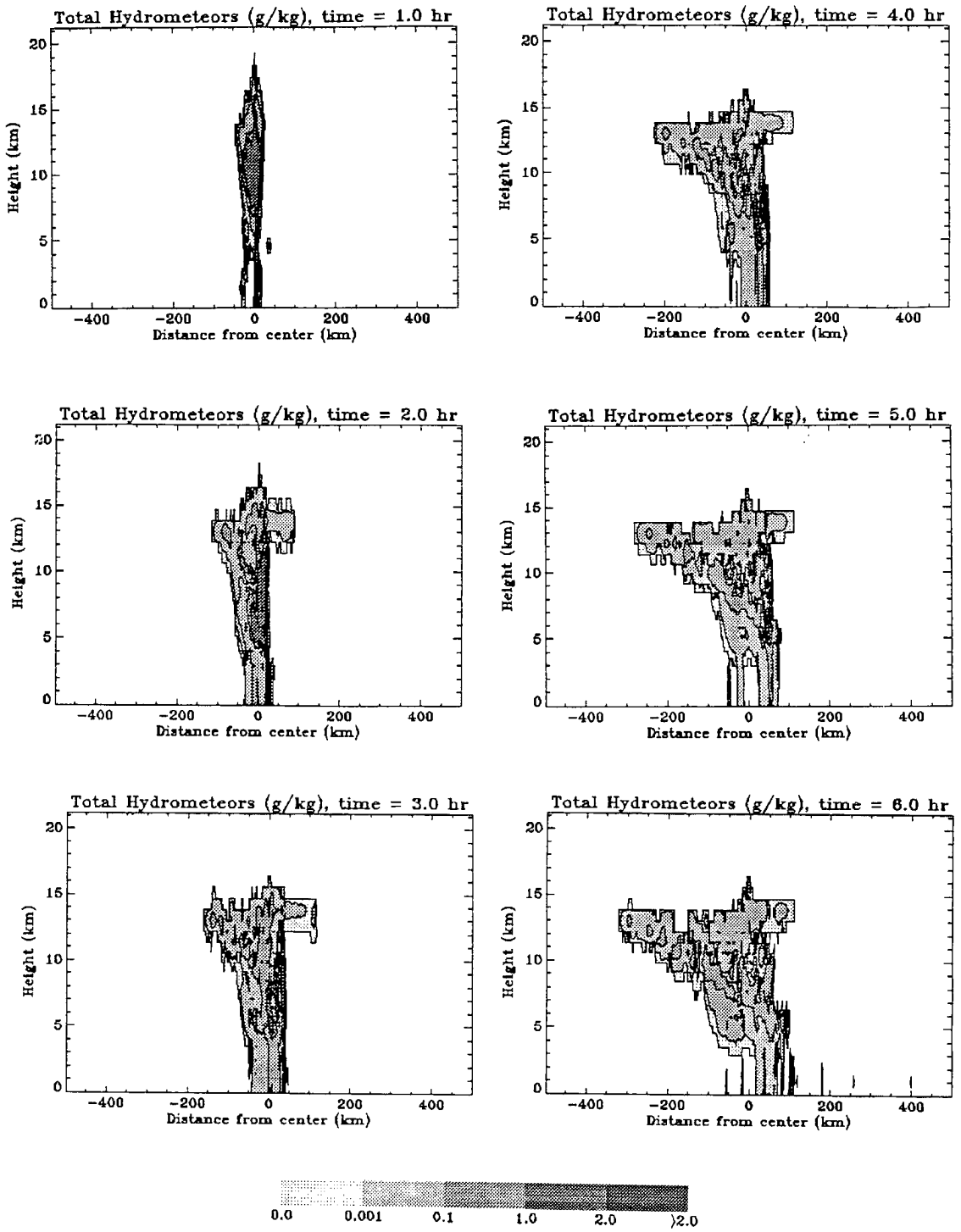

Figure 5.13: Simulated two dimensional field (X-Z cross-section) of total hydrometeor mixing ratio (g/kg) as predicted by the RAMS cloud model at (a) 1 hour, (b) 2 hours, (c) 3 hours, (d) 4 hours, (e) 5 hours, and (f) 6 hours into the simulation of the DUNDEE cloud cluster.

to be larger than those observed from the radar. This may be due to the fact that the radar is incapable of sensing small ice particles in the upper levels. For example, the horizontal scale comparison between the simulation and the radar observation are reasonable only if we consider areas below the 10 km height level. In addition, a sloping total hydrometeors feature is also simulated at this time. For example, the decaying convection seems to have a slope of 45 degree with respect to the surface, which is similar to observations (i.e., 40 degree slope of convection in Chapter 4).

The cloud cluster enters into its decaying stage between 4 and 7 hour into the simulation as the domain total hydrometeor content slowly evaporates and shrinks in size. Some new shallow convection is also initialized in front of the cloud cluster at this time. The MCS at the 6 hour of the simulation (given in Fig. 5.13f) is characterized as a weak decaying stratiform cloud system with an extensive anvil region that fills almost half of the model domain.

The lifetime of the simulated DUNDEE system is approximately 6 to 7 hours which compares well to the radar observations. The simulated system moves northward (from left to right) at an approximate speed of 4 m/s compared well to the 5 m/s observed speed from both Doppler data and satellite cloud motion fields. The slower speed of the simulated system, again, may be due to the weaker winds utilized in the initial sounding.

5.3.3 Dynamical Fields

The time series of the X-Z cross-sections of the horizontal and vertical motion predicted by the cloud model are shown in Figs. 5.14 and 5.15, respectively. A 30 km horizontal averaging operator has again been applied to the vertical motion fields to obtain Fig 5.15. During the intensification stage, the horizontal motion (given in Fig. 5.14a) is significantly altered by the cloud cluster as indicated by the bending of the contour lines at the location x = 0 km. A low level gust front is evident in simulation at this time near the location at x = 20 km as the surface environmental easterlies inflow collide with the surface westerlies outflow produced by the cloud cluster. The vertical motion field (shown in Fig. 5.15a) at this time generally shows strong upward motion inside and near the front

of the cloud cluster. Downward motion is also evident at a distance ahead and behind the cloud system.

As the area of the cloud expands in size from the second (shown in Fig. 5.14b and 5.15b) to the fourth simulated hour (given in Figs. 5.14d and 5.15d), the perturbation horizontal and vertical motion fields again show an expansion in size caused by the simulated DUNDEE cloud cluster. The vertical cross-sections of horizontal and vertical velocity predicted at the 3 hour simulation time indicate a circulation similar to those of the EMEX simulation (i.e., a low level inflow into the leading convection, a low level outflow behind this convection, an upper level outflow in front, and a upper level outflow to the rear of the system). The upper level outflows to the front and rear of the system again help to carry cloud particles away from the convective cells and produce the stratiform anvil clouds in front of and behind the main MCS. The low level northerly wind ahead of the system continuously feeds the convective region of the cloud cluster with warm moist air. The convective updrafts at the third hour into the simulation show upright structure in the convective cells. Behind this cell, an upper level upward motion field is found above an area of downward motion. These features are consistent with the observed vertical motion fields (i.e., Fig. 4.16). However, the observed tilting of the convective updraft is missing in the simulation. In front of and far away from the cloud system, broad-scale downward compensating air motion is observed. Downward/upward motions are also found scattered inside/below the cloud deck at the anvil region. As the cloud cluster enters its decaying stage (shown in Figs. 5.14d and 5.15d) the horizontal wind again slowly recovers to its pre-cloud condition and the vertical motion field continues to weaken.

5.3.4 Thermodynamical Fields

The time series of the X-Z cross-section of the potential temperature perturbation and pressure perturbation fields for the DUNDEE simulation are given in Figs. 5.16 and 5.17. Figures 5.16a and 5.17a show a general pattern, similar to the EMEX simulation (i.e, in-cloud warming and a cooling at the surface under the cloud cluster) at the intensification stage. These temperature patterns translate to low pressure anomalies at the surface and higher pressure anomalies aloft at and near the cloud cluster. At the region away from

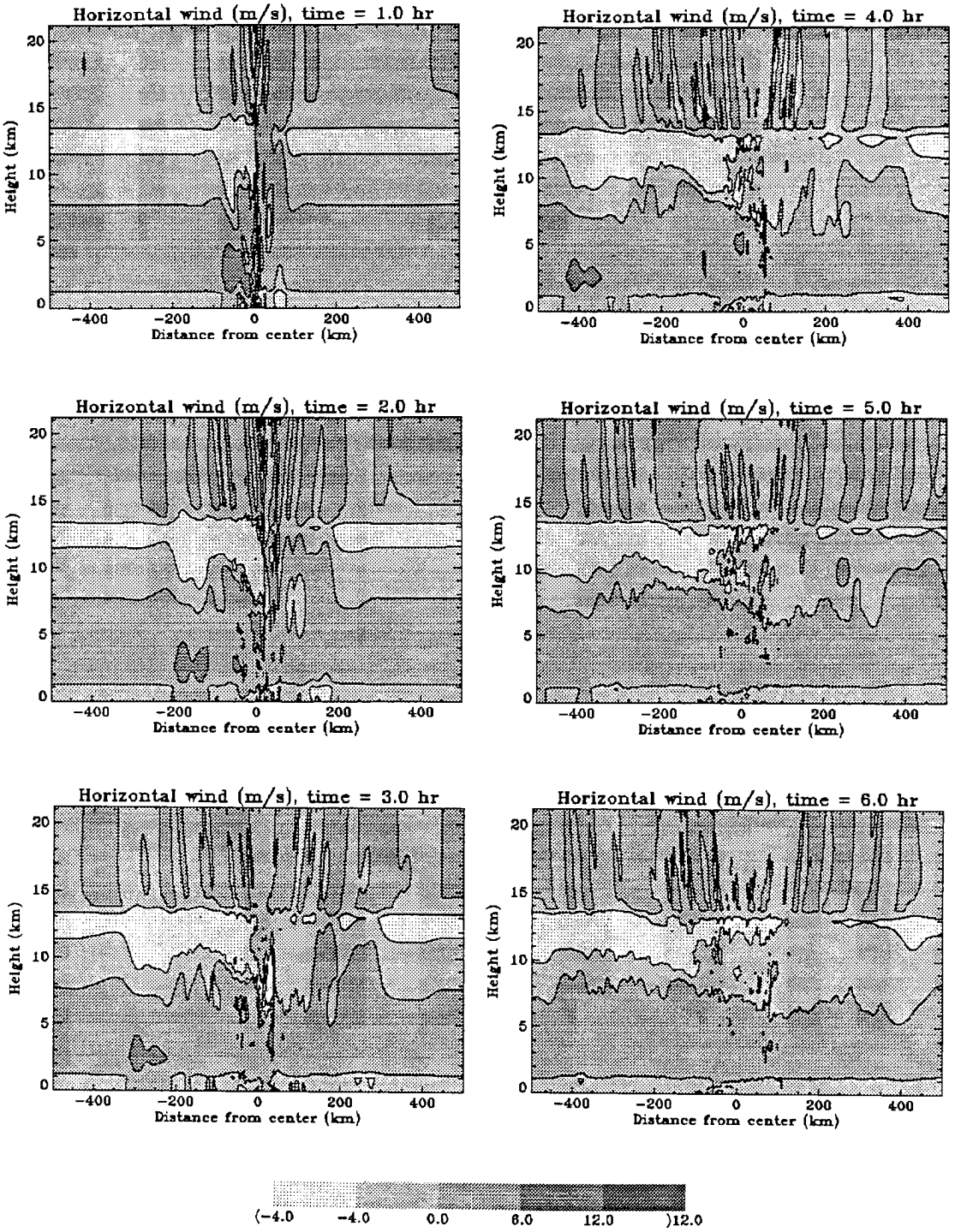

Figure 5.14: Simulated two dimensional (X-Z cross-section) fields of horizontal wind (m/s) as given by the RAMS cloud model at (a) 1 hour, (b) 2 hours, (c) 3 hours, (d) 4 hours, (e) 5 hours, and (f) 6 hours into the simulation of the DUNDEE cloud cluster.

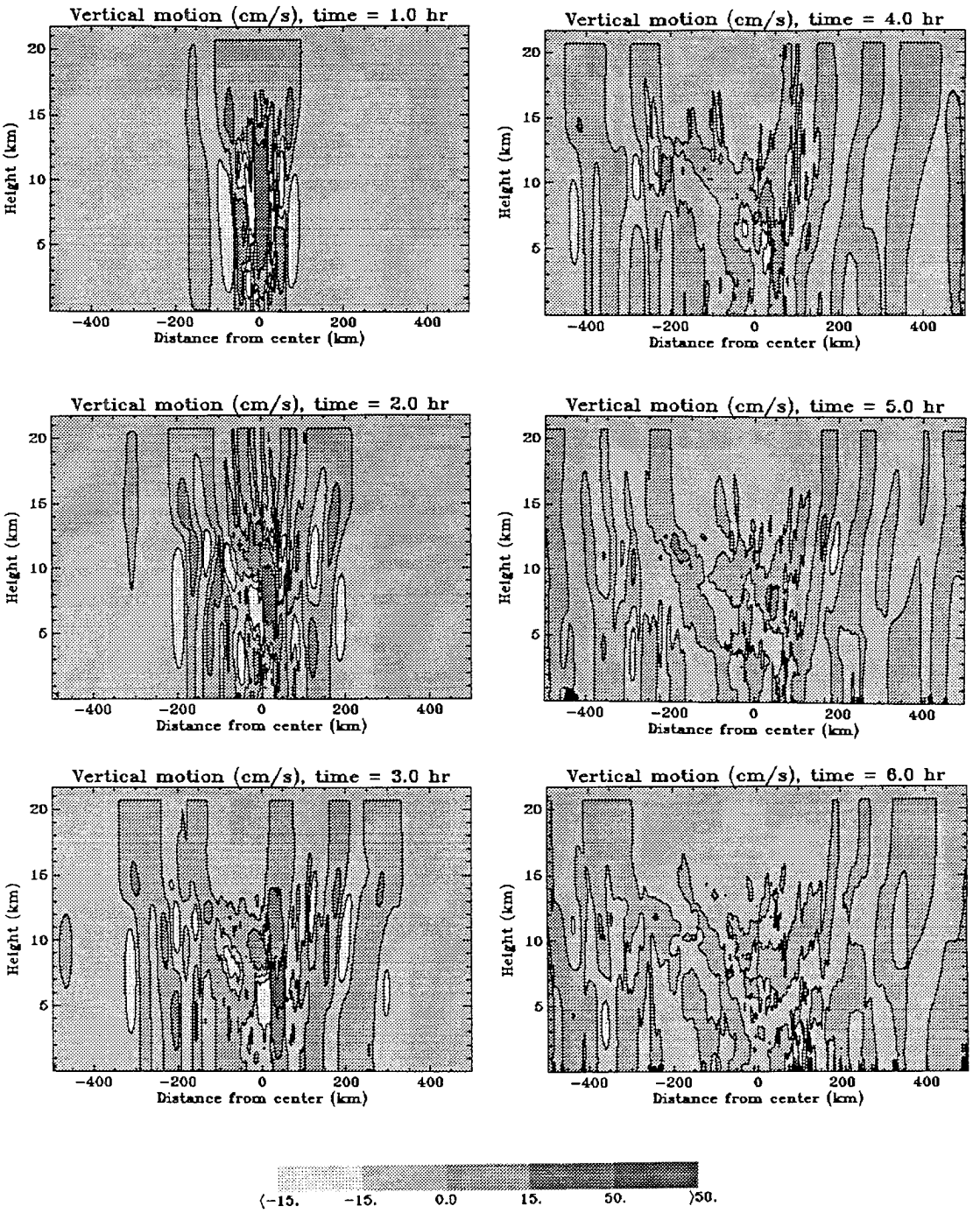

Figure 5.15: Simulated two dimensional (X-Z cross-section) fields of vertical motion (cm/s) as given by the RAMS cloud model at (a) 1 hour, (b) 2 hours, (c) 3 hours, (d) 4 hours, (e) 5 hours, and (f) 6 hours into the simulation of the DUNDEE cloud cluster.

the cluster, weak subsidence warming creates a broad area of high pressure. The low pressure at the low level and the high pressure aloft are symmetric around the center of the system due to the lower vertical shear condition of the background environment. A gravity wave anomaly train excited by the convection is also shown to propagating away from the source region.

At the mature stage (i.e., between the second and the fourth hour of the simulation), the potential temperature perturbation (given in Fig. 5.16b to d) shows a complicated pattern of heating and cooling at the cluster location. Some distance away from the cloud system, a symmetric warming pattern is evident as the heating generated by the cloud system slowly propagate away from the center toward the side of the model. This is again due to the low shear environment of this case which allows waves to propagate equally in both directions. Within the region of cloudiness, cooling exists in the mid-levels and extends to the surface, and a surface cool pool is still evident at this stage. Furthermore there is evidence of increasing radiative cooling near the cloud top region at this stage. The pressure perturbation pattern (shown in Fig. 5.17b and c) resembles much of the same features as the temperature fields with low pressure away from the cloud region due to propagating heating source. In the cloud region, low pressure anomalies aloft and high pressure anomalies below are evident. The pressure perturbation field (given in Fig. 5.17b) at the surface contains a meso-high in the vicinity of the convection and a meso-low in the region to the rear and in the front of the cloud system. This surface pressure patterns are common to the observed features in both mid-latitude and tropical mesoscale convective systems. Gravity waves are continuously excited by the convective region. In contrast to the EMEX simulation, trapping of these waves is not as evident in this case due to lower vertical shear conditions.

As the system approaches its decaying stage (given in Fig. 5.16e to f and Fig. 5.17e to f), it is marked by a general warming/lower pressure aloft (except near the cloud top) and cooling/higher pressure below. Radiative coolings near the cloud top region are very strong at this time. Similar to the EMEX case, gravity waves cease to exist during the decaying stage and this lack of wave activity is again correlated well with the disappearance of the convective region in the cloud cluster.

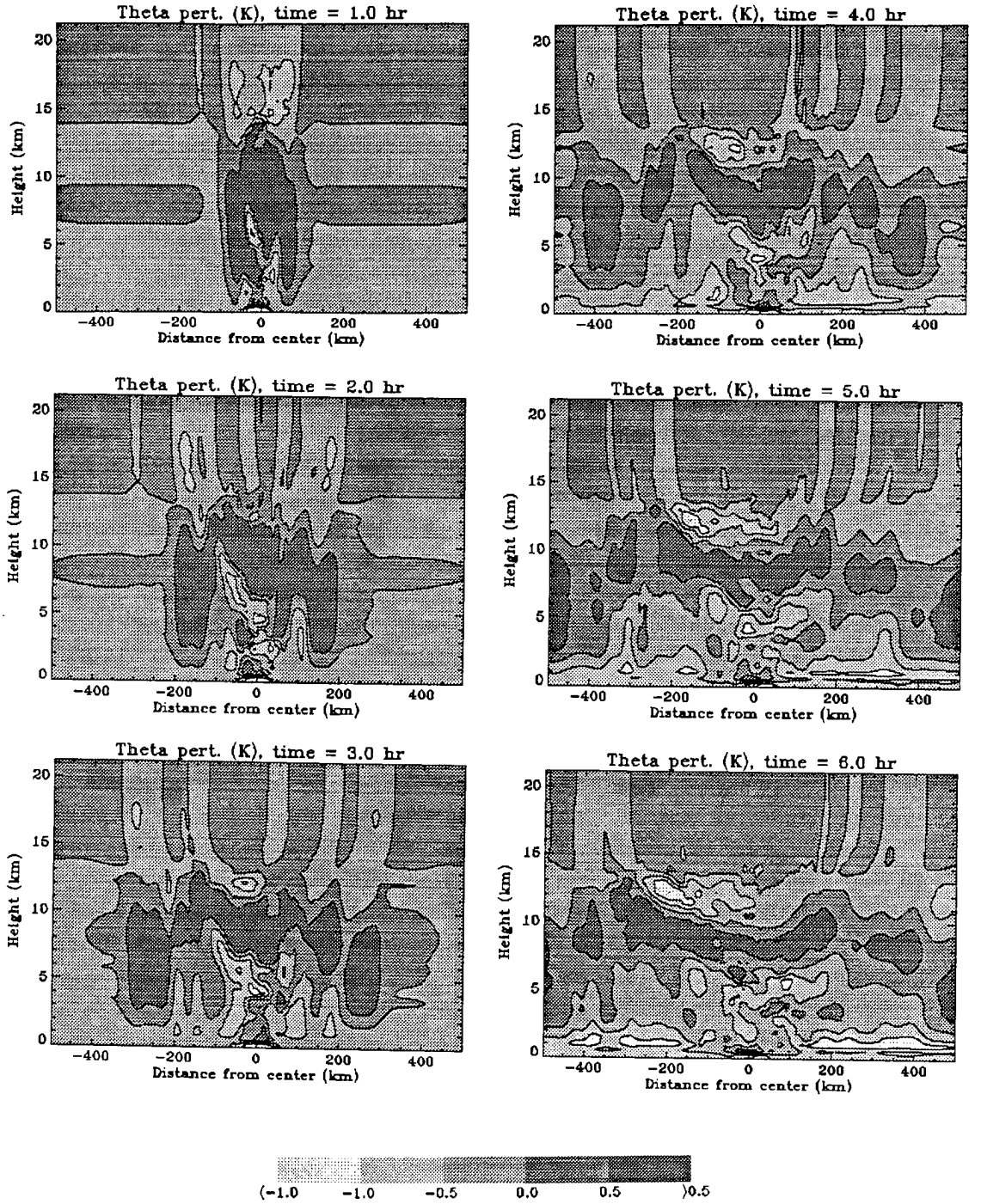

Figure 5.16: Simulated two dimensional (X-Z cross-section) fields of potential temperature perturbation (k) as predicted by the RAMS cloud model at (a) 1 hour, (b) 2 hours, (c) 3 hours, (d) 4 hours, (e) 5 hours, and (f) 6 hours into the simulation of the DUNDEE cloud cluster.

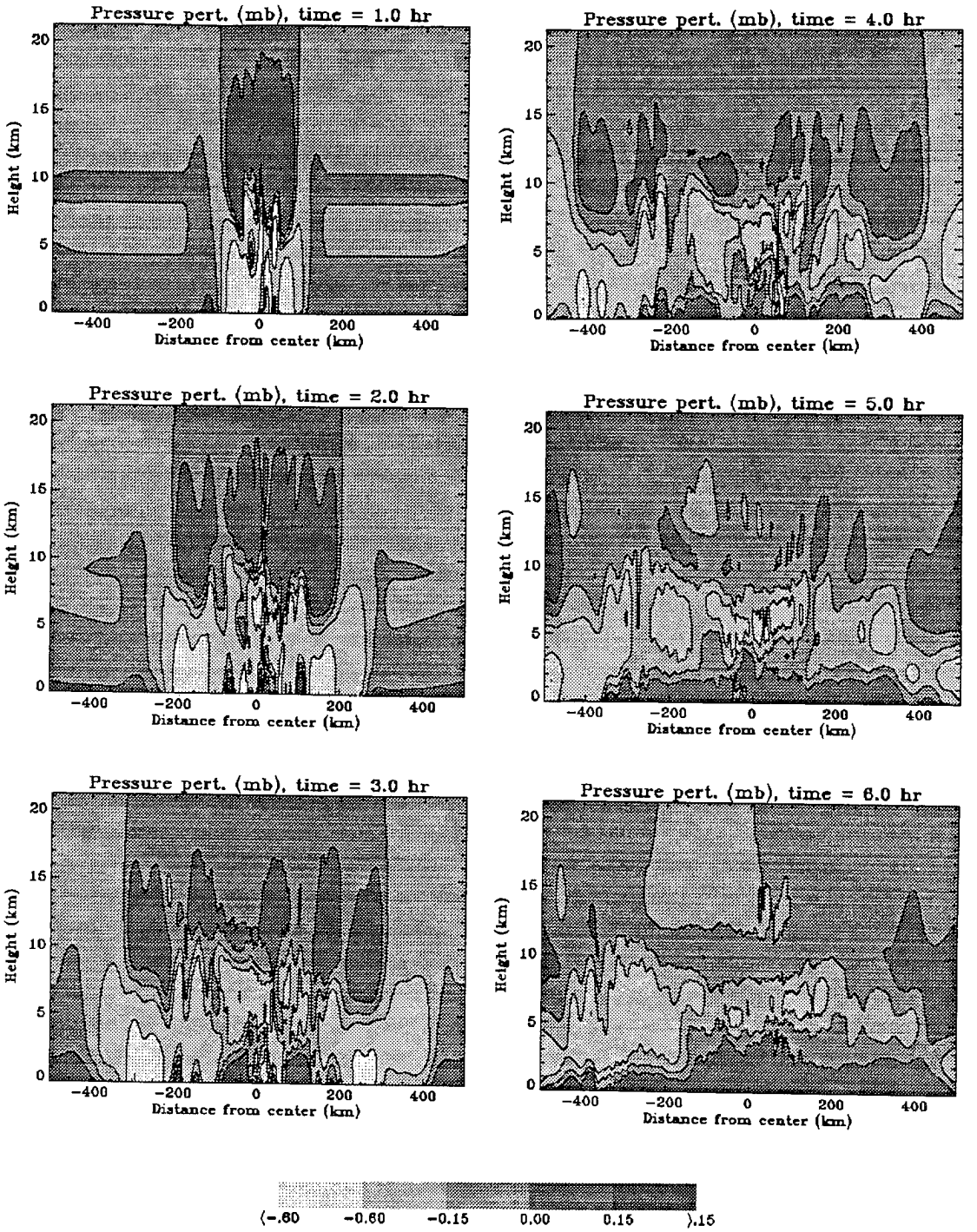

Figure 5.17: Simulated two dimensional (X-Z cross-section) fields of pressure perturbation (mb) as predicted by the RAMS cloud model at (a) 1 hour, (b) 2 hours, (c) 3 hours, (d) 4 hours, (e) 5 hours, and (f) 6 hours into the simulation of the DUNDEE cloud cluster.

5.3.5 Water Fields

A more detailed breakdown of the water perturbation fields during the DUNDEE simulation is presented in Figs. 5.18 to 5.20. Similar to the EMEX case, significant amounts of water in the form of vapor, liquid, and solid phase (shown in Fig. 5.18a to Fig. 5.20a) are transported vertically from the lower levels during the intensification stage of this cloud cluster. A lower level drying exists behind the cloud system as shown Fig. 5.18a. The individual breakdown of the solid and liquid water (given in appendix B) at this time shows ice crystals and aggregates to be the most significant water species above the melting level (at about 5 km) with pristine ice being the most abundant water species above 10 km. Graupels are only concentrated in the area of strong convection and extended from near the surface to about the 15 km level, which is much higher than highest graupel level (i.e., 8 km) in the EMEX case. This higher level is due to the stronger vertical motion field in the DUNDEE case. The rainwater and cloud water dominated the cloud system at the lower levels. These results are again similar to the EMEX simulation.

At the mature stage, the water perturbation patterns remain very much the same as during the intensification stage. However, the area coverage of the water perturbation fields has been increased significantly as shown in Fig 5.18b, c to Fig. 5.20 b, c. While cells of cloud water scatter across the convective region below the 10 km level, both the rain water and graupel are found only in the convection region and some regions in the decaying cell. The graupel mixing ratio at this time is located between the 1 and 10 km levels in the convective region. The highest graupel level is again higher than the corresponding highest graupel level in the EMEX case indicating the stronger convection in the DUNDEE case. The rain water mixing ratio spreads across the convective region below the 7 km surface and the stratiform area below the melting level (i.e., 5 km surface). Regions of large rain water mixing ratio are also predicted at the surface in the convective region. Ice crystals and aggregates in the simulated cloud system are located above the freezing level (above 5 km). Ice crystals are mostly found between cloud top and 8 km and aggregates are located at lower levels in the stratiform region. High mixing ratios of both ice crystals and aggregates are also found in the convective region. The thin anvils

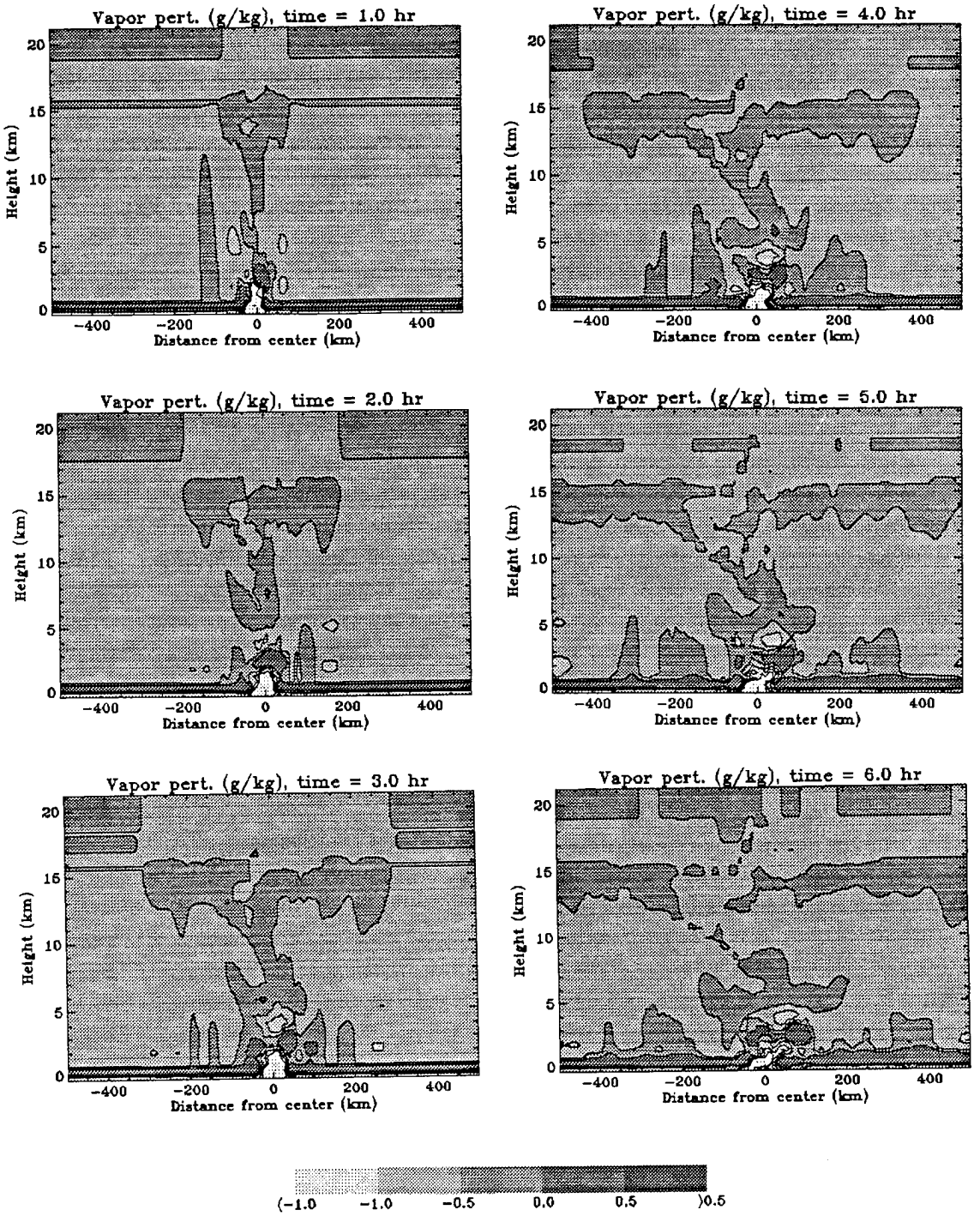

Figure 5.18: Simulated two dimensional (X-Z cross-section) mixing ratio fields (g/kg) of water vapor perturbation as predicted by the RAMS cloud model at (a) 1 hour, (b) 2 hours, (c) 3 hours, (d) 4 hours, (e) 5 hours, and (f) 6 hours into the simulation of the DUNDEE cloud cluster.

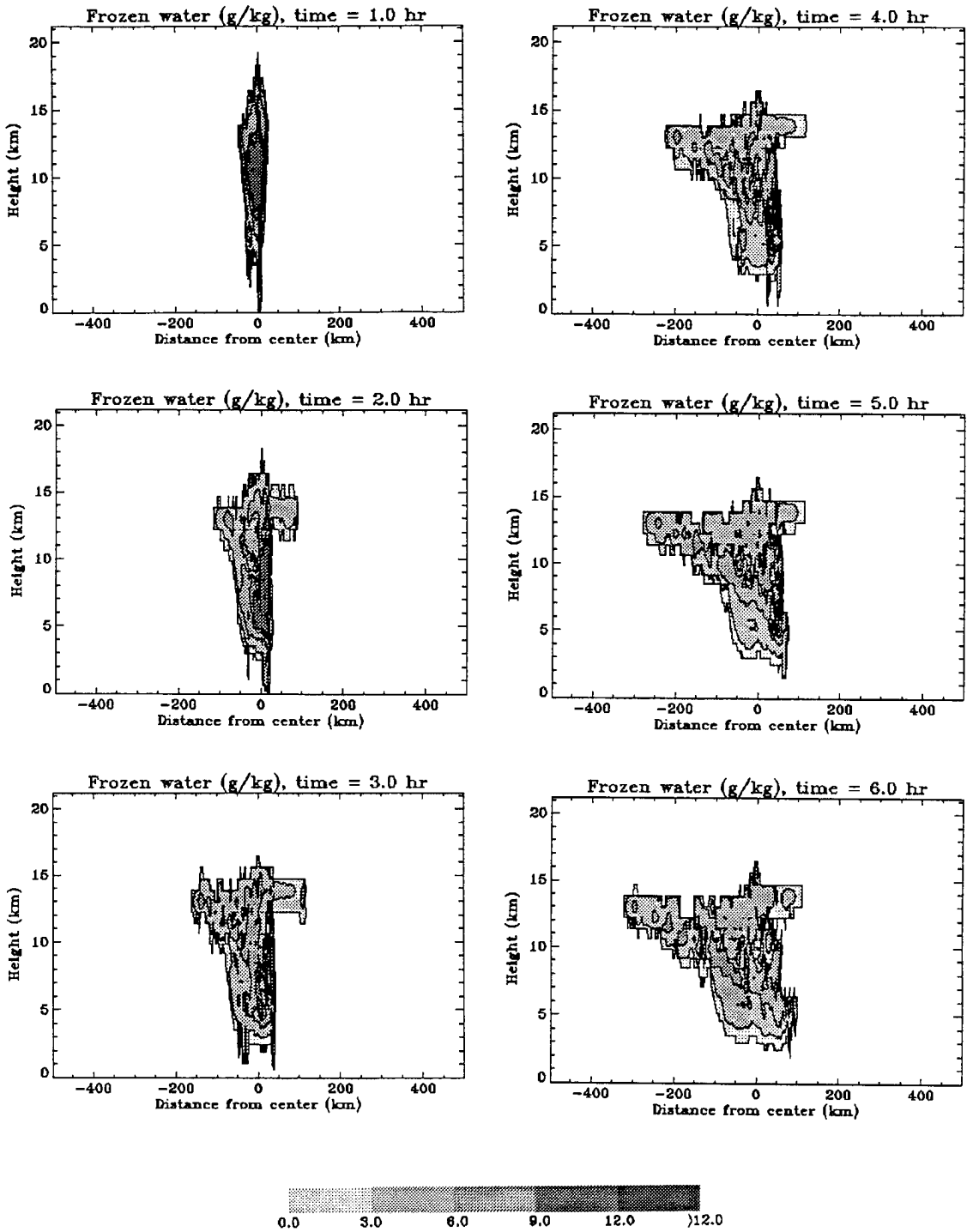

Figure 5.19: Simulated two dimensional (X-Z cross-section) mixing ratio fields (g/kg) of total ice water species as predicted by the RAMS cloud model at (a) 1 hour, (b) 2 hours, (c) 3 hours, (d) 4 hours, (e) 5 hours, and (f) 6 hours into the simulation of the DUNDEE cloud cluster.

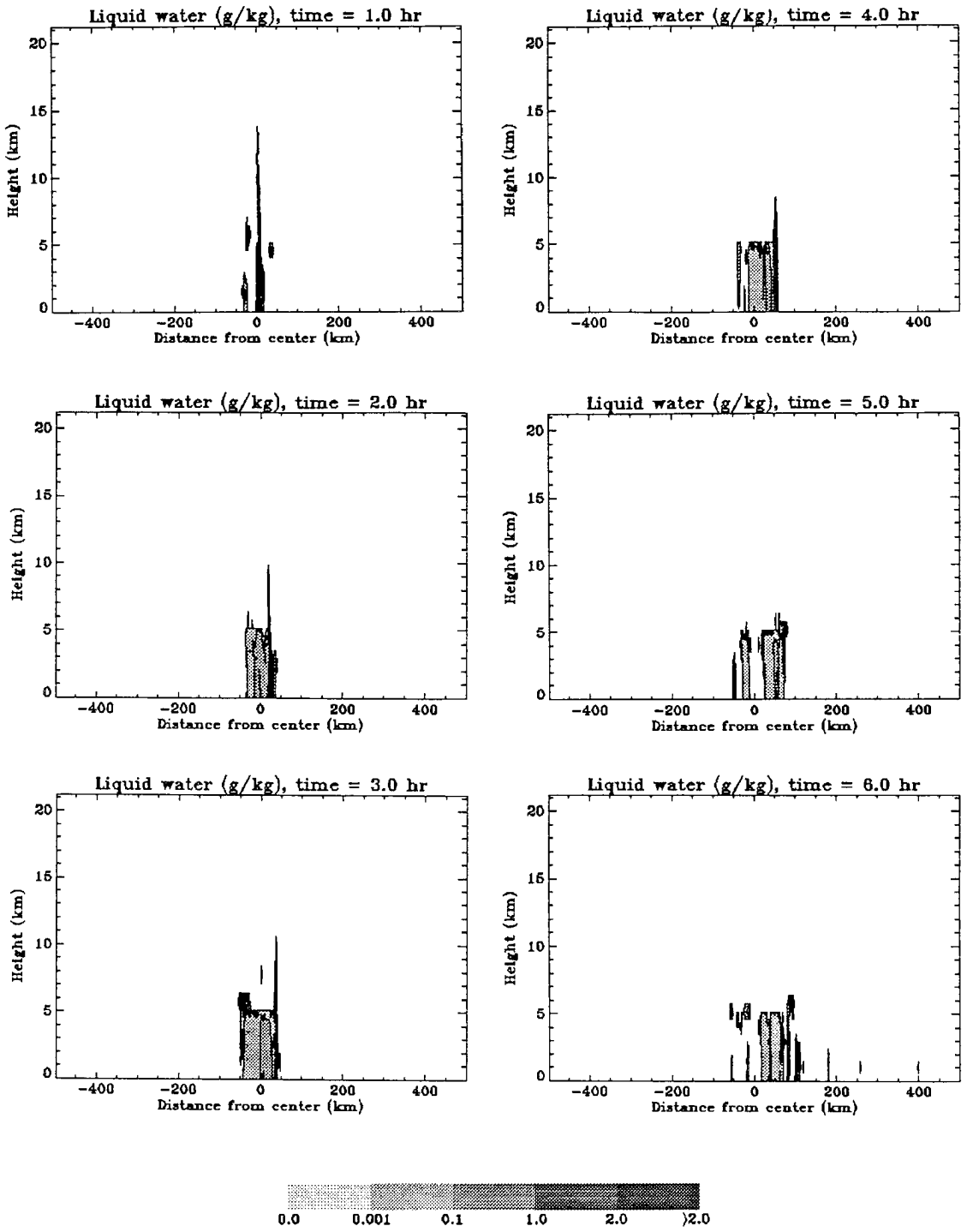

Figure 5.20: Simulated two dimensional (X-Z cross-section) mixing ratio fields (g/kg) of total liquid water species as predicted by the RAMS cloud model at (a) 1 hour, (b) 2 hours, (c) 3 hours, (d) 4 hours, (e) 5 hours, and (f) 6 hours into the simulation of the DUNDEE cloud cluster.

located to the front and to the rear of the system are composed of mostly ice crystals. Above this level, ice crystals are dominant. These features are very similar to the EMEX simulation.

In the decaying stage, the water fields (given in Fig. 5.18d-f to Fig. 5.20d-f) continue to show the influences of the cloud system. The water vapor perturbation field again shows a general moistening aloft and drying below. This is again consistent with observations which suggest that the effects of MCSs is to dry out the lower levels. This lower level drying is also consistent with observations of the large-scale field.

5.4 Summary

This chapter describes the simulation of the two squall-type cloud clusters. Even though these simulations generally agree well with the observed cloud systems, some disagreements do exist. In addition this chapter also highlights significant similarities of the dynamical, thermodynamical, and water fields of the two cloud simulations. For example, both simulations exhibit distinct stages within their life cycle (i.e., intensification, mature, and decaying stage), which can be identified from the time series of the domain peak vertical motion field and the domain total hydrometeor field. The lifetime of these two simulations is on the order of 6 to 7 hours. Furthermore, the presence of these two simulated MCSs can significantly alter the dynamics, thermodynamics, and moisture fields of the simulated atmosphere.

The few major differences between these two simulations can be related to the initial conditions and the timing of the system. For example, the DUNDEE simulation contains much stronger vertical motions compared to the EMEX case. The simulated peak vertical motion fields in the DUNDEE case are twice as large as those found in the EMEX system. This stronger vertical motion field in the DUNDEE system can be accounted for by the higher CAPE value and weaker vertical shear environment of the monsoonal break period of the DUNDEE case. The DUNDEE squall cluster also moves at a much slower speed than the EMEX case. This is due to the weaker wind profile of the DUNDEE environment. This lower propagation speed may also help to maintain stronger convective activity in

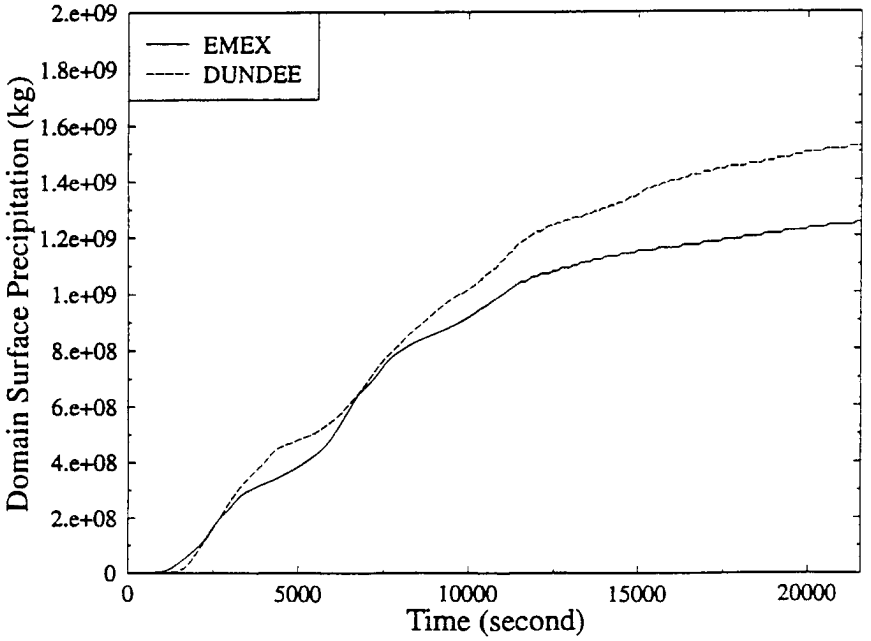

Figure 5.21: Comparison of the time series of domain accumulated surface precipitation between the EMEX (solid line) and the DUNDEE (dashed line) simulation.

the DUNDEE system. The DUNDEE simulation also has more surface precipitation than the EMEX case (shown in Fig. 5.21), which is also indicative of more vigorous convection by the DUNDEE system. In addition, the DUNDEE system also retains significant more water, in term of cloud waters and aggregate particles during both the intensification and the mature stage of the MCS, than those of the EMEX case (given in Fig. 5.22). This larger storage of water in the DUNDEE case helps to produce more surface precipitation during the later part of the DUNDEE simulation. Furthermore, this storage term also explains the similarity in the accumulated surface precipitation during the first half of both the DUNDEE and the EMEX simulation disputing the large differences in the time history of their domain integrated total hydrometeor fields (i.e., Figs. 5.2 and 5.12). While the EMEX cluster has a significant in-cloud radiative warming after its mature stage, the DUNDEE simulation has strong cloud top radiative cooling. This difference can be accounted for by the timing of the two systems (i.e., EMEX case occurs during the day time and the DUNDEE system occurs mostly at night). The effects of these radiative heating differences on the larger-scale environment and the MCS itself are the subjects of the next two chapters.

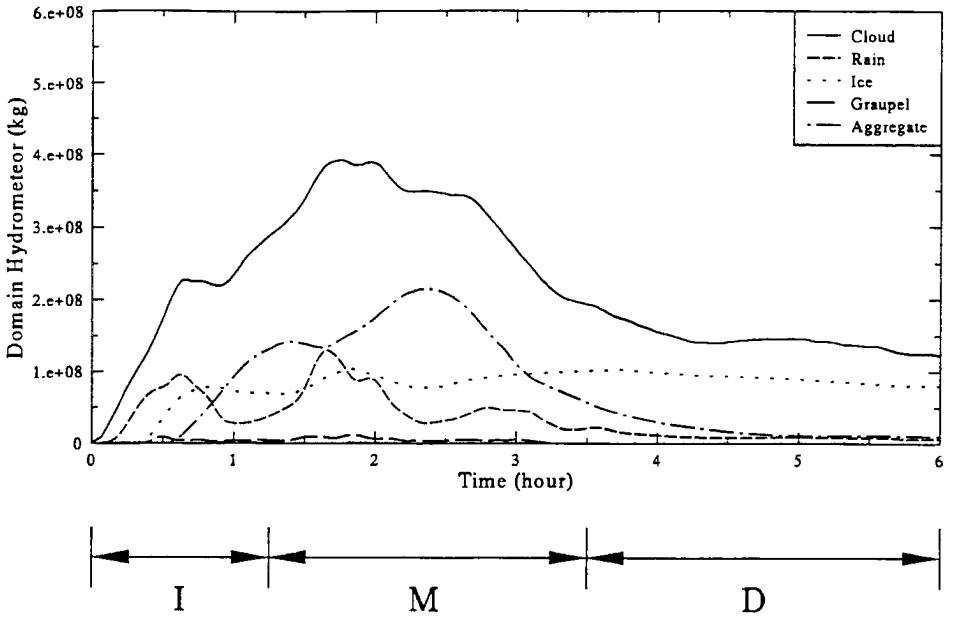

Figure 5.22: The time series of the simulated EMEX-9 domain integrated cloud water field (solid), rain field (short dashed), ice crystal field (dotted), Graupel field (long dashed), and aggregate field (dot-dashed). The intensification, mature, and decaying stages are also shown in the figure as I, M, and D, respectively.

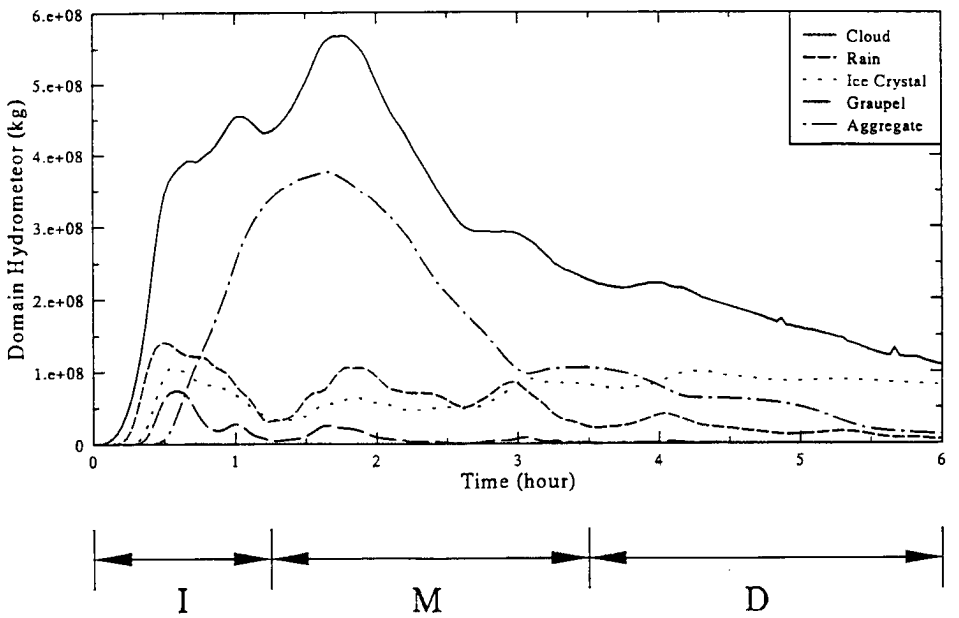

Figure 5.23: The time series of the simulated DUNDEE domain integrated cloud water field (solid), rain field (short dashed), ice crystal field (dotted), Graupel field (long dashed), and aggregate field (dot-dashed). The intensification, mature, and decaying stages are also shown in the figure as I, M, and D, respectively.

Chapter 6

RADIATIVE BUDGET SIMULATIONS

This chapter describes calculations of the total (i.e., solar plus infrared) radiative budget and radiation heating distributions associated with tropical MCSs and the change of these distributions through the life cycle of the cloud clusters. These results are based on information provided by the cloud simulations highlighted in last chapter. In order to describe both the spatial characteristics and temporal evolution of the radiative budget fields associated with these tropical systems, radiation calculations are carried out hourly for the first six hours of both the EMEX and DUNDEE cloud simulation and the results are shown in Secs. 1 and 2 below. Since the EMEX and the DUNDEE simulation occurred at two completely opposite period of the day (i.e., the EMEX is a daytime case and the DUNDEE was primarily a nocturnal system), these timing differences will significantly influence the total radiative budget and radiative heating profile of these two systems. In addition these radiation simulations will also demonstrate how the total (solar plus infrared) radiation budget of the atmosphere is significantly perturbed by the presence of these MCSs. Section 6.3 will give a summary of these results.

6.1 Spatial Structures of the Cloud Radiation Budget

The spatial structures of the cloud radiation fields (i.e., infrared, solar, and total) associated with both EMEX and DUNDEE cloud cluster are illustrated in this section using the radiation calculations during the mature stage (i.e., the third hour into the simulation) of the MCSs. In general most of the discussion in this section can also be used in describing the cloud radiation fields for other stages of these systems. A more detailed examination of the temporal variabilities of these cloud radiation fields will be given in the later section. Since the modeled radiation fields between the two cases are similar in

many areas during the mature stage, only the EMEX calculations will be shown below to avoid duplication of statements. However, additional discussion for the DUNDEE cloud cluster is included if the modeled calculations diverge significantly between the two cases.

6.1.1 Infrared Radiative Budget

The simulated X-Z cross-section of the infrared (IR) radiative heating rate and its horizontal and vertical (clear and cloudy region) statistics at the third hour into the EMEX-9 cloud cluster are shown in Figs. 6.1 and 6.2, respectively. During the mature stage of this MCS, the X-Z cross-section of the simulated infrared radiative heating rates highlights the dominance of infrared cooling in both the clear sky (i.e., near the edge of the figure) and at the cloud top of the MCS (i.e., between x = -180 km and x = 130 km). Since the infrared optical depths are directly related to the total hydrometeor mixing ratio fields, one expects a high correlation between the spatial structure of the simulated infrared heating/cooling rates in Fig. 6.1 and the spatial structure of the total hydrometeor mixing ratios that were presented in the last chapter (i.e., Fig. 5.3c). This strong correlation is evident in our model results. The strong infrared cooling extends well into the upper portions of the anvil. Infrared heating exists inside and near the cloud base area in the convective and the stratiform region and at the base of the thin anvil cloud as well. The maximum values of IR radiative heating and cooling rates (shown in Fig. 6.2) found in this simulated radiation field are 36.5 and 32.3 K/day, respectively. The magnitude of these values is almost the same. These extreme values are located in the upper level of the convective and stratiform area. While the vertical profile of IR cooling rate in the clear sky (given in Fig. 6.2a) shows very little variation from its mean values, the IR heating/cooling rate in the cloud region, on the other hand, contains significant amount of both vertical (given in Fig. 6.2b) and horizontal variations (given in Fig. 6.2c). These variations are mostly due to the changes in hydrometeors field inside the MCS. Similar results are also noted for the DUNDEE cloud cluster. However, the maximum infrared heating (i.e., 35 K/day) and cooling rates (such as 28 K/day) at the third hour into the DUNDEE simulation are somewhat lower than the EMEX case.

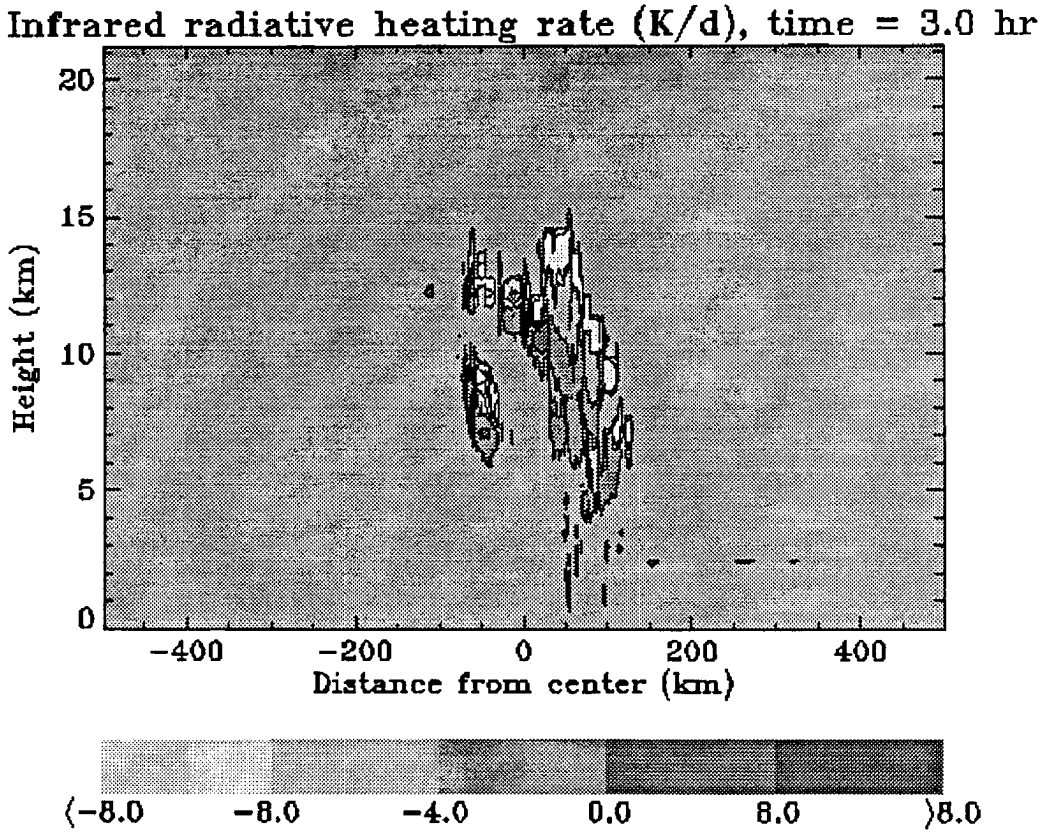

Figure 6.1: Two-dimensional (X-Z) cross-section of infrared radiative heating field (K/day) as diagnosed by the two-stream radiation model at 3 hours into the EMEX simulation.

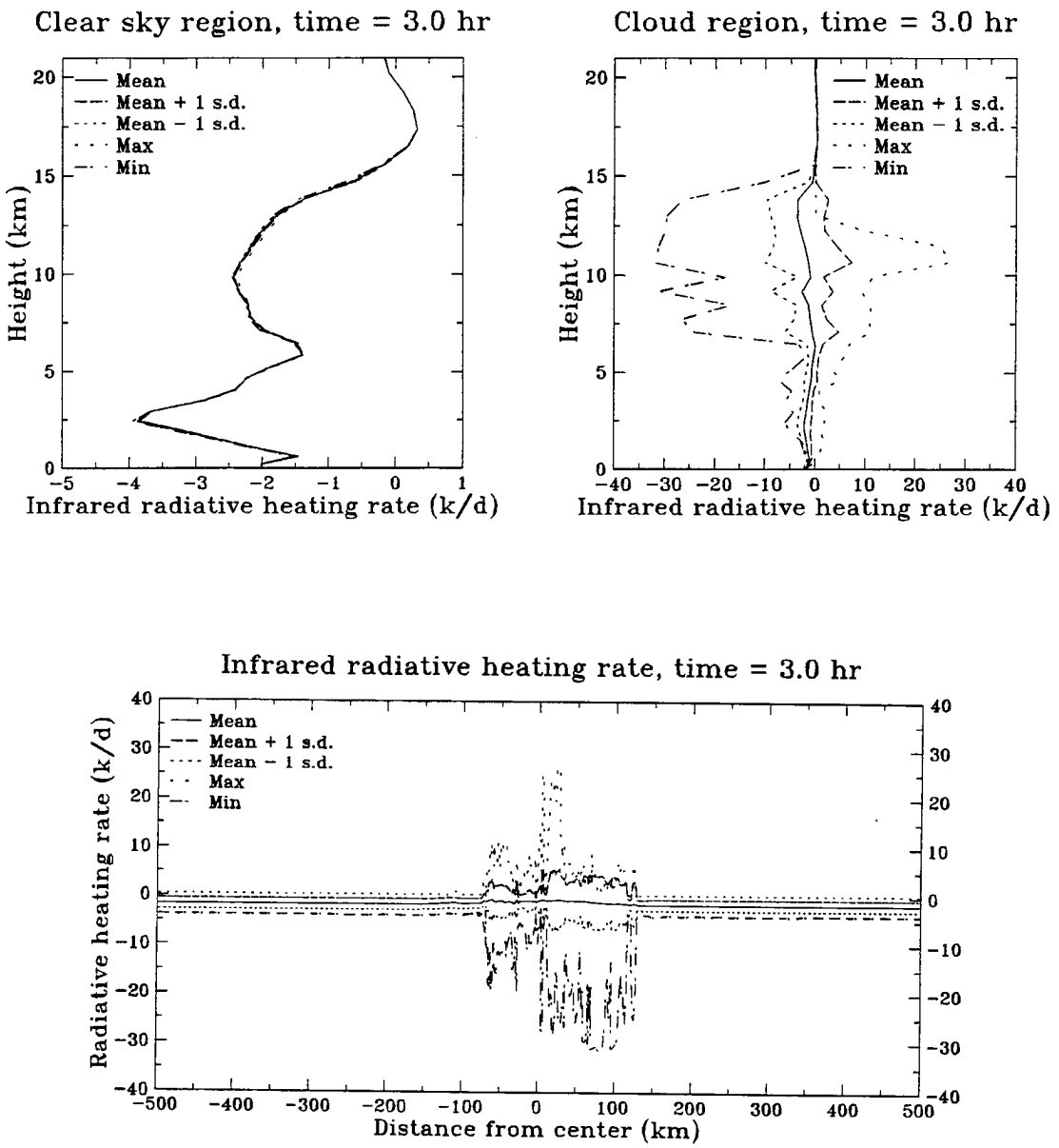

Figure 6.2: The vertical variability of infrared heating rate for (a) the clear sky region, (b) the cloud region, and (c) the horizontal variability of infrared heating field at 3 hours into the EMEX simulation (solid: mean, dashed: mean plus one standard deviation, short dotted: mean minus one standard deviation, long dotted: maximum, dash-dotted: minimum).

The infrared radiative energy budgets of the system as a function of horizontal position at the third hour into the EMEX-9 simulation are shown in Fig. 6.3 in the form of the net convergence of infrared flux into the atmosphere and the net infrared flux at the surface. These variables measure the radiative energy budget in the atmosphere and at the surface. The former quantity is calculated from the difference between the net infrared fluxes at the top of the atmosphere and those at the surface. The results indicate that the surface and the atmosphere lose radiative energy (i.e., negative values of net fluxes in the figure) in both the clear sky and the cloud region. The clear sky atmospheric infrared energy loss can be as large as 240 W/m^2 for the background EMEX atmosphere. This figure also shows how the cloud system acts to increase the flux to the surface and also how the net tropospheric infrared flux is decreased relatively to the clear sky net flux. While the increase in the net IR flux at the surface due to the presence of the EMEX MCS is about 10 to 25 W/m^2, the decrease in outgoing IR flux at the top of the model atmosphere is as large as 200 W/m^2 in the convective region of the cloud cluster. This relative radiant energy surplus into the earth-atmosphere system is indicative of the significant greenhouse effect of these tropical clouds system (i.e., Stephens and Greenwald (1991) and others). These atmospheric and surface radiative budget features are also consistent with those of the DUNDEE simulation. The differences in the simulated atmospheric radiative budget between the clear skies and the cloudy regions are also similar to the observed atmospheric radiative budget deduced from the GATE experiment (Cox and Griffith, 1978). The maximum simulated EMEX-9 upward infrared brightness temperature values (not shown), which are calculated from the upward spectral infrared fluxes at top of the model atmosphere, are -76° C and -55° C for the convective and the stratiform regions, respectively. These values are consistent with observations from both the GMS satellite and the radiometeric measurements from the NASA ER-2 aircraft, as given in last chapter. Furthermore, the differences in the simulated outgoing longwave radiation (OLR) between the clear skies and the cloudy regions are also similar to the observed OLR measurements of the tropical convective ocean region deduced from the Earth Radiation Budget Experiment (ERBE) data (Ockert-Bell and Hartmann, 1992).

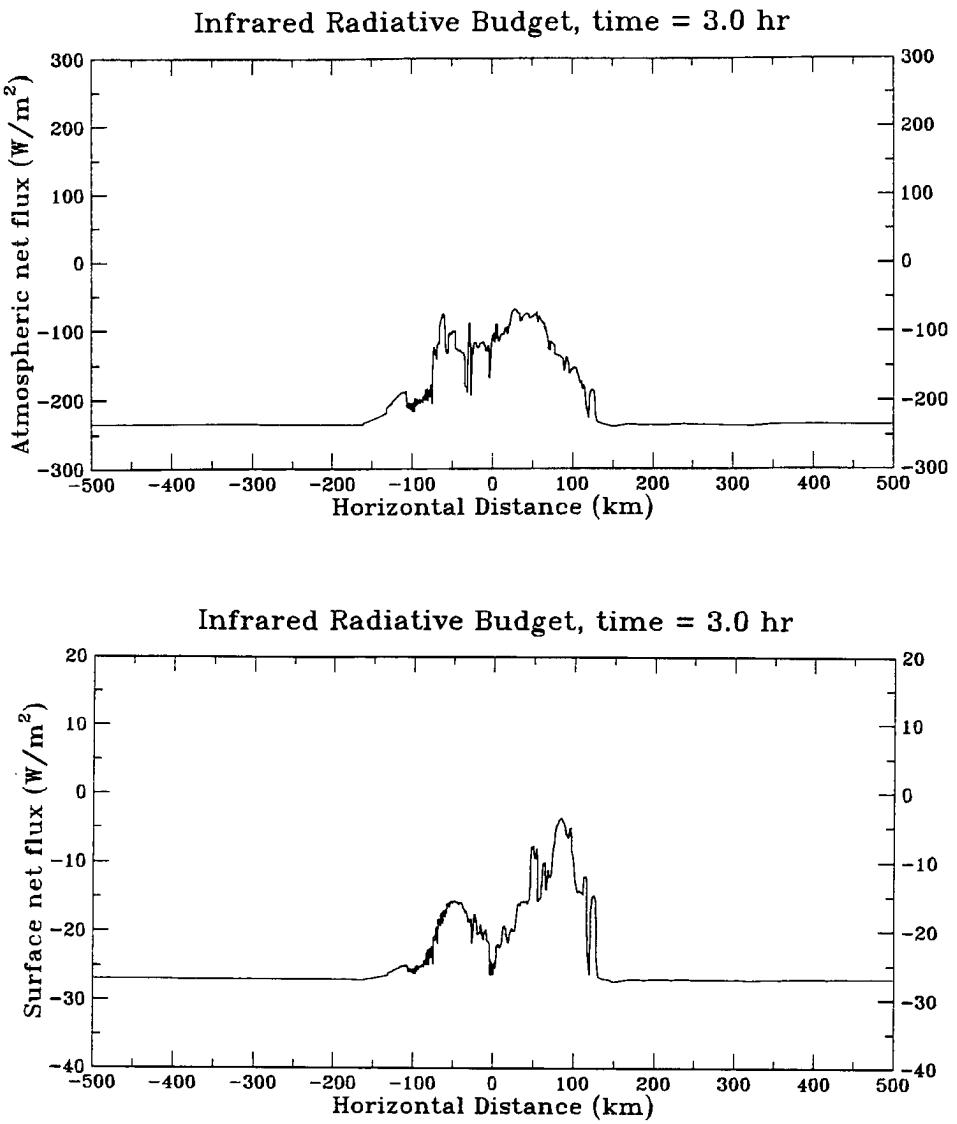

Figure 6.3: The infrared radiative budgets (W/m^2) as a function of the domain horizontal distance for (a) the atmosphere and (b) the surface at 3 hours into the EMEX simulations

6.1.2 Shortwave Radiative Budget

The simulated shortwave (SW) radiative heating rate and its horizontal and vertical statistics at the third hour (i.e., 0816 LST) into the EMEX-9 cloud cluster are shown in Figs. 6.4 and 6.5, respectively. These shortwave radiation fields are presented in a manner similar to the IR results. The X-Z vertical cross-section of the solar heating rates (shown in Fig. 6.4), calculated assuming solar insolation corresponding to 0816 LST, indicates a substantial in-cloud solar heating near the cloud top regions and inside the cloud at this time. The maximum value of the simulated solar heating in Fig. 6.5 is about 33 K/day and this maximum is located in the upper portions of the convection region. The spatial structures of the simulated solar heating rates in Fig. 6.4 again correlate well to the spatial structure of the total hydrometeor fields in the previous chapter (i.e., Fig. 5.3c). Solar heating penetrates significantly into the cloud according to Fig. 6.5b. While there are little variations of solar heating in the clear sky region, the solar heating rates in the cloudy region show significant vertical (given in 6.5b) and horizontal (shown in 6.5c) variations. These findings are similar to the infrared radiative budgets and are due to the variations of the hydrometeor fields inside the MCS. Unlike the EMEX case, the solar heating does not enter into the radiative calculations of the DUNDEE cloud cluster since the sun has already set by the third hour (i.e., 1830 LST) into the DUNDEE simulation.

The shortwave radiative budget at the third hours (i.e., 0816 LST) into the EMEX-9 cloud cluster is shown in Fig. 6.6 in the form of the horizontal variation of the net convergence of shortwave energy in the model atmosphere, the net shortwave flux at the surface, and the percentage of transmission, absorption, and albedo across the model domain. One striking feature between the solar and the infrared energy budget of this cloud cluster is evident in comparing Fig. 6.3 and 6.6. While the cloud cluster seems to have a smaller effect (about 30 W/m^2) on the net shortwave energy budget of the atmosphere, the surface shortwave energy budget shows a significant modification (as large as 500 W/m^2 at this time) due to the cloud system. The infrared radiative effects, by contrast, are larger in the atmosphere than at the surface. While the downward shortwave flux (not shown) at the surface is generally less than 150 W/m^2 beneath the most opaque convective and

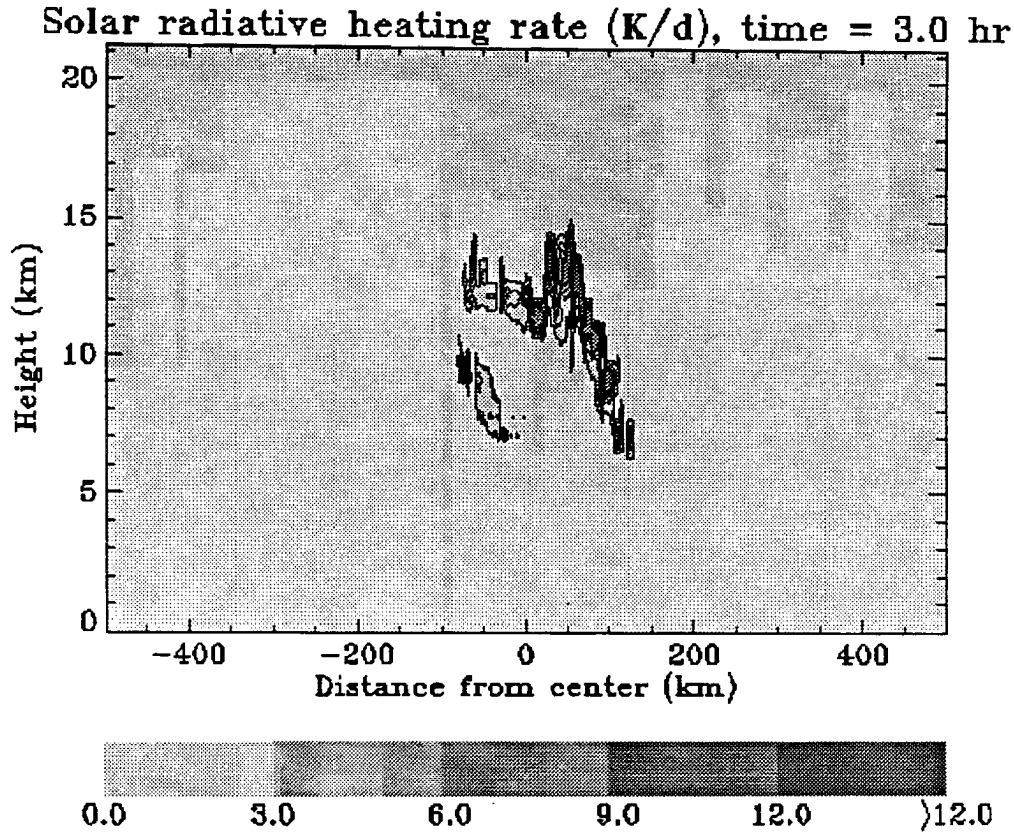

Figure 6.4: Two-dimensional (X-Z) cross-section of shortwave radiative heating field (K/day) as diagnosed by the two-stream radiation model at 3 hours into the EMEX simulation.

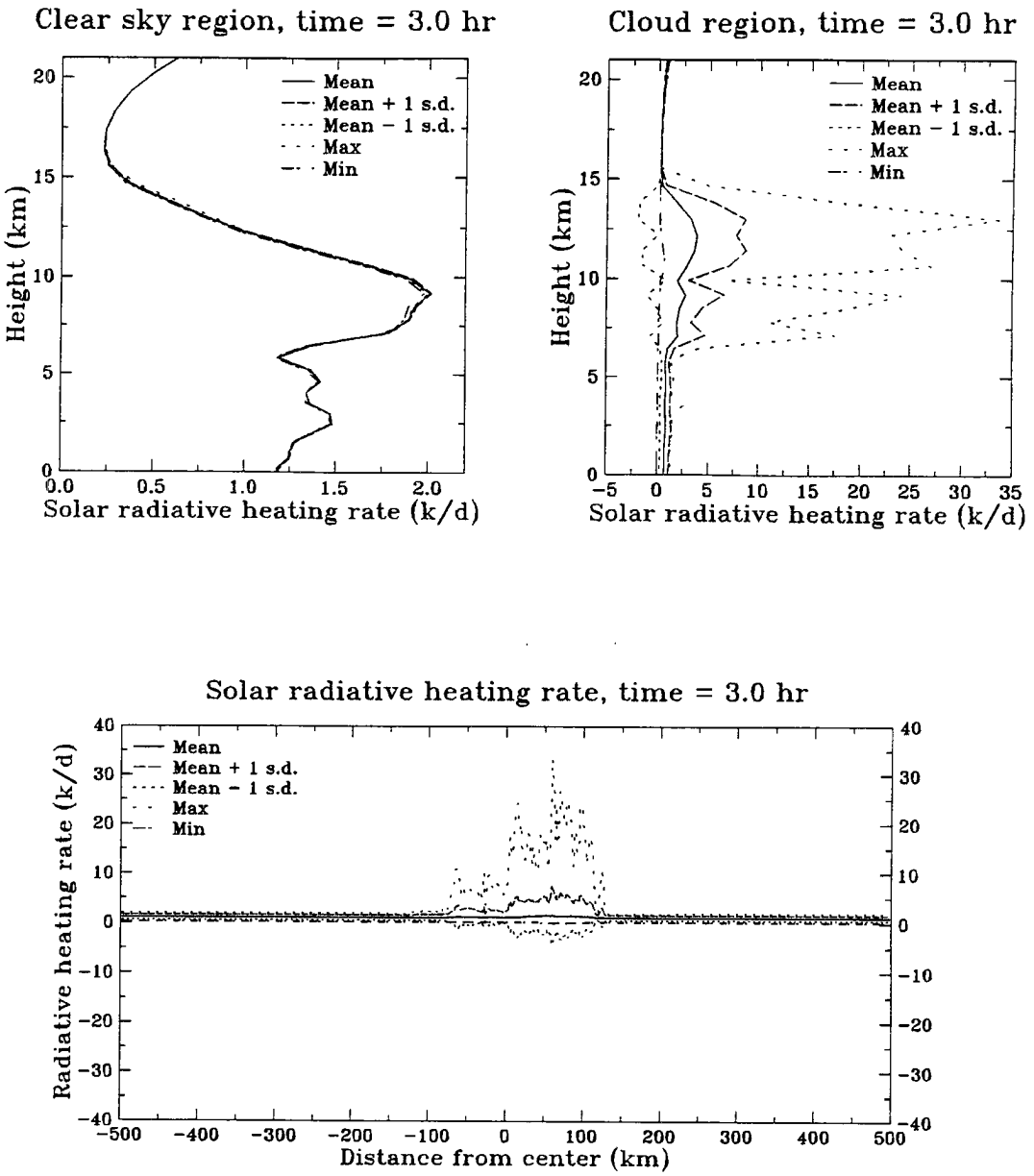

Figure 6.5: The vertical variability profile of shortwave heating rate for (a) the clear sky region, (b) the cloud region, and (c) the horizontal variability of shortwave heating field at 3 hours into the EMEX simulation (solid: mean, dashed: mean plus one standard deviation, short dotted: mean minus one standard deviation, long dotted: maximum, dash-dotted: minimum).

stratiform cloud regions, larger amount of solar radiation is transmitted through the optically thin anvil regions. Figure 6.6 also indicates that the shortwave absorption in the atmosphere is only slightly increased (up to 5% or less) by the presence of the tropical cloud cluster against the background clear sky value (about 15%) at this time (0816 LST). However, the presence of the MCS significantly alters the vertical disposition of this heating. The shortwave heating increases in the upper troposphere at cloud top but is reduced significantly below cloud base, especially at the surface. The upward reflected shortwave flux has a maximum above the convective and stratiform regions of the MCS. According to the figure the shortwave albedo, absorption, and transmission are approximately 70-75%, 25%, and 5-10%, respectively, for the convective region (highlighted as region A); 25-70%, 21%, and 9-54%, respectively, for the stratiform region (region B); and 9-25%, 19%, and 56-72%, respectively, for the thin anvil region (region C). The transmission values quoted for the stratiform region are similar to the average transmission value deduced from the P-3 aircraft measurements during the decaying stage of the EMEX-9 cloud cluster system. Even though we do not have specific observation of albedo for this case, the simulated albedo values in Fig. 6.6 agree well with the observed albedo values of the tropical convective ocean region deduced from the ERBE data (Ockert-Bell and Hartmann, 1992).

6.1.3 Total Radiative Budget

Figures 6.7 and 6.8 combine the results of the previous diagrams and present the 2-D vertical cross-sections of the total radiative heating rate (solar plus infrared) and its variabilities, respectively, for the EMEX-9 cloud cluster. These diagrams demonstrate the combined effects of the infrared and solar radiative transfer processes. The total radiative heating rates show a continuous cloud top cooling as well as cloud base heating at this time. While the total radiative cooling is confined only to an area near the cloud top region, the total radiative heating penetrates much deeper into the cloud cluster system. This is due to the fact that most of the IR cooling below the cloud top is canceled by the SW heating in the same area at this time. As the solar insolation increases with increasing solar elevation angle, this SW heating can further decrease the area of total

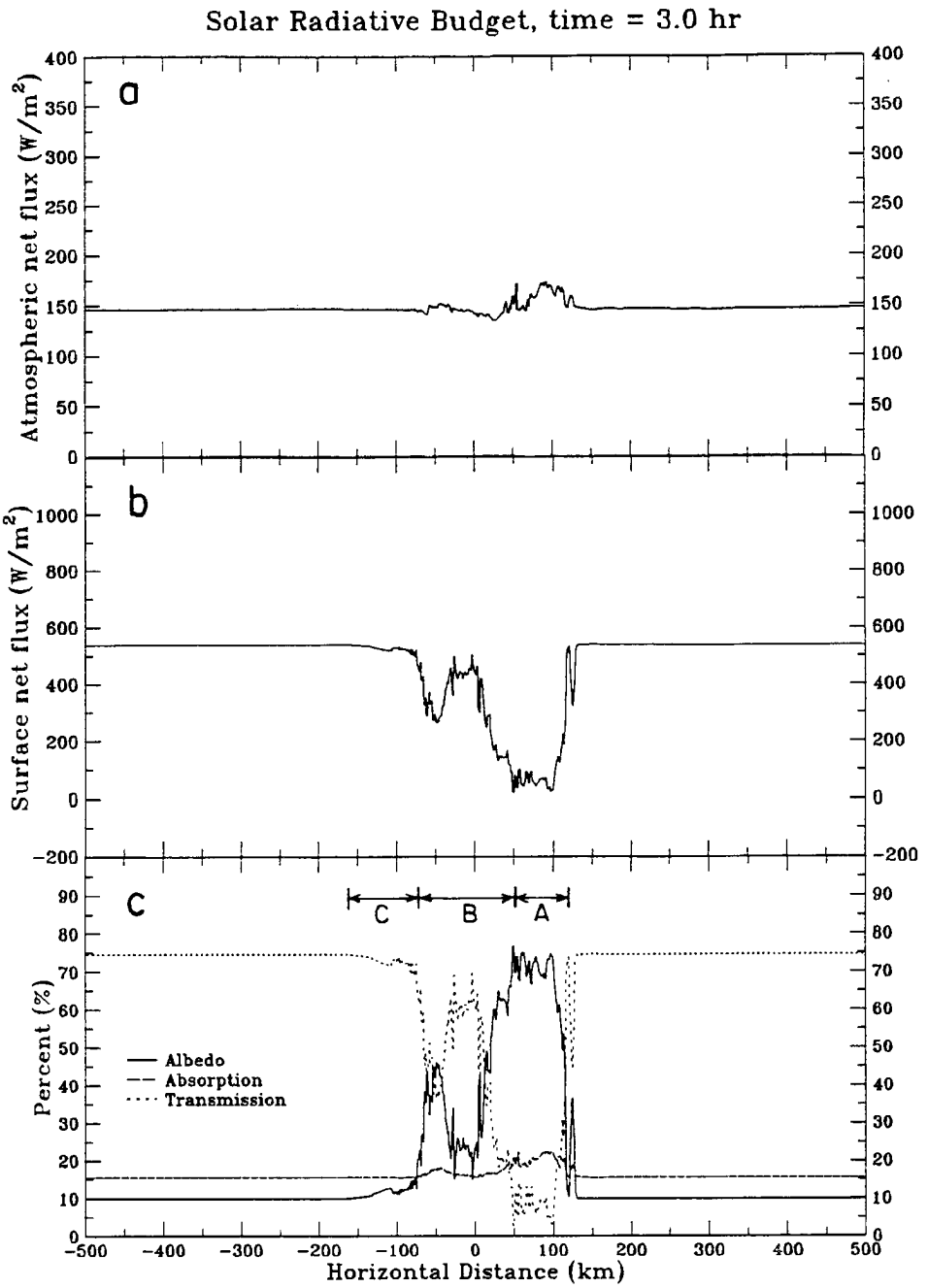

Figure 6.6: (a) The shortwave radiative budgets (W/m^2) as a function of the domain horizontal distance for (a) the atmosphere, (b) the surface, and (c) the earth-atmosphere system in term of shortwave transmission (%) to the surface (dotted), shortwave albedo (%) at top of the atmosphere (solid), and shortwave absorption (%) in the atmosphere (dashed) as a function of the domain horizontal distance, as diagnosed by the two-stream radiation model at 3 hours into the EMEX simulation. The convective, stratiform, and thin anvil regions are highlighted in A, B, and C, respectively, in (c).

cloud top cooling as shown by the analyses in the later section. In the thinner anvil region, both SW and IR heating add to create an area of positive total radiative heating. The maximum values of total radiative heating and cooling in Fig. 6.8 are 39.9 K/day and 15.4 K/day, respectively. The maximum heating in this case is almost twice as large as the maximum cooling due to canceling effects by SW and IR processes. While the mean value of the total radiative heating profile in the clear sky region (Fig. 6.8a) shows a cooling below the 15 km level, the mean value of total radiative heating rates in the cloud region (Fig. 6.8b), on the other hand, gives a net heating below cloud top (approximately 15 km level) and a net cooling near cloud top. Significant vertical and horizontal inhomogeneity (demonstrated in Fig. 6.8b and c, respectively) in the total radiative heating rates are also found, which are similar to the the results found in the infrared and the solar heating fields.

The total radiative heating fields at the third hour (i.e., 1830 LST) into the DUNDEE cloud cluster (shown in Fig. 6.9) diverge significantly from those presented in the EMEX case (i.e., Fig. 6.7) due to the lack of solar radiation at this time. In the absence of solar heating, the DUNDEE cloud system shows a strong total radiative cooling extending well into the upper portions of the anvil and a strong total radiative heating inside and near the cloud base area in the convective and stratiform region, and at the base of the thin anvil cloud. This total radiative heating/cooling profile is due entirely to infrared radiative processes and its structure is similar to those shown in Fig. 6.1. The maximum values of the total radiative heating and cooling rates for the DUNDEE case at this time are 35 K/day and 28 K/day, respectively.

The horizontal distribution of total (solar plus infrared) net flux convergence into the atmosphere and the total net flux at the surface (given in Fig. 6.10) for the EMEX-9 cloud cluster show that the MCS can significantly modify the total radiative budget of the atmosphere. Relative to the clear sky condition, the net radiative effects of this MCS at 0818 LST are the reduction of the total radiative energy at the surface (as large as 500 W/m^2) and the decrease of radiative energy loss in the atmosphere (as large as 200 W/m^2). The clear sky values can be identified by the values defined at the edge of the model

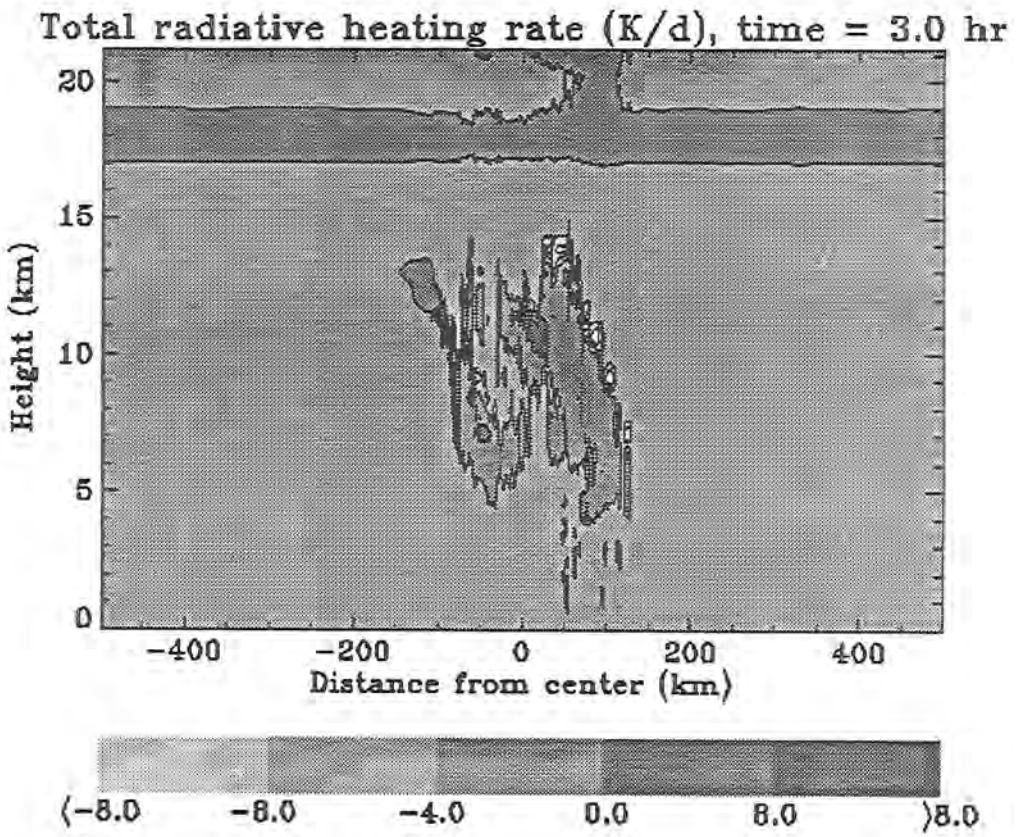

Figure 6.7: Two-dimensional (X-Z) cross-section of total (infrared plus solar) radiative heating field (K/day) as diagnosed by the two-stream radiation model at 3 hours into the EMEX simulation.

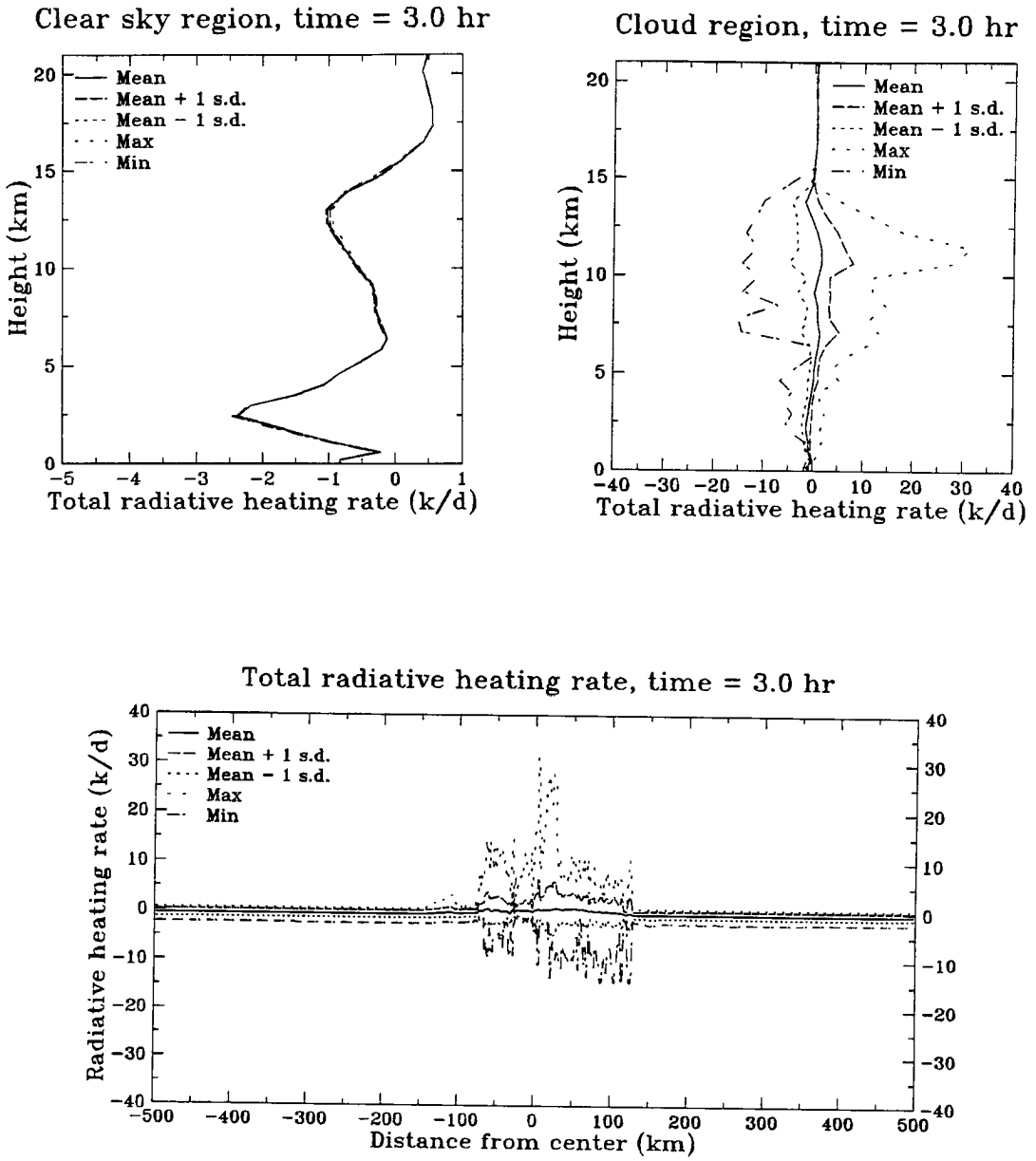

Figure 6.8: The vertical variability of total (infrared plus solar) heating rate for (a) the clear sky region, (b) the cloud region, and (c) the horizontal variability of total heating field at 3 hours into the EMEX simulation (solid: mean, dashed: mean plus one standard deviation, short dotted: mean minus one standard deviation, long dotted: maximum, dash-dotted: minimum).

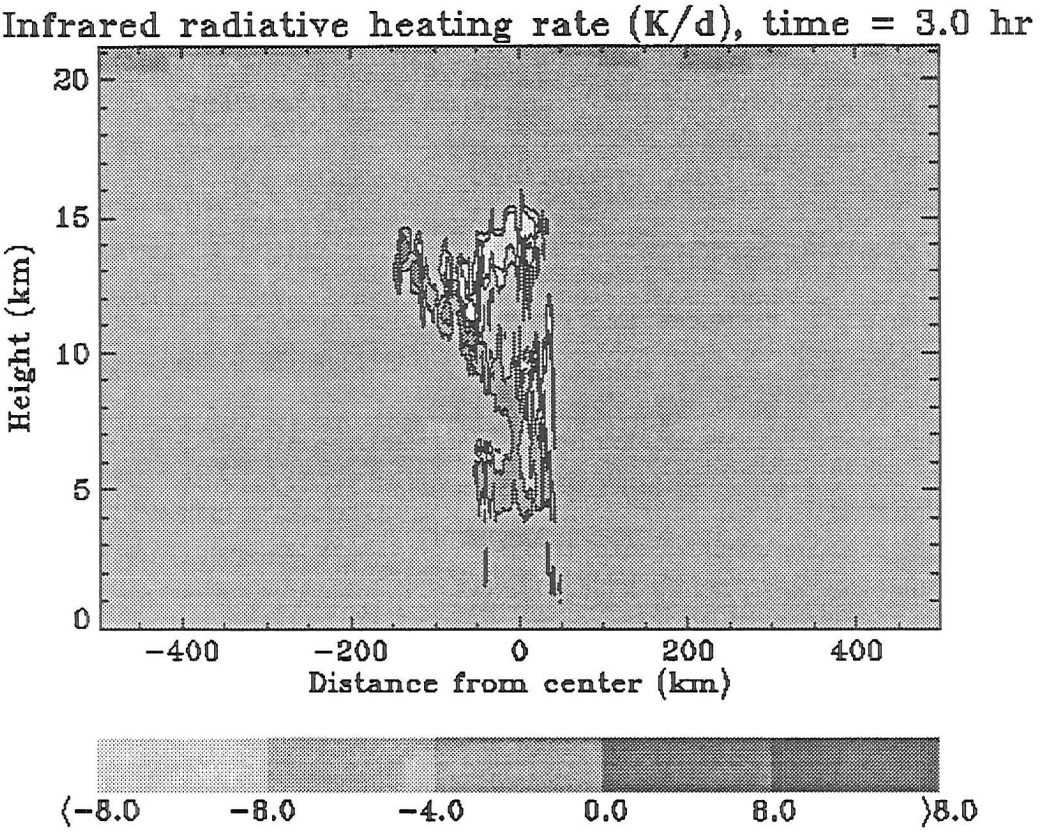

Figure 6.9: Two-dimensional (X-Z) cross-section of total (infrared plus solar) radiative heating field (K/day) as diagnosed by the two-stream radiation model at 3 hours into the DUNDEE simulation.

domain. The reduction in the total surface net flux is caused by the decrease in shortwave transmission in the present of the MCS and it is the largest at the convection region. The influence of cloud on the longwave fluxes largely occurs in the atmosphere in the form of a significant reduction in the column net flux divergence. This infrared effect occurs throughout the entire cloud region. Although the shortwave effects do not significantly contribute to the clear sky and cloudy sky total net flux convergence differences, it does serve to raise the background energy level of the atmosphere by canceling some of the longwave energy losses throughout the entire model atmosphere. This can be seen when Figs. 6.3a, 6.6a, and 6.10a are compared. The total net loss of atmospheric radiative energy can be further reduced by these solar effects as the solar insolation increases. We will show in the later section that the combination of increases in the shortwave insolation and the infrared greenhouse effects of the MCS can work constructively to create an area of total radiative energy surplus (i.e., positive value of total net atmospheric radiative flux) in the cloud region. Depending on the thermodynamics and dynamics of the background environment, this radiative heat source can be important in the subsequent evolution of the tropical MCSs as shown in the next chapter.

Similar to the total heating profile, the total radiative budgets for the DUNDEE simulation (shown in Fig. 6.11) at this time (i.e., 1830 LST) also significantly different from those found for the EMEX case (i.e., Fig. 6.10) due to lack of solar radiation. In the absence of solar heating, the DUNDEE atmosphere looses total radiative energy to space in both the clear sky and the cloudy region. Thus the atmospheric total radiative energy budget remains negative throughout the model domain. These atmospheric total radiative energy losses, however, are significantly reduced inside the cloud clusters. Furthermore, the surface radiative energy budget for the DUNDEE case increases, instead of decreases, in the presence of the MCS due to absence of the solar radiation. This suggests that the DUNDEE cloud cluster acts to enhance the radiative input into both the surface and the atmosphere. These relative in-cloud radiative heat sources can also be important in the subsequent evolution of the tropical MCSs as shown in the next chapter.

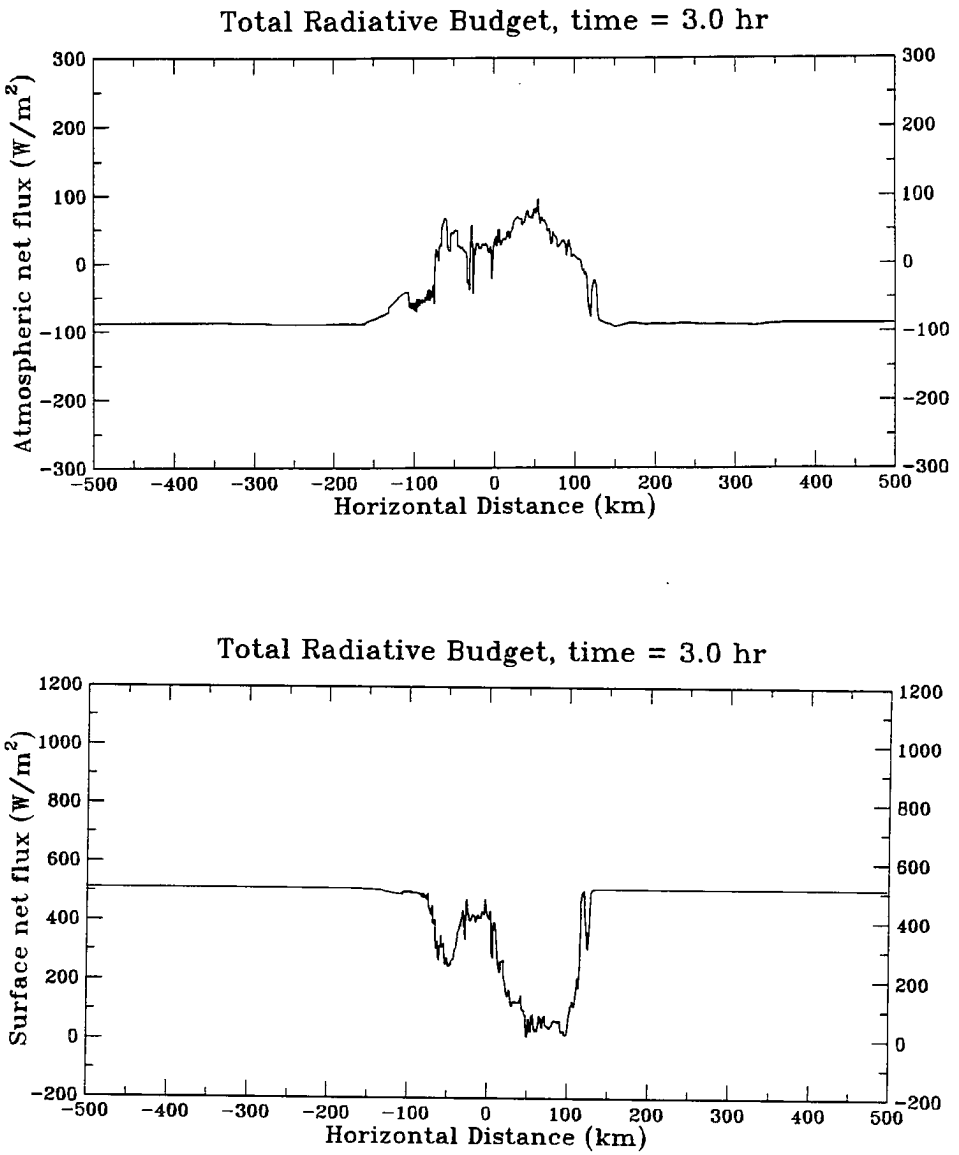

Figure 6.10: Total (infrared plus solar) radiative budgets (W/m^2) as a function of the domain horizontal distance for (a) the atmosphere and (b) the surface as diagnosed by the two-stream radiation model at 3 hours into the EMEX simulation.

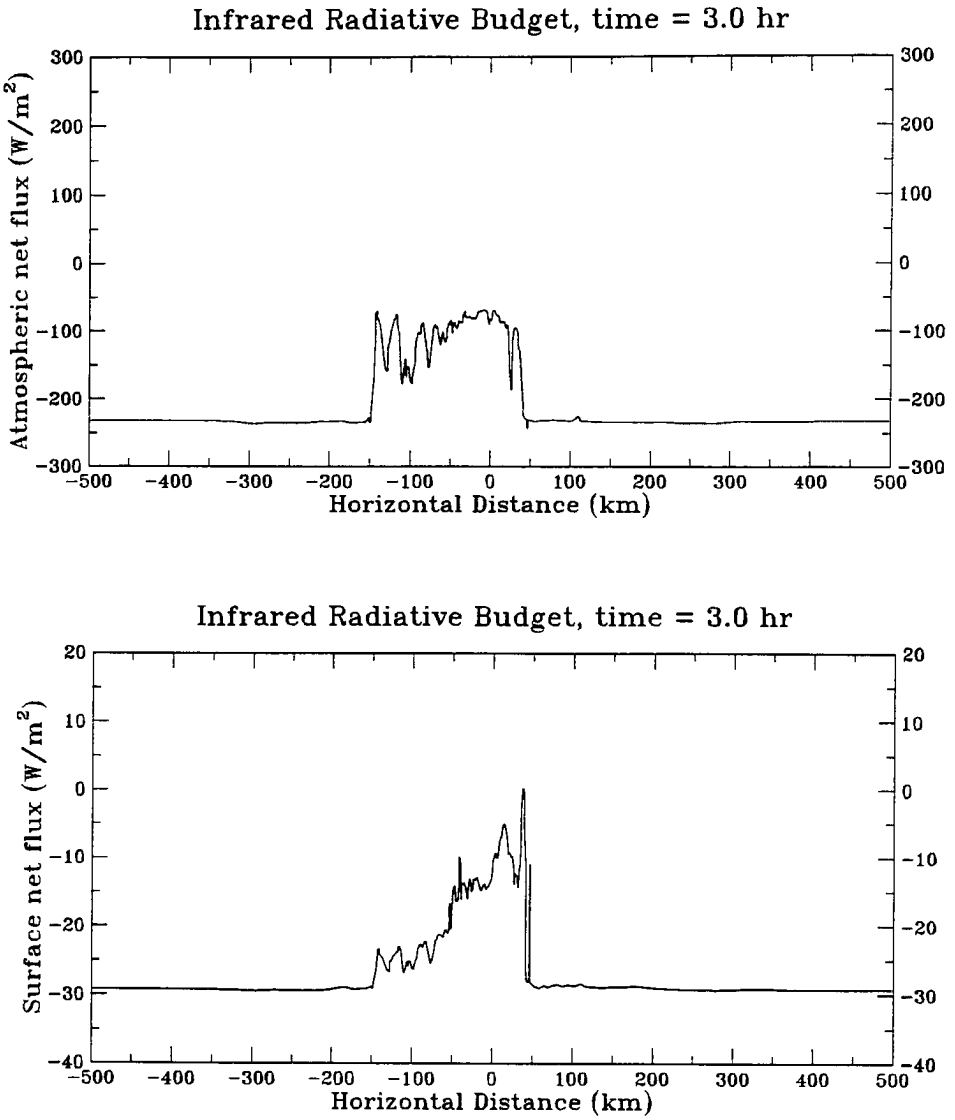

Figure 6.11: Total (infrared plus solar) radiative budgets (W/m^2) as a function of the domain horizontal distance for (a) the atmosphere and (b) the surface as diagnosed by the two-stream radiation model at 3 hours into the DUNDEE simulation.

6.2 Temporal Evolution of the Cloud Radiation Budget

The temporal evolution of the cloud radiative budget and radiative heating fields calculated using the 2-stream radiation model for both the EMEX and the DUNDEE system are presented in this section in a form similar to the previous sections (i.e., X-Z cross-section of the radiative heating, the surface energy budget, and the atmospheric energy budget). Vertical profiles of the mean radiative heating/cooling rates in the clear sky and the cloudy region, as well as the time series of the domain-average, column-integrated radiative heating are then discussed to address the temporal radiative effects of the cloud cluster on the radiative budget of the tropical atmosphere.

6.2.1 Radiative Heating and Radiative Budgets

The time series of X-Z cross-sections of the infrared radiative heating/cooling fields for the life cycle of the simulated EMEX-9 MCS (given Fig. 6.12) shows a continuous cloud top cooling and cloud base heating throughout the entire life cycle of the MCS. While the magnitude of this cloud top IR cooling and cloud base IR heating does not change significantly over the life cycle of the cloud system, the area influenced by this infrared radiative heating/cooling increases as the MCS expands with time. A closer examination on the time series of the horizontal profiles of infrared atmospheric (shown in Fig. 6.13) and surface (given in Fig. 6.14) energy budgets show similar cloud effects. While the increases of surface IR net flux (relative to the clear sky value) and the decrease in the net IR flux loss in the atmosphere (relatively to the clear sky value) in the cloud region remain on the order of 10 to 25 W/m^2 and 150 to 200 W/m^2, respectively, throughout the life cycle of the MCS, the area coverage of these infrared effects increases with time as the cloud cluster enlarges in size. This suggests a significant modulation of the domain-integrated IR surface and atmospheric energy budgets by the cloud cluster throughout the life cycle of these tropical MCSs. Similar results are also found in the modeled infrared radiation fields of the DUNDEE cloud cluster.

The time series of the X-Z cross-section of the solar radiative heating fields for the EMEX-9 cloud cluster (given in Fig. 6.15) reveals similar patterns as those found in

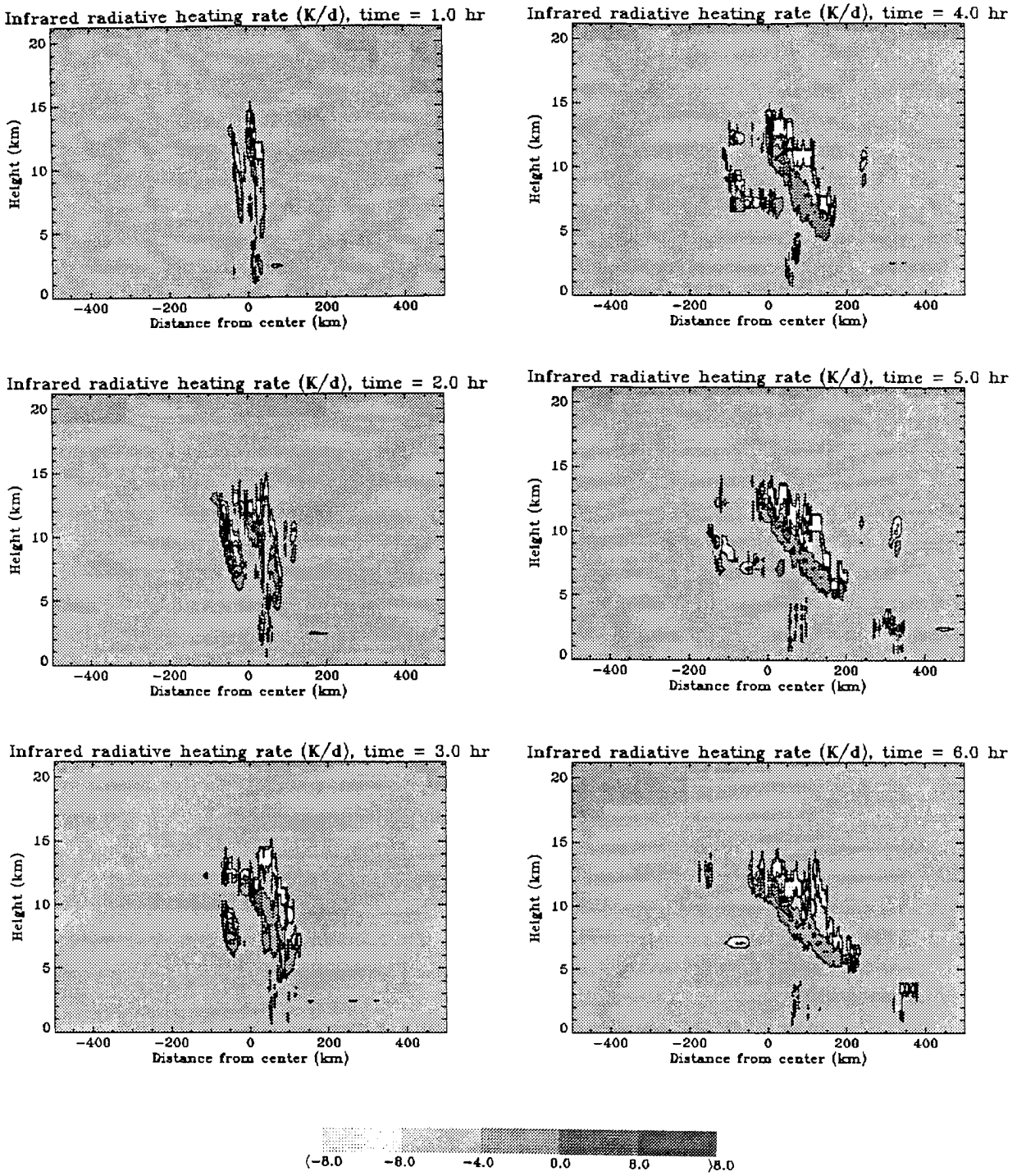

Figure 6.12: Two-dimensional (X-Z) cross-section of infrared radiative heating field (K/day) at (a) 1 hour, (b) 2 hours, (c) 3 hours, (d) 4 hours, (e) 5 hours, and (f) 6 hours into the EMEX cloud simulation as diagnosed by the two-stream radiation model .

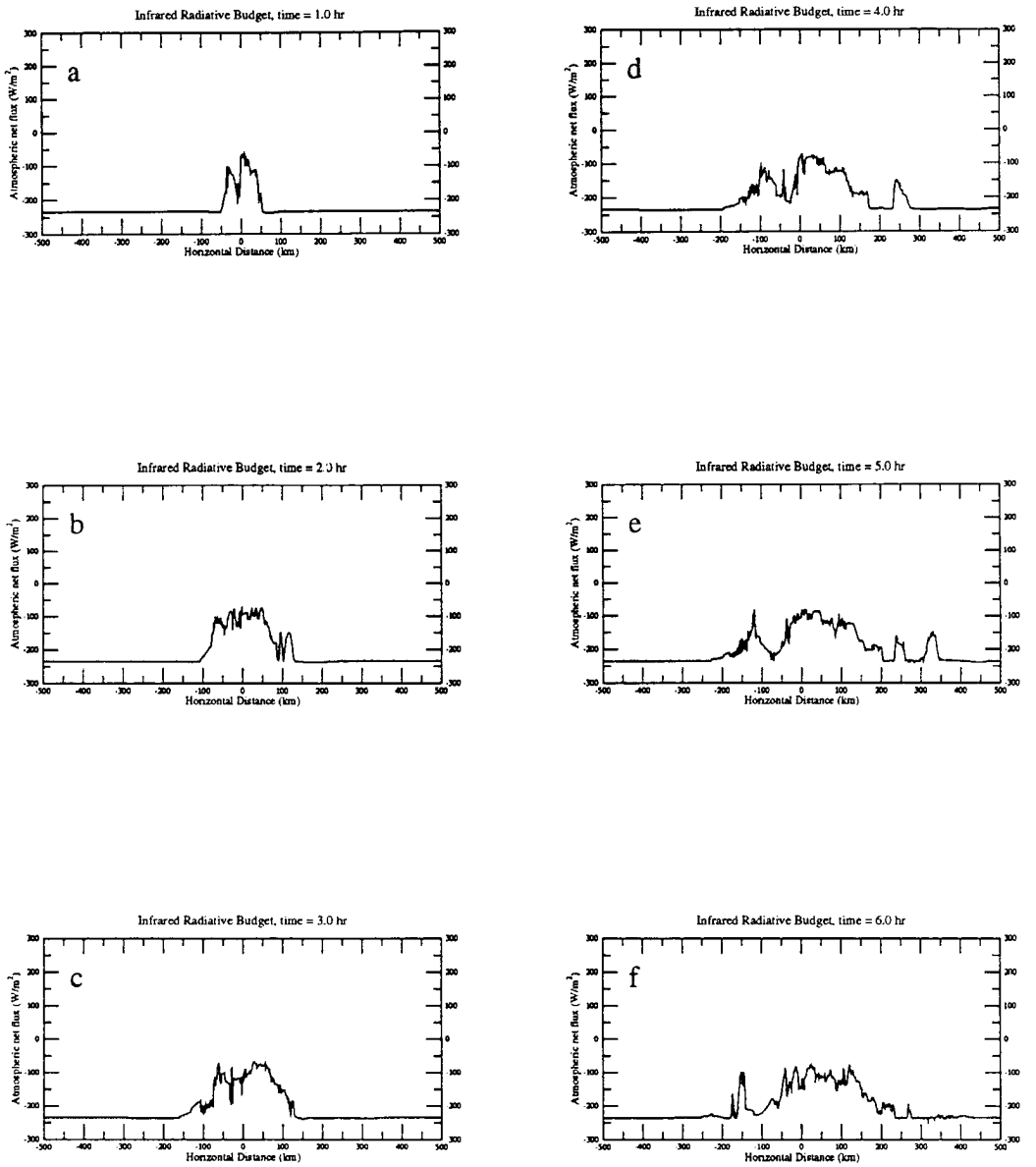

Figure 6.13: Atmospheric infrared radiative budgets (W/m^2) as a function of the domain horizontal distance as diagnosed by the two-stream radiation model at (a) 1 hour, (b) 2 hours, (c) 3 hours, (d) 4 hours, (e) 5 hours, and (f) 6 hours into the EMEX cloud simulation.

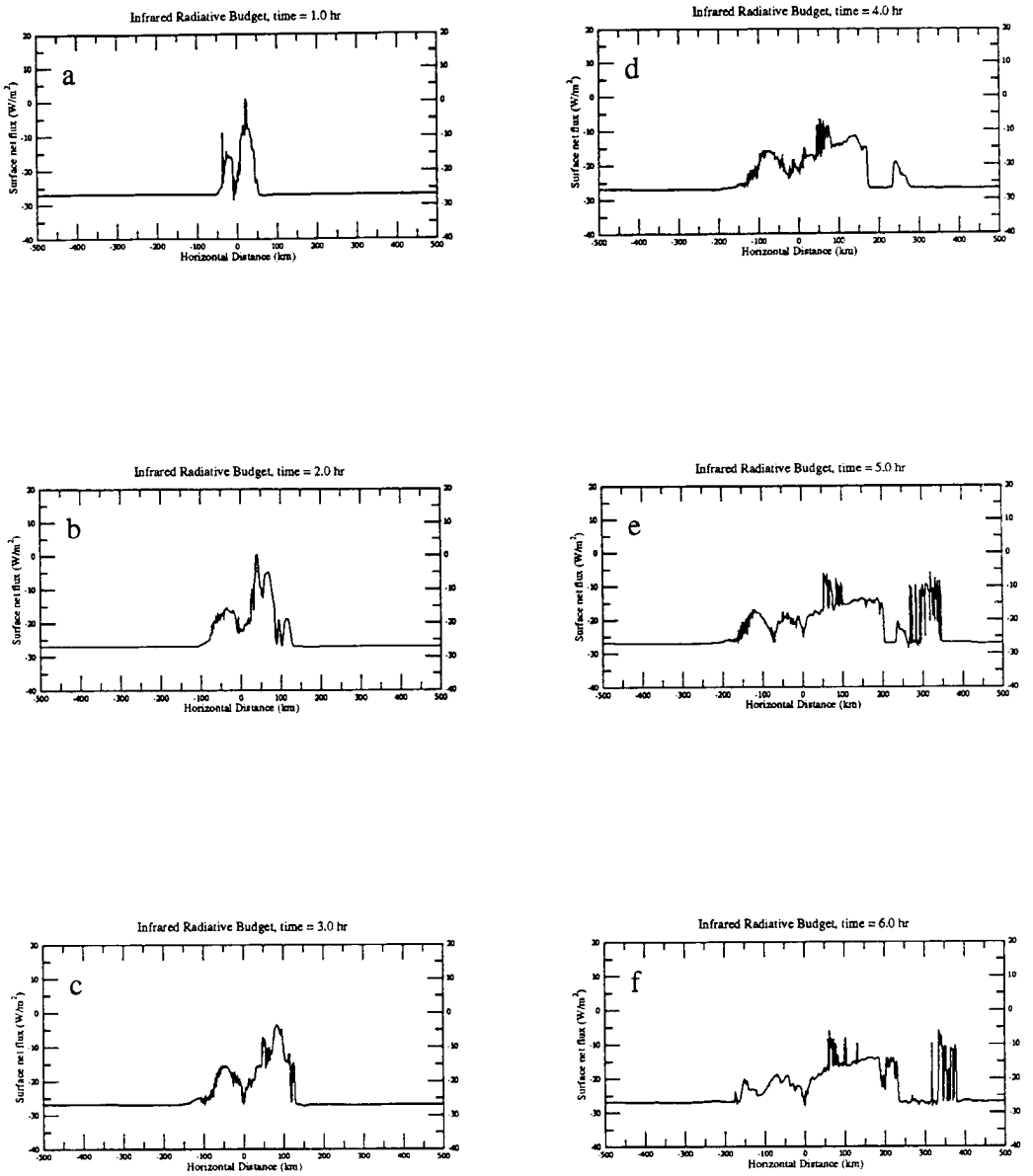

Figure 6.14: Surface infrared radiative budgets (W/m^2) as a function of the domain horizontal distance as diagnosed by the two-stream radiation model at (a) 1 hour, (b) 2 hours, (c) 3 hours, (d) 4 hours, (e) 5 hours, and (f) 6 hours into the EMEX cloud simulation.

the infrared results. Specifically, the areal influences of the the solar heating increases as the MCS enlarges in size. The corresponding shortwave energy budget distribution for the atmosphere (shown in Fig. 6.16) and the surface (given in Fig. 6.17) shows that the temporal effect of the cloud cluster is to continuously decrease the SW energy transmitted onto the surface (instantaneous values are as large as 1000 W/m^2) and to increase both SW the energy storage in the atmosphere (instantaneous values are as large as 200 W/m^2) and the SW energy reflected back to space (not shown). The magnitude of these changes is a function of solar insolation with the largest modification occurring at local noon when the insolation is the largest. This effect, however, is not readily apparent in Fig. 6.15. Further examination of the numerical values which produce Fig. 6.15 do suggest that a gradual increase of solar heating rate occurs in both the clear sky and the cloudy region as solar elevation angle increases with time. Since the areal influence of these solar effects also increases as the cloud expands in size, the domain-integrated solar atmospheric/surface energy budget also increases/decreases over the life cycle of this tropical MCS. Furthermore, the solar insolation also affects the background energy storage of the clear atmosphere by increasing its value to about 225 W/m^2 at 1116 LST.

Unlike the EMEX case, the DUNDEE cloud cluster results in decreased solar insolation as the system matures. Specifically, the effects of solar radiation (not shown) are not important to the total radiative budget/heating of this system after the first two hours of the simulation. During the first two hours, the results of solar calculations are similar to those of the EMEX case. For example, significant solar heating occurs near the cloud top region of the MCS and strong solar effects are also seen in the atmospheric and surface energy budgets. These effects, however, decrease quickly as sunset (i.e., 1800 LST) approaches.

The time series of the X-Z cross-section of the total (infrared plus solar) radiative heating fields for the EMEX-9 cloud cluster (given in Fig. 6.18) shows a strong cloud top cooling and cloud base heating during the early hours of the cloud system. These cloud top cooling patterns, however, are slowly replaced by radiative heating as the in-cloud solar absorption becomes stronger in time due to stronger solar insolation. At the

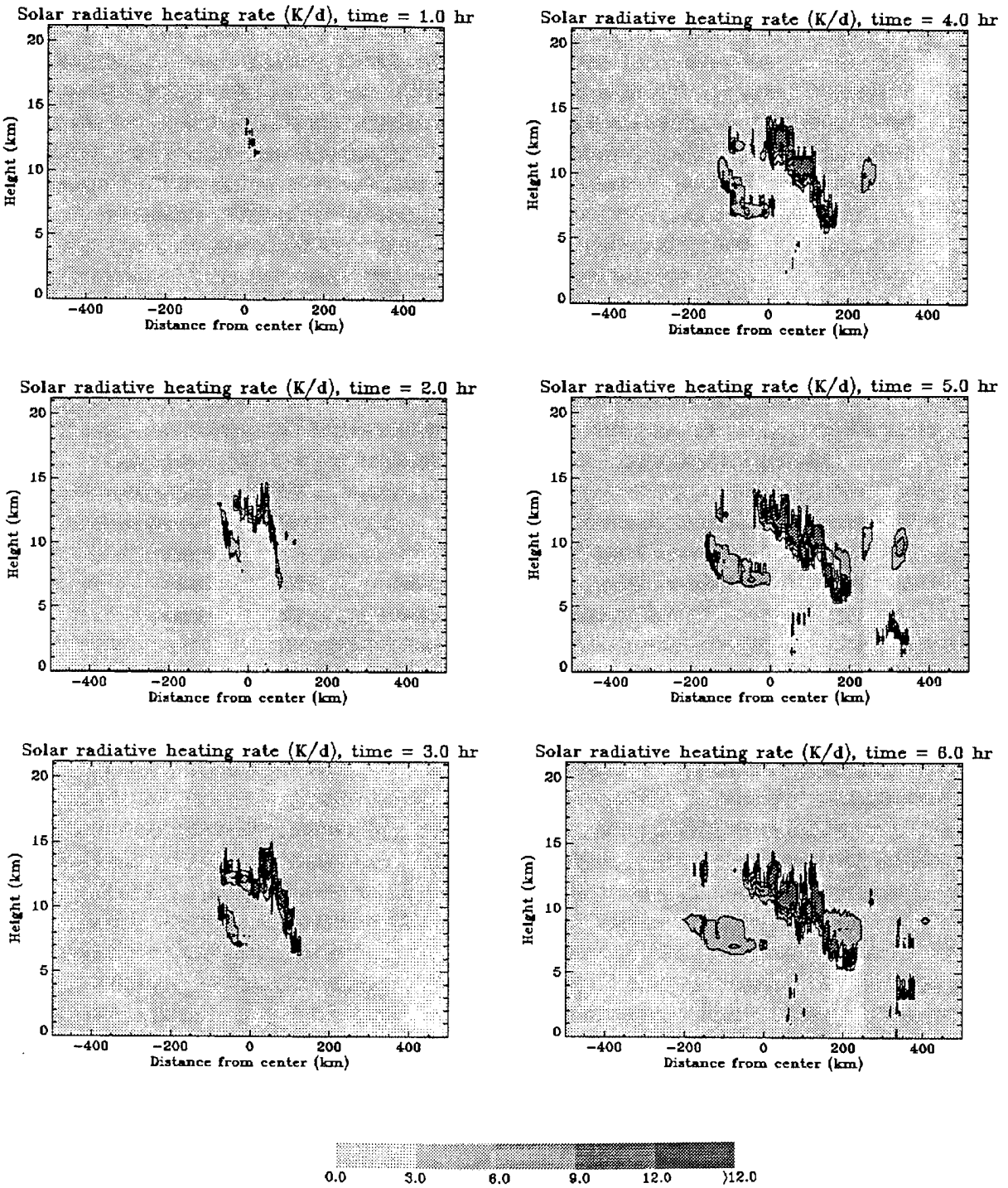

Figure 6.15: Two-dimensional (X-Z) cross-section of shortwave radiative heating field (K/day) at (a) 1 hour, (b) 2 hours, (c) 3 hours, (d) 4 hours, (e) 5 hours, and (f) 6 hours into the EMEX cloud simulation as diagnosed by the two-stream radiation model.

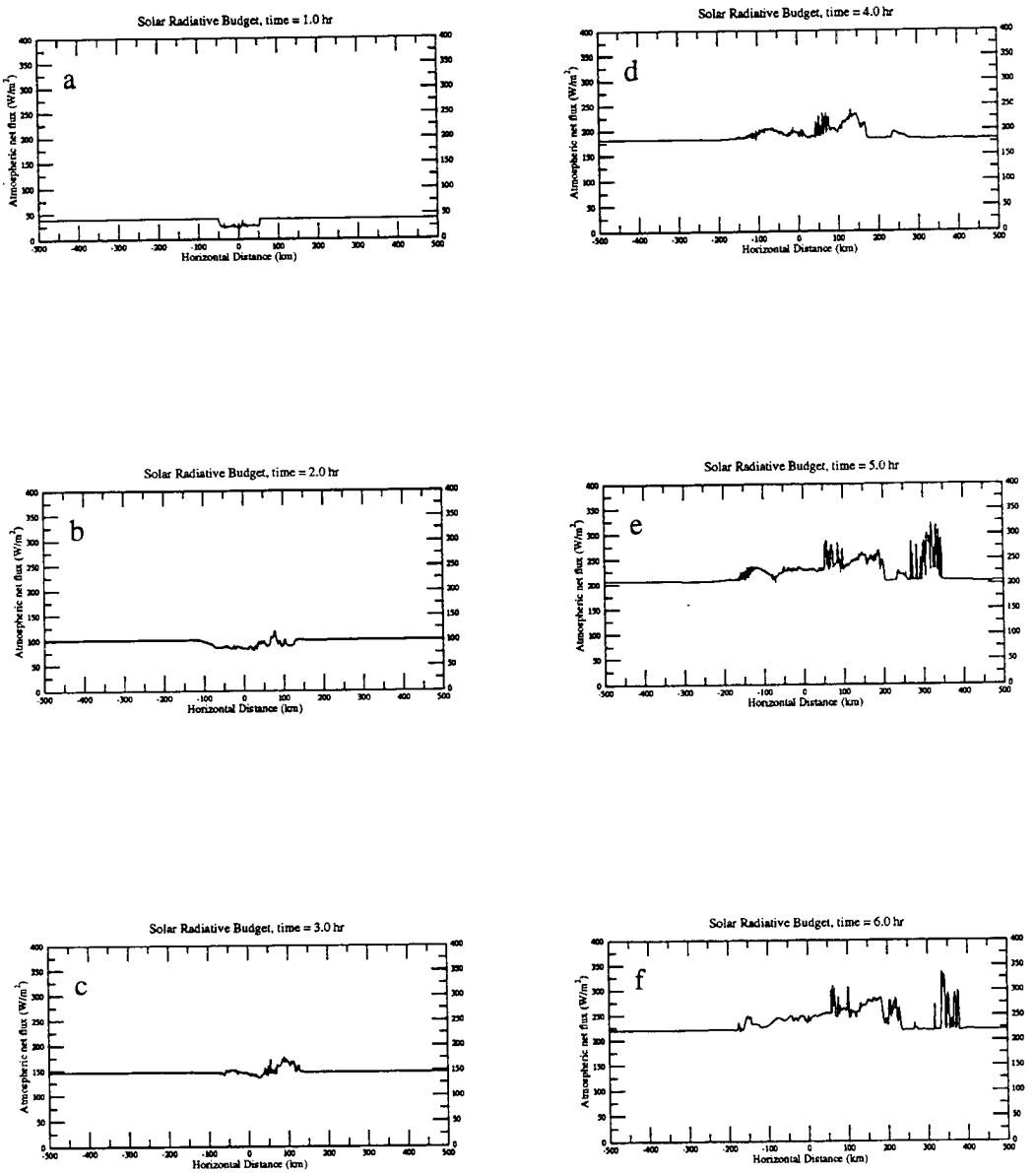

Figure 6.16: Atmospheric solar radiative budgets (W/m^2) as a function of the domain horizontal distance as diagnosed by the two-stream radiation model at (a) 1 hour, (b) 2 hours, (c) 3 hours, (d) 4 hours, (e) 5 hours, and (f) 6 hours into the EMEX cloud simulation.

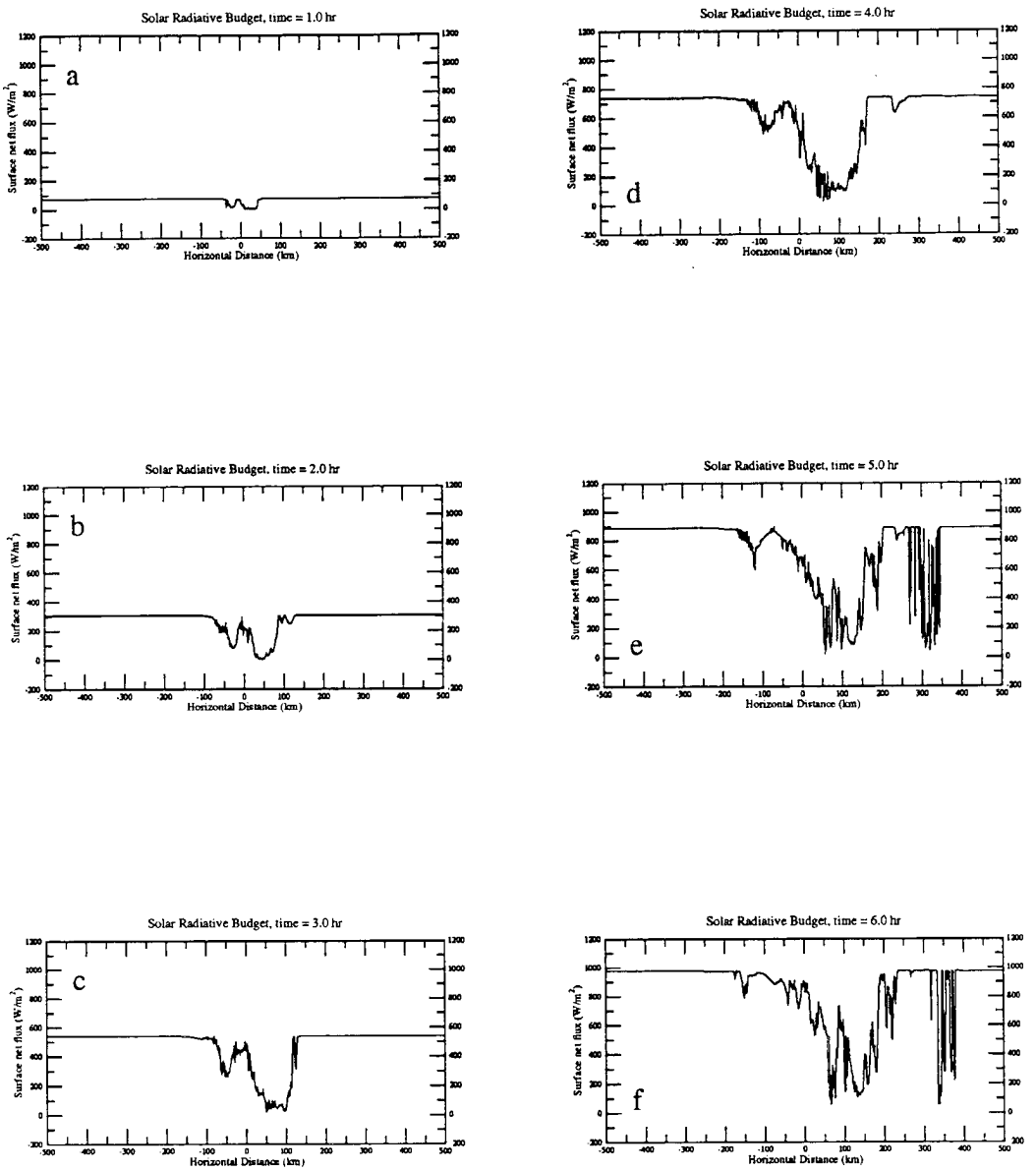

Figure 6.17: Surface solar radiative budgets (W/m^2) as a function of the domain horizontal distance as diagnosed by the two-stream radiation model at (a) 1 hour, (b) 2 hours, (c) 3 hours, (d) 4 hours, (e) 5 hours, and (f) 6 hours into the EMEX cloud simulation.

sixth hour into the simulation, the cloud top radiative cooling only occurs in a very small region near the cloud top while the rest of the cloud cluster exhibits a stronger radiative heating. The corresponding total atmospheric (shown in Fig. 6.19) and surface (given in Fig. 6.20) energy budget for the cloud cluster show the compensating effects of the IR and solar radiative processes. Relative to the clear sky, these figures suggest the continuous influences of the EMEX-9 MCS on the surface radiative energy budget. Specifically, these effects increase with time as solar insolation increases. For example, the reduction of the net surface flux is only 50 W/m^2 during 0618 LST as compared to 950 W/m^2 at 1118 LST. This large reduction in net surface flux values near noon time suggests that the EMEX-9 MCS is an effective sink to the total surface radiative energy budget. The MCS also has a large influence on the atmospheric energy budget. Specifically, Fig. 6.19 shows that the EMEX-9 MCS is an effective IR heat source for the atmosphere by reducing the loss of infrared radiation to space by the clear sky. Furthermore, this figure also suggests that shortwave radiation can be important in raising the total background radiative energy level of the free atmosphere. Figure 6.19 shows that a combination of the larger solar insolation and the infrared effects from the EMEX-9 cloud cluster can work to produce a large area of net radiative heating in the atmosphere, especially near local noon.

The evolution of the total radiative heating and radiative budget profile for the DUNDEE cloud cluster differs significantly with those of the EMEX case due to decreasing solar insolation with time in the DUNDEE case. The sequences of the X-Z cross-sections of the total (infrared plus solar) radiative heating fields for the DUNDEE cloud cluster are given in Fig. 6.21. In the first two hours of the simulation, the total heating shows a narrow region of cloud top cooling and strong heating inside the cloud. This is due to the strong solar effects near the cloud top which help to cancel most of the cloud top cooling at these times. As the solar effects diminish, the infrared processes begin to overtake the total radiative heating/cooling of this MCS. The total radiative heating fields after the second hour show continuous cloud top infrared cooling and cloud based infrared heating until the end of the simulation. The corresponding total atmospheric and surface energy budget are given in Fig. 6.22 and 6.23, respectively. Relative to the clear sky value, these

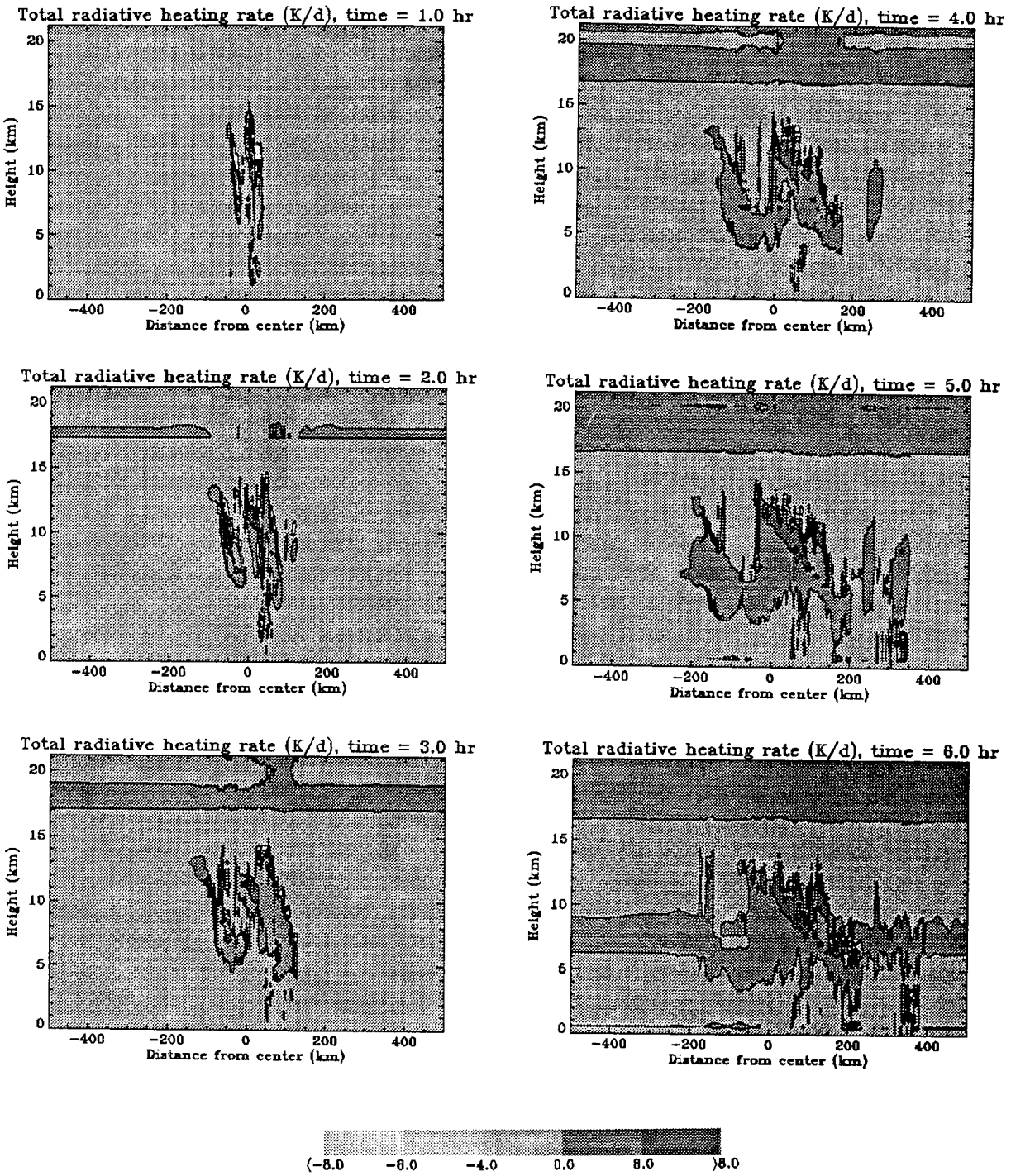

Figure 6.18: Two-dimensional (X-Z) cross-section of total (infrared plus solar) radiative heating field (K/day) at (a) 1 hour, (b) 2 hours, (c) 3 hours, (d) 4 hours, (e) 5 hours, and (f) 6 hours into the EMEX cloud simulation as diagnosed by the two-stream radiation model.

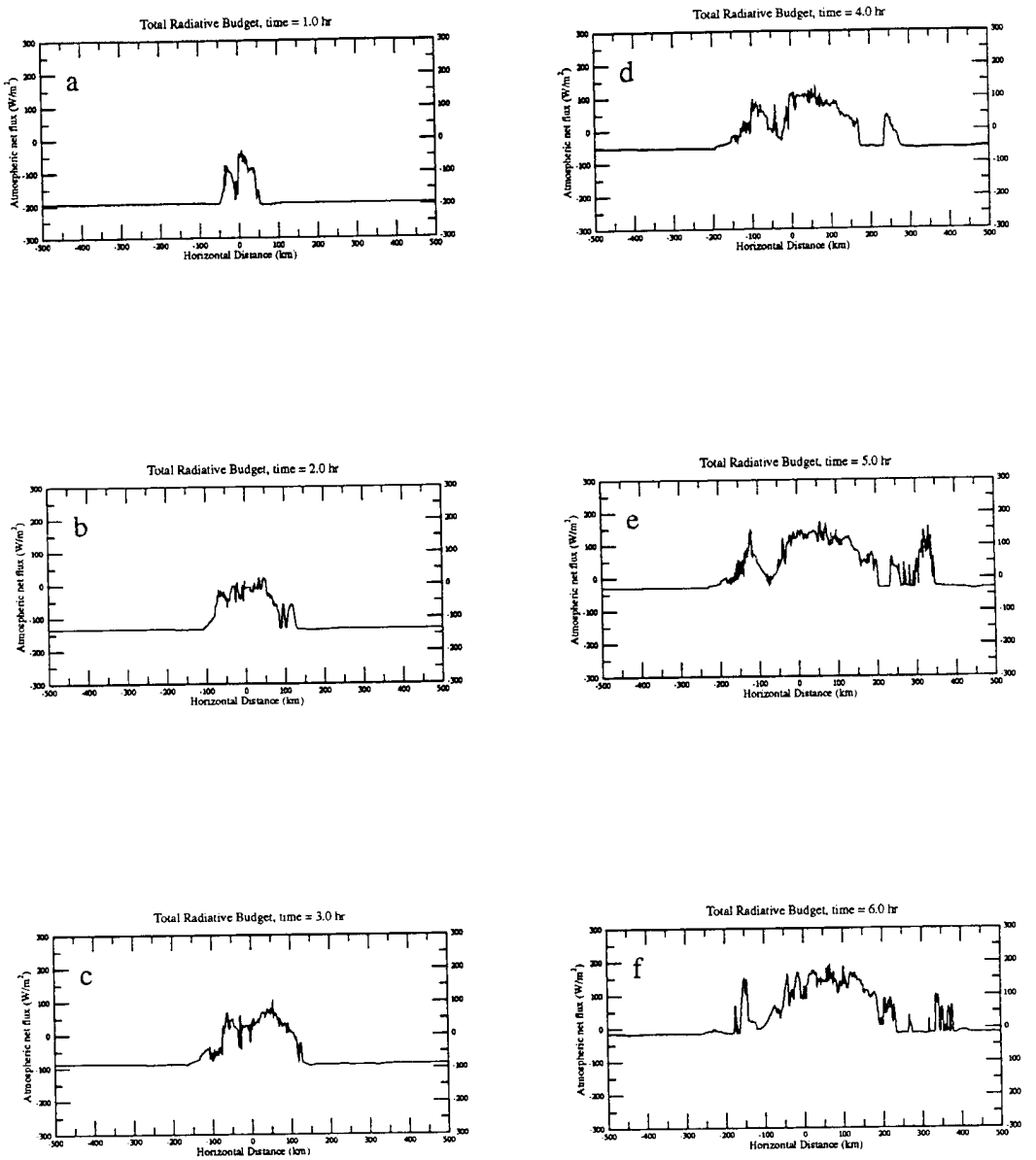

Figure 6.19: Atmospheric total (infrared plus solar) radiative budgets (W/m^2) as a function of the domain horizontal distance as diagnosed by the two-stream radiation model at (a) 1 hour, (b) 2 hours, (c) 3 hours, (d) 4 hours, (e) 5 hours, and (f) 6 hours into the EMEX cloud simulation.

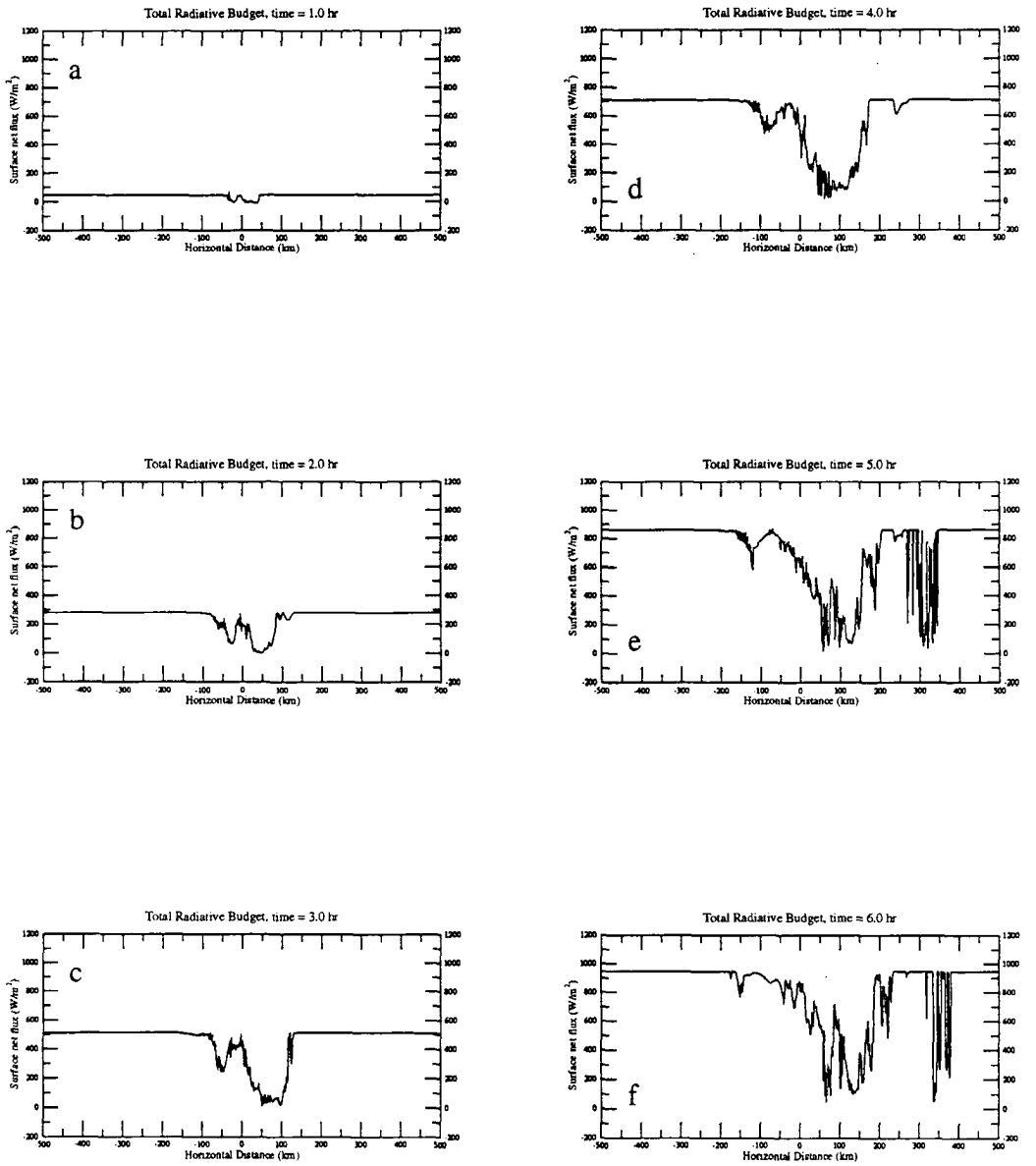

Figure 6.20: Surface total (infrared plus solar) radiative budgets (W/m^2) as a function of the domain horizontal distance as diagnosed by the two-stream radiation model at (a) 1 hour, (b) 2 hours, (c) 3 hours, (d) 4 hours, (e) 5 hours, and (f) 6 hours into the EMEX cloud simulation.

figures suggest the continuous influence of the DUNDEE MCS on both the surface and the atmospheric radiative energy budget. While the surface effects decrease significantly after the sunset (i.e., after the second hour), the atmospheric effects of the MCS remain constant (about 150 to 200 W/m^2) throughout the simulation, indicating the greenhouse infrared influence of these tropical MCSs. These figures also show that the background/clear sky value of both the atmospheric and surface radiative energy budget decreases systematically as sunset approaches and these values remain negative throughout the rest of the simulation. This is opposite to those of the EMEX case, which shows a systematic increase due to increasing solar insolation. These negative values also occur in the cloudy region as well. Their magnitudes, however, are significantly reduced. Comparison of this case with the EMEX-9 cloud cluster suggest that the atmosphere (clear sky and the cloudy region) is continuously cooled by radiation during the night time. The clear sky cools significantly more than the cloudy region. During the day time, the cloudy region, however, can experience significant radiative heating even though the clear sky continue to cool by radiation at the same time. These differences in radiative budget between the clear skies and the cloudy atmosphere can lead to strong clear-to-cloudy gradient in radiative heating as suggested by Gray and Jacobson (1977) and Cox and Griffith (1978).

6.2.2 Vertical Profile of Radiative Heating

To analyze the changes in the vertical profile of the radiative heating associated with the evolution of the EMEX-9 and DUNDEE cloud clusters, areal averages of the radiative heating fields for the background clear sky area, the disturbed cloudy region, and the differences between these two regions are calculated. The latter quantility represents the perturbations of radiative heating due to the presence of MCSs. These results are discussed below for the intensification stage (i.e., the first hour), the mature stage (i.e., the third hour), and the decaying stage (i.e., the sixth hour) of the simulation, respectively. Since there are significant variations in these heating rates (as shown in the previous sections), these composited profiles only serve as a first-order estimate of the effects of these cloud systems in the model atmosphere.

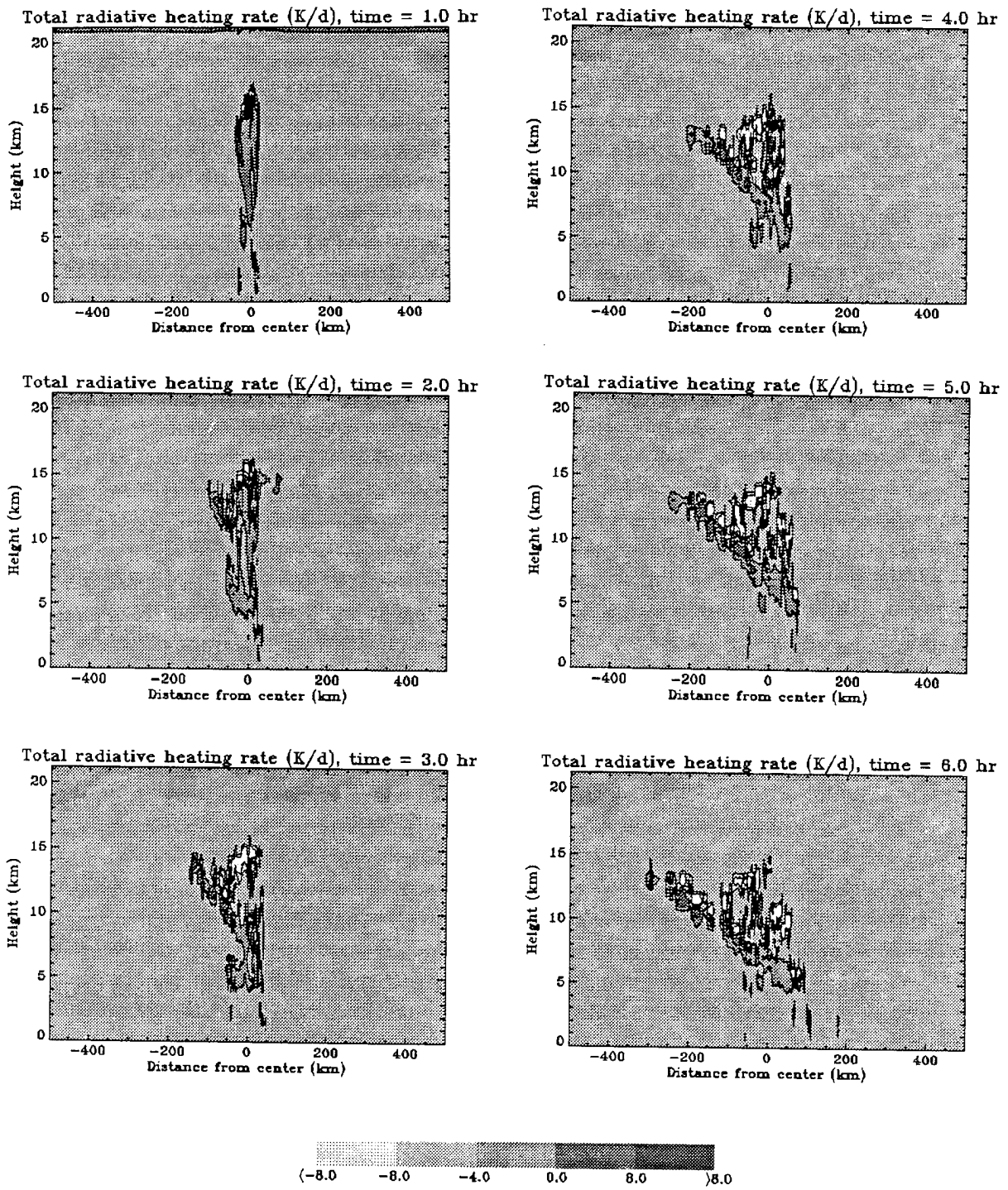

Figure 6.21: Two-dimensional (X-Z) cross-section of total (solar plus infrared) radiative heating field (K/day) at (a) 1 hour, (b) 2 hours, (c) 3 hours, (d) 4 hours, (e) 5 hours, and (f) 6 hours into the DUNDEE cloud simulation as diagnosed by the two-stream radiation model.

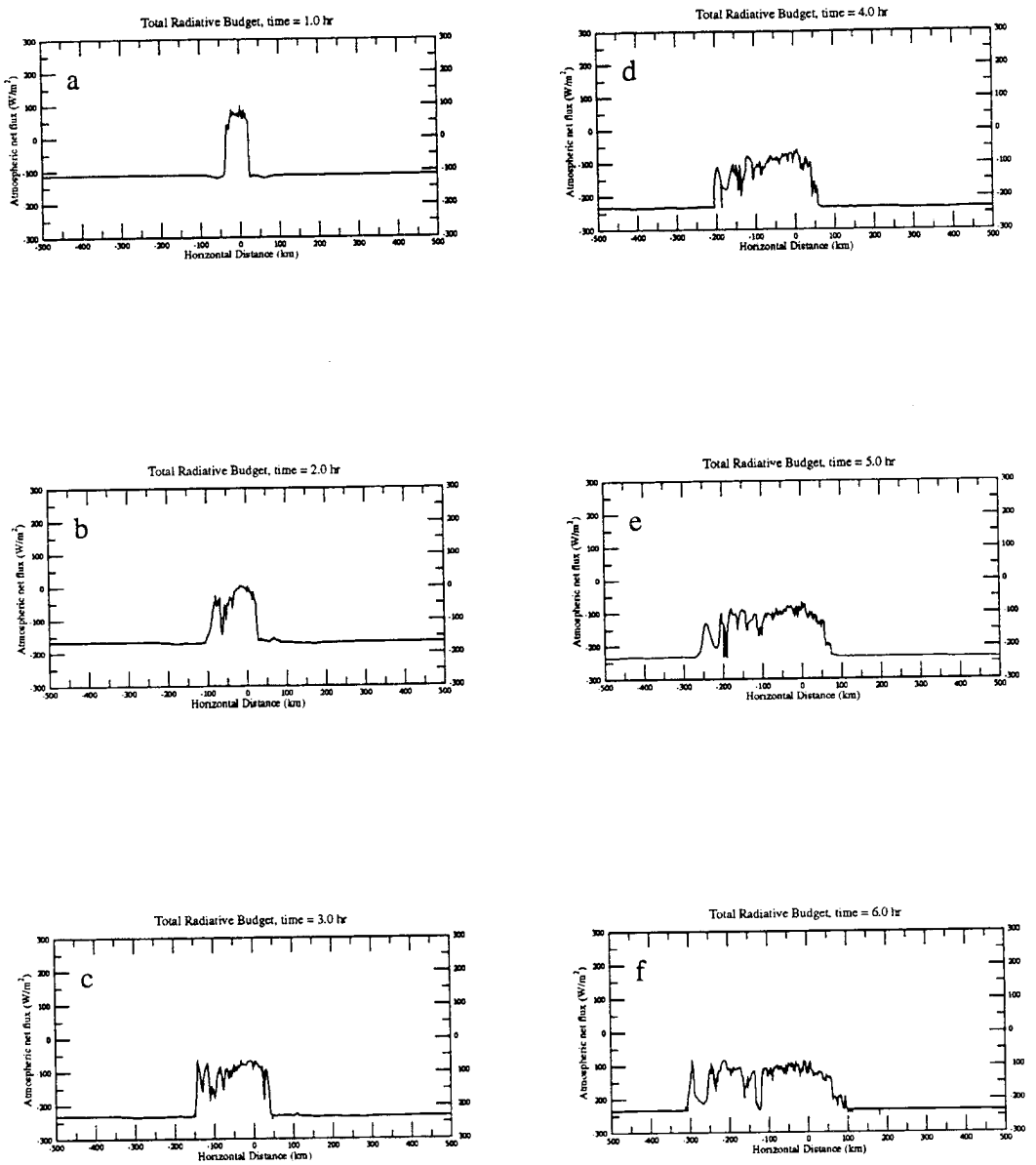

Figure 6.22: Atmospheric total (solar plus infrared) radiative budgets (W/m^2) as a function of the domain horizontal distance as diagnosed by the two-stream radiation model at (a) 1 hour, (b) 2 hours, (c) 3 hours, (d) 4 hours, (e) 5 hours, and (f) 6 hours into the DUNDEE cloud simulation.

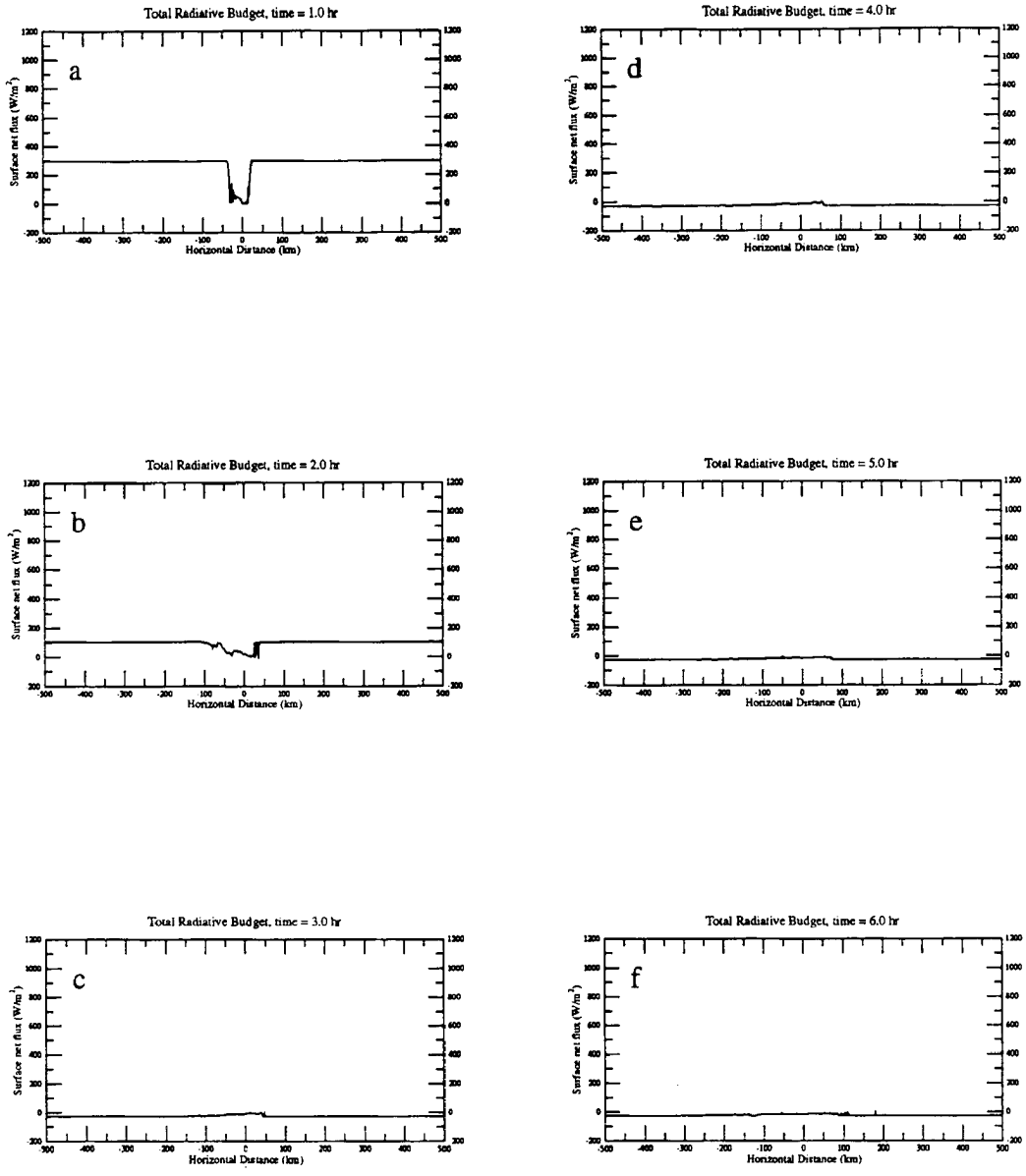

Figure 6.23: Surface total (solar plus infrared) radiative budgets (W/m^2) as a function of the domain horizontal distance as diagnosed by the two-stream radiation model at (a) 1 hour, (b) 2 hours, (c) 3 hours, (d) 4 hours, (e) 5 hours, and (f) 6 hours into the DUNDEE cloud simulation.

During the intensification stage (i.e., 0616 LST) of the EMEX-9 cloud cluster, the total (solar plus infrared) radiative heating profile in the clear sky region (shown in Fig. 6.24a) is predominantly one of cooling below 15 km and heating above this level due to the dominance of the infrared cooling over the clear sky solar heating in the troposphere at this early morning hour. The strong infrared cooling rate also appears in the total heating profile of the cloud region (given in Fig. 6.24b) except in the area near 7.5 km where infrared heating dominates. The mean solar heating in the cloud region is small at this time due to the low value of solar insolation. The solar heating, however, will increase significantly with time as shown in the later analyses. There is also a double peak in the cloud infrared cooling rate near the cloud top region at this time. The total perturbation radiation heating profile (given in Fig. 6.24c) shows that the effects of the EMEX-9 MCS at this time are to cool the upper levels of the troposphere and to heat the area in the middle and the lower levels. These effects are mostly due to infrared radiative processes since the solar effects are quite small at 0616 LST.

The corresponding radiative heating profile for the DUNDEE cloud cluster during its intensification stage (i.e., 1430 LST) is given in Fig. 6.25. The total (solar plus infrared) radiative heating profile in the clear sky region (shown in Fig. 6.25a) is similar to those of the EMEX case with cooling below 15 km and heating above this level. The total heating profile in the cloudy region (given in Fig. 6.25b), however, shows strong cooling only near the cloud top region. This is significantly different from those of the EMEX case and is due to the strong solar heating at this time which helps cancel some of the infrared effects near the cloud top. Maximum value of total heating is also found at about 12 km level due to both solar and infrared heating. A deep layer of heating is also found between 7.5 and 14 km. At the lower levels, radiative cooling dominates. The total perturbation radiation heating profile between the clear sky and the cloudy atmosphere (shown in Fig. 6.25c) indicates cooling near the cloud top and strong heating below. The maximum perturbation heating is about 8 K/day and is located at about 12.5 km. This strong heating is due to the combined effects of both solar and infrared processes as shown by the dashed and the dotted line in the figure.

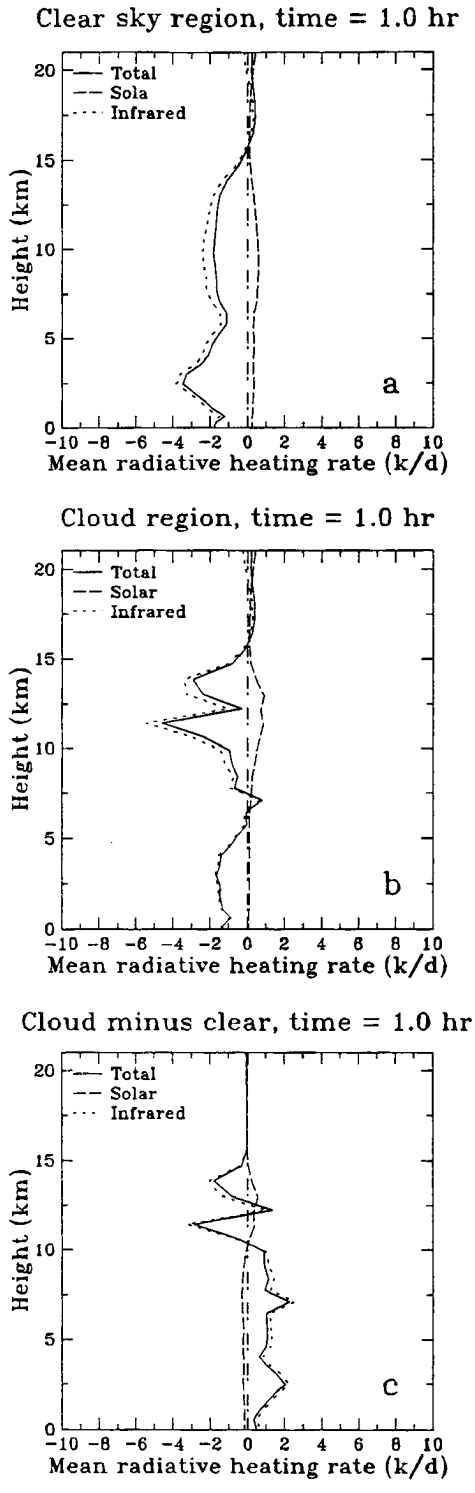

Figure 6.24: The vertical profile of spectral radiative heating (K/day), including solar (dashed), infrared (dotted), and total (solid) for (a) the clear sky condition, (b) the cloud cluster system and (c) the difference between (b) and (a) at 1 hour into the EMEX simulation. The zero line (dashed-dotted) is also drawn in the figure for reference.

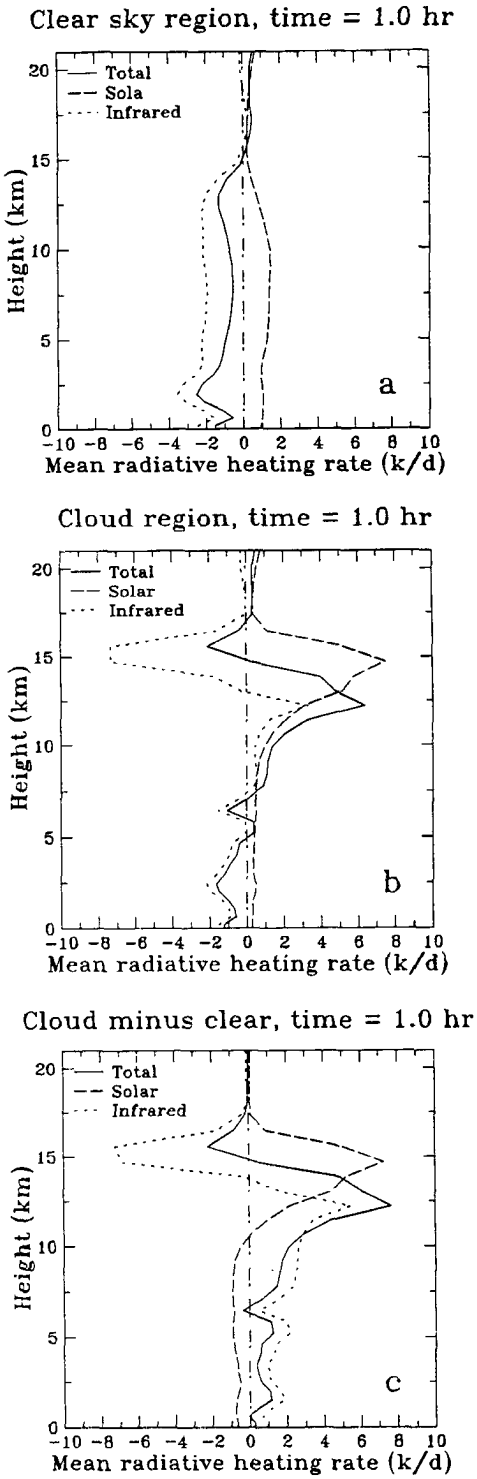

Figure 6.25: The vertical profile of spectral radiative heating (K/day), including solar (dashed), infrared (dotted), and total (solid) for (a) the clear sky condition and (b) the cloud cluster system and (c) the difference between (b) and (a) at 1 hour into the DUNDEE simulation. The zero line (dashed-dotted) is also drawn in the figure for reference.

The composite vertical profiles of radiative heating for the clear sky condition, the three different cloud regions identified in Fig. 6.6c, the entire cloud region, and the corresponding cloud perturbation profile are shown in Fig. 6.26 for the mature stage of the EMEX-9 MCS (i.e., 0816 LST). The total (solar plus infrared) radiative heating profile in the clear sky region (shown in Fig. 6.26a) does not change significantly from those found in the previous time period. This profile again shows cooling below 15 km and heating above this level due to the dominance of the infrared cooling over the clear sky solar heating below 15 km. There is also a small increase in solar heating in the troposphere compared to the earlier time. The profile in the convective region (given in Fig. 6.26b) exhibits cloud top cooling between 10 and 15 km, a layer of in-cloud radiative heating between 3.5 and 10 km, and small radiative cooling below 3.5 km. The spectral breakdown of the radiative heating profile in this region shows that the heating rates occur as a small residual of the difference between the large infrared cooling rates and the large solar heating values. Comparisons between the clear sky profile (i.e., Fig. 6.26a) and this profile show the significance of both in-cloud solar heating and in-cloud infrared cooling, especially near cloud top. The radiative profile corresponding to the stratiform region (shown in Fig. 6.26c) resembles that of the convective region. The layer of in-cloud radiative heating, however, is much deeper and extends to about 12.5 km in the stratiform region. Stronger cloud base infrared heating also exists in this region. The spectral breakdown of this profile again emphasizes how the net radiative heating is largely a result of the canceling effects of longwave and shortwave radiation. The profile in the thin anvil region (given in Fig. 6.26d) resembles that of the clear sky region with radiative cooling dominating the shape of the profile except in a small region around 13 km. The magnitude of the composited heating rates in the anvil region, relative to clear sky, also shows both solar and infrared heating of the order of 1 to 2 K/day, indicating that the anvil region is radiatively heated by both solar and infrared radiation. The radiative heating profile averaged over the entire cloud domain (shown in Fig. 6.26e) resembles the heating profile found in the stratiform region since the stratiform region contributes the majority of the area of the cloud cluster system. Comparison between the clear sky profile in Fig.

6.26a and this profile indicates how the cloud cluster leads to a systematic warming of the atmospheric column below 14 km. The temporal effects of solar heating appear in these figures as an increase of the total heating in the upper levels.

The composited vertical profiles of the radiative heating for the mature stage of the DUNDEE MCS (i.e., 1830 LST) is shown in Fig. 6.27 in a way similar to Fig. 6.26 for the EMEX system. Since the sun had already set by this time, the effect of solar heating is zero in this figure. The total radiative heating is due entirely to the effects of infrared processes. The total radiative heating profile in the clear sky region (given in Fig. 6.27a) has changed slightly from those found in the previous time period due to the lack of solar heating. This profile shows cooling throughout the vertical column due to the dominance of the infrared cooling processes. While the profile in the convective and the stratiform region (given in Fig. 6.27b and c, respectively) exhibits strong cooling throughout the entire profile, the results in the thin anvil region (shown in Fig. 6.27d) indicates strong heating in the area between 12 and 14 km and cooling in the remaining portion of the profile. This suggests that the base of the anvil region can be radiatively-heated by infrared radiation. The radiative heating profile averaged over the entire domain (given in Fig. 6.27e) resembles the heating profile found in the stratiform region since the stratiform region contributes the majority of the area of the cloud cluster system. Comparisons between the clear sky profile in Fig. 6.27a and this profile indicates how the cloud cluster leads to a systematic warming of the atmospheric column below 12.5 km.

The spatial averaged profiles of the total radiative heating rate during the decaying stage (i.e., 1116 LST) of the EMEX-9 MCS are shown in Fig. 6.28. Comparison of these clear sky profiles with those of the earlier time (i.e., Fig. 6.24a) shows how the magnitude of the solar heating has increased at this time, whereas the infrared heating remains similar in magnitude to that calculated at 0816 LST. The total cloud heating profile in Fig. 6.28b is also significantly different from the previous time. This vertical profile exhibits a narrow region of cloud top total radiative cooling between 13 and 15 km and a deep layer of total radiative heating between 4 and 13 km. The maximum value of the total heating rate in the profile is located at about 10 km level, or 5 km below the cloud top at this time. This

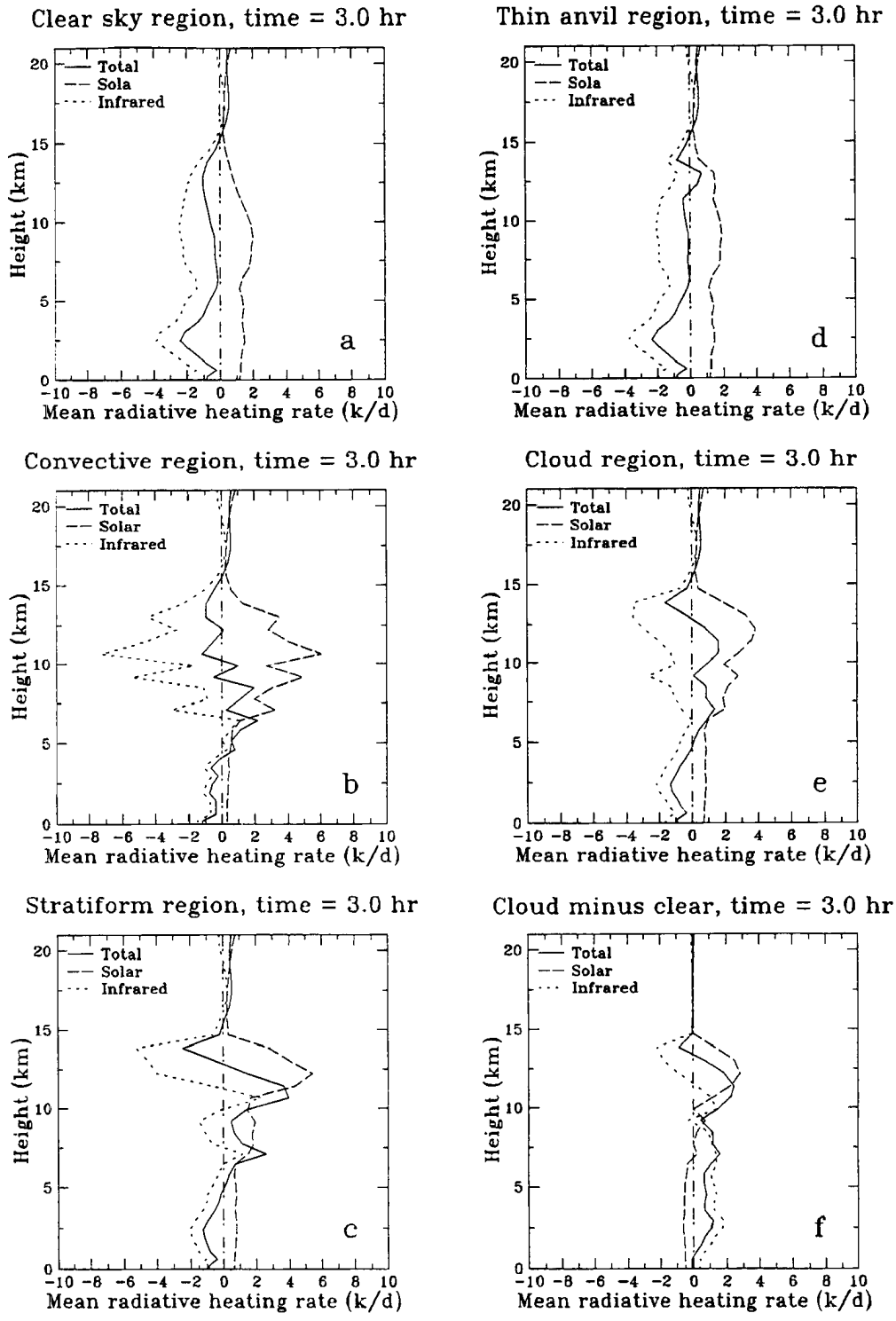

Figure 6.26: The vertical profile of spectral radiative heating (K/day), including solar (dashed), infrared (dotted), and total (solid) for (a) the clear sky condition, (b) the convective region, (c) the stratiform region, (d) the thin anvil region, (e) the cloud cluster system, and (f) the difference between (e) and (a) at 3 hours into the EMEX simulation. The zero line (dashed-dotted) is also drawn in the figure for reference.

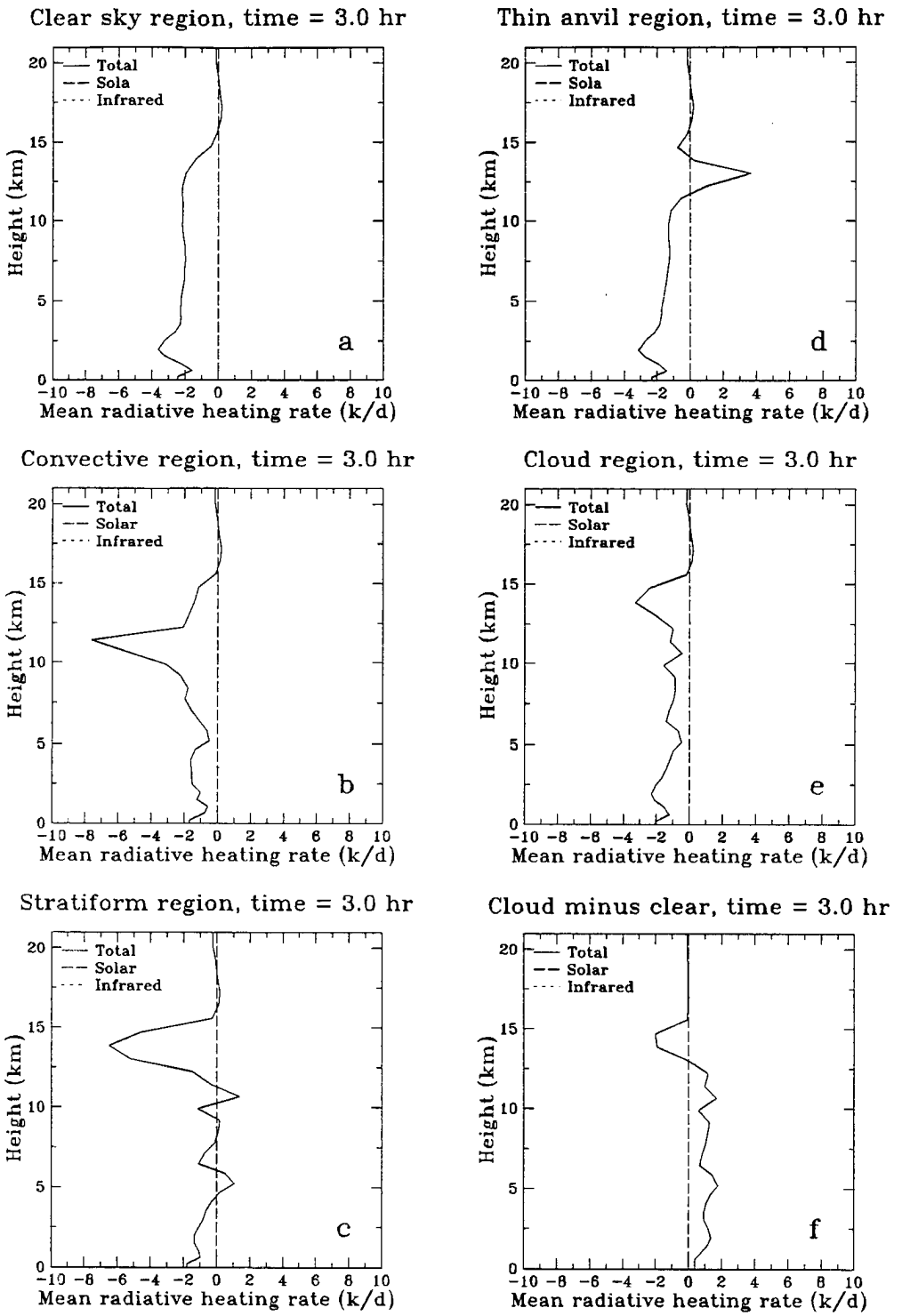

Figure 6.27: Vertical profile of spectral radiative heating rate (K/day), including solar (dashed), infrared (dotted), and total (solid) for (a) the clear sky region, (b) the convective region, (c) the stratiform region, (d) the thin anvil region, and (e) the entire cloud cluster region at 3 hours into the DUNDEE simulation. The zero line (dashed-dotted) is also drawn in the figure for reference.

maximum is due to solar heating which is able to penetrate much further inside the cloud than infrared cooling. This figure also shows how the strong cloud top infrared cooling is offset largely by the equally strong solar heating at 1116 LST. The cloud-induced radiative heating perturbation at 1116 LST (shown in Fig. 6.28c), again reinforces the finding that the net effect of the cloud system is to warm the atmosphere below cloud top. The individual breakdown of this radiative heating perturbation profile suggests that infrared processes dominate this perturbation in the lower and middle troposphere, whereas solar heating controls the magnitude in the upper troposphere except in the area near the cloud top.

The corresponding average profiles of the total radiative heating rate after six hour into the DUNDEE simulation (i.e., 2130 LST) are shown in Fig. 6.29. Comparison of these clear sky profiles with those of Fig. 6.25a shows the infrared heating remains similar to that calculated at 1630 LST. The total cloud system radiative heating profile in Fig. 6.29b still exhibits strong total radiative cooling throughout the entire vertical profile due to lack of solar heating in the radiation calculation. The cloud minus clear sky difference of radiative heating at 2130 LST (shown in Fig. 6.29c), representing the radiative heating induced by the cloud cluster system, shows that the net effect of the DUNDEE cloud system is to cool the upper troposphere near the cloud top and to warm the atmosphere below cloud top. This radiative heating profile is completely governed by the infrared processes at this time.

6.2.3 Domain-Averaged Radiative Heating

The evolution of the domain-averaged atmospheric column flux divergence is shown in Figs. 6.30 and 6.31 for the duration of the EMEX and the DUNDEE cloud simulation, respectively. These radiative fluxes were diagnosed every hour during the first six hours of the simulations and the results are averaged over a domain sizes of 500 km around the center of the model domain. The main purpose of this exercise was to address the effects of this cloud-induced radiative heating/forcing on the model atmosphere. This atmospheric column flux represents the surplus/deficit of the radiative energy over entire atmospheric vertical column, over the specific model horizontal domain. A positive value indicates

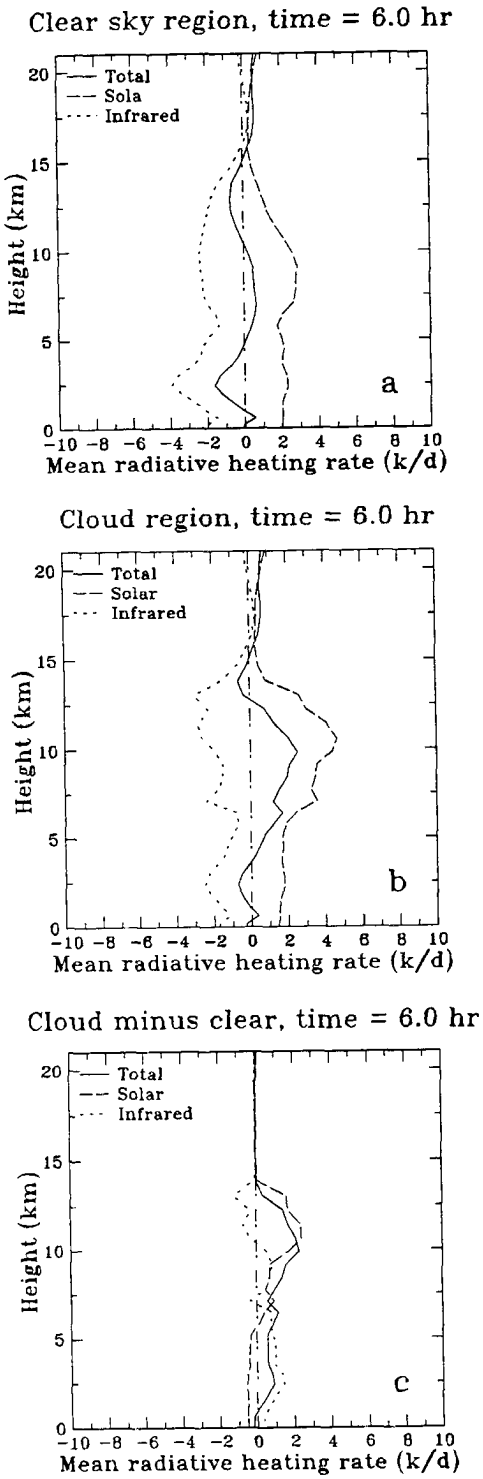

Figure 6.28: The vertical profile of spectral radiative heating (K/day), including solar (dashed), infrared (dotted), and total (solid) for (a) the clear sky condition, (b) the cloud cluster system, and (c) the difference between (b) and (a) at 6 hours into the EMEX simulation. The zero line (dashed-dotted) is also drawn in the figure for reference.

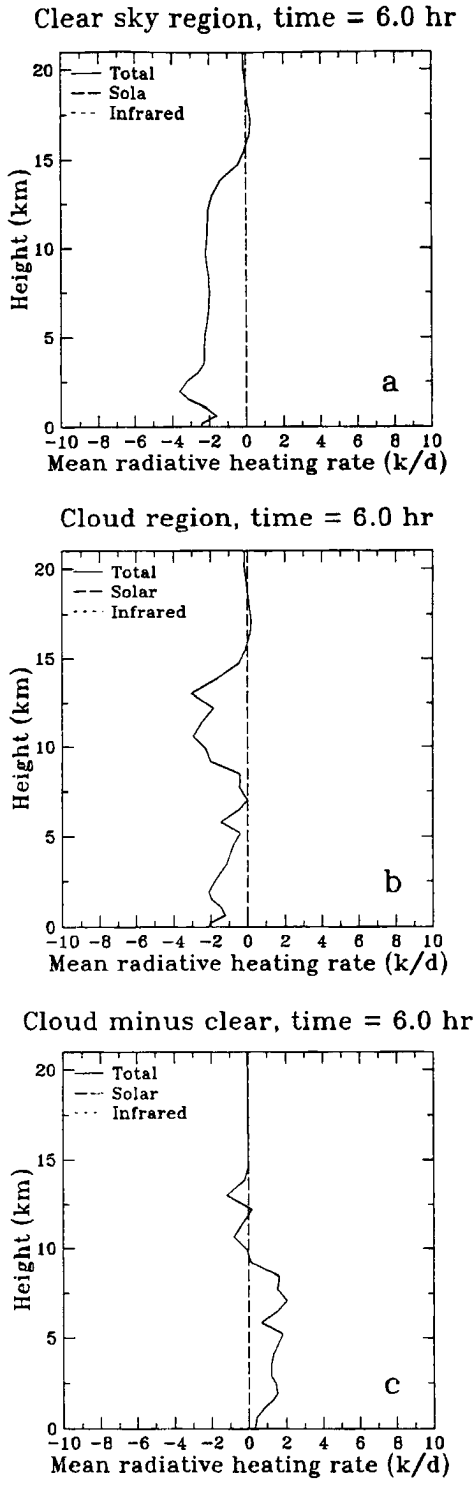

Figure 6.29: The vertical profile of spectral radiative heating (K/day), including solar (dashed), infrared (dotted), and total (solid) for (a) the clear sky condition and (b) the cloud cluster system and (c) the difference between (b) and (a) at 6 hours into the DUNDEE simulation. The zero line (dashed-dotted) is also drawn in the figure for reference.

that the atmosphere (containing both clear sky and cloud cluster) gains radiative energy and negative values correspond to loss of this radiative energy. The evolution of the net solar, infrared, and total (solar plus infrared) flux divergences for the duration of the cloud simulation is shown on the left scale while the column-averaged heating rate is given on the right scale. Clear sky values are also included (shown in dashed line) for comparison. The time scale for the EMEX case is given on the x-axis and spans from 0300 to 1200 LST. The sunrise and the time of initialization for the EMEX-9 cloud cluster (i.e., 0516 LST) is also indicated on Fig. 6.30. The time scale for the DUNDEE case, on the other hand, is from 1300 to 2200 LST. Sunset is also indicated on Fig. 6.31 and the DUNDEE convection was triggered at about 1530 LST.

The net effect of the cloud cluster on the domain-averaged tropospheric radiation budget is clearly evident in these diagrams. As the cloud system evolves (i.e., the fractional area covered by the cloud system in the model domain increases), the total radiative column flux divergence systematically increases from the clear sky minimum. While total radiative column flux divergence in the EMEX case continues to increase and becomes positive after 0900 LST, the values for the DUNDEE case, however, remain negative due to the lack of solar heating in the later part of the cloud life cycle. The difference between the clear sky and the cloudy sky total (solar plus infrared) column fluxes for the EMEX and the DUNDEE case is approximately 100 and 75 W/m^2 (or approximately 1.0 and 0.75 K/day), respectively, at the end of the six hours simulation. Of this 100 W/m^2 in the EMEX case, about 75 W/m^2 arises from infrared absorption primarily in the stratiform region of the cloud, while the remaining 25 W/m^2 are due to solar absorption in the cloudy atmosphere. This is consistent with the DUNDEE results. As illustrated in Fig. 6.28c, the solar heating effect, relative to clear sky, is concentrated in the upper troposphere, whereas the infrared heating, relative to clear sky, is found in the lower to middle troposphere. Figures 6.30 and 6.31 also show how the solar heating varies systematically with the daily cycle of the sun. Furthermore the values of EMEX's solar heating exceeds the clear sky values only during the decaying phase of the system when the extensive stratiform cloud coincides with the low solar zenith angles. This indicates that both the effects of solar

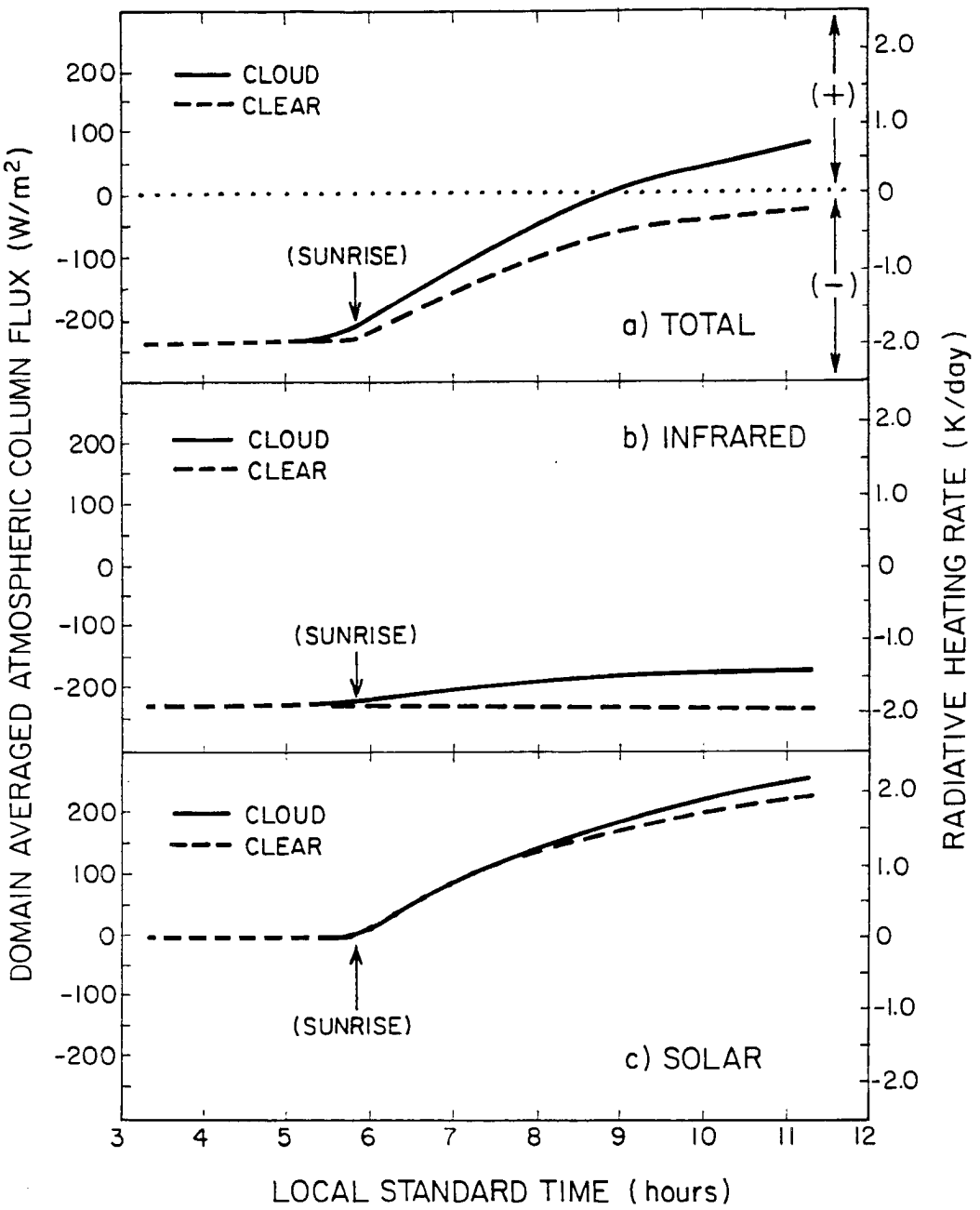

Figure 6.30: Temporal change of domain-averaged atmospheric column radiative budget in W/m^2 (right label) and domain-averaged atmospheric column radiative heating field in K/day (left label) of the EMEX simulated cloud cluster (solid) and of the simulated clear sky case (dashed) for (a) total radiation (top panel), (b) infrared radiation (middle panel), and (c) solar radiation (bottom panel). The arrow in the figure indicates the time of sunrise. The cloud model is initialized at approximately 0516 LST.

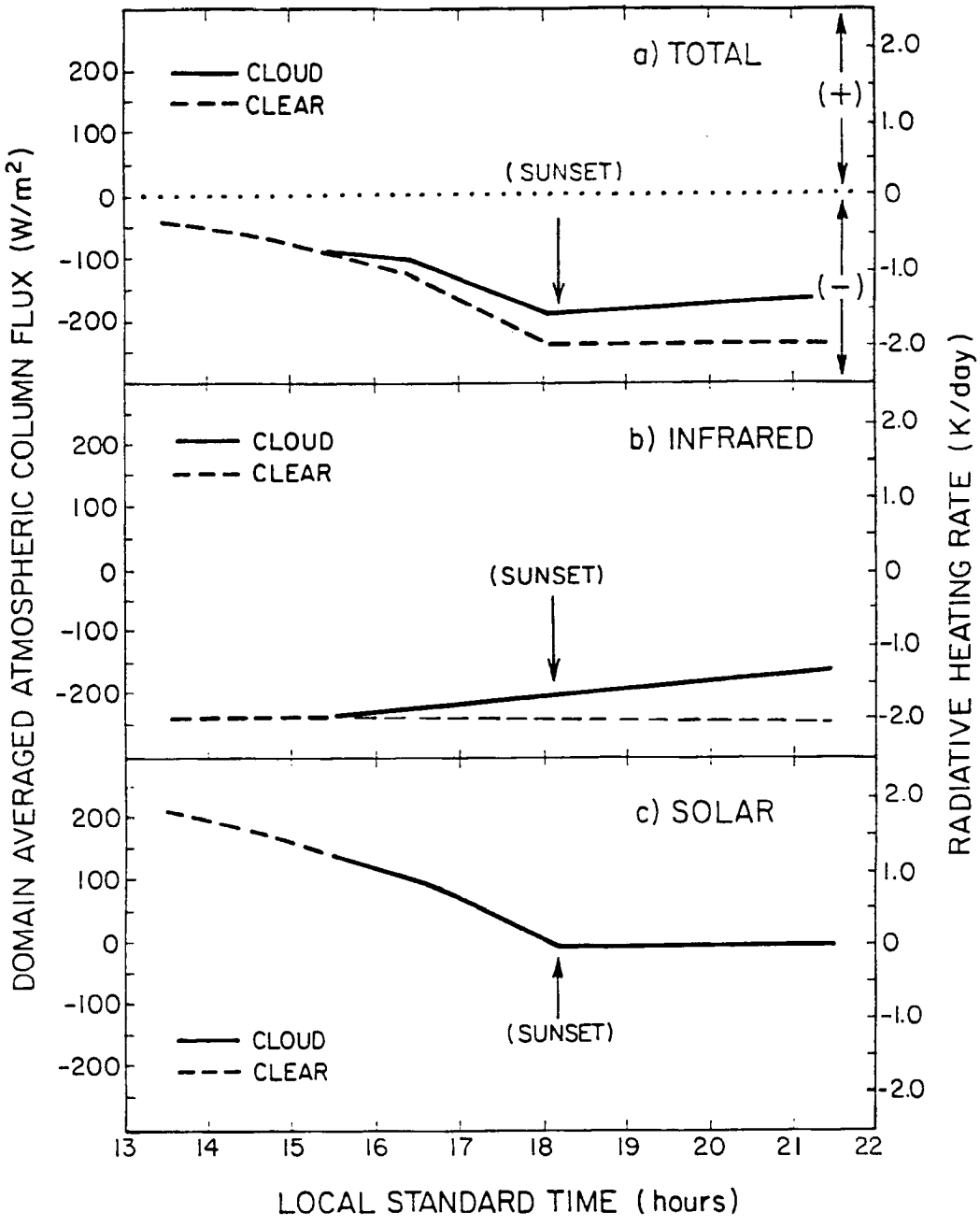

Figure 6.31: Temporal change of domain-averaged atmospheric column radiative budget in W/m^2 (right label) and domain-averaged atmospheric column radiative heating field in K/day (left label) of the simulated DUNDEE cloud cluster (solid) and of the simulated clear sky case (dashed) for (a) total radiation (top panel), (b) infrared radiation (middle panel), and (c) solar radiation (bottom panel). The arrow in the figure indicates the time of sunset. The cloud model is initialized at approximately 1530 LST.

angle and the fractional cloud cover area are important in determining the total solar heating caused by these cloud systems during the daytime hours. The DUNDEE case, on the other hand, shows lack of solar effects due to decreasing solar insolation at the time of simulation. The infrared column flux divergence increases throughout the life cycle of both cloud systems with the largest difference from the clear sky values also occurring during the latter stages of the life cycle when the model domain is covered by stratiform cloud and when the fractional area of cloud cover in the model is the largest. The more extensive is the stratiform cloudiness in the model domain, the greater is the reduction of longwave atmospheric column flux divergence. The results from this figure show how the EMEX-9 and the DUNDEE cloud system radiatively heats the tropical atmosphere.

6.3 Summary

This chapter presented the results of radiation calculations for the EMEX and the DUNDEE cloud cluster. These profiles were derived from a two-stream radiative transfer model using information provided by the RAMS cloud model. The results in this chapter show that the tropical atmosphere is significantly perturbed by the presence of tropical MCSs. The net effects of the MCSs on the radiation budget are

1. the increase in the infrared emission to the surface and the decrease of the net infrared energy loss from the atmosphere relative to the clear sky emission. This reduction in the IR column net flux divergence may be as large as 200 W/m^2 in some areas of the cloud and is indicative of the significant greenhouse effect of these clouds.

2. During the daytime, tropical cloud cluster can significant change the shortwave transmission to the surface, the shortwave albedo of the atmosphere, and the solar absorption in the atmosphere. The calculated low values of transmission in the convective region indicate how the MCS, and specifically the deep convective portions and the thick trailing stratiform region, not the areas of thin cirrus, significantly reduces the solar flux to the surface relative to the clear sky values.

3. Both the daytime and the night time vertical structure of the total (infrared and solar) radiative heating associated with the entire tropical MCSs is dominated by the heating profile in the stratiform region of the cloud system. Furthermore, the daytime shortwave fluxes at the surface are most influenced by the deeper convective portions of the cloud.

4. The daytime total radiative heating in the upper troposphere, especially near the cloud top region, is a result of the sensitive balance between the solar and the infrared heating in this region. The shortwave heating rate can be as large as the longwave cooling rate in this cloud top region, especially at local noon. The night time structure, however, is one of infrared cooling only. The vertical structure of the radiative heating in the anvil region also shows heating by both solar and infrared radiation.

5. The net radiative effect of the tropical MCS during the daytime, relative to the surrounding clear sky region, is one of radiatively heating the atmosphere below the cloud top region through both solar and infrared heating, and infrared cooling in a narrow area near the cloud top. The vertical profile of this net heating also indicates the importance of solar heating in the upper troposphere and infrared heating in the middle and lower troposphere. The corresponding effects during the night time is radiative heating of the atmosphere below the cloud top and cooling near the cloud top region.

6. During the daytime, the tropical MCSs also create an area of net radiative energy convergence into the atmosphere, even though the clear sky region still cools by the radiative effects. This positive radiative energy convergence is due to both the increase background radiative energy level by solar insolation and the infrared greenhouse effect of the cloud cluster.

7. During the night time, the effects of tropical MCSs are to create an area of relative radiative heat source in the cloudy region, with respect to the clear skies. This

relative radiative energy convergence is due to the infrared greenhouse effect of the cloud cluster.

The importance of the tropical cloud cluster systems on the radiative budget of the tropical atmosphere is further emphasized by the evolution of the domain-averaged atmospheric column flux divergence for the duration of the MCSs. As the EMEX-9 cloud system evolves during the daytime, the net column radiative energy loss of the atmosphere decreases and eventually becomes positive as the cloud system decays and transforms into a decaying mid-to upper tropospheric stratiform cloud system. This change in the column flux divergence translates into a total column radiative heating rate of approximately 1.0 K/day (relative to the clear sky radiative cooling rate). While the solar component of this total domain-averaged column heating is small and concentrated in the upper troposphere, the infrared contribution is large and spread over the lower and middle troposphere. The magnitude of this relative warming depends on the size of the stratiform area (i.e., cloud hydrometeor fields and fraction cloud area in the domain) and also on the solar zenith angle. Similar results are also obtained for the DUNDEE simulations.

It is reasonable to speculate, as Gray and Jacobson (1977) do, that this radiative heating of the environment by the MCS as reported in this chapter may provide a significant forcing in sustaining the tropical MCS. Study of the basic feedback processes between radiative heating and evolution of the tropical cloud cluster is now pursued in the next chapter.

Chapter 7

RESPONSES OF TROPICAL MCS SIMULATIONS TO RADIATION

The results describe in the previous chapter suggest that the presence of cloud clusters, as observed during EMEX and DUNDEE, can significantly influence the radiative budget and radiation heating profile of the tropical atmosphere regardless of the dynamical and thermodynamical conditions of their surrounding environments. Once this cloud-induced radiative heat source is formed, it may act to modify the air motion and the latent energy budget within the cloud clusters further (e.g., Stephens and Wilson, 1980), which can lead to changes in the characteristics (i.e., total surface precipitation and lifetime) of these tropical MCSs. A positive feedback between cloud and radiation (such as changes in radiative heating which lead to further dynamical development of the cloud clusters or formations of new cloud masses) may play an important role in the overall energy budget and circulation of both the cloud clusters and the tropical atmosphere. For example, the differential radiative budget/heating between the clear skies and the cloudy atmosphere has been proposed to force large-scale secondary circulation and to enhance deep convection in the maritime tropics (Albrecht and Cox, 1975; Gray and Jacobson, 1977; and Cox and Griffith, 1978). In this chapter we will study cloud-radiative feedback associated with differential radiative heating/cooling between the clear skies and the cloudy atmosphere and their relationship to the background tropical environment by examining the responses of the tropical atmosphere to the differential radiative heating/cooling and the sensitivity of the tropical cloud cluster simulations to radiation using the RAMS cloud/mesoscale model. Section 7.1 will highlight the proposed cloud microphysics-radiation-thermodynamics-dynamics couplings within the tropical MCSs. This hypothesized feedback is a refined theory of Gray and Jacobson (1977). It is based on results from many sets of numerical experiments and will be illustrated in Section 7.2 and 7.3 below. A final summary is given in Section 7.4.

7.1 Hypothesized Feedback

The temperature profile in the tropical atmosphere may be closely approximated by a moist adiabatic profile, except near the surface level. This temperature structure suggests that the source of energy for most tropical MCSs is at the surface level. Without this supply of energy from the surface, most convections or MCSs can not last very long in a normal undistributed tropical atmosphere. For example, tropical cyclones draw their energy from the underlining warm ocean water and decay as they enter into cold water. In order to maintain tropical MCSs under both fixed background environment and constant surface conditions, cloud feedback processes have to communicate effectively with this surface energy. This is especially important for oceanic cloud clusters since surface heating does not play an essential role in the redevelopment of these systems. Since the presence of a cloud clusters create a cloud-induced radiative heat source in the atmosphere with respect to surrounding clear skies, it is possible that this atmospheric heat source can feedback to modify the MCS through coupling with this surface energy.

One possible form of coupling between the cloud-induced atmospheric radiative heating and the surface energy supply is through the existence of secondary circulations induced by the differential radiative heating/cooling between the clear skies and the cloudy atmosphere. This radiation-induced circulation mechanism was first proposed by Gray and Jacobson (1977) to explain the observed early morning maximum in deep convection over the maritime tropics. This mechanism was also suggested by radiation budget measurements from the GATE experiment (Cox and Griffith, 1978) and large-scale diagnosed model calculation of Albrecht and Cox (1975). In addition, numerical simulation of tropical MCS by Tao *et al.* (1993) also pointed to the importance of this feedback mechanism in enhancing both the convection and the surface precipitation in their simulated cloud cluster. In this chapter, we will refine the details of this feedback process for both daytime and night time scenarios and their relationships to both the background environments and the infrared radiative cooling process of the atmosphere.

7.1.1 Basic Physical Mechanism

The idea behind this feedback process is quite simple as schematically shown in Fig. 7.1. As the cloud grows, the radiative heating/cooling differences between the clear skies and the cloudy atmosphere begin to increases due to cloud microphysics-radiation interactions (such as the results given in Chapter 6). The thermodynamical response of the atmosphere to this differential radiative heating/cooling are such as to set up horizontal pressure gradients between the clear skies and the cloudy atmosphere. While the exact vertical profiles of these horizontal pressure gradients are a function of the vertical structures of the differential radiative heating/cooling, which may vary significantly between the daytime and the night time cases, the lower level pressure gradient patterns, on the other hand, depend only on the integrated column temperature above those levels through the hydrostatic nature of the atmosphere. Since the cloud cluster radiatively heats more (i.e., Fig. 7.1a) and cools less (such as Fig. 7.1b) than the surrounding clear skies during the daytime and night time situations, respectively, these radiative heating/cooling structures should produce a hydrostatically lower pressure at the lower levels of the atmosphere underneath the cloud cluster and a higher pressure in the surrounding clear skies. The dynamical responses of the atmosphere to this thermodynamically-induced low pressure patterns are to create a circulation which has a convergence at the surface and resulting upward motions in the lower levels of the cloudy regions. This radiation-induced secondary circulation and its resultant surface convergence, if significant in strength, can transfer energy from the surface and the lower levels into the MCS and lead to further development of the tropical cloud cluster. For example, this concept is similar to the lowering central surface pressure inside the tropical cyclones by latent heating in the atmosphere which helps maintain the tropical cyclones by forcing surface convergence. Furthermore, this secondary circulation will probably be most capable in modifying the later stage (i.e., decaying stage) of the MCSs when latent heatings/coolings are weak. Since the enhanced tropical MCS can then create further radiative heating through cloud microphysics-radiation interaction, which in turn, can feedback to the thermodynamics and dynamics of the tropical MCS, this cloud microphysics-radiation-thermodynamics-dynamics coupling process is therefore a positive feedback to the tropical MCSs.

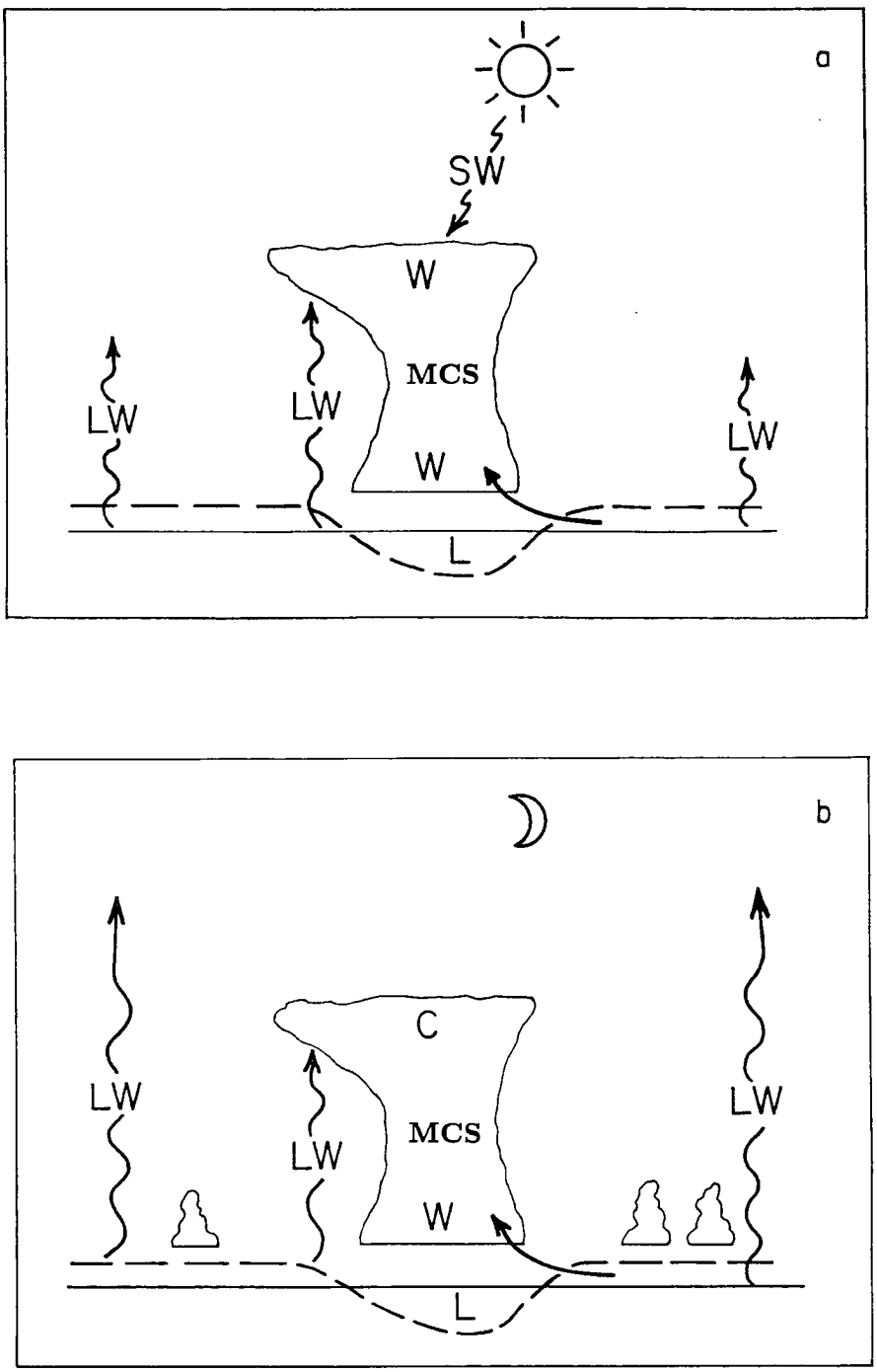

Figure 7.1: Schematic of the Coupling process between cloud radiative forcing and tropical cloud clusters for (a) daytime and (b) night time condition.

7.1.2 The Role of Background Environments

Since this feedback process relies on the secondary circulation and forced surface convergence to transfer energy from surface reservoir to the MCS, its strength will naturally be sensitive to the background environmental conditions (i.e., to low level stability and to vertical shear) in which the MCS is embedded. Specifically, this feedback will be most effective for background environments characteristized by unstable lower levels and weak vertical shear. Under this situation, the cloud-induced radiative feedback described in this section can significantly enhances both the daytime and the night time convection which can lead to additional changes in the energy, momentum, and water budget of the tropical atmosphere. Since this type of environment can be found in the TOGA-COARE region over the western Pacific ocean, it is reasonable to speculate that the diurnal differences in tropical convection may be weaker in this region.

As lower level stability increases, this feedback will weaken due to the capping effects of stability. Under weak shear conditions, physical processes that weaken lower level stability (i.e., infrared radiative cooling at night) can play an important role in modifying the behaviors of the tropical convection by providing an unstable environment to this cloud-radiative feedback. In this scenario the persistence of infrared coolings at night weaken or destroy the lower level stability and allow the feedback between the radiatively-induced secondary circulation and the tropical MCSs to occur. Under the same background environments, this coupling between the infrared destabilization of the atmosphere and the radiatively-induced secondary circulation, however, breaks down or weakens during the daytime due to the effect of solar heating in reducing the amount of total radiative cooling in the atmosphere. Thus, the cloud-radiative feedback described here can lead to significant differences in the diurnal signatures of tropical convection (i.e., stronger convection at night) if the environment is characteristized by stable lower levels and weak vertical shear. Since the infrared destabilizing process requires a significant amount of time to be effective due to the small value of atmospheric infrared cooling rate, one will expect the maximum effect of this cloud-induced radiative forcing and its resultant deep convection to occur during the early morning hours of the day. Since this type of environment can be

found in most maritime tropical regions, these diurnal signatures in tropical convections should be a common feature of the tropical atmosphere.

In addition to low level stability, this cloud-radiative feedback process will also be affected by vertical shear profile. As vertical shear increases, this feedback will weaken since shear tends to distort the vertical stacking of heating, reducing the net effect of this heating on the column and thus weakening the pressure drop. Under these conditions, the intensity of these tropical convection should be dominated by the large-scale dynamics. Examples of this type of environment include the conditions associated with the passage of both the monsoon systems and the westerly burst events.

In the following sections, we will show details of this proposed feedback process and its relationship to the background environments using numerical simulations.

7.2 Responses of the Tropical Atmosphere to Differential Radiative Heating/Cooling

Since the cloud radiation-induced secondary circulation is the key to the proposed cloud microphysics-radiation-thermodynamics-dynamics coupling process, it is therefore important to show the nature of this circulation before performing any additional sensitivity experiments. In this section, we will illustrate the responses of the tropical atmosphere to differential radiative heating/cooling between the clear skies and the cloudy atmosphere. Specifically, we would like to address

- whether this differential radiative heating/cooling can result in a secondary circulation that enhances both surface convergence and lower level upward vertical motions in the cloudy region, and
- estimate the strength of the circulation?

Two mesoscale numerical experiments are performed to show the responses of the atmosphere to both the daytime and night time differential radiative heating/cooling. The setup of these experiments involves prescribing the cloudy radiative heating/cooling profile for an area of 50 km at the center of the model and its clear sky counterpart elsewhere

across the model domain. The vertical profiles of the radiative heating/cooling are taking from Fig. 6.28 (i.e., solid line for the daytime case and dotted line for night time condition). The sounding data for these experiments are taken from Fig. 5.21. In order to simplify our analysis further, we will focus only on dry simulations with a background atmosphere at rest. Even though these dry simulations can significantly underestimate the strength of the secondary circulation due to lack of condensational and evaporative processes, they are a useful tool in visualizing the secondary circulation. The strength reduced from these simulations is used here as an estimate for the lower limit of the circulation due to the prescribed differential profile of radiative heating. We will compare the strength of the circulation in these dry simulations with those in the cloud simulations in the next section. The results of the simulations for both the daytime and the night time cases are given below.

7.2.1 Daytime Conditions

The mesoscale model responses to the daytime differential radiative heating and cooling are given in Fig. 7.2 in the form of the model X-Z cross-section of pressure perturbation, horizontal velocity perturbation, and vertical motion perturbation field after one hour into the simulation.

The results indicate that the atmospheric responses to this differential radiative heating profiles are such as to create a lower pressure region at the lower levels and a high pressure region above in the upper levels, respectively, relative to the surrounding clear skies (shown in Fig. 7.2a). The patterns for the absolute value of pressure perturbation show low pressure in the middle troposphere, sandwiched by higher pressure aloft and below. These pressure patterns suggest general rising motion in the lower troposphere. The lowest pressure values occur at a level 4 km above the surface in the cloudy region. The circulations for this case (shown in Fig. 7.2b and c) consist of upward motion in the cloudy region and downward motion in the clear sky area. These figures also show surface convergence and upward vertical motion in the lower levels of the cloudy regions as a response to the differential radiative heating between the clear skies and the cloudy

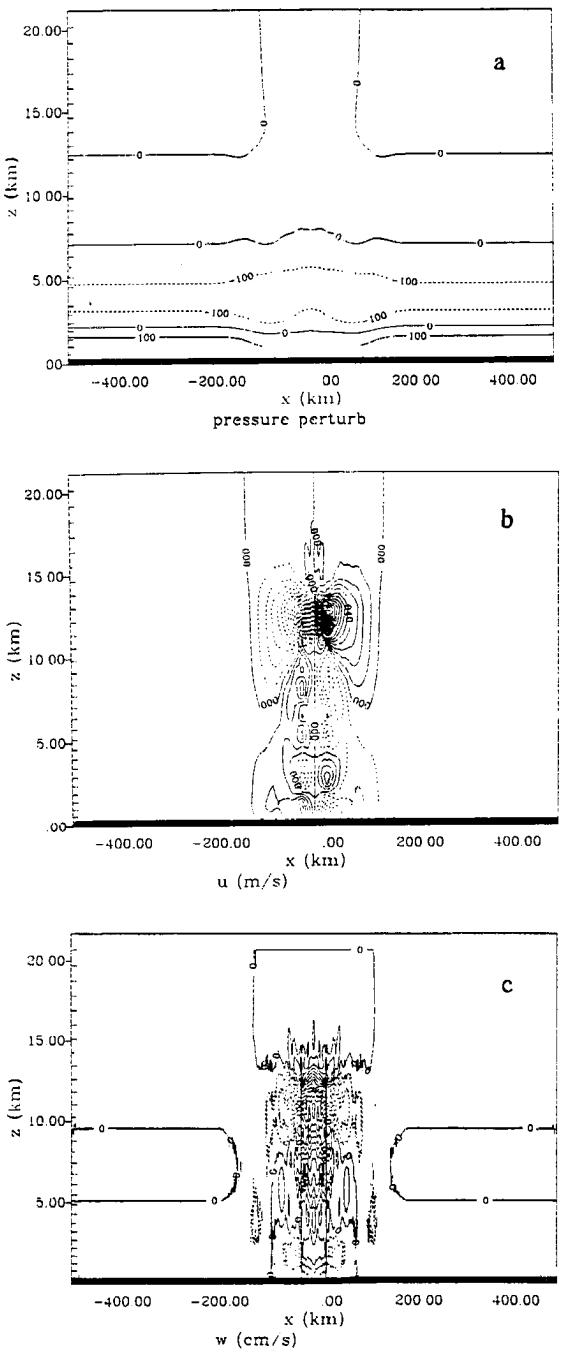

Figure 7.2: The daytime mesoscale responses, including (a) pressure perturbation (tenth of mb), (b) horizontal velocity perturbation (m/s), and (c) vertical motion perturbation (cm/s), to differential radiative heating and cooling between clear skies and the cloudy atmosphere.

atmosphere. This is consistent with the hypothesized feedback outlined in the previous section.

The horizontal surface pressure gradient produced by this differential radiative heating and cooling is not very large in the dry simulation. The drop in the surface pressure between the clear skies and the cloudy region at this time is estimated on the order of 0.25 to 0.5 millibar. This pressure difference can translate into a secondary circulation with vertical motions on the order of 5 to 10 cm/s at the 1 km vertical levels. Since the vertical motions of this secondary circulation are not very strong, the significance of this cloud microphysics-radiation-thermodynamics-dynamics feedback to the evolution of tropical MCS may be quite limited. Specifically, this feedback process may be only relevant to those cases that have (1) an unstable background temperature structure and weak vertical shear profile and (2) stable lower levels, weak shear profile, and some kinds of destabilizing mechanism in the lower levels of the atmosphere (i.e., infrared cooling of the atmosphere). For such cases, the surface convergence produced by the differential radiative heating and cooling can provide a significant source of energy to the tropical MCSs by lifting warm and moist surface air parcels into the cloud systems. We will investigate the sensitivity of the daytime tropical MCSs to radiative forcings in Section 7.3.

7.2.2 Night Time Case

The mesoscale responses of the atmosphere to the night time differential radiative cooling are shown in Fig. 7.3 in a format similar to Fig. 7.2.

The results again indicate that the differences in the radiative cooling structures between the clear skies and the cloudy atmosphere can create a lower/higher pressure regions in the lower/upper levels of the cloudy area, respectively, relative to the surrounding clear sky conditions (shown in Fig. 7.3a). This response is similar to the daytime case even though the dominant process for this case is due mainly to radiative cooling instead of heating. The patterns for the absolute value of the pressure perturbation, however, are quite different from those of the daytime case. These patterns consist of higher values near the surface and lower values aloft, suggesting general downward accelerations throughout the model domain due to the effects of radiative cooling at night. The circulations for

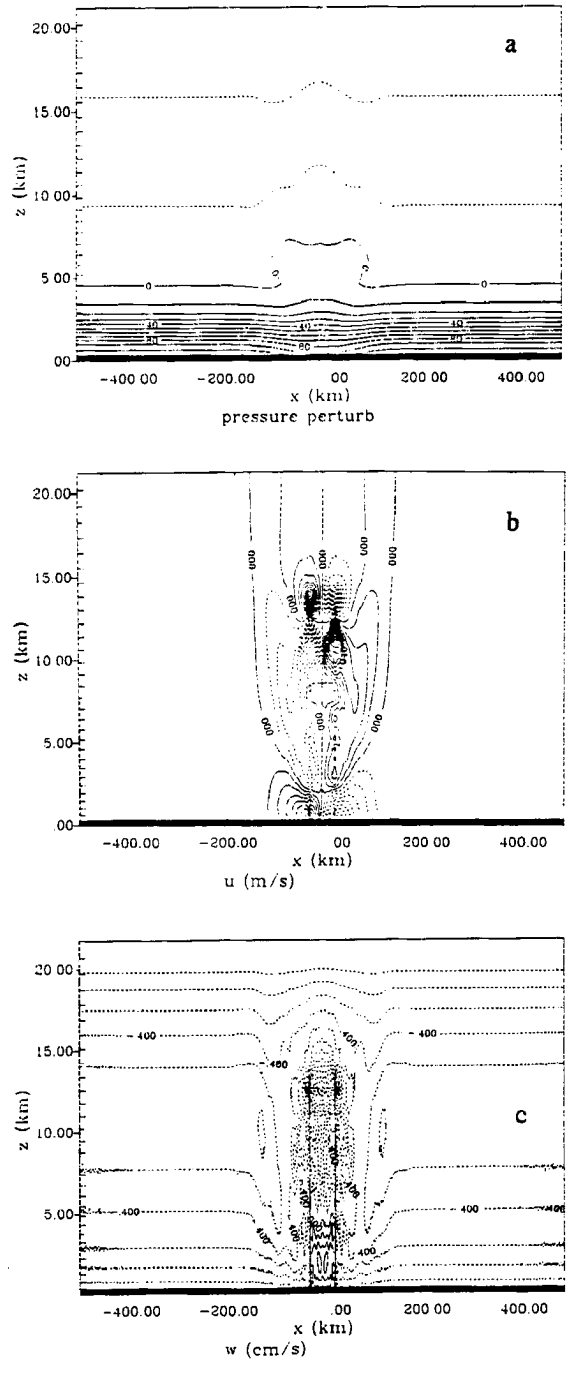

Figure 7.3: The night time mesoscale responses, including (a) pressure perturbation (tenth of mb), (b) horizontal velocity perturbation (m/s), and (c) vertical motion perturbation (cm/s), to differential radiative heating and cooling between clear skies and the cloudy atmosphere.

this case (shown in Fig. 7.3b and c) consist of downward motion everywhere in the model domain except at lower level of the cloudy region, where upward motion exists. This upward motion is caused by surface convergence which is induced by a horizontal differential pressure gradient in the area (i.e., lower pressure in the cloudy region and higher pressure in the clear sky area). This is again consistent with the hypothesized feedback outlined in the previous section and with the circulation obtained from the large scale diagnosed study of Albrecht and Cox (1975).

The horizontal surface pressure gradient produced by this differential radiative cooling at night is again not very large in the dry simulation. The drop in the surface pressure between the clear skies and the cloudy region at six hours into the simulation is of the same order as the daytime case. This suggests that the magnitude of the resultant secondary circulation and the upward vertical motions at lower levels in the cloudy region is not very large (i.e., similar in magnitude to the daytime case). Therefore, the effects of this cloud microphysics-radiation-thermodynamics-dynamics feedback may be most effective, again, for cases which have (1) an unstable background temperature structure and weak vertical shear profile and (2) stable lower levels, weak shear profile, and some kinds of destabilizing mechanism in the lower levels of the atmosphere (i.e., infrared cooling of the atmosphere). In such cases, the surface convergence produced by the differential radiative cooling can help to modify the tropical MCS by drawing an additional supply of surface energy into the cloud system. We will examine the sensitivity of the night time tropical MCSs to cloud radiative forcing in the next section.

7.3 Sensitivity of the Tropical MCS to Radiation

The results in the last section illustrate the effects of differential radiative heating between the clear skies and the cloudy atmosphere in producing a secondary circulation which enhances surface convergence and upward motion at the lower levels of the cloudy regions. This cloud radiation-induced secondary circulation is consistent with the proposed coupling processes outlined in Section 7.2. Furthermore the results also suggest that this hypothesized cloud microphysics-radiation-thermodynamics-dynamics feedback may

be only significant for background environments characterized by (1) an unstable lower levels and weak vertical profile of shear and (2) stable lower levels, weak shear profile, and some kinds of destabilizing mechanism in the lower levels of the atmosphere (i.e., infrared cooling of the atmosphere). In this section we will explore this issue further using tropical MCS simulations. Specifically, we would like to address

- the sensitivities of tropical MCS simulations to radiation, and
- whether these sensitivities are affected by the background environments in which these MCSs are embedded and by the infrared cooling process of the atmosphere. If the hypothesized feedback given in Section 7.2 operates in these tropical MCS simulations, the results would show a dependency on both the background environments and the infrared cooling process.

In order to answer these questions, three sets of cloud-radiation experiments based on the modified DUNDEE background conditions in Table 7.1 were conducted. These experiments are identified for weak and strong shear and for two cases of lower level stability. In order to concentrate on the effect of atmospheric heat source on the evolution of the tropical MCS, we further limit our studies to fixed surface conditions to eliminate the effects of surface heating/cooling that may affect the simulations. Under each set of experiments, three different cloud simulations representing different levels of radiation treatment in the model are also presented. They include a cloud simulation without any radiation processes (hereafter refer to as NORAD), a second cloud simulations including only infrared radiation (hereafter refer to as IRONLY), and a third simulation with full radiative processes but with fixed solar insolation corresponding to its local noon value (hereafter refer to as MAXSW). While the differences between NORAD and IRONLY experiments represent the effects of infrared radiative processes during night time condition, the disparities among NORAD and MAXSW experiments symbolize the influences of total radiative processes (infrared plus solar) during the noon time condition. Furthermore, the differences between IRONLY and MAXSW experiments serve to highlight the relevance of solar heating processes in cloud.

Table 7.1: List of background environment associated with the sensitivity studies.

Case	Name	Vertical Shear	Lower level Stability
1	WU	Weak	Unstable
2	WS	Weak	Stable
3	SU	Strong	Unstable

In the first set of experiments (hereafter refer to as WU), we will examine the coupling between cloud-induced radiative forcing and a tropical MCS simulation which is embedded in an environment possessing weak vertical shear and unstable lower levels. These experiments are intended to highlight the effects of the proposed feedback processes since this background environment should produce the greatest sensitivity between experiments with radiative processes (i.e., IRONLY and MAXSW) and those without radiation (i.e., NORAD) as suggested by results from Sec. 7.3. The second and the third set of experiments (hereafter referred to as WS and SU, respectively), on the other hand, are designed to examine the effects of stronger lower level stability and stronger vertical shear in limiting the overall feedback between cloud-induced radiative heating and the evolution of tropical MCS. According to the hypothesized feedback outlined in Section 7.2 and the results suggested in Section 7.3, these two sets of experiments are expected to give a much reduced sensitivity to radiative processes. In addition, the second set of experiments is also used (1) to illustrate the effects of atmospheric infrared cooling at night in aiding the feedback between cloud-induced radiative heating and the evolution of the tropical MCS and (2) to highlight the differences in the intensity of convection between the daytime (i.e., MAXSW) and the night time (i.e., IRONLY) systems. The IRONLY results of this case should show significantly more sensitivity to radiative forcing than the MAXSW case once the infrared destabilization of the atmosphere is strong enough to offset the lower level stability and allowing the feedback between the radiatively induced secondary circulation and the tropical MCSs to occur at night. These cloud simulations were started using the initialization technique outlined in Chapter 5 and integrated forward in time. The results of the radiation sensitivity experiments are presented below by examining the differences in

- the temporal structures of the model peak vertical motion field,
- the time series of the domain integrated total hydrometeor mass,
- the temporal patterns of the domain integrated accumulated surface precipitation field,
- the horizontal structures of the column integrated total hydrometeor mass,
- the spatial distribution of the column integrated mean temperature field, and
- the horizontal patterns of the surface pressure profile.

While the peak vertical motion field is used as a measure of the convective activity of the cloud cluster, the domain integrated total hydrometeors and the domain integrated accumulated surface precipitation fields are indicators for the release of latent energy during the lifetime of these tropical systems. Large latent heat release may be loosely associated with larger total hydrometeors or higher values of accumulated surface precipitation.

7.3.1 WU Case

The sensitivity of the WU experiments to radiation are examined in this section. This set of experiments is marked by a background environment which has a weak vertical shear profile and unstable lower levels and should show the greatest sensitivity to radiation. Three radiation experiments (i.e., NORAD, IRONLY, and MAXSW) are carried out and their results are present in Fig. 7.4 and 7.5 below. According to the hypothesis, cloud-radiative feedback should be present in both the daytime (i.e., MAXSW) and the night time (IRONLY) experiments by enhancing additional convection in the cloud simulation.

The model peak vertical motion fields for this case (given in Fig. 7.4a) show that all three radiation experiments evolved with a similar time history during the first hour of the simulation (i.e., the intensification stage of the MCS), suggesting a limited impact of radiative processes in modifying the structures of the cloud cluster. The modeled peak vertical motion fields from all three radiation experiments begin to diverge from each other after one hour into the simulation. The separation in the time series signify how the effects

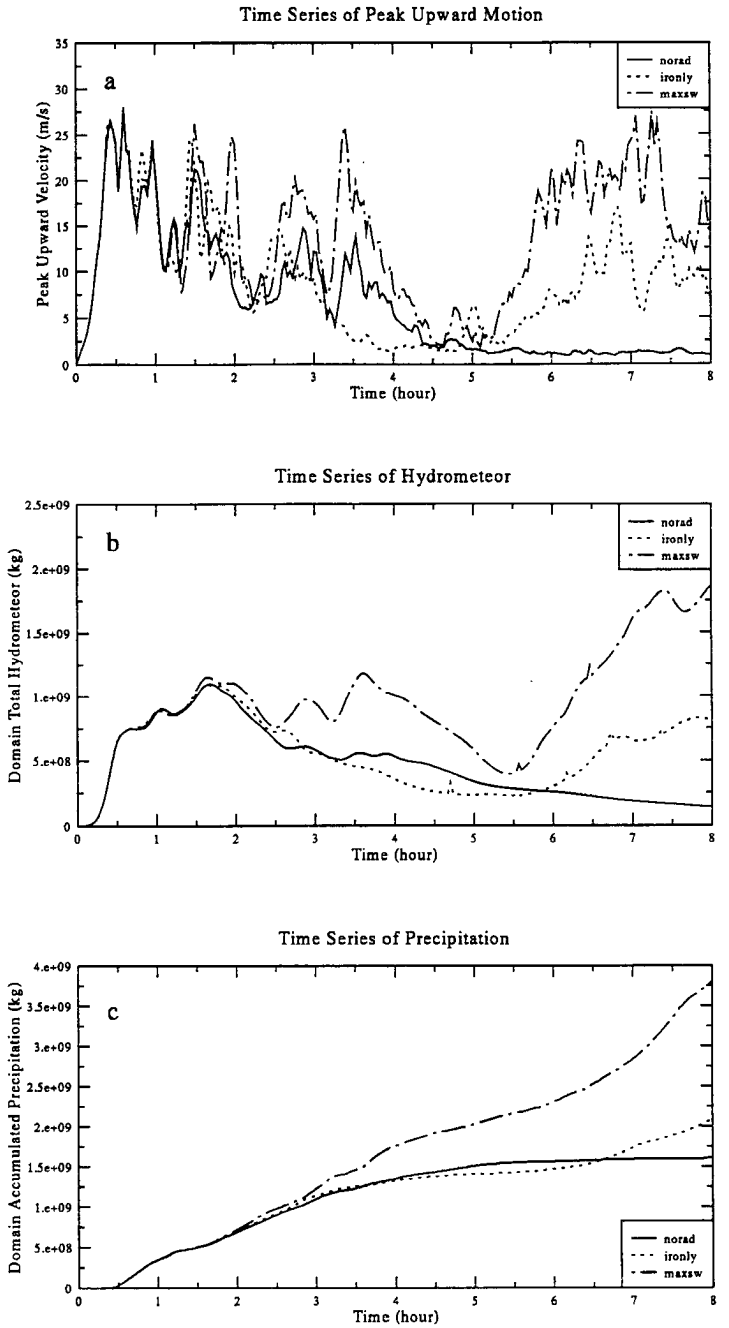

Figure 7.4: Time series of (a) model peak upward vertical motion field, (b) domain integrated total hydrometeor field, and (c) domain integrated accumulated surface precipitation field for the NORAD (solid line), the IRONLY (dotted line), and the MAXSW (dot-dashed line) experiments using the WU environment.

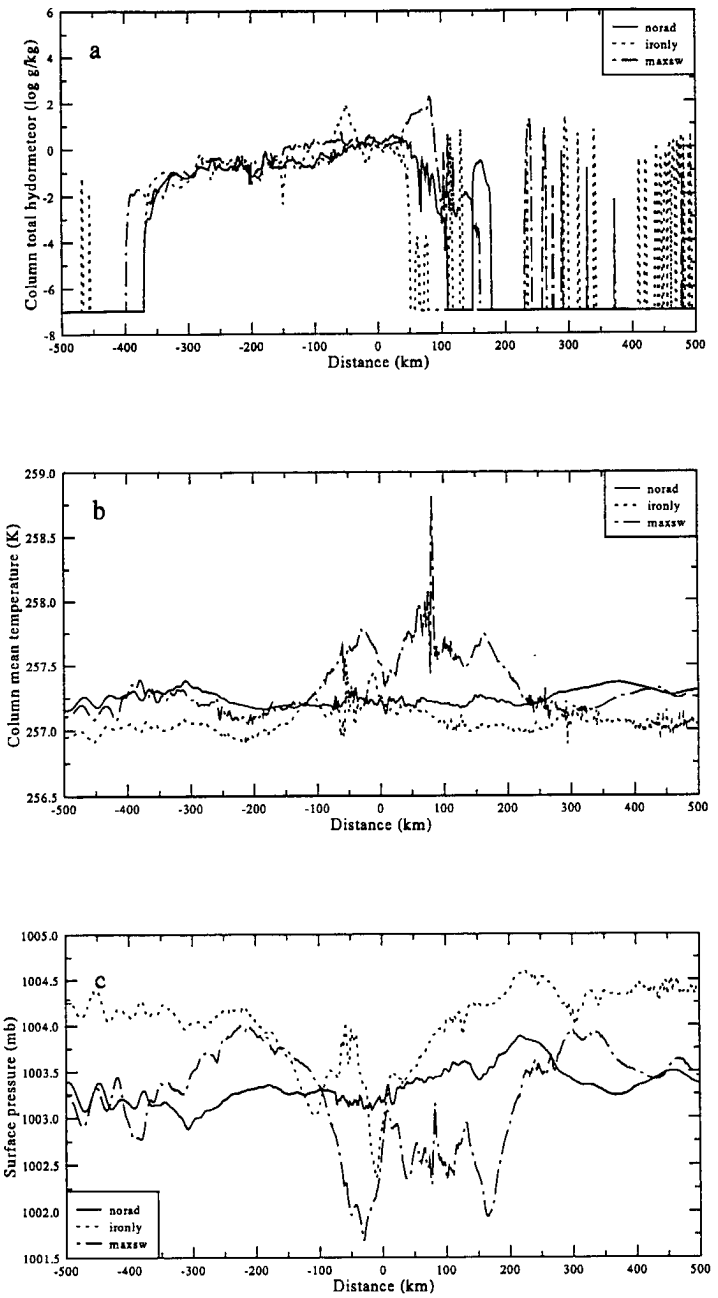

Figure 7.5: Horizontal cross section of the model (a) column integrated total hydrometeor, (b) column mean temperature, and (c) surface pressure for the NORAD (solid line, the IRONLY (dotted line) and the MAXSW (dot-dashed line) experiments after seven hours into the simulations using the WU enironment

of radiative heating begin to modify the convective activity of this cloud cluster as the system evolves beyond the initial intensification stage. At these times, the structures of the peak vertical motion time series are very complicated. There are many strong pulses of upward motion due to the growing convective cells in the MCS. According to this figure, the MAXSW experiment with both infrared and solar radiative processes and the IRONLY experiment with only infrared radiation show a significantly greater value of peak vertical motion field than the NORAD experiment in the later stage of the cloud simulation (i.e., after the fifth hour) due to formation of new convective cells in the radiation experiments. For example, the peak upward velocity at seven hours into the simulation for both the MAXSW and the IRONLY experiment are about 25 m/s and 12.5 m/s, respectively, while values smaller than 2.5 m/s exist in the NORAD experiments. The stronger convective activity implied by these vertical motion values suggests cloud-induced radiative forcing can significantly alter the characteristics of this tropical MCS simulation by aiding the formation of new convective elements in the cloud clusters which is consistent with the notion of the feedback proposed.

The domain-integrated total hydrometeor fields (given in Fig. 7.4b) show a behavior similar to that of the peak vertical motion field. Specifically, the domain-integrated total hydrometeor content for all three experiments start out with a similar time history during the first hour of the simulation due to the dominance of the dynamical processes in the initial stage of the cloud cluster. As time progresses, these profiles begin to diverge from each other and the effects of radiative forcing in modifying the latent energy budget of this system is implied in these results. The largest values of hydrometeor mass shown in Fig. 7.4b occur for the MAXSW experiment. For example, the values for the mass of total hydrometeors for the MAXSW experiment at eight hours into the simulation are six times as large as those found in the NORAD experiment. The differences between the IRONLY and the NORAD experiment are also large at the end of the simulation with IRONLY case having twice as much total hydrometeor mass than the NORAD case. The extra total hydrometeor mass appeared in both the MAXSW and IRONLY simulation is due to formation of new convective elements in the cloud clusters and implies an enhanced

release of latent heat created by the interaction between radiation and the cloud cluster itself.

The domain-integrated surface accumulated precipitation (given in Fig. 7.4c) also exhibits a behavior similar to the results given in Fig. 7.4a and b. The amounts of domain-integrated surface accumulated precipitation between the three cases are similar early in the simulation. As time progresses, the evolution of precipitation for each experiment diverge from each other again illustrating the effects of radiative forcing in modifying the characteristics of this system. While the domain-integrated surface accumulated precipitation for the MAXSW experiment shows a continuous increase throughout the entire simulation period, the domain-integrated surface accumulated precipitation for the NORAD experiment, on the other hand, seems to level off after the fourth hour into the simulation. The MAXSW experiment has about 130% more surface precipitation at the end of the eight hours period than the other NORAD experiment which is consistent with the suggestion of both enhanced convective activity and enhanced cloud hydrometeor mass generated during the evolution of this MCS when radiative processes act. The differences in the accumulated precipitation between the IRONLY and the NORAD are also significant. After eight hours of simulation, the IRONLY case has about 33% more precipitation than the NORAD case. These radiation experiments again reinforce the important of radiation in modifying the latent energy budget of this cloud cluster. The larger sensitivity in the MAXSW experiment is indicative of the stronger effect of the radiative heat source in forcing stronger surface convergence and in producing more surface precipitation. The weaker sensitivity of the IRONLY case (i.e., respect to the MAXSW case) is due to the smaller domain-integrated total hydrometeor content during the mature and the later stage of the IRONLY cloud cluster. Thus, this smaller hydrometeor content leads to a smaller differential radiative heating and to a smaller sensitivity shown in Fig. 7.4c.

The column-integrated total hydrometeor fields (shown in Fig. 7.5a) at the seventh hour of simulation time show that the tropical MCS is located somewhere between 150 km and -375 km. The actual boundary of the MCS varies slightly between all three experiments. Since the total hydrometeor in the figure is given in a logarithmic scale, the

increase in the number on the y axis represents an increase of an order of magnitude 10 in the actual total hydrometeor values. The new convective elements are clearly visible in the figure for both MAXSW (at 75 KM) and IRONLY (at -50 KM) simulation but are missing in the NORAD experiment at this time. In addition, there are also significant amounts of shallow convection ahead of this MCS in the MAXSW and the IRONLY case due to radiative destabilization of the clear sky atmosphere. The largest number of these shallow convective elements occurs in the IRONLY experiment.

Figure 7.5b presents the column-mean distribution of temperature across the model domain for all three experiments at the seventh hour of simulations time. While the temperature profile for the NORAD experiment is relatively flat across the model domain, the MAXSW and the IRONLY experiments, on the other hand, posses significantly more horizontal structures due to the effects of new convection in the MCS caused by the effects of radiation in the model domain. The effects are larger in the MAXSW experiment indicating stronger convection with this system. Figure 7.5b also shows the effects of infrared cooling in decreasing the overall values of mean temperature across the entire model domain of the IRONLY experiment as compared to the other two experiments. The MAXSW simulation also shows slightly cooler temperature values than the NORAD experiment in the clear sky region due to effects of the clear sky radiative cooling processes. The temperature values inside the cloudy region in both the MAXSW and the IRONLY simulations, on the other hand, are much warmer than their clear sky counterpart. This is due to the dominance of diabatic heating processes caused by the newly initialized convection associated with the MCS in both the MAXSW and the IRONLY simulation.

The effects of these temperature values and temperature gradients at this time manifest themselves in surface pressure changes (shown in Fig. 7.5c) through the hydrostatic nature of the atmosphere (i.e., the column mean temperature is inversely proportional to surface pressure). Specifically, both the MAXSW and the IRONLY experiments produce a large surface gradient from the cloudy regions to clear sky regions due to effects of new convection in the MCS caused by radiation. The NORAD experiment, on the other hand, has a relatively flat surface pressure pattern indicating lack of convection in this simulation. The cooler model temperature in the clear sky region of both the MAXSW and the

IRONLY simulations also shows up as a higher surface pressure values in Fig. 7.5c. The surface pressure values under the cloudy region, on the other hand, are lower than the clear sky values due to the effects of newly initialized convection in both MAXSW and IRONLY simulation. The surface pressure difference between the clear skies and cloudy region for both the IRONLY and the MAXSW experiments is on the order of 2 mb, which is about four to eight times larger than those found in the dry simulations of Section 7.3 and is indicative of the effects of moist processes in enhancing the strength of this cloud-radiation-induced secondary circulation.

7.3.2 WS Case

The sensitivities of the WS experiments to radiation are examined in this section. These simulations are marked by a background environment of weak vertical shear profile and stable lower levels. These experiments should show a lesser sensitivity to radiative processes if the hypothesized feedback is correct. Furthermore, this case should also have the greatest differences in the sensitivity between the IRONLY and the MAXSW experiments due to the destabilizing effects of the atmospheric infrared cooling mentioned in the previous section. The results of these experiment are presented in Fig. 7.6 and 7.7 below. Unlike the previous case, the differences in the peak vertical motion fields (given in Fig. 7.6a) between all three experiments are very small except near the end of the IRONLY experiment. Similar results are also shown in the domain-integrated total hydrometeor field (i.e., Fig. 7.6b) and the domain-integrated accumulated precipitation field (shown in Fig. 7.6c). This small sensitivity is a result of strong low level stability of the background in decoupling the feedback process between the cloud-radiative forcing and the surface source of energy through capping the secondary circulation.

According to the hypothesis, physical processes that weaken this lower level stability (i.e., infrared radiative cooling at night) can play an important role in modifying the behaviors of the tropical convection embedded in a weak shear condition by providing an unstable environment for this cloud-radiative feedback to occur. Furthermore, the hypothesis also suggests that this may lead to significant differences in the diurnal signatures of tropical convection due to the effect of solar heating in weakening this destabilizing process.

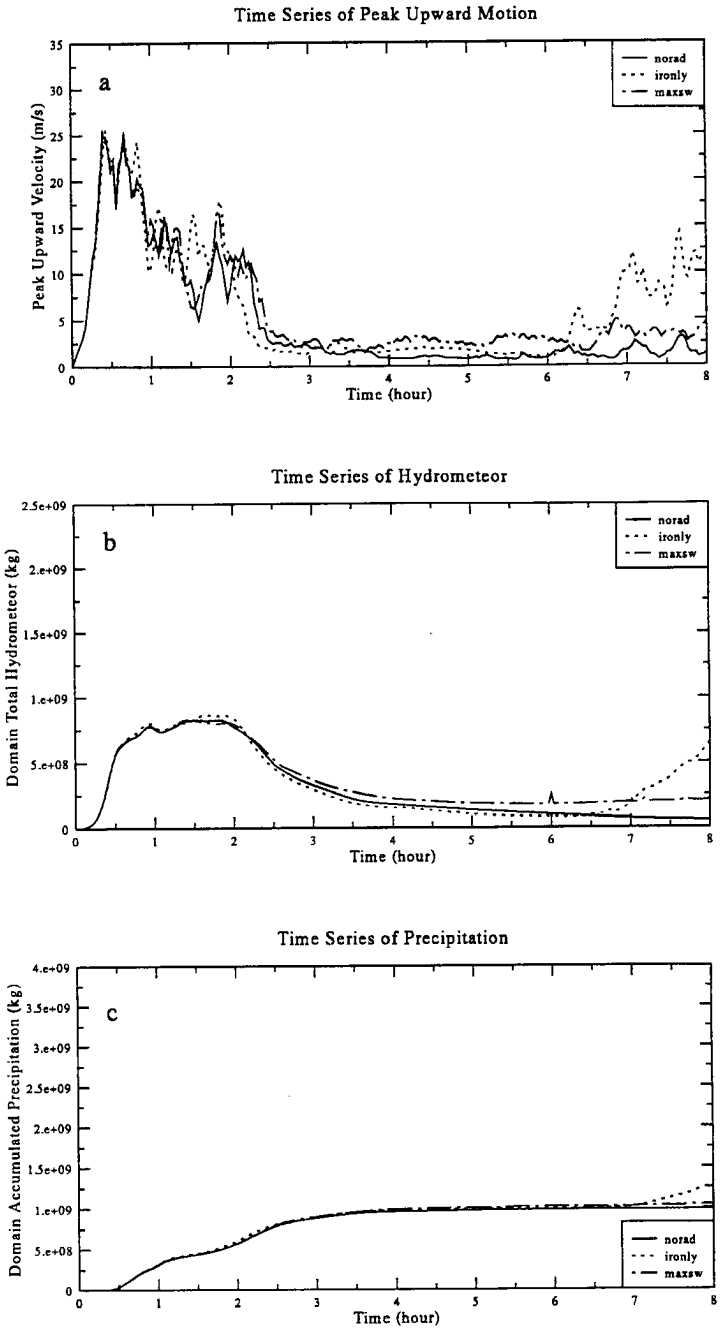

Figure 7.6: Time series of model (a) peak upward vertical motion field, (b) domain total hydrometeor field, and (c) domain accumulated surface precipitation field for the NORAD (solid line), the IRONLY (dotted line), and the MAXSW (dot-dashed line) experiments using the WS environment.

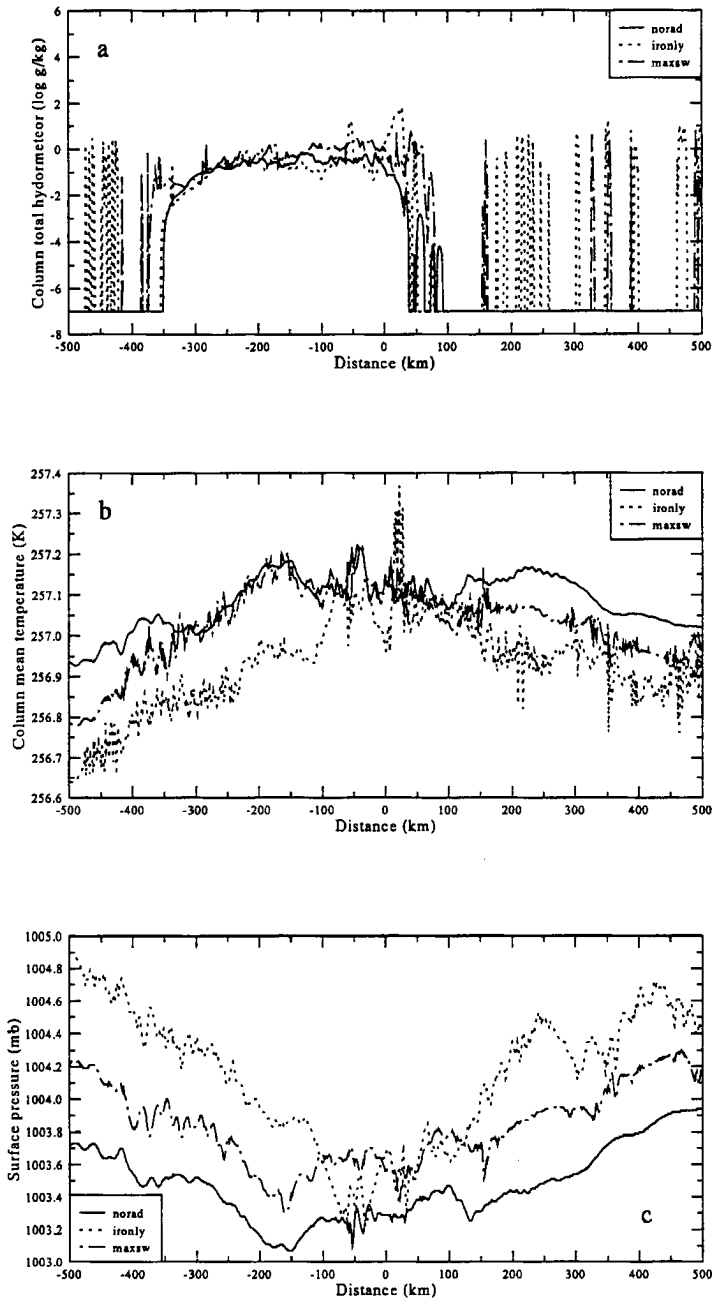

Figure 7.7: Horizontal cross section of the model (a) column integrated total hydrometeor, (b) column mean temperature, and (c) surface pressure for the NORAD (solid line, the IRONLY (dotted line) and the MAXSW (dot-dashed line) experiments after eight hours into the simulations using the WS environment

These two processes are well simulated by the cloud model. For example, the stronger sensitivity at the end of the IRONLY simulation is due to effects of infrared radiative cooling of the atmosphere at night in aiding the secondary circulation to overcome the stability of the lower level. Since the surface conditions are fixed in the model, the radiative cooling of the atmosphere decreases the atmospheric stability at night and allows the feedback between the cloud-induced radiative secondary circulation and the tropical MCS to occur. The peak vertical motion (given in Fig. 7.6a) near 7.5 hours into the IRONLY simulation is of the order of 15 m/s as compared to 3 m/s for both the MAXSW and the NORAD experiment at this time. Similar increases in the total hydrometeor and precipitation fields for the IRONLY simulation are also noted in Fig. 7.6b and c, respectively. According to these results, the combined effects of these two processes (i.e., cloud-induced secondary circulation and infrared radiative cooling) are the key in explaining the diurnal variations of tropical cloud cluster embedded in a background environments characteristized by a weak vertical shear profile and stable lower levels. To further illustrate this destabilizing effect in aiding the formation of new convection in the IRONLY experiment, the column integrated total hydrometeor fields (shown in Fig. 7.7a) at eight hours in the simulation are used. This figure shows that the tropical MCS is located somewhere between 100 km and -375 km. Shallow convection ahead of the MCS in both IRONLY and MAXSW simulations is also visible at this time due to radiative clear sky destabilization. The major differences between the three experiments are the presence of convection (at 30 km) in the IRONLY simulation. This is indicative of the effects of atmospheric infrared cooling in aiding the feedback between cloud induced radiative forcing and the tropical MCS. Similar changes are also noted in the column mean temperature (given in Fig. 7.7b) and the surface pressure field (shown in Fig 7.7c) in the IRONLY simulation. The magnitude of these changes, however, is much small than those in Fig. 7.5a (i.e., the WU case) due to the weaker convection at this time as indicated by the time series of the total hydrometeor and the precipitation field in Fig. 7.6 b and c.

7.3.3 SU Case

The sensitivities of the SU experiments to radiation are examined in this section. This set of experiments is marked by a background environment which has a high vertical shear profile and an unstable low level. It is also expected that these experiments show a reduced sensitivity to radiative processes. Unlike the previous case, the cause of this insensitivity is due to effects of strong vertical shear rather than lower level stability. The results of these experiments (i.e., NORAD, IRONLY, and MAXSW) are presented Fig. 7.8 and 7.9 below. Due to the lack of new convection (i.e., Fig. 7.9a), the sensitivity of these MCS simulations to radiation in Fig. 7.8 are very small. These results indicate the important role of shear in modifying the overall feedback processes between cloud radiative forcing and the cloud cluster. In a highly sheared environment, the radiative feedback processes are severely limited since shear distort the vertical stacking of energy underneath the cloud cluster (i.e., Fig. 7.9b) and weaken the surface pressure gradient (shown in Fig. 7.9c) that is needed to start new convection. Thus radiative processes do not play an important role in the overall system evolution of this tropical MCS simulation.

7.4 Summary

In this chapter, we investigated the role of cloud radiative feedback on the energy budget and circulation of the tropical atmosphere and the tropical cloud clusters. A hypothesized feedback, which couples the cloud radiative effects to the tropical cluster/atmosphere through interactions of surface supply of energy and differential radiative heating between clear and cloudy sky regions, is proposed. This proposed cloud-radiation coupling, which allows the feedback between cloud microphysics, radiation, thermodynamics, and dynamics, is a refinement of work by Gray and Jacobson (1977). In the current study, we have added details of the feedback process with regard to the background environmental conditions, atmospheric infrared radiative cooling, and have further expanded this feedback to include daytime case. Numerical experiments are used to illustrate this theory. The results from these experiments are consistent with the hypothesized feedback and indicate that

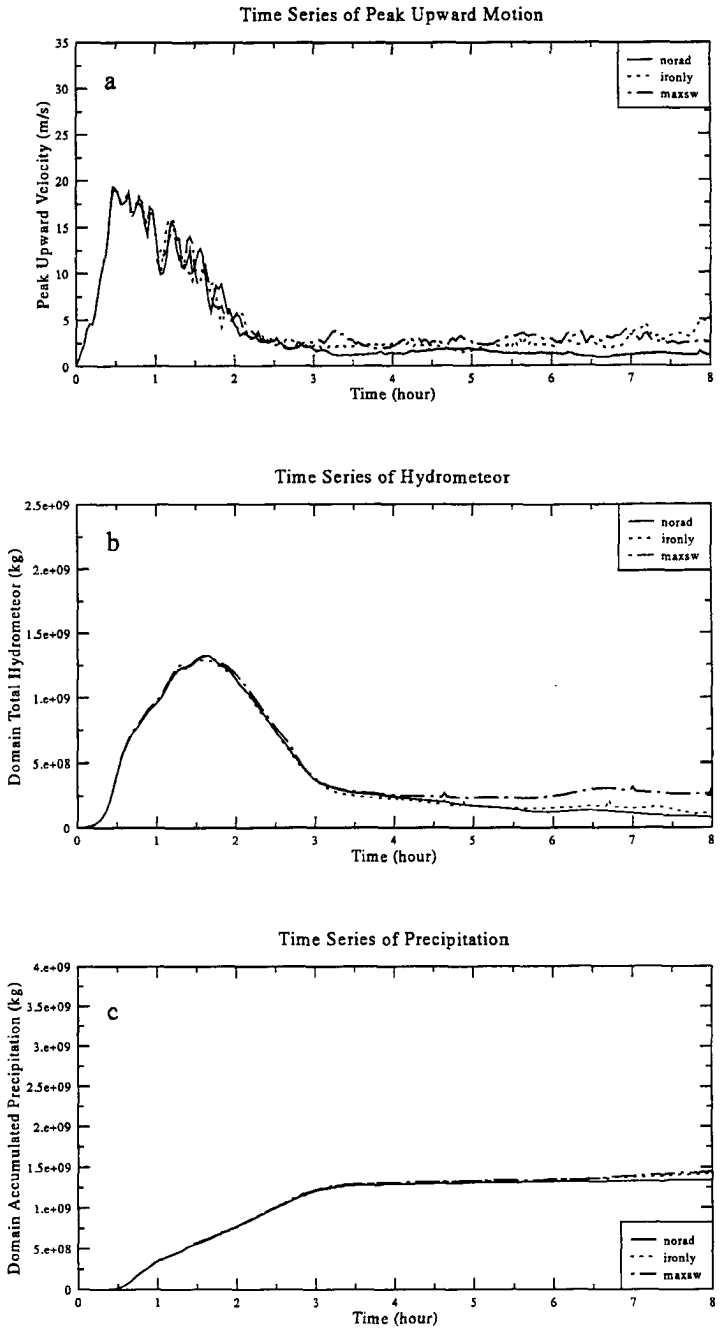

Figure 7.8: Time series of model (a) peak upward vertical motion field, (b) domain total hydrometeor field, and (c) domain accumulated surface precipitation field for the NORAD (solid line), the IRONLY (dotted line), and the MAXSW (dot-dashed line) experiments using the SU environment.

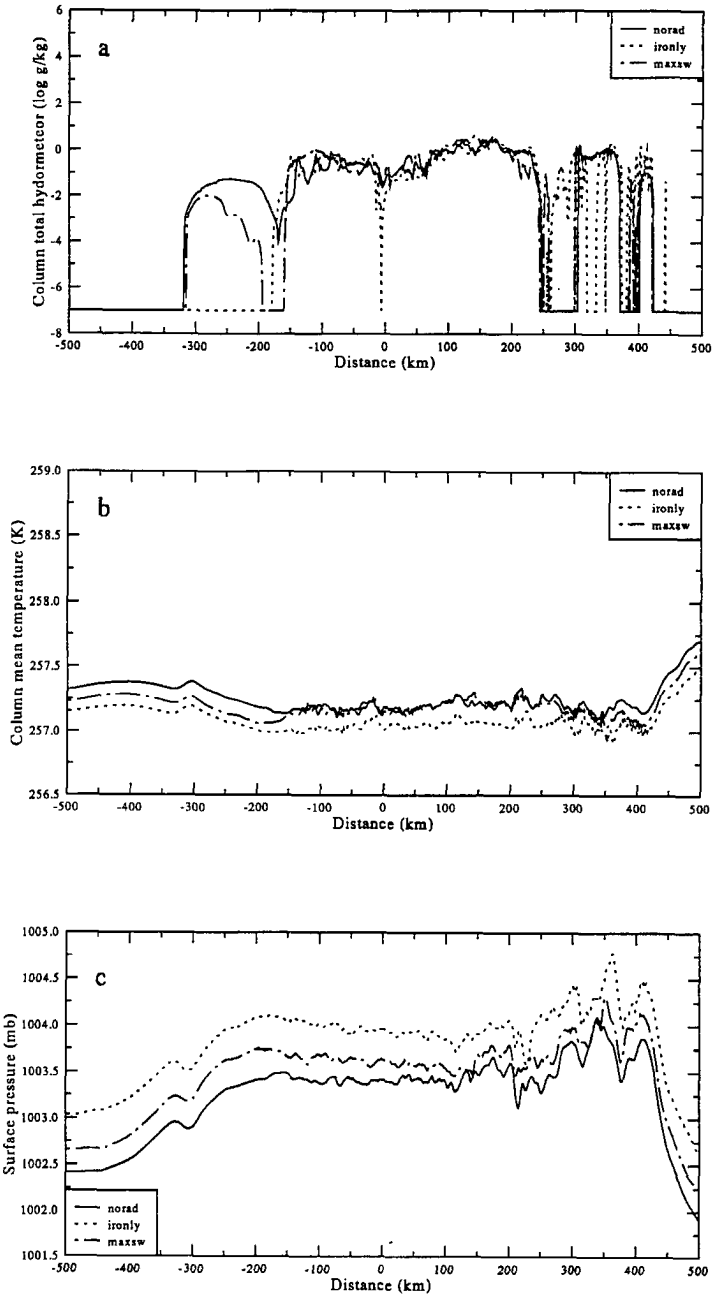

Figure 7.9: Horizontal cross section of the model (a) column integrated total hydrometeor, (b) column mean temperature, and (c) surface pressure, for the NORAD (solid line, the IRONLY (dotted line) and the MAXSW (dot-dashed line) experiments after five hours into the simulation using the SU environment

- the effects of differential radiative heating/cooling between the clear skies and the cloudy atmosphere can produce a secondary circulation which enhances surface convergence in the cloudy region.

- Under the specific background conditions, the induced secondary circulation can significantly alter the evolution and energy budgets of tropical MCS simulations by enhancing the supply of energy to the cloud clusters.

- The strength of this feedback between tropical MCSs and radiation is a function of both the vertical shear profile and the low level stability conditions of the background environments. These sensitivities arise naturally due the fact that the proposed feedback process relies on the weak surface convergence to enhance the tropical MCSs.

- This cloud-radiative coupling process is most effective in modifying the energy budget and the circulation of the tropical MCSs and their surrounding tropical atmosphere when the background atmosphere has a weak vertical shear profile and unstable lower levels. In such background environment, the results also indicate that this cloud radiative coupling process can operate in both daytime and night time conditions. Since this type of environment can be found in the TOGA-COARE region over the western Pacific ocean, it is reasonable to speculate that the diurnal differences in tropical convection may be weaker in this region.

- As the background low level stability increases, the effects of this feedback decrease. This is due to the capping effect of strong stable surface layer in limiting the cloud-radiative coupling. Physical processes (i.e., infrared radiative cooling at night) that destabilizes the lower level, however, can play an important role in modifying the tropical convection for this environment. For example, the results demonstrate that the effect of infrared radiative cooling in (a) aiding the cloud-induced secondary circulation to overcome the low level stability conditions at night and (b) leading to further enhancement of the tropical MCS through the supply of the surface energy. The combined effects of these two processes (i.e., cloud-induced secondary circulation

and infrared radiative cooling) seem to be the key in explaining the diurnal changes in tropical convections for background environments characteristized by a weak vertical shear profile and stable lower levels. Since this environment can be found in most tropical regions, this cloud-radiative feedback can lead to significant differences in the diurnal signatures of tropical convections (i.e., stronger convection in the early morning and weaker convection during the daytime). These results are consistent to the diurnal convection features observed by Gray and Jacobson (1977) and Mapes (1992).

- Furthermore, the feedback is also sensitivity to the vertical shear profile of the environment. As the shear increases, the feedback decreases. In this case, the surface convergence is severely limited since the surface low pressure beneath the cloudy region is distorted by the strong shear profile. In this situation, the intensity of this tropical convection is more likely be control by the large-scale processes. Examples of this type of profile can be found during the passage of both the monsoon systems and the westerly burst events

Chapter 8

SUMMARY AND CONCLUSION

It is generally recognized that most of the weather occurring in the tropics is associated with the passage of the tropical mesoscale convective systems (MCSs) or the tropical cloud clusters. These systems, once formed, last 6 to 12 hours and are thought to provide significant impacts on the dynamics, thermodynamics, radiation, and the water budgets of the larger-scale atmosphere. The goal of this research aims to improve the scientific understanding on the nature (i.e., spatial/temporal characteristics and variability) of the radiative heating/budget associated with these tropical MCSs and the possible effects of radiation on both the tropical atmosphere and the evolution of the tropical MCSs. A combination of cloud model simulations using the Regional Atmospheric Modeling System (RAMS), radiation calculations utilizing a detailed multiband two-stream radiation model, analyses of observation for two case studies of tropical squall line that occurred during the Equatorial Mesoscale Experiment (EMEX), the Stratospheric Tropospheric Exchange Program (STEP), the Australian Monsoon Experiment (AMEX), and the Down Under Doppler and Electricity Experiment (DUNDEE), and comparisons with other published results are used to achieve this goal.

The following sections summarizes the results obtained from this study. Conclusions and suggestions regarding further work will be given in Secs. 8.5 and 8.6, respectively.

8.1 The Observed Tropical Cloud Clusters

The observational data for two case studies of tropical squall line are obtained from field experiments (EMEX-STEP-AMEX and DUNDEE) conducted during southern hemisphere summer near or at the northern coast of Australia using various data platforms (i.e., aircraft, satellites, ships, Dopplar radar). These programs provide a unique and valuable

data set on both the structures and the evolution of these maritime and continental tropical MCSs, the larger scale environment in which they form, and the interactions between these two. These data are mainly used to provide initial conditions for the cloud cluster simulations and to facilitate intercomparisons between observations and cloud model results in this study. Data analyses of these two cases indicate striking differences in the large-scale environment in which these systems formed. For example, the EMEX case was an oceanic system and formed during the early morning in a synoptically-disturbed monsoonal condition. This strong large-scale forcing had significantly contributed to the longer life span (i.e., 12 hrs) and faster propagation speed (i.e., 12 m/s) of the EMEX system. The DUNDEE MCS, on the other hand, is initialized by the strong late-afternoon surface heating over a relatively calm and undisturbed environment of the northern Australian continent. The weaker wind condition and the lack of large-scale forcing had resulted in the slow propagation speed (i.e., 5 m/s) and the shorter life span (i.e., 6-9 hours) of the DUNDEE MCS, respectively. Although, there are significant differences in the larger-scale features of these two systems, the internal structures of these tropical MCSs exhibits qualitatively similar structures. For example, both systems had a rearward-sloping squall-type structure (i.e, 17 degree for the EMEX case and 40 degree for the DUNDEE MCS) during the mature stage and reaches an altitude of about 15-16 km. The larger slope of the DUNDEE MCS is probably due to the weak vertical shear profile of the DUNDEE atmosphere. Thus the DUNDEE convection appears to be more erect than the EMEX case. They both had a distinct convective region (i.e., 40 km wide for the EMEX case and 25 km wide for the DUNDEE case) and a trailing stratiform area, which are similar to MCSs found in the tropics and mid-latitudes. In addition, extended area of cirrus anvil cloud are observed in both MCSs. These two case also show significant cluster-to-cluster interactions and they both seem to dry out the lower atmosphere. The composite aircraft shortwave radiation data from the stratiform region shows a significant attenuation of shortwave flux through the cloud (the estimated transmission is 14% at the cloud based). The upward and downward solar flux profiles are almost parallel to each other in the atmosphere inside and below the cloud base of the EMEX cloud cluster suggesting very

little solar heating in these regions. The upward and downward infrared radiation fluxes measured in the EMEX MCS also show little infrared heating above and below the cloud cluster.

8.2 The Simulations of Tropical MCSs

The Regional Atmospheric Modeling System (RAMS) is used in simulating the structures of both the EMEX and DUNDEE cloud cluster. The information obtained from these simulations are used in the calculations of the radiative budget and radiative heating profile of these two systems. The results of the cloud model simulations for these two tropical cloud clusters, in general, agree well with observations. Some disagreements, however, do exist due to uncertainties in the initial conditions and to the two dimensionality of the cloud simulations. The simulated life cycle of these two tropical systems are very similar. Due to the strong CAPE value associated with the initial thermodynamical sounding, the simulated DUNDEE cloud cluster is significantly stronger than the EMEX simulation. However, the EMEX simulation moves much faster than the DUNDEE case due to the stronger initial wind sounding. The simulated speed of the EMEX and the DUNDEE case is 9 m/s and 4 m/s and these values are consistent with, but smaller than, the observed speed of the cloud clusters (i.e., 12 m/s for the EMEX case and 5 m/s for the DUNDEE case). The physical size of the simulated MCSs are also broadly agree with the observations. In addition, the simulated tilts of the rearward sloping convection during the mature stage of these systems are on the order of 16 degree and 45 degree for the EMEX system and the DUNDEE MCS, respectively. This is consistent with the observed slopes (i.e., 17 degree for the EMEX case and 40 degree for the DUNDEE system) in these MCSs. The simulated circulations during the mature stage of these cloud clusters show a low level inflow into the leading convection, a low level outflow behind this convection, an upper level outflow in front, and an upper level outflow to the rear. This is consistent with circulation of MCS found elsewhere in the tropics. Furthermore, the water perturbation analyses for both simulations during the decaying stage shows significant moistening aloft and drying below due to he vertical transport of water from the lower atmosphere to aloft by the cloud cluster.

8.3 The Radiative Budget/Heating Calculations Associated with the Simulated Tropical MCSs

The spatial characteristics and temporal variability of the radiative budget and radiative heating profile for the simulated EMEX and DUNDEE cloud cluster are calculated using a multiband two stream radiative model. The results of these calculations agree well with previous studies on the radiative budget of these tropical MCSs. While the influences of solar heating are significant in modifying the total (infrared plus solar) radiative budget/heating profiles of the daytime EMEX cloud cluster, the DUNDEE simulation, on the other hand, is only influenced by infrared process due to the nocturnal nature of this system. In the infrared spectrum, the effects of both the mature EMEX and the mature DUNDEE MCS are to decrease the net outgoing infrared energy to space and to increase the net infrared flux to the surface. Relative to the clear sky region, these reductions of energy loss to space can be translated into smaller column infrared cooling rates in the cloudy regions. During the daytime the presence of mature EMEX MCS can significantly decrease the shortwave transmission to the surface, increase the shortwave albedo of the atmosphere, and increase solar absorption in the atmosphere. Relative to the clear sky the effects of EMEX MCSs are to redistribute the solar heating from the surface to the upper troposphere (i.e., increasing column heating rates in the cloudy region). While the net effect of EMEX MCS during its mature stage is the reduction of total (solar plus infrared) radiation energy into the surface and the decrease of total (solar plus infrared) radiative energy loss in the atmosphere, the net effect of the mature DUNDEE MCS, on the other hand, is the increase of total (infrared only) radiation energy to the surface in addition to the decrease of total (infrared only) radiation loss in the atmosphere. The mean vertical structure of the in-cloud total (infrared plus solar or infrared only) radiative heating/cooling profile in these tropical MCSs is dominated by heating/cooling profile in the stratiform area of the cloud cluster due to the large area coverage of this region. The temporal effects of MCSs are to increase the radiative convergence/column radiative heating of the atmosphere. These effects can be larger than 1 K/day or 100 W/m^2 depending on the structures of the hydrometeor fields and the value of solar insolation. Relative to the clear sky, the presence of these tropical systems are to radiatively heat the atmosphere.

8.4 The Responses of Tropical MCSs to Radiation

According to the radiation calculations, the presence of cloud clusters can significantly influence the radiative budget and radiation heating profile of the tropical atmosphere regardless of the dynamical and thermodynamical conditions of their background environments. Once this cloud-induced radiative heat source is formed, it may act to modify the air motion and the latent energy budget within the cloud clusters further, which can lead to changes in the characteristics of these tropical MCSs. Since a positive feedback between cloud and radiation may play an important role in the overall energy budget and longevity of these cloud clusters, a more detailed study on the responses of the tropical MCS to these radiative impact is undertaken in this research. A hypothesized feedback, which is based on the interactions of surface supply of energy and differential radiative heating/cooling between the clear skies and the cloudy atmosphere, is proposed to couple the cloud radiative effect to the tropical clusters and the tropical atmosphere. This proposed cloud-radiation coupling, which allows the feedback between cloud microphysics, radiation, thermodynamics and dynamics, is a refinement of work by Gray and Jacobson (1977). In the current research, we have explored this feedback process relative to the background environmental conditions, the atmospheric infrared radiative cooling, and have further expanded this feedback to include the daytime case. Numerical simulations are used to illustrate this theory. The results from these experiments are consistent with the proposed feedback. Specifically, the strength of this feedback between tropical MCSs and radiation is a function of both the vertical shear profile and the low level stability conditions of the background environments due to the facts that the proposed feedback process relies on secondary circulation and surface convergence to enhance the tropical MCSs. This cloud microphysics-radiation-thermodynamics-dynamics coupling is most effective in modifying the energy budget and the circulation of the tropical MCSs and their surrounding tropical atmosphere when the background atmosphere has a weak vertical shear profile and an unstable low level. As the background lower levels stability or the environmental shear increases, the effects of this feedback decrease. In addition, infrared radiative cooling of the atmosphere also plays an important role in the feedback process by destabilizing the lower level of the atmosphere.

8.5 Conclusion

The basic conclusion of this work includes the following.

- Data analyses of two tropical MCSs indicate that significant similarities exist in the internal structures of these tropical systems dispute differences in the larger scale environments in which they are embedded.

- The results of the numerical cloud model simulations for these two tropical cloud clusters, in general, agree well with observation. However, some disagreements do exist. These uncertainties could be traced to the initial conditions and to the two dimensionality of the cloud simulations.

- The presence of tropical MCSs can significantly perturb the radiation budget and the radiative heating profile of both the larger scale tropical atmosphere and the surface. These perturbations can be as large as 200 and 1000 W/m^2 for the atmosphere and the surface radiation budget, respectively.

- The radiation budget and radiative heating calculations associated with tropical MCSs also indicate significant spatial variability/inhomogeneity due mostly to changes in the structures of hydrometeors within these cloud systems. This suggests the importance of microphysical process in modifying the overall radiative budgets of the tropical MCSs.

- While the major effect of tropical MCSs in the infrared spectrum is to decrease the net outgoing radiative energy to space and to increase the net infrared flux to the surface, the consequences on solar heating are to redistribute the vertical solar heating from the surface to the upper troposphere through reduction in surface solar insolation and an increase of solar absorption in the atmosphere.

- The temporal radiative effects of these MCSs on larger scale atmosphere are the increases in the domain average radiative convergence/column radiative heating with time. These increases are due mainly to increases in cloudiness (i.e., larger infrared

greenhouse effects) and secondary to the increases in solar insolation (i.e., larger value of in cloud solar absorptions).

- While the combined effects of both solar and infrared processes can create an area of positive energy surplus in the atmosphere underneath the cloud clusters during the daytime hours, the greenhouse effects of these tropical systems can cause an area of relative energy surplus in the cloudy region with respect to the clear skies. These energy sources in the atmosphere are shown to be important in modifying the structures and evolution of the tropical MCSs for background environments characteristized by a weak vertical shear and unstable lower levels.

- The effects of differential radiative heating/cooling between the clear sky and the cloudy atmosphere can produce a secondary circulation which enhances surface convergence and upward vertical motion in the cloudy region. These results are consistence with the proposed cloud-induced secondary circulations of Gray and Jacobson (1977). Although the strength of this circulation and its resultant surface convergence is not very strong, under specific background conditions (i.e., weak vertical shear and unstable lower levels), this induced secondary circulation can significantly alter the evolution and energy budgets of tropical MCS simulations by enhancing the supply of energy to the cloud clusters. This supply significantly extends the lifetime of these systems during both daytime and night time conditions. Since a large part of the western Pacific region, including the TOGA-COARE area, is characteristized by a very unstable lower level and weak vertical shear profile, the cloud radiative feedback described in this research can play an important role in the energy and water budget of this region. In addition, it is also reasonable to speculate that the diurnal differences in tropical convection may be weaker in this region.

- In addition, the combined effects of infrared radiative cooling in the atmosphere and cloud induced secondary circulation are also shown to enhance the night time MCSs for background environments characteristized by a weak vertical shear and stable lower levels. During the daytime, the lack of atmospheric destabilizing effects by the

radiative cooling severely limits the cloud feedback in these environments since the cloud-induced secondary circulation is unable to break through the stable lower levels. Since a large portion of the tropical oceanic regions are characteristized by weak vertical shear profile and stable lower levels, the combined effects of atmospheric radiative cooling and cloud induced secondary circulation can play a significant role in the understanding of the diurnal variations of tropical convections in these regions.

- These sensitivities may also have important consequences in the modeling of the equilibrium regional climate system using cloud-resolving numerical model (i.e., Lau *et al.*, 1993) since the final solutions of these regional climate simulations may be sensitive to the initial profile of wind shear and lower level stability due to cloud radiative interaction.

8.6 Suggestions and Comments

Although the results of this study point to the importance of radiative effects in modifying both the radiative budget/heating profile of the tropical atmosphere and the evolution of tropical MCSs, additional work is still needed to provide further evidence and support for these cloud-radiative interactions. Particularly,

- Additional cloud simulations based on a three dimensional (3-D) frame work are also desirable to improve model simulations and radiative budget and heating calculation. Statistical information from these 3-D simulations (i.e., radiation, Q1, Q2, and mass divergence field) can also be used for direct comparison with the observations.

- Further budget analyses of tropical MCSs (i.e., water and energy budgets) using better temporal resolution is also needed to capture the detailed effects of radiation in these cloud clusters.

- Since hydrometeors play an important role in the radiative budget and radiative heating profile of these tropical MCSs, more detailed studies on the microphysical processes within these tropical MCSs are also desired to improve the radiative calculations of these systems.

- There is a need to improve the quality of the radiation calculations in the numerical model to include effects of cloud inhomogeneity. Horizontal radiative forcing may be important in these tropical MCS due to their large horizontal sizes.

- Finally, additional observational studies and model simulations (i.e., on the cloud scale and on the scale of the general circulation) are also desirable to address the frequency of the cloud-radiative interaction described in this work and their effects on the energy budget of the tropical atmosphere.

REFERENCES

Ackerman, T. P., K. -N. Liou, F. P. J. Valero, and L. Pfister, 1988: Heating rates in tropical anvils. *J. Atmos. Sci.*, **45**, 1606-1623.

Albrecht, B., and S. K. Cox, 1975: The large-scale response of the tropical atmosphere to cloud-modulated infrared heating. *J. Atmos. Sci.*, **32**, 16-24.

Arakawa, A., and V. R. Lamb, 1977: Computational design of the basic dynamical processes of the UCLA circulation model. *Methods in Computational Physics*, **17**, Academic Press, 173-265.

Arhrens, C.D., 1982: Meteorology Today: An introduction to weather, climate and the environment. *West Publishing Company.*

Barker, H. W., 1992: solar radiative transfer through clouds possessing isotropic variable extinction coefficient. *Quart. J. Roy. Meteor. Soc.*, **118**, 1145-1162.

Brown, J. M., 1979: Mesoscale unstaturated downdrafts driven by rainfall evaporation: A numerical study. *J. Atmos. Sci.*, **36**, 313-338.

Carlson, T., and J. Prospero, 1977: Saharan air outbreaks: Meteorology, aerosals, and radiation. *Report of the U.S. GATE Central Program Workshop, Boulder, Colorado*, 57-58.

Cifelli, R., and S. A. Rutledge, 1993: Vertical motion structure in maritime continent mesoscale convective system: Results from a 50 MHZ profiler. *Accepted by J. Atmos. Sci.*

Chang, C.-P., 1976: Vertical structure of tropical waves maintained by internally-induced cumulus heating *J. Atmos. Sci.*, **33**, 729-739.

Charney, J. G., and A. Eliassen, 1964: On the growth of the hurricane depression. *J. Atmos. Sci.*, **21**, 68-75.

Chauzy, S., M. Chong, A. Delannoy, and S. Despiau, 1985: The June 22 tropical squall line observed during COPT 81 experiment: Electrical signature associated with dynamical structure and precipitation. *J. Geophys. Res.*, **90**, 6091-6098.

Chen, C., and W. R. Cotton, 1983: A one-dimensional simulation of the stratocumulus-capped mixed layer. *Bound.-Layer Meteor.*, **25**, 289-321.

Chen, C., and W. R. Cotton, 1987: The Physics of the marine marine stratocumulus-capped mixed layer. *J. Atmos. Sci.*, **44**, 2951-2977.

Chen, S., and W. R. Cotton, 1988: The sensitivity of a simulated extratropical mesoscale convective system to longwave radiation and ice-phase microphysics. *J. Atmos. Sci.*, **45**, 3897-3910.

Chong, M., P. Amayenc, G. Scialom, and J. Testud, 1987: A tropical squall line observed during the COPT81 experiment in West Africa. Part I: Kinematic structure inferred from dual-doppler radar data. *Mon. Wea. Rev.*, **115**, 670-694.

Chou, M.-D., 1984: Broadband water vapor transmission functions for atmospheric IR flux computations. *J. Atmos. Sci.*, **41**, 1775-1778.

Chou, M.-D., 1990: Parameterizations for the absorption of solar radiation by O_2 and CO_2 with application to climate studies. *J. Climate*, **3**, 209-217.

Chou, M.-D., and A. Arking, 1980: Computation of infrared cooling rates in the water vapor bands. *J. Atmos. Sci.*, **37**, 855-867.

Chou, M.-D., and A. Arking, 1981: An efficient method for computing the absorption of solar radiation by water vapor. *J. Atmos. Sci.*, **38**, 798-807.

Chou, M.-D., and L. Peng, 1983: A parameterization of the absorption in the 15 μm spectral region with application to climate sensitivity studies. *J. Atmos. Sci.*, **40**, 2183-2192.

Churchill, D. D., and R. A. Houze, Jr., 1991: Effects of radiation and turbulence on the diabatic heating and water budget of the stratiform region of a tropical cloud cluster. *J. Atmos. Sci.*, **48**, 903-922.

Churchill, D. D., and R. A. Houze, Jr., 1984: Development and structure of winter monsoon cloud clusters on 10 December 1978. *J. Atmos. Sci.*, **41**, 933-960.

Clark, T. L., 1977: A small-scale dynamic model using a terrain-following coordinate transformation. *J. Comput. Phys.*, **24**, 186-215.

Cotton., W. R., and G. J. Tripoli, 1978: Cumulus convection in shear flow: Three dimensional numerical experiments. *J. Atmos. Sci.*, **35**, 1503-1521.

Cotton, W. R., M. A. Stephens, T. Nehrkorn, and G. J. Tripolie, 1982: The Colorado State University three-dimensional cloud/mesoscale model-1982, Part II: An ice parameterization. *J. Rech. Atmos.*, **16**, 295-320.

Cotton, W. R., G. J. Tripoli and R. M. Rauber, 1986: Numerical simulation of the effects of varying ice crystal nucleation rates and aggregation processes on orographic snowfall. *J. Climate Appl. Meteor.*, **25**, 1658-1680.

Cotton, W. R., and R. A. Anthes, 1989: Storm and Cloud Dynamics. *Academic Press*, New York, 883pp.

Cox, S. K., and K. T. Griffith, 1978: Estimates of radiative divergence during Phase III of the GARP Altantic Tropical Experiment: II. Analysis of Phase III results. *J. Atmos. Sci.*, **36**, 586-601.

Cram, J. M., R. A. Pielke, and W. R. Cotton, 1992: Numerical simulations and analysis of a prefrontal squall line. I: Observations and basic simulation results. *J. Atmos. Sci.*, **49**, 189-208.

Danielson, E. F., 1982: A dehydration mechanism for the stratosphere. *Geophy. Res. Letters*, **9**, 605-608.

Davis, J. M., T. B. McKee, and S. K. Cox, 1978: Solar absorption in clouds of finite horizontal extent. Atmos. Sci. Pap. No. 282, Colorado State University, 92 pp.

Dudhia, J., 1989: Numerical study of convection observed during the Winter Monsoon Experiment using a mesoscale two-dimensional model. *J. Atmos. Sci.*, **46**, 3077-3109.

Dutton, J. A., and G. H. Fichtl, 1969: Approximate equations of motion for gases and liquids. *J. Atmos. Sci.*, **26**, 241-254.

Gamache, J. F., and R. A. Houze, Jr., 1982: Mesoscale air motions associated with a tropical squall line. *Mon. Wea. Rev.*, **110**, 118-135.

Gamache, J. F., and R. A. Houze, Jr., 1983: Water budget of a mesoscale convective system in the tropics. *J. Atmos. Sci.*, **40**, 1835-1850.

Gamache, J. F., and R. A. Houze, Jr., 1985: Further analysis of the composite wind and thermodynamic structure of the 12 September GATE Squall line. *Mon. Wea. Rev.*, **113**, 1241-1259.

Gal-Chen, Tzvi, and R. C. J. Somereville, 1975: On the use of a corrdinate transformation for the solution of the Navier-Stokes equations. *J. Comput. Phys.*, **17**, 209-228.

Gray, W. M., and R. W. Jacobson, Jr., 1977: Diurnal variation of deep cumulus convection. *Mon. Wea. Rev.*, **105**, 1171-1188.

Hamilton, R. A., and J. W. Archbold, 1945: Meteorology of Nigeria and adjacent territory. *Quart. J. Roy. Meteor. Soc.*, **71**, 231-262.

Harshvardhan, and M. D. King, 1993: Comparative accuracy of diffuse radiative properties computed using selective multiple scattering approximations. *J. Atmos. Sci.*, **50**, 247-259.

Hartmann, D. L., H. H. Hendon, and R. A. Houze, Jr., 1984: Some implications of the mesoscale circulations in tropical cloud clusters for large-scale dynamics and climate. *J. Atmos. Sci.*, **41**, 113-121.

Heymsfield, A. J., K. M. Miller, and J. D. Spinhirne, 1990: The October 27-28, 1986, FIRE IFO cirrus case study: cloud microstructure. *Mon. Wea. Rev.*, **118**, 2313-2328.

Hill, G. E., 1974: Factors controlling the size and spacing of cumulus clouds as revealed by numerical experimentsx. *J. Atmos. Sci.*, **31**, 646-673.

Holland, G. J., J. L. McBride, R. K. Smith, D. Jasper, and T. D. Keenan, 1986: The BMRC Australian Monsoon Experiment: AMEX. *Bull. Amer. Metero. Soc.*, **67**, 1466-1472.

Houze, R. A., Jr., 1976: GATE radar observations of a tropical squall line. *Preprints 17th conf. Radar Meteorology*, Seattle, Amer. Meteor. Soc., 384-389.

Houze, R. A., Jr., 1977: Structure and dynamics of a tropical squall-line system. *Mon. Wea. Rev.*, **105**, 1540-1567.

Houze, R. A., Jr., 1982: Cloud clusters and large-scale vertical motions in the tropics. *J. Meteor. Soc. Japan*, **60**, 396-410.

Houze, R. A., Jr., 1989: Observed structure of mesoscale convective systems and implications for large-scale heating. *Quart. J. Roy. Meteor. Soc.*, **115**, 425-461.

Houze, R. A., Jr., P. V. Hobbs, P. H. Herzegh and D. B. Parson, 1979: Size distributions of precipitation particles in frontal clouds. *J. Atmos Sci.*, **36**, 156-162.

Houze, R. A., Jr., and A. K. Betts, 1981: Convection in GATE. *Rev. Geophys. Space Phys.*, **19**, 541-576.

Houze, R. A., Jr., and E. N. Rappaport, 1984: Air motions and precipitation structure of an early summer squall line over the eastern tropical Atlantic. *J. Atmos. Sci.*, **41**, 553-574.

Houze, R. A., Jr., S. J. Bograd, and B. Mapes, 1988, An atlas of horizontal patterns of radar reflectivity observed during EMEX aircraft missions. Department of Atmospheric Sciences, University of Washington.

Johnson, R. H., and P. J. Hamiltion, 1988: The relationship of surface pressure features to the precipitation and air flow structure of an intense midlatitude squall line. *Mon. Wea. Rev.*, **116**, 1444-1472.

Jonhson, R. H., 1982: Vertical motion in near-equatorial winter monsoon convection. *J. Meteor. Soc. Jpn.*, **60**, 682-690.

King, D. M., and Harshvardhan, 1986: Comparative accuracy of selected multiple scattering approximations. *J. Atmos. Sci.*, **43**, 784-801.

Klemp, J. B., and D. K. Lilly, 1978: Numerical simulation of hydrostatic mountain waves. *J. Atmos. Sci.*, **35**, 78-107.

Klemp, J. B., and R. B. Wilhelmson, 1978: simulations of right- and left-moving storms produced through storm splitting. *J. Atmos. Sci.*, **35**, 1097-1110.

Kneizys, F. X., E. P. Shettle, W. O. Gallery, J. H. Chetwynd, Jr., L. W. Abreu, J. E. A. Selby, R. W. Fenn, and R. A. McClatchey, 1980: Atmospheric transmittance/radiance: computer code LOWTRAN 5. Report No. AFGL-TR-80-0067, Air Force Geophysics Lab, Hanscom AFB, Ma., 200pp.

Lafore, J.-P., and M. W. Moncrieff, 1989: A numberical investigation of the organization and interaction of the convective and stratiform regions of tropical squall lines. *J. Atmos. Sci.*, **46**, 521-544.

Lau, K. M., C. H. Sui, and W. K. Tao, 1993: A preliminary study of the tropical water cycle and its sensitivity to surface warming. *Bull. Amer. Metero. Soc.*, **74**, 1313-1321.

Leary, C. A., and R. A. Houze, Jr., 1979: Melting and evaporation of hydrometeors in precipitation from the anvil clouds of deep tropical cumulonimbus anvils. *Geophys. Res. Lett.*, **6**, 613-616.

LeMone, M. A., 1983: Momentum flux by a line of cumulonimbus. *J. Atmos. Sci.*, **40**, 1815-1834.

Lilly, D. K., 1967: The representation of small-scale turbulence in numerical simulation experiments. *Proc. IBM Sci. Comput. Symp. Environ. Sci.*

Lilly, D. K., 1988: Cirrus outflow dynamics. *J. Atmos. Sci.*, **45**, 1594-1605.

Lindzen, R. S., 1974: Wave-CISK in the tropic *J. Atmos. Sci.*, **31**, 156-179.

Liou, K.-N., 1980: Introduction to atmospheric radiation. *Academic Press.*

Lious, J. F., 1979: A parametric model of vertical eddy fluxes in atmosphere. *Boundary-Layer Meteorol.*, **17**, 187-202.

Manton, M. J., and W. R. Cotton, 1977: Parameterization of the atmospheric surface layer. *J. Atmos. Sci.*, **34**, 331-334.

Mapes B. E., and R. A. Houze, Jr., 1992: Cloud cluster and superclusters over the oceanic warm pool. *Mon. Wea. Rev.*, **121**, 1398-1415.

Moncrieff, M. W., and M. J. Miller, 1976: The dynamics and simulation of tropical cumulonimbus and squall lines. *Q. J. R. Meteorol. Soc.*, **102**, 373-394.

Nicholls, M. E., 1987: A comparison of the results of a two-dimensional numerical simulation of a tropical squall line with observations. *Mon Wea. Rev.*, **115**, 3055-3077.

Nicholls, M. E., and M. J. Weissbluth, 1988: A comparison of two-dimensional and quasi-three-dimensional simulations of a tropical squall line. *Mon. Wea. Rev.* **116**, 2437-2452.

Nitta, T., and S. Esbensen, 1974: Heat and moisture budget analyses using BOMEX data. *Mon. Wea. Rev.*, **102**, 17-28.

Ockert-Bell, M. E., and D. L. Hartmann, 1992: The effect of cloud type on the earth's energy balance: Results for selected regions. *J. Clim.*, **5**, 1157-1171.

Ooyama, K., 1964: A dynamical model for the study of tropical cyclone development. *Geofis. Int.*, **4**, 187-198.

Paltridge, G. W., and C. M. R. Platt, 1976: Radiative processes in meteorology and climatology. *Elsevier*, 318pp.

Pielke, R. A., W. R. Cotton, R. L. Walko, C. J. Tremback, W. A. Lyons, L. D. Grasso, M. E. Nicholls, M. D. Moran, D. A. Wesley, T. J. Lee, and J. H. Copeland, 1992: A comprehensive meteorological modeling system - RAMS. *Meteorol. Atmos. Phys.*, **49**, 69-91.

Ramage, C. S., 1971: Monsoon Meteorology. *Academic Press*, New York, 296pp.

Ramanathan, V., and W. Collins, 1991: Thermodynamic regulation of ocean warming by cirrus clouds detected from observations of the 1987 El Nino. *Nature*, **37-6321**, 27-32.

Ramaswamy, V., and Freidenreich, S. M., 1991: Solar radiative line-by-line determination of water vapor absorption and water cloud extinction in inhomogeneous atmospheres. *J. Geophys. Res.*, **96(D5)**, 9133-9157.

Riehl, H., and J. S., Malkus, 1958: On the heat balance in the equatorial trough zone. *Geophysica*, **6**, 503-538.

Riehl, H., and J. S., Malkus, 1961: Some aspects of hurricane Daisy. *Tellus*, **13**, 181-213.

Roberts, R. E., J. E. A. Selby and L. M. Biberman, 1976: Infrared continuum absorption by atmospheric water vapour in the 8-12 micron window. *Appl. Opt.*, **15**, 2085-2090.

Russell, P. B., E. F. Danielsen, R. A. Craig, and H. B. Selkirk, 1991: The NASA Spring 1984 Stratosphere-Troposphere Exchange Experiment: Science Objectives and Operations. *J. Geophy. Res.*, **96, D9**, 17401-17404.

Russell, P. B., L. Pfister, and H. B. Selkirk, 1993: The Tropical Experiment of the Stratosphere-Troposphere Exchange Project (STEP): Science Objectives, Operations, and Summary Findings.*J. Geophy. Res.*, **98, D5**, 8563-8589.

Rutledge, S. A., 1986: A diagnostic modeling study of the stratiform region associated with a tropical squall line. *J. Atmos. Sci.*, **43**, 1356-1377.

Rutledge, S. A., E. R. Williams, and T. D. Keenan, 1992: The Down Under Doppler and Electricity Experiment (DUNDEE): Overview and preliminary results. *Bull. Am. Meteorol. Soc.*, **73**, 3-16.

Simpson, J., R. F. Adler, and G. R. North, 1988: A proposed tropical rainfall measuring mission (TRMM) satellite. *Bull. Amer. Meteor. Soc.*, **69**, 278-295.

Slingo, and H. M. Schrecker, 1982: On the shortwave properties of stratiform water clouds. *Quart. J. Roy. Meteor. Soc.*, **108**, 407-426.

Srivastava, R. C., T. J. Matejka, and T. J. Lorello, 1986: Doppler radar study of the trailing anvil region associated with a squall line. *J. Atmos. Sci.*, **43**, 356-377.

Stackhouse, P. W., Jr, and G. L. Stephens, 1991: A theoretical and observational study of the radiative properties of cirrus: Results from FIRE 1986. *J. Atmos. Sci.*, **48**, 2044-2059.

Stackhouse, P. W., Jr, and G. L. Stephens, 1989: A theoretical and observational comparision of cirrus cloud radiative properties. Paper no. 452, Department of Atmospheric Science, Colorado State University, 117pp.

Stamnes, K., and S.-C. Tsay, 1991: Optimum spectral resolution for computing atmospheric heating and photodissociation rates. *Submitted to J. Spect. Rad. Transf.*

Stephens, G. L., 1978: Radiative properties of extended water cloud: II Parameterization. *J. Atmos. Sci.*, **35**, 2123-2132.

Stephens, G. L., and T. J. Greenwald, 1991: The earth's radiation budget and its relation to atmospheric hydrology. Part II: Observation of cloud effects. *Accepted by J. Geophy. Res.*

Stephens, G. L., and K. J. Wilson, 1980: Response of a deep cumulus convection model to changes in radiative heating. *J. Atmos. Sci.*, **37**, 421-434.

Stevens, D. E., R. S. Lindzen, and L. J. Shapiro, 1977: A new model of tropical waves incorporating momentum mixing by cumulus convection. *Dyn. Atmos. Oceans*, **1**, 365-425.

Stuhlmann, R., and G. L. Smith, 1988a: A study of cloud-generated radiative heating and its generation of available potential energy. Part I: Theoretical background. *J. Atmos. Sci.*, **45**, 3911-3927.

Stuhlmann, R., and G. L. Smith, 1988b: A study of cloud-generated radiative heating and its generation of available potential energy. Part II: Results for a climatological zonal mean January. *J. Atmos. Sci.*, **45**, 3928-3943.

Takano Y., and K.-N. Liou, 1989: Solar radiative transfer in cirrus clouds. I. Single-scattering and optical properties of hexagonal ice crystal. *J. Atmos. Sci.*, **46**, 3-19.

Tao, W.-K., J. Simpson, and S.-T. Soong, 1987: Statistical properties of a cloud ensemble: A numerical study. *J. Atmos. Sci.*, **44**, 3175-3187.

Tao, W.-K., J. Simpson, C.-H. Sui, B. Ferrier, S. Lang, J. Scala, M.-D. Chou, and K. Pickering, 1993: Heating, moisture, and water budgets of tropical and midlatitude squall lines: Comparisons and sensitivity to longwave radiation. *J. Atmos. Sci.*, **50**, 673-690.

Thorpe, A. J.,, M. J. Miller, and M. W. Moncrieff, 1982: Two-dimensional convection in non-constant shear: A model of mid-latitude squall lines. *Q. J. R. Meteorol. Soc.*, **108**, 739-762.

Tripoli, G. J., 1986: A numerical investigation of an orogenic mesoscale convection system. PH.D. Thesis, Dep. Atmos. Sci., Colorado State Univ.

Tripoli, G. J., and W. R. Cotton, 1980: A numerical investigation of several factors contribution to the observed variable intensity of deep convection over Florida. *J. Appl. Meteor.*, **19**, 1037-1063.

Tripoli, G., J., and W. R. Cotton, 1981: The use of ice-liquid water potential temperature as a thermodynamic variable in deep atmospheric models. *Mon. Wea. Rev.*, **109**, 1094-1102.

Tripoli, G., J., and W. R. Cotton, 1982: The Colorado State University three-dimensional cloud/mesoscale model-1982. Part I: General theoretical framework and sensitivity experiments. *J. Rech. Atmos.*, **16**, 185-220.

Wallace, J. M., and P. V. Hobbs, 1979: Atmospheric science: An introductory survey. *Academic Press.*

Webster, P. J., and G. L. Stephens, 1980: Tropical upper-tropospheric extended clouds: Inferences from winter MONEX. *J. Atmos. Sci.*, **37**, 1521- 1541.

Webster, P. J., and R. A. Houze, Jr., 1991: The Equatorial Mesoscale Experiment (EMEX): An Overview. *Bull. Amer. Meteor. Soc.*, **72**, 1481-1505.

William, M., and R. A. Houze, Jr., 1987: Satellite-observed characteristics of winter monsoon cloud cluster. *Mon. Wea. Rev.*, **115**, 505-519.

Xu, K.-M., and S. K. Krueger, 1991: Evaluation of cloudiness parameterizations using a cumulus ensemble model. *Mon. Wea. Rev.*, **119**, 342-367.

Yamasaki, M., 1969: Large-scale disturbances in the conditional unstable atmosphere in low latitudes. *Pap. Meteorol. Geophys.*, **20**, 298-336.

Yanai, M., S. Esbensen, and J. Chu, 1973: Determination of bulk properties of tropical cloud clusters from large-scale heat and moisture budget. *J. Atmos. Sci.*, **30**, 611-627.

Zipser, E. J., 1977: Mesoscale and convective-scale downdrafts as distinct components of squall line structure. *Mon. Wea. Rev.*, **105**, 1568-1589.

Appendix A

TABLES OF SPECTRAL OPTICAL CONSTANTS

Table A.1: Spectral optical properties of cloud droplets

No.	Bandwidth (cm^{-1})	Ext ($km^{-1}\frac{g}{m^3}^{-1}$)	ω_o	gg
1	20 – 340	9.85302e+01	0.374492	0.365
2	340 – 540	1.28484e+02	0.463252	0.752
3	540 – 620	1.21307e+02	0.457336	0.816
4	620 – 720	1.15363e+02	0.454763	0.854
5	720 – 800	1.07187e+02	0.443059	0.881
6	800 – 980	1.05252e+02	0.498768	0.910
7	980 – 1100	1.33598e+02	0.667443	0.909
8	1100 – 1380	1.29327e+02	0.658374	0.885
9	1380 – 1900	1.19074e+02	0.623883	0.881
10	1900 – 2620	1.14684e+02	0.760810	0.831
11	2600 – 3300	1.11748e+02	0.667483	0.879
12	3300 – 4000	1.09370e+02	0.646314	0.927
13	4000 – 4600	1.09478e+02	0.951917	0.850
14	4600 – 5300	1.08458e+02	0.926371	0.854
15	5300 – 6000	1.07494e+02	0.984570	0.846
16	6000 – 7000	1.07189e+02	0.978996	0.851
17	7000 – 12850	1.05283e+02	0.998128	0.855
18	12850 – 13150	1.04392e+02	0.999965	0.860
19	13150 – 14300	1.04183e+02	0.999975	0.861
20	14300 – 14450	1.04053e+02	0.999992	0.862
21	14450 – 14550	1.04048e+02	0.999994	0.862
22	14550 – 25000	1.03364e+02	0.999999	0.866
23	25000 – 31746	1.02538e+02	0.999997	0.868
24	31746 – 35710	1.02303e+02	0.999992	0.868

Table A.2: Spectral optical properties of raindrops

No.	Bandwidth (cm^{-1})	Ext ($km^{-1}\frac{g}{m^3}^{-1}$)	ω_o	gg
1	20 – 340	2.51192e+00	0.561701	0.883
2	340 – 540	2.40376e+00	0.558350	0.928
3	540 – 620	2.38763e+00	0.557200	0.935
4	620 – 720	2.37931e+00	0.551720	0.946
5	720 – 800	2.37126e+00	0.542556	0.961
6	800 – 980	2.36667e+00	0.523852	0.981
7	980 – 1100	2.3673e+00	0.524433	0.980
8	1100 – 1380	2.36285e+00	0.529516	0.973
9	1380 – 1900	2.35563e+00	0.532089	0.970
10	1900 – 2620	2.34917e+00	0.535869	0.967
11	2600 – 3300	2.34443e+00	0.544206	0.953
12	3300 – 4000	2.34043e+00	0.532288	0.972
13	4000 – 4600	2.33898e+00	0.579787	0.950
14	4600 – 5300	2.33728e+00	0.560736	0.956
15	5300 – 6000	2.33575e+00	0.726239	0.917
16	6000 – 7000	2.33438e+00	0.677990	0.924
17	7000 – 12850	2.33103e+00	0.958144	0.889
18	12850 – 13150	2.32908e+00	0.998641	0.885
19	13150 – 14300	2.32873e+00	0.999038	0.885
20	14300 – 14450	2.32851e+00	0.999683	0.885
21	14450 – 14550	2.32842e+00	0.999730	0.885
22	14550 – 25000	2.32706e+00	0.999934	0.884
23	25000 – 31746	2.32531e+00	0.999835	0.881
24	31746 – 35710	2.32483e+00	0.999629	0.879

Table A.3: Spectral optical properties of ice crystals

No.	Bandwidth (cm^{-1})	Ext ($km^{-1}\frac{g}{m^3}^{-1}$)	ω_o	gg
1	20 – 340	4.23720e+01	0.569121	0.296
2	340 – 540	4.65846e+01	0.641416	0.593
3	540 – 620	4.51557e+01	0.551421	0.669
4	620 – 720	4.39810e+01	0.524670	0.746
5	720 – 800	4.26316e+01	0.517073	0.785
6	800 – 980	3.96638e+01	0.500670	0.824
7	980 – 1100	4.27036e+01	0.561704	0.852
8	1100 – 1380	4.26357e+01	0.558005	0.849
9	1380 – 1900	4.15348e+01	0.546718	0.869
10	1900 – 2620	4.07039e+01	0.595295	0.831
11	2600 – 3300	4.00394e+01	0.585872	0.854
12	3300 – 4000	3.93595e+01	0.657257	0.917
13	4000 – 4600	3.96096e+01	0.907854	0.847
14	4600 – 5300	3.91383e+01	0.810024	0.847
15	5300 – 6000	3.92534e+01	0.951150	0.840
16	6000 – 7000	3.90356e+01	0.894511	0.846
17	7000 – 12850	3.87060e+01	0.997735	0.854
18	12850 – 13150	3.84836e+01	0.999927	0.860
19	13150 – 14300	3.84657e+01	0.999959	0.861
20	14300 – 14450	3.84452e+01	0.999975	0.862
21	14450 – 14550	3.84383e+01	0.999977	0.863
22	14550 – 25000	3.82945e+01	0.999994	0.866
23	25000 – 31746	3.81171e+01	0.999985	0.866
24	31746 – 35710	3.80705e+01	0.999966	0.864

Table A.4: Spectral optical properties of aggregates

No.	Bandwidth (cm^{-1})	Ext ($km^{-1}\frac{g}{m^3}^{-1}$)	ω_o	gg
1	20 – 340	1.24569e+00	0.571569	0.911
2	340 – 540	1.22669e+00	0.549030	0.942
3	540 – 620	1.22403e+00	0.553386	0.936
4	620 – 720	1.22288e+00	0.557067	0.931
5	720 – 800	1.22190e+00	0.561502	0.927
6	800 – 980	1.22033e+00	0.542012	0.960
7	980 – 1100	1.21992e+00	0.527916	0.978
8	1100 – 1380	1.21910e+00	0.533571	0.970
9	1380 – 1900	1.21785e+00	0.533758	0.971
10	1900 – 2620	1.21670e+00	0.536017	0.968
11	2600 – 3300	1.21589e+00	0.552097	0.945
12	3300 – 4000	1.21516e+00	0.527461	0.982
13	4000 – 4600	1.21494e+00	0.531716	0.976
14	4600 – 5300	1.21464e+00	0.529436	0.978
15	5300 – 6000	1.21439e+00	0.547547	0.965
16	6000 – 7000	1.21414e+00	0.535051	0.972
17	7000 – 12850	1.21356e+00	0.920825	0.904
18	12850 – 13150	1.21321e+00	0.996457	0.895
19	13150 – 14300	1.21316e+00	0.998005	0.894
20	14300 – 14450	1.21310e+00	0.998757	0.894
21	14450 – 14550	1.21310e+00	0.998877	0.894
22	14550 – 25000	1.21287e+00	0.999708	0.892
23	25000 – 31746	1.21257e+00	0.999235	0.885
24	31746 – 35710	1.21249e+00	0.998281	0.881

Table A.5: Spectral optical properties of graupel particles

No.	Bandwidth (cm^{-1})	Ext ($km^{-1}\frac{g}{m^3}^{-1}$)	ω_o	gg
1	20 – 340	2.31120e+00	0.569343	0.889
2	340 – 540	2.24813e+00	0.546775	0.945
3	540 – 620	2.23916e+00	0.551145	0.940
4	620 – 720	2.23528e+00	0.555140	0.935
5	720 – 800	2.23188e+00	0.560000	0.930
6	800 – 980	2.22590e+00	0.540830	0.961
7	980 – 1100	2.22535e+00	0.526664	0.978
8	1100 – 1380	2.22271e+00	0.533020	0.970
9	1380 – 1900	2.21855e+00	0.533894	0.969
10	1900 – 2620	2.21474e+00	0.536666	0.966
11	2600 – 3300	2.21202e+00	0.552933	0.941
12	3300 – 4000	2.20938e+00	0.529960	0.976
13	4000 – 4600	2.20885e+00	0.562389	0.956
14	4600 – 5300	2.20785e+00	0.534710	0.967
15	5300 – 6000	2.20699e+00	0.614605	0.937
16	6000 – 7000	2.20618e+00	0.560547	0.952
17	7000 – 12850	2.20422e+00	0.958804	0.899
18	12850 – 13150	2.20307e+00	0.998435	0.894
19	13150 – 14300	2.20289e+00	0.999120	0.894
20	14300 – 14450	2.20275e+00	0.999452	0.894
21	14450 – 14550	2.20279e+00	0.999505	0.894
22	14550 – 25000	2.20192e+00	0.999871	0.892
23	25000 – 31746	2.20091e+00	0.999662	0.885
24	31746 – 35710	2.20064e+00	0.999241	0.881

Appendix B

INDIVIDUAL BREAKDOWN OF THE SIMULATED WATER FIELDS

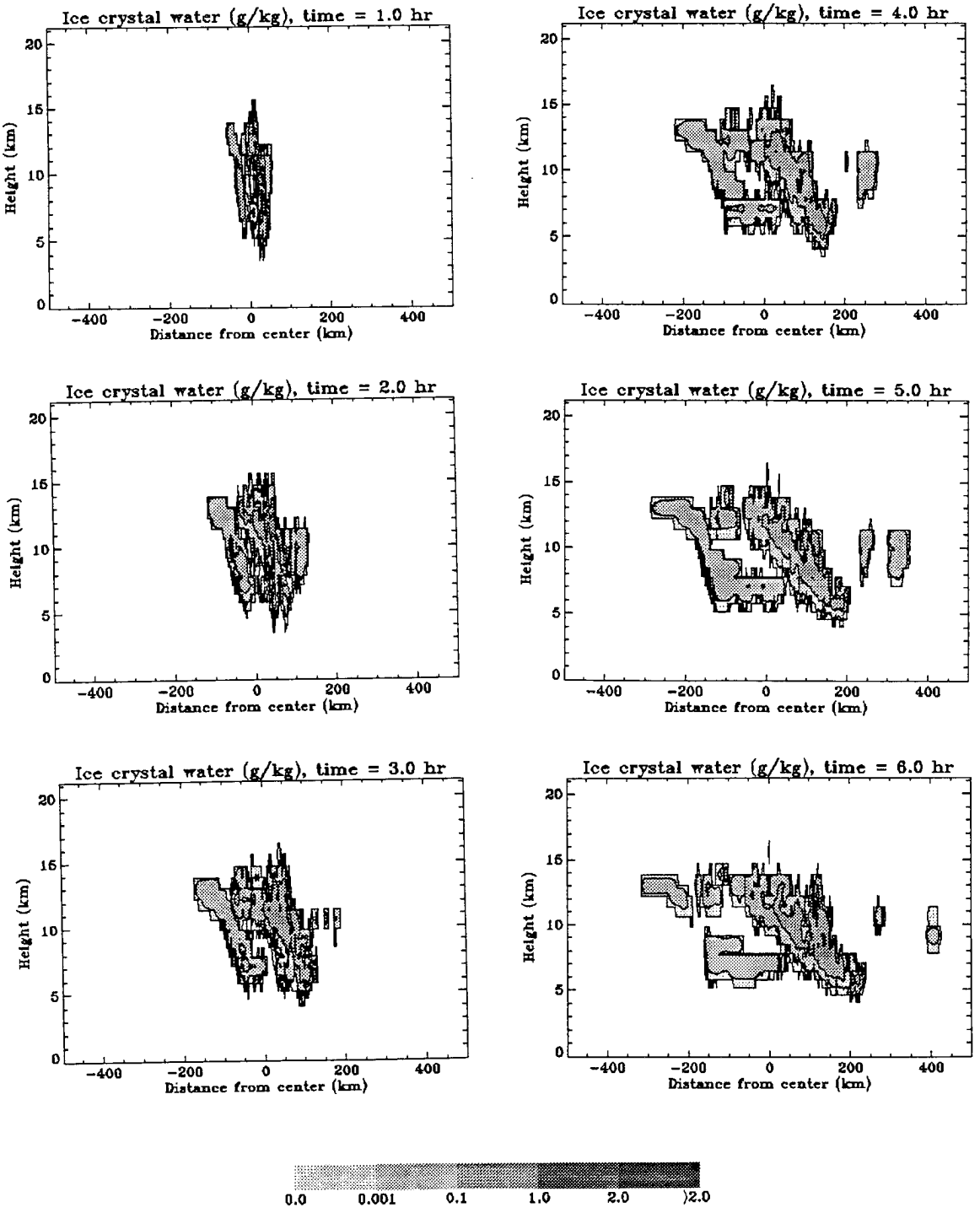

Figure B.1: Simulated two dimensional (X-Z cross-section) mixing ratio fields (g/kg) of ice crystals, as predicted by the CSU-RAMS cloud model at (a) 1 hour, (b) 2 hours, (c) 3 hours, (d) 4 hours, (e) 5 hours, and (f) 6 hours into the simulation of the EMEX-9 cloud cluster.

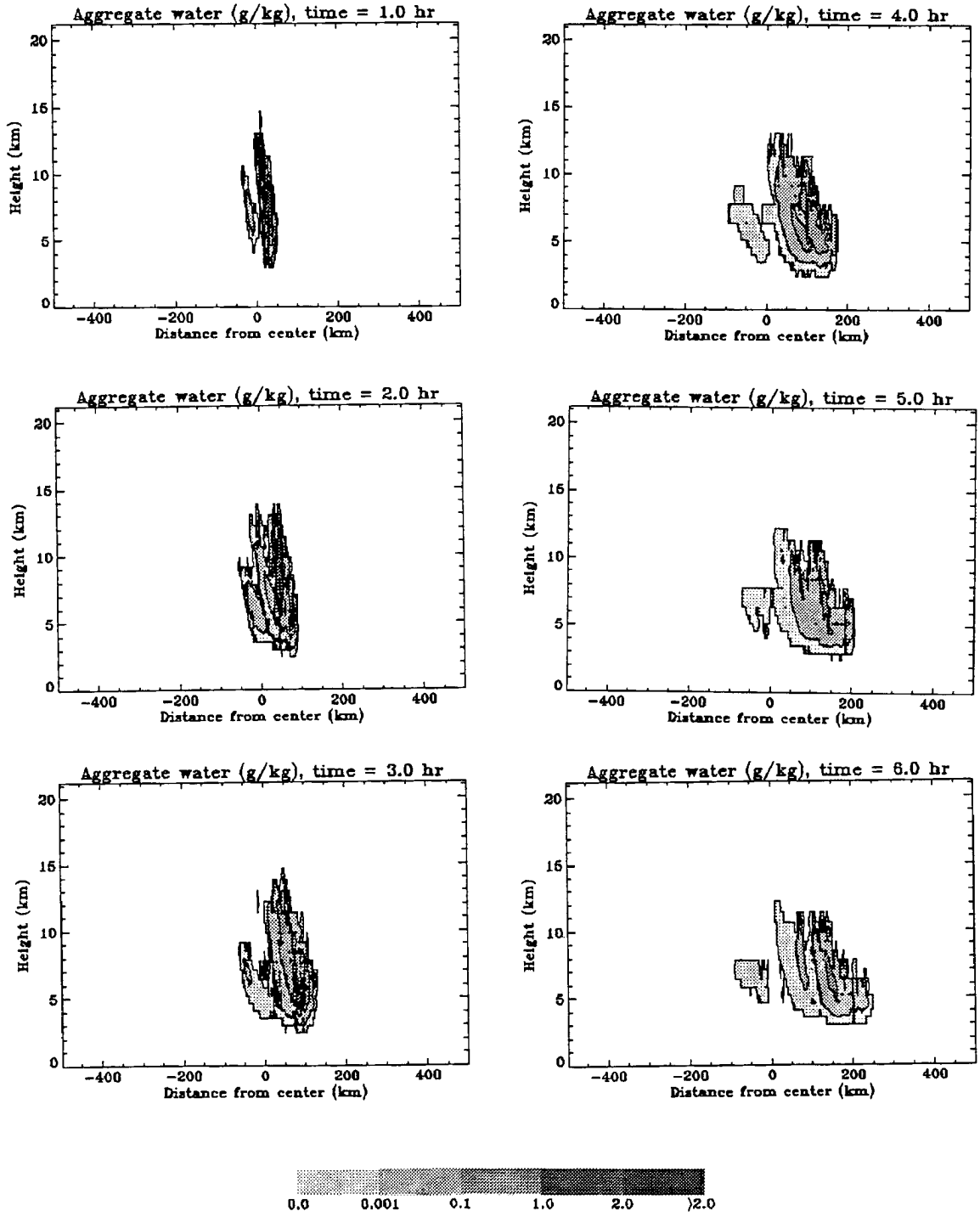

Figure B.2: Simulated two dimensional (X-Z cross-section) mixing ratio fields (g/kg) of aggregates as predicted by the CSU-RAMS cloud model at (a) 1 hour, (b) 2 hours, (c) 3 hours, (d) 4 hours, (e) 5 hours, and (f) 6 hours into the simulation of the EMEX-9 cloud cluster.

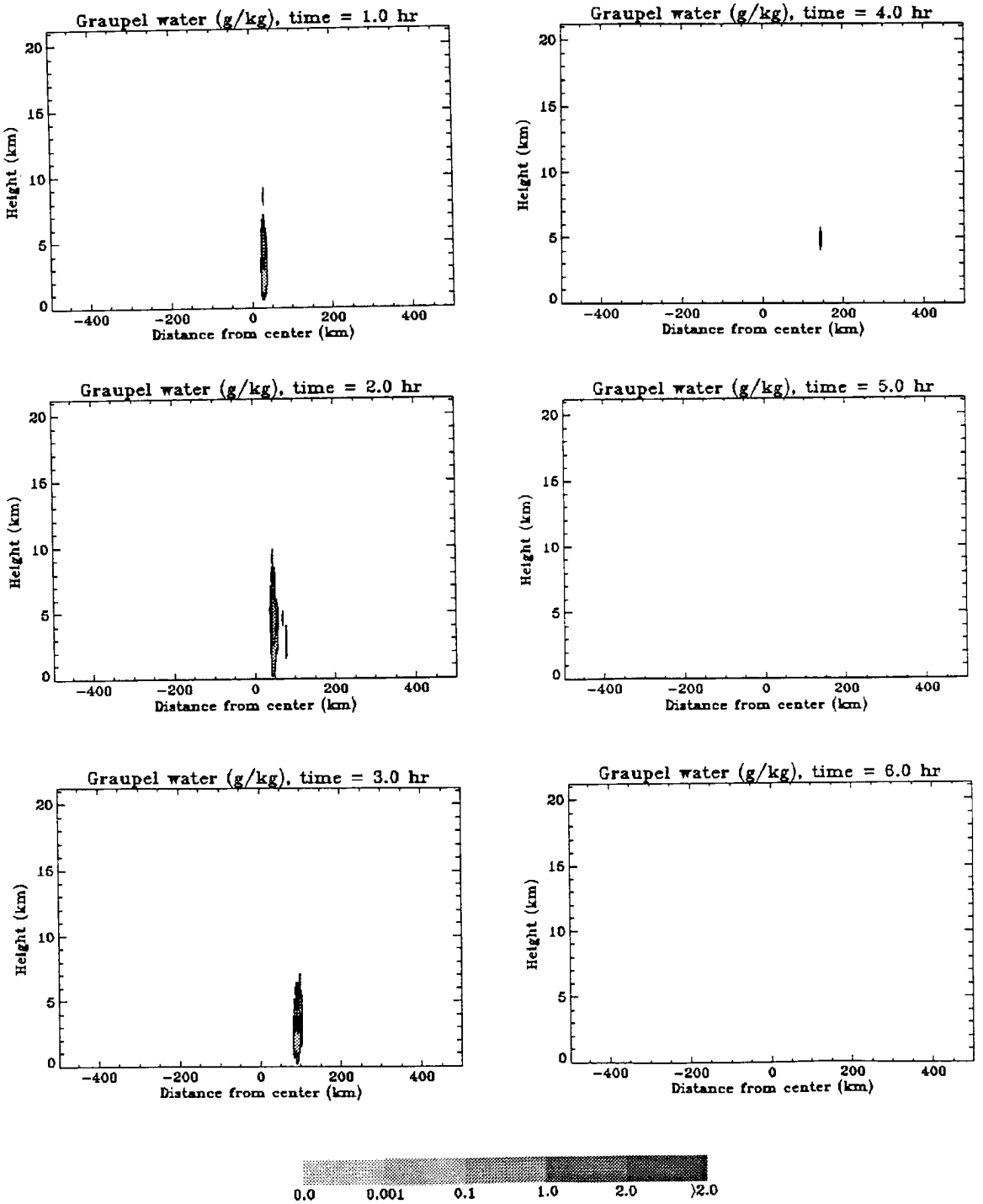

Figure B.3: Simulated two dimensional (X-Z cross-section) mixing ratio fields (g/kg) of graupels as predicted by the CSU-RAMS cloud model at (a) 1 hour, (b) 2 hours, (c) 3 hours, (d) 4 hours, (e) 5 hours, and (f) 6 hours into the simulation of the EMEX-9 cloud cluster.

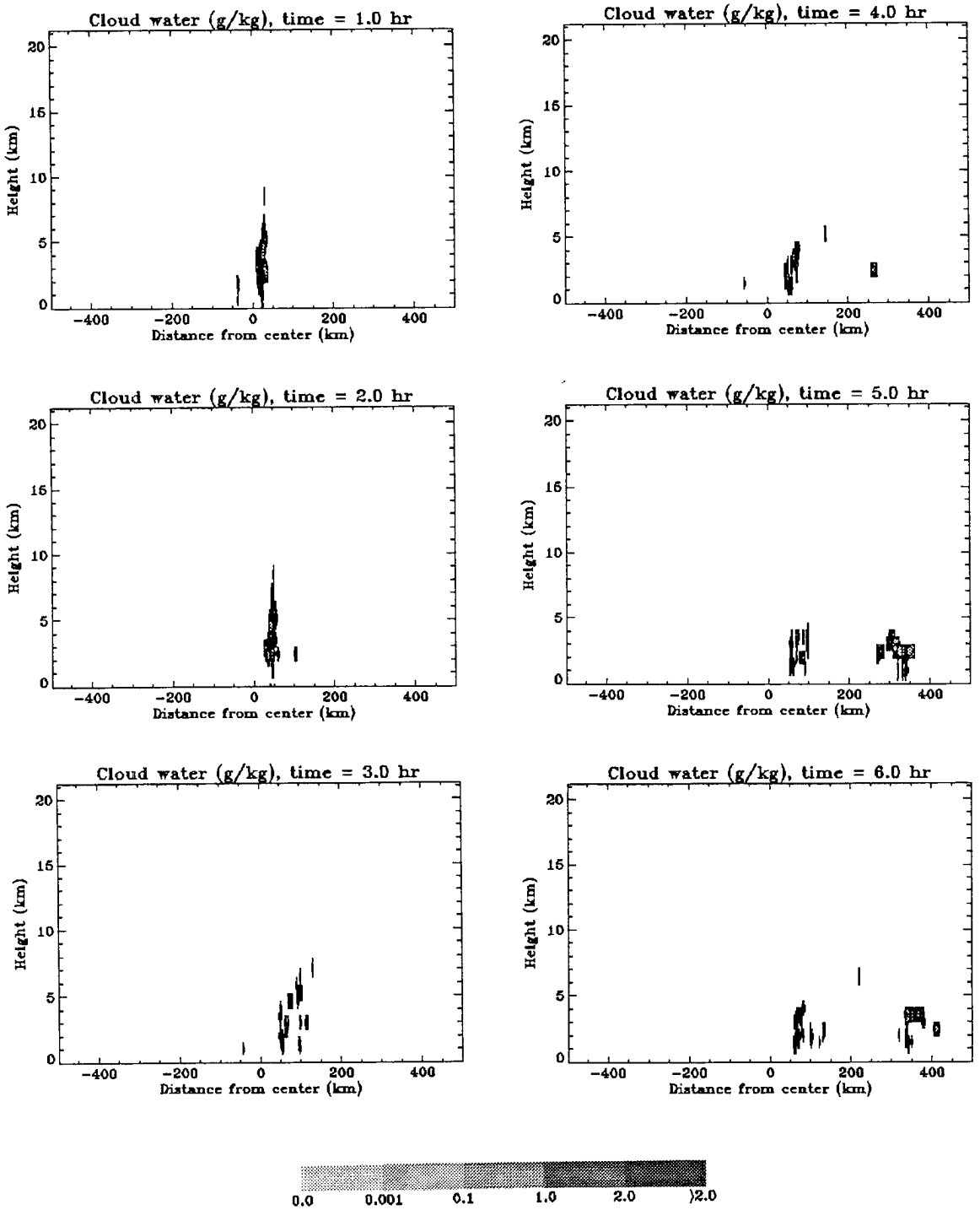

Figure B.4: Simulated two dimensional (X-Z cross-section) mixing ratio fields (g/kg) of cloud water as predicted by the CSU-RAMS cloud model at (a) 1 hour, (b) 2 hours, (c) 3 hours, (d) 4 hours, (e) 5 hours, and (f) 6 hours into the simulation of the EMEX-9 cloud cluster.

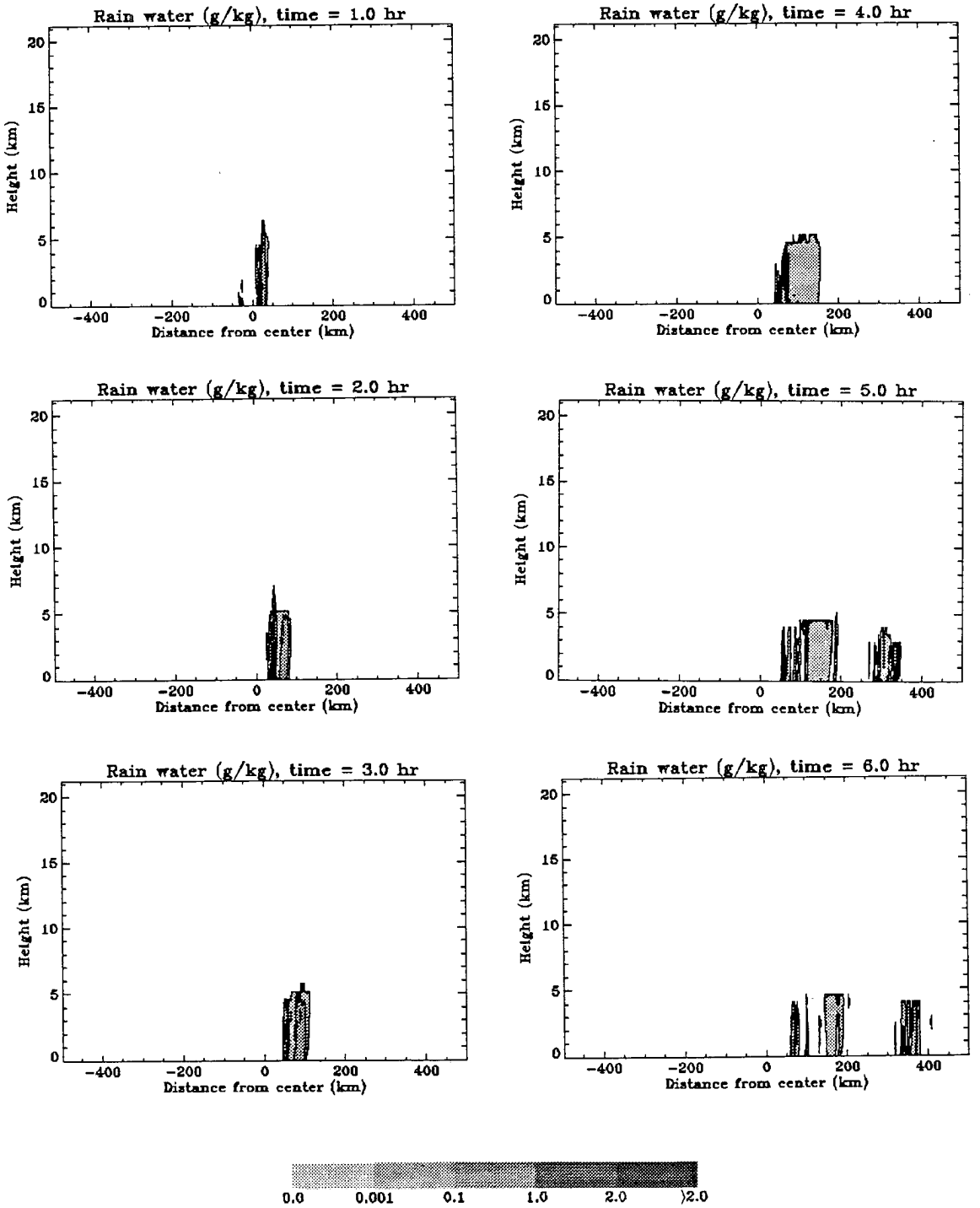

Figure B.5: Simulated two dimensional (X-Z cross-section) mixing ratio fields (g/kg) of rainwater as predicted by the CSU-RAMS cloud model at (a) 1 hour, (b) 2 hours, (c) 3 hours, (d) 4 hours, (e) 5 hours, and (f) 6 hours into the simulation of the EMEX-9 cloud cluster.

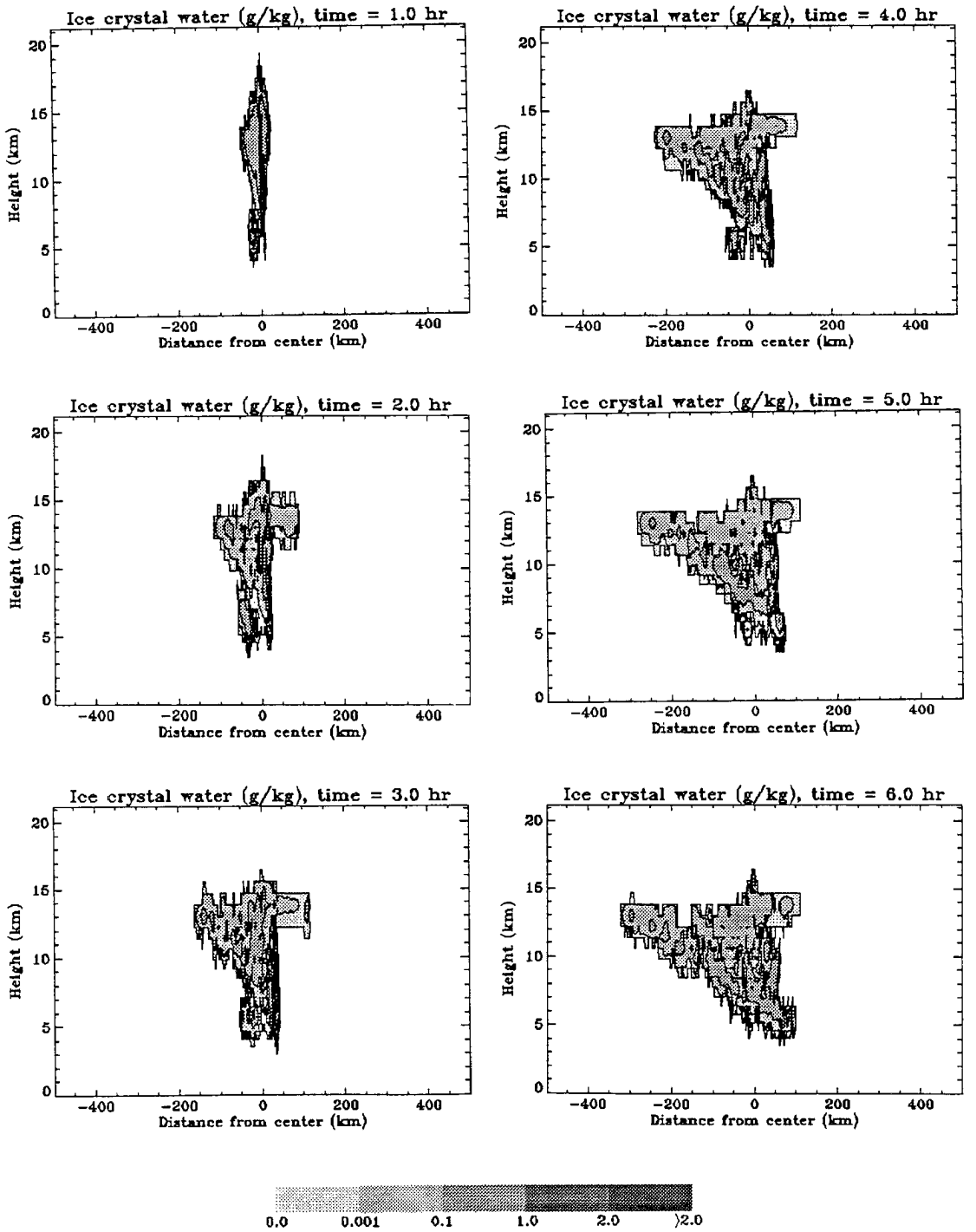

Figure B.6: Simulated two dimensional (X-Z cross-section) mixing ratio fields (g/kg) of ice crystals, as predicted by the CSU-RAMS cloud model at (a) 1 hour, (b) 2 hours, (c) 3 hours, (d) 4 hours, (e) 5 hours, and (f) 6 hours into the simulation of the DUNDEE cloud cluster.

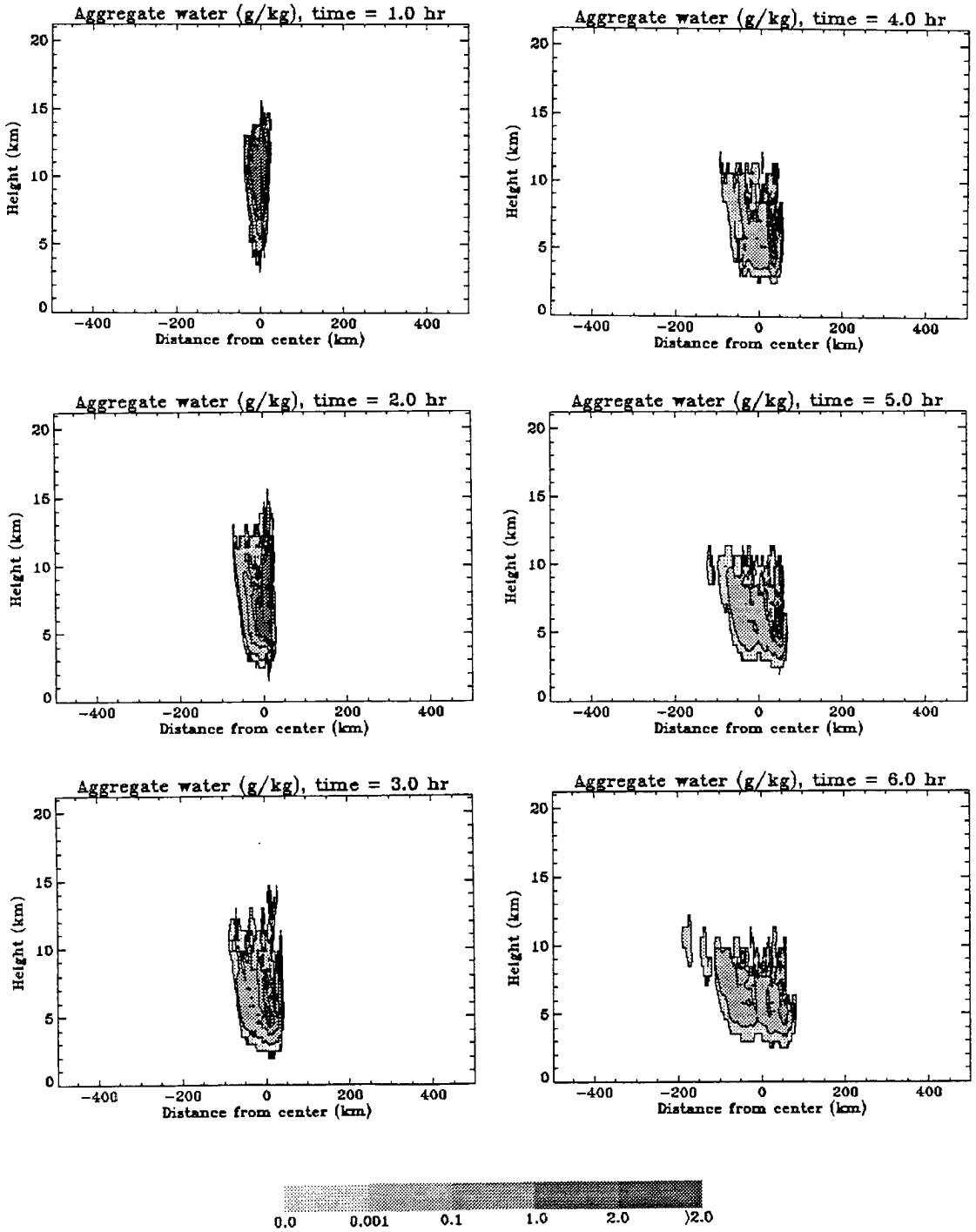

Figure B.7: Simulated two dimensional (X-Z cross-section) mixing ratio fields (g/kg) of aggregates as predicted by the CSU-RAMS cloud model at (a) 1 hour, (b) 2 hours, (c) 3 hours, (d) 4 hours, (e) 5 hours, and (f) 6 hours into the simulation of the DUNDEE cloud cluster.

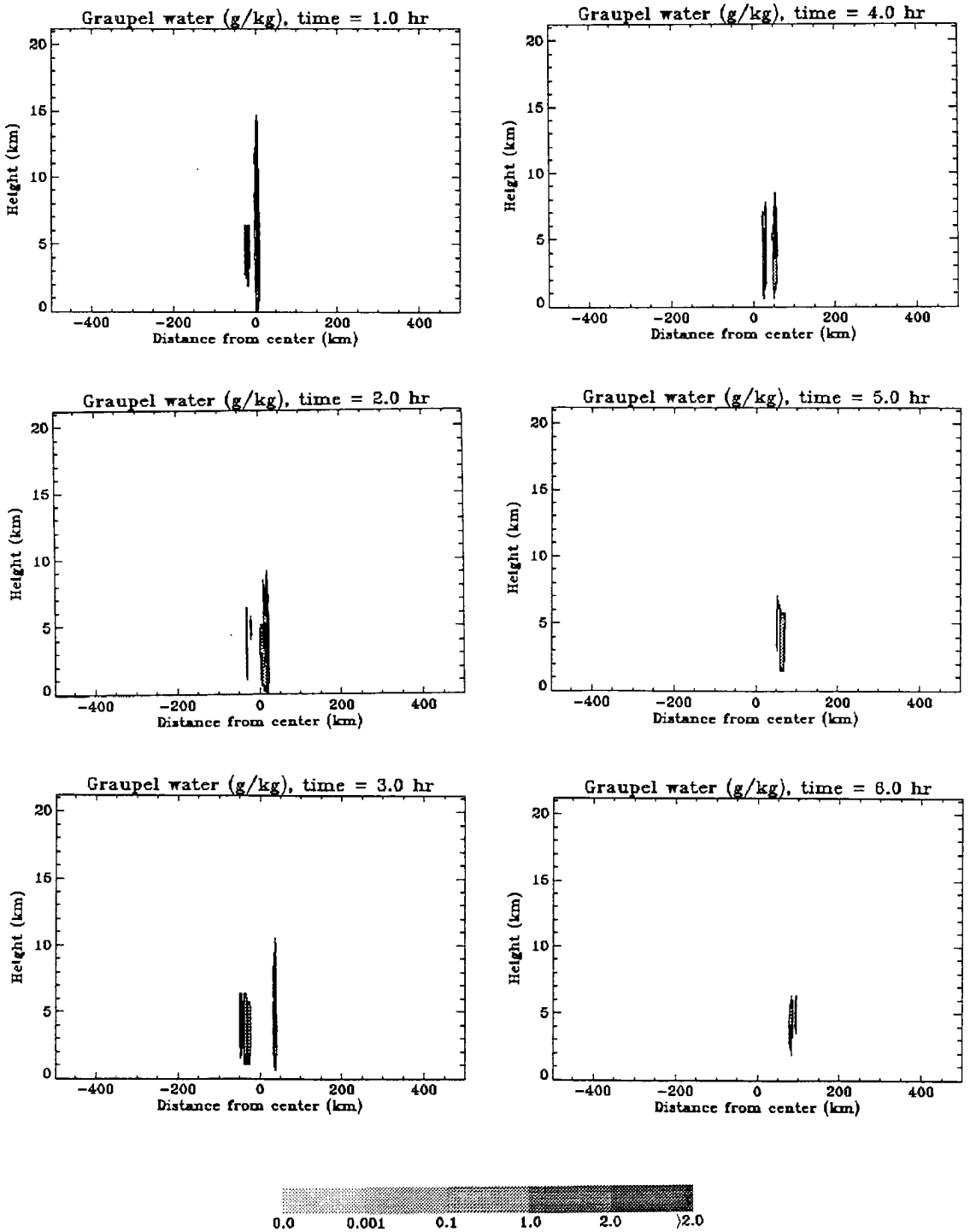

Figure B.8: Simulated two dimensional (X-Z cross-section) mixing ratio fields (g/kg) of graupels as predicted by the CSU-RAMS cloud model at (a) 1 hour, (b) 2 hours, (c) 3 hours, (d) 4 hours, (e) 5 hours, and (f) 6 hours into the simulation of the DUNDEE cloud cluster.

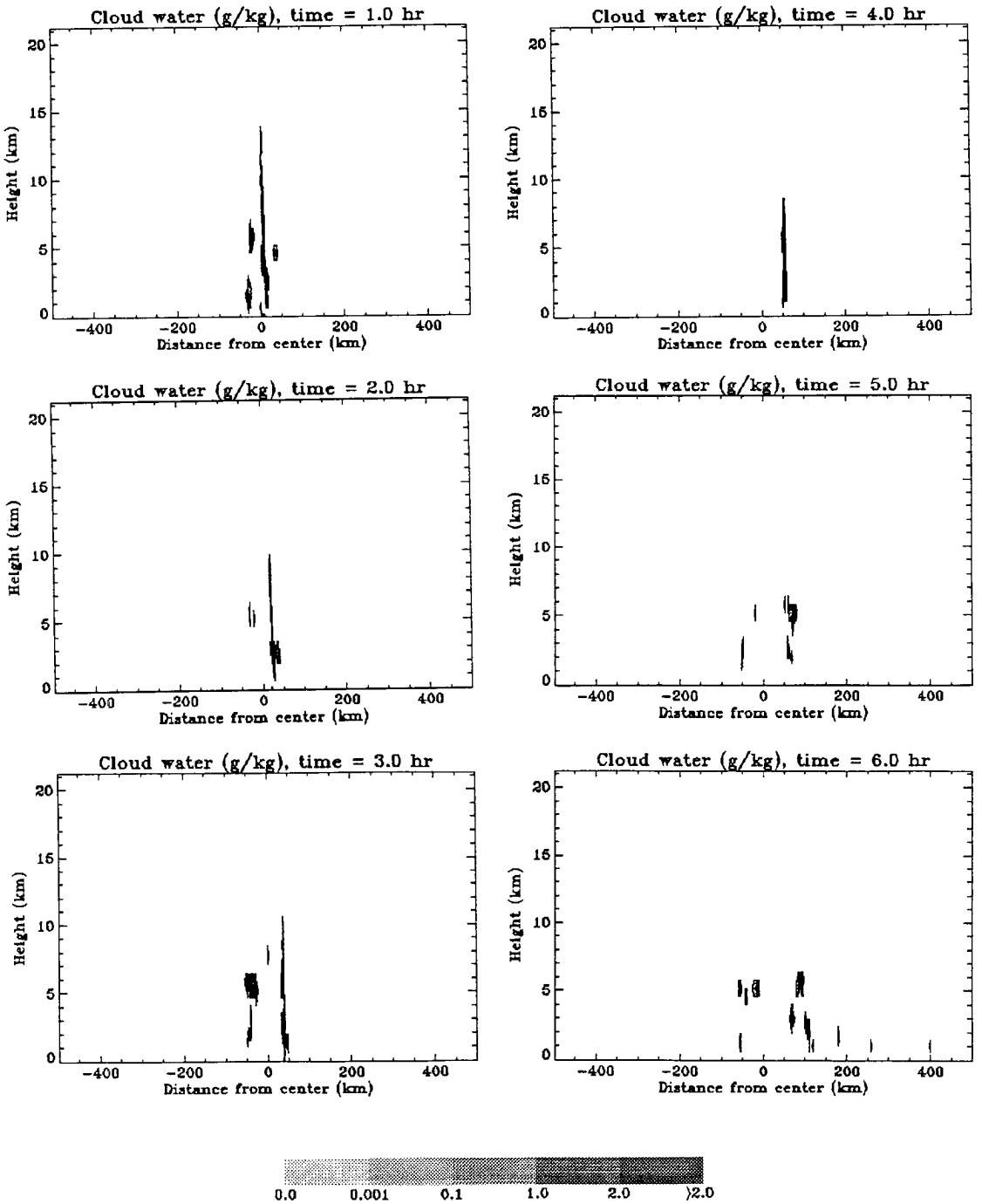

Figure B.9: Simulated two dimensional (X-Z cross-section) mixing ratio fields (g/kg) of cloud water as predicted by the CSU-RAMS cloud model at (a) 1 hour, (b) 2 hours, (c) 3 hours, (d) 4 hours, (e) 5 hours, and (f) 6 hours into the simulation of the DUNDEE cloud cluster.

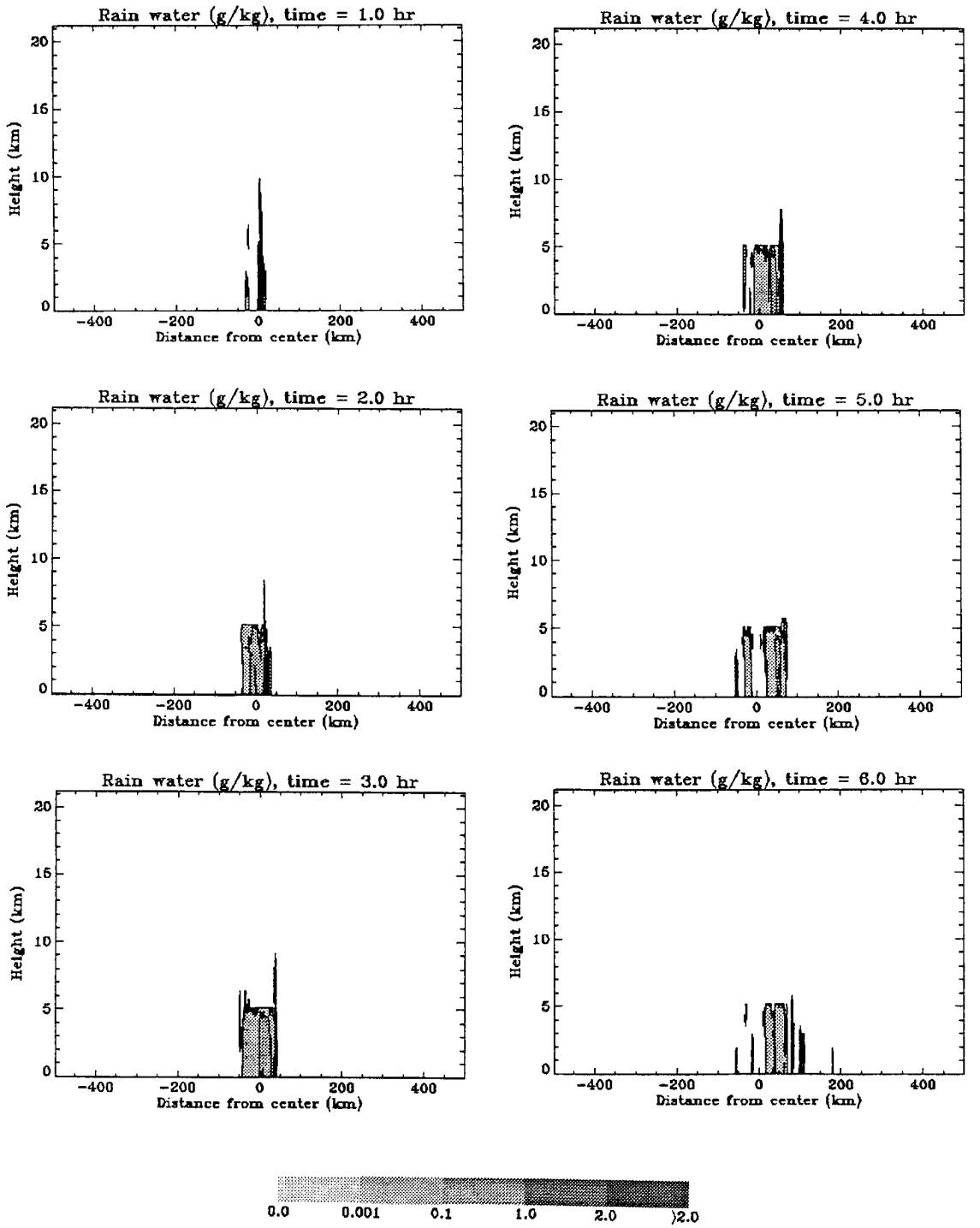

Figure B.10: Simulated two dimensional (X-Z cross-section) mixing ratio fields (g/kg) of rainwater as predicted by the CSU-RAMS cloud model at (a) 1 hour, (b) 2 hours, (c) 3 hour, (d) 4 hours, (e) 5 hours, and (f) 6 hours into the simulation of the DUNDEE cloud cluster.